



**Sum Frequency Generation Spectroscopy of  
Imidazolium–based Ionic Liquids with Cyano–functionalized  
Anions at Gas–Liquid and Solid–Liquid Interfaces**

---

**A Dissertation Presented to  
the Faculty of the Department of Chemistry  
University of Houston**

---

**In Partial Fulfillment  
of the Requirements for the Degree  
Doctor of Philosophy**

---

**By  
Chariz Y. Peñalber  
December 2012**

**Sum Frequency Generation Spectroscopy of  
Imidazolium-based Ionic Liquids with Cyano-functionalized  
Anions at Gas-Liquid and Solid-Liquid Interfaces**

---

Chariz Y. Peñalber

APPROVED:

---

Dr. Steven Baldelli, Chairman

---

Dr. Roman R. Czernuszewicz

---

Dr. Arnold M. Guloy

---

Dr. Allan J. Jacobson

---

Dr. Gila E. Stein

---

Dr. Mark A. Smith, Dean  
College of Natural Sciences and Mathematics

## ACKNOWLEDGEMENTS

My graduate experience here at the University of Houston has been a peculiar journey in creating new and innovative ideas in science, particularly in chemistry. In many ways, this journey has not only enabled me to steepen the slope of my learning curve; more than that, it became an avenue for me to build worthwhile relationships with colleagues in the field, as well as with people to whom I now would like to extend my deepest gratitude.

To my advisor, Dr. Steven Baldelli, I am most grateful of your constant presence at the lab, your encouragement, enthusiasm, and terrible dedication to the science. Your commendable work ethic has definitely influenced my character and it is safe to say that all these years of working with you has marked me for life (particularly on my right palm). All that you have taught me, both in and out of chemistry, I know I shall carry along with me for years to come. Thank you for helping me strive to reach my full potential, and for reinforcing my passion to learn something new on a daily basis.

To members of my research group, who have individually and collectively contributed to the success of my projects; thanks to Zlata, Joon Hee, Greggy, Emma, Michael, Dien, Quan, Ming, Rebecca, Jack, Marj, Tren, and Imee. My special thanks particularly to Cherry, for the long hours of training and introducing me to the details of the work. Also to Gabi, for the ionic liquid samples you have contributed (plus great cooking recipes).

To my favorite Motley crew at the department, Mark, Roger, Chris, Danny, and Pam. Random Friday lunches with you have always been a breath of fresh air. Your

pleasant company has made the difficult days of graduate school bearable. I especially appreciate Mark and Roger for helping me with glass-blowing, fixing vacuum pumps, and teaching me essential skills to perform the ‘manly work’. Our ‘counseling sessions’ on the days when my sanity was hanging by a thread, are proof of how much you both have become an integral part of my life. I could always use the good jokes y’all have and those stories of life’s little lessons. Really, I now believe that “it all started with the armadillo.”

To my friends whom I met here in Houston, no amount of words here can capture just how much you all have blessed me. Thank you to Dindi (my sister and roomie), Cata, Kim, Albert, Enrix, Ruji, Mike, John Glenn, Nissa, Solo, Maurice, John, Matty, Nathan, James, The Peñas, The Summers, The Pauls, my UH choir group, my Caritas Family, and my CNC friends. To Rads, thank you for ‘coercing’ me to apply to graduate school. To Thomas, you have never failed to do your best to help me when you could. Thank you for being so patient with me especially in editing all my manuscripts. To Joytoy, who has been the best sister and friend to me, I can’t imagine what it would have been like without you. There are just too many things that you’ve done for me. Through these years, you have truly been my family. To the Bohuslav family, I am so grateful of your kind and generous hearts. Thank you for giving me a home away from home, in its truest sense. For caring about me so genuinely, accepting me as I am and treating me as if I was your own.

To my family in the Philippines, especially to my parents, Abraham and Tita, I dedicate this thesis to you. The discipline and love you showed me has carried me through. You have always been my inspiration from the very start, I love you.

To The One in Whose Hands I was fearfully and wonderfully made, the highest honor and praise.

**Sum Frequency Generation Spectroscopy of  
Imidazolium–based Ionic Liquids with Cyano–functionalized  
Anions at Gas–Liquid and Solid–Liquid Interfaces**

---

**An Abstract of a Dissertation**

**Presented to**

**the Faculty of the Department of Chemistry**

**University of Houston**

---

**In Partial Fulfillment**

**of the Requirements for the Degree**

**Doctor of Philosophy**

**By**

**Chariz Y. Peñalber**

**December 2012**

## ABSTRACT

As essential media currently used in several technological applications, the accurate molecular level description of ionic liquids (ILs) at the gas-liquid interface is of utmost importance. The inherently surface-sensitive technique, sum frequency generation (SFG) spectroscopy, in combination with bulk-sensitive vibrational spectroscopic techniques such as FTIR and Raman, have been used in this report to characterize the surface of cyano-containing ILs, such as [BMIM][SCN], [BMIM][DCA], [BMIM][TCM], and [EMIM][TCB] at the gas-liquid interface. By structural variation of the anion while keeping the cation constant, emphasis on the molecular arrangement of the anion at the gas-liquid interface was reported.

Vibrational modes seen in the C–H stretching region revealed the presence of the cation with an orientation independent of the type of anion. A similar arrangement at the surface as reported in previous studies was found. All three anions of varying symmetry, namely, [DCA]<sup>−</sup> ( $C_{2v}$ ), [TCM]<sup>−</sup> ( $D_{3h}$ ), and [TCB]<sup>−</sup> ( $T_d$ ) in ILs [BMIM][DCA], [BMIM][TCM] and [EMIM][TCB] were significantly tilted from the surface plane, while the linear [SCN]<sup>−</sup> in [BMIM][SCN] exhibited poor ordering, seen in the absence of its C–N stretching mode in the SFG vibrational spectra.

Likewise, all four ILs in contact with two different solid salt surfaces, BaF<sub>2</sub>(111) single crystal and solid NaCl{100}, were discussed in this report. These studies described the nature of an ionic liquid–(solid) salt interface, contributing a new understanding to the molecular-level interactions involved in salts. Results showed that [BMIM]<sup>+</sup> cations adhered closely *via* Coulombic interactions to the negatively-charged

NaCl{100} surface, while [SCN]<sup>-</sup>, [TCM]<sup>-</sup>, and [DCA]<sup>-</sup> anions revealed a strong electrostatic affinity to the positively-charged BaF<sub>2</sub>(111) surface. Ions of the ionic liquid adsorbed to the solid salt surface to form a Helmholtz-like electric double layer.

At the BaF<sub>2</sub>(111)–[EMIM][TCB] interface, however, a strongly-bound layer of anions populating the first layer resulted to a much larger counter-ion charge delivered near the crystal salt surface than required to effectively neutralize the initial surface charge from the crystal. As a result, strong resonances from the cation were observed at the BaF<sub>2</sub>(111) surface, suggesting a more complicated structure of the double layer at the interface, than a simple Helmholtz-type model.

# TABLE OF CONTENTS

TITLE PAGE.....	i
SIGNATURE PAGE.....	ii
ACKNOWLEDGEMENTS.....	iii
ABSTRACT TITLE PAGE.....	v
ABSTRACT.....	vii
TABLE OF CONTENTS.....	ix
LIST OF FIGURES.....	xiii
LIST OF TABLES.....	xvii
Chapter 1: Introduction.....	1
1.1. Surface Science Techniques and Vibrational Spectroscopic Studies on Ionic Liquids..	2
1.2. Related Literature.....	5
1.2.1. Air–Liquid Interfaces.....	5
1.2.2. Solid–Liquid Interfaces.....	7
1.3. Objective and Scope of the Study.....	14
1.3.1. Imidazolium Ionic Liquids with Cyano–functionalized Anions.....	14
1.3.2. Summary of Chapters.....	16
1.4. References.....	19
Chapter 2: Theoretical Background.....	24
2.1. Vibrational Spectroscopy.....	24
2.1.1. Infrared Spectroscopy.....	25
2.1.2. Raman Spectroscopy.....	27
2.1.3. Nonlinear Optical Spectroscopy.....	30
2.1.3.1. Sum Frequency Generation (SFG).....	32
2.2. Summary.....	36
2.3. References.....	38
Chapter 3: Experimental Treatment.....	40
3.1. Ionic Liquid Samples.....	40

3.1.1.	[BMIM][SCN] .....	40
3.1.2.	[BMIM][DCA].....	42
3.1.3.	[BMIM][TCM] and [EMIM][TCB].....	42
3.2.	Purification and Preparation Prior To Measurements .....	43
3.2.1.	Drying Under High Vacuum .....	43
3.2.2.	Purity Analysis .....	47
3.2.2.1.	Chloride Analysis .....	47
3.2.2.2.	Water Content.....	52
3.3.	SFG Spectroscopic Measurements .....	53
3.3.1.	Nd:YAG Laser.....	53
3.3.2.	Optical Parametric Generation/Amplification System .....	54
3.3.3.	SFG Optical Setup.....	57
3.3.4.	Signal Detection System.....	60
3.3.5.	Calibration and Standards.....	61
3.4.	SFG at the Air–Liquid Interface.....	65
3.4.1.	SFG Cell .....	65
3.4.2.	Data Collection and Analysis .....	67
3.5.	SFG at the Solid Salt–Liquid Interface .....	68
3.5.1.	IL–BaF <sub>2</sub> (111) Interface .....	68
3.5.2.	IL–NaCl{100} Interface.....	69
3.5.3.	Purge Box Design and Setup.....	73
3.5.4.	Data Collection and Analysis .....	76
3.6.	Infrared Spectroscopy.....	76
3.7.	Raman Spectroscopy .....	77
3.8.	References .....	78
Chapter 4:	Surface Characterization of Imidazolium–based Ionic Liquids with Cyano–functionalized Anions at the Gas–Liquid Interface Using Sum Frequency Generation Spectroscopy .....	80
4.1.	Introduction .....	80
4.2.	Experimental Method .....	83
4.2.1.	Samples .....	83
4.2.2.	Data Collection and Analysis .....	83

4.3.	Results and Discussion .....	85
4.3.1.	Peak Assignments .....	85
4.3.2.	Infrared Spectra .....	85
4.3.3.	Raman Spectra .....	86
4.3.4.	SFG Spectra .....	89
4.4.	Conclusion .....	100
4.5.	References .....	101
Chapter 5: Observation of Charge Inversion of an Ionic Liquid at the Solid Salt–Liquid Interface by Sum Frequency Generation Spectroscopy .....		105
5.1.	Introduction .....	105
5.2.	Experimental Method .....	108
5.3.	Results and Discussion .....	109
5.4.	Conclusion .....	115
5.5.	References .....	116
Chapter 6: Sum Frequency Generation Spectroscopy of Imidazolium–based Ionic Liquids with Cyano–functionalized Anions at the Solid Salt–Liquid Interface .....		119
6.1.	Introduction .....	119
6.2.	Experimental Method .....	121
6.2.1.	Samples .....	121
6.2.2.	Experimental Setup and Sample Preparation Prior to SFG Measurements.....	121
6.2.3.	SFG Spectroscopy System and Data Collection .....	122
6.3.	Results and Discussion .....	123
6.3.1.	SFG Spectra .....	123
6.3.2.	Peak Assignments .....	124
6.3.3.	NaCl{100} Surface .....	125
6.3.4.	BaF <sub>2</sub> (111) Surface .....	132
6.3.5.	Discussion .....	136
6.4.	Conclusion .....	142
6.5.	Supporting Information .....	143
6.6.	References .....	146

Chapter 7: Concluding Remarks .....	149
APPENDIX.....	151
A: Phosphonium Ionic Liquids .....	151
I. Tetraalkylphosphonium–based Ionic Liquids at the Air–Liquid Interface.....	151
II. Tetraalkylphosphonium–based Ionic Liquids at Solid–Liquid Interfaces.....	169
B: Supplementary Information.....	172
I. NMR Spectra .....	172
II. Infrared Spectra .....	181
III. Raman Spectra .....	182

## LIST OF FIGURES

Fig. 1-1. Numbering scheme of [BMIM] <sup>+</sup> .....	5
Fig. 1-2. Molecular orientation of [BMIM] <sup>+</sup> at the gas–liquid interface. ....	5
Fig. 2-1. Energy level diagrams illustrating the two types of Raman Scattering.....	29
Fig. 2-2. Components of the incident electric fields with respect to the plane of incidence, $xz$ plane.....	34
Fig. 2-3. Energy level transitions for different vibrational spectroscopic techniques: Infrared absorption, SFG nonlinear spectroscopy and Raman Spectroscopy (inelastic) .....	37
Fig. 3-1. Reflux setup for the synthesis of [BMIM][Cl] .....	41
Fig. 3-2. Appearance of [BMIM][Cl] after reflux reaction.....	41
Fig. 3-3. Synthesis routes for the preparation of [BMIM][DCA] (A) and [BMIM][SCN] (B) ionic liquids.....	42
Fig. 3-4. Custom-built glass vacuum line with base pressure $\sim 2 \times 10^{-6}$ Torr.....	44
Fig. 3-5. Heated drying of [BMIM][Cl] on vacuum line prior to further characterization .....	45
Fig. 3-6. Vacuum cell used for drying ionic liquids up to $\sim 10^{-5}$ Torr. ....	45
Fig. 3-7. Calibration curve using [BMIM][Cl] .....	49
Fig. 3-8. Calibration curve using [EMIM][Cl] .....	49
Fig. 3-9. Nd:YAG laser system.....	53
Fig. 3-10. Top view of LaserVision OPG/OPA system with beam configuration.....	54
Fig. 3-11. Beam path and setup dimensions (in inches) from OPG/OPA system to sample stage.....	56
Fig. 3-12. Overall scheme of SFG optical setup .....	57
Fig. 3-13. SFG sample stage and beam configuration .....	59
Fig. 3-14. SFG detection system.....	60
Fig. 3-15. SFG spectrum of 0.038 mm polystyrene standard .....	62
Fig. 3-16. SFG spectrum of gold at the C–H region.....	63
Fig. 3-17. SFG spectrum of gold at the C–N region.....	63
Fig. 3-18. SFG spectrum of standard hexadecanol solution (aqueous) in <i>ssp</i> and <i>psp</i> polarizations .....	64
Fig. 3-19. Vacuum cell for SFG measurements at the air–liquid interface .....	65

Fig. 3-20. SFG cell for air-liquid measurements with filtration setup attached to vacuum line for drying .....	66
Fig. 3-21. Schematic illustration of solid-liquid SFG cell configuration for SFG measurements at the IL-BaF <sub>2</sub> (111) interface .....	68
Fig. 3-22. Experimental setup for IL-BaF <sub>2</sub> (111) interface studies .....	70
Fig. 3-23. Experimental setup for IL-NaCl{100} interface studies .....	71
Fig. 3-24. Experimental setup for vacuum drying of empty NaCl{100}-liquid interface cell prior to introducing IL sample .....	72
Fig. 3-25. Schematic illustration and dimensions of novel purge box design for SFG spectroscopic measurements at the IL-NaCl{100} interface .....	73
Fig. 3-26. Configuration of purge box assembly on SFG setup during real-time data acquisition .....	74
Fig 4-1. Imidazolium cation structure with numbering scheme, and structures of various anions involved in this work: a) thiocyanate [SCN] <sup>-</sup> , b) dicyanamide [DCA] <sup>-</sup> , c) tricyanomethanide [TCM] <sup>-</sup> , and d) tetracyanoborate [TCB] <sup>-</sup> .....	82
Fig 4-2. FTIR spectra of ionic liquids plotted near the C-N stretching region (1900-2300 cm <sup>-1</sup> ) and near the C-H stretching region (2700-3300 cm <sup>-1</sup> ), offset for clarity .....	86
Fig 4-3. Raman spectra of ionic liquids plotted near the C-N stretching region (1900-2300 cm <sup>-1</sup> ) and near the C-H stretching region (2700-3300 cm <sup>-1</sup> ), offset for clarity .....	87
Fig 4-4a. Sum frequency spectra of ionic liquids in the C-H stretching region at polarization combinations <i>ssp</i> (A), and <i>ppp</i> (B) .....	92
Fig 4-4b. . Sum frequency spectra of ionic liquids in the C-H stretching region at polarization combinations <i>sps</i> (C), and <i>pss</i> (D) .....	93
Fig 4-5. Sum frequency spectra of ionic liquids in the C-N stretching region at <i>ssp</i> polarization combination for [BMIM][SCN] (a), [BMIM][TCM] (b), [EMIM][TCB] (c) and both <i>ssp</i> and <i>ppp</i> combinations for [BMIM][DCA] (d) .....	94
Fig 4-6. [DCA] <sup>-</sup> anion showing C <sub>2</sub> axis of symmetry .....	96
Fig. 5-1. Sum frequency spectra ( <i>ssp</i> ) in the C-H stretching region of [BMIM][DCA] in contact with solid surfaces, NaCl{100} and BaF <sub>2</sub> (111). Spectra are offset by 0.05 .....	109

Fig. 5-2. Sum frequency spectra ( <i>ssp</i> ) in the C–N stretching region of [BMIM][DCA] in contact with solid surfaces, NaCl{100} and BaF <sub>2</sub> (111). Spectra are offset by 1.65 .....	110
Fig. 5-3. Helmholtz model for the molecular structure of [BMIM][DCA] in contact with solid single crystal salt surfaces, NaCl{100} and BaF <sub>2</sub> (111). .....	115
Fig. 6-1. Sum frequency spectra at the IL–NaCl{100} interface near the C–H stretching region at different polarization combinations .....	127
Fig. 6-2a. Sum frequency spectra at [BMIM][SCN]–BaF <sub>2</sub> (111) and [BMIM][DCA]–BaF <sub>2</sub> (111) interfaces near the C–N stretching region at different polarization combinations .....	128
Fig. 6-2b. Sum frequency spectra at [BMIM][TCM]–BaF <sub>2</sub> (111) and [EMIM][TCB]–BaF <sub>2</sub> (111) interfaces near the C–N stretching region at different polarization combinations .....	129
Fig. 6-3. Sum frequency spectra of [EMIM][TCB]–BaF <sub>2</sub> (111) interface in the C–H stretching region at different polarization combination.....	130
Fig. 6-1S. SFG spectra of IL–NaCl(100) interface: A) near the C–H stretching region in <i>pss</i> ; and B) near the C–N stretching region in <i>ssp</i> and <i>ppp</i> polarizations.....	143
Fig. 6-2S. SFG spectra of IL–BaF <sub>2</sub> (111) interface: A) near the C–H stretching region in <i>ssp</i> and <i>ppp</i> ; and B) near the C–N stretching region in <i>pss</i> polarization .....	144
Fig. 6-3S. SFG spectra of [EMIM][TCB]–BaF <sub>2</sub> (111) interface near the C–H stretching region in <i>pss</i> .....	145
Fig. 6-4S. SFG spectra of [BMIM][SCN]–BaF <sub>2</sub> (111) interface near the C–N stretching region at all polarization combinations .....	145
Fig. A-1. Structures of the ionic liquids investigated, which includes a series of six different alkyltrioctylphosphonium chlorides, trioctyl(5-cyanopentyl)phosphonium bromide, trihexyl(3-cyanopropyl)phosphonium bromide, tetradecyl(tri- <i>n</i> -hexyl)-phosphonium tetracyanoborate and methyl(diethyl)butylphosphonium bis{(trifluoromethyl)sulfonyl}amide .....	152
Fig. A-2. Structures of the ionic liquids tetrabutylphosphonium chloride [P <sub>4444</sub> ]Cl, tributyl(4-methoxybutyl)phosphonium chloride [P <sub>444-BuOMe</sub> ]Cl and trioctyl(2-methoxyethyl)phosphonium chloride [P <sub>888-EtOMe</sub> ]Cl.....	153
Fig. A-3. Sum frequency spectra of alkyltrioctylphosphonium chlorides, [P <sub>888n</sub> ]Cl where <i>n</i> = 4, 5, 8, 10, 12 and 14 at polarization combinations <i>ssp</i> (a), <i>ppp</i> (b), <i>sps</i> (c), and <i>pss</i> (d). The offsets are 0.50, 0.50, 0.15 and 0.15, respectively.....	159

Fig. A-4. Sum frequency spectra of tetraalkylphosphonium ionic liquids with various anions at polarization combinations <i>ssp</i> (a), <i>ppp</i> (b), <i>sps</i> (c), and <i>pss</i> (d). The offsets are 0.18, 0.25, 0.05 and 0.05, respectively .....	162
Fig. A-5. Sum frequency spectra of [P <sub>8 8 8 EtOMe</sub> ]Cl and [P <sub>8 8 8 4</sub> ]Cl at polarization combinations <i>ssp</i> (a), <i>ppp</i> (b), <i>sps</i> (c), and <i>pss</i> (d). The offsets are 0.20, 0.20, 0.06 and 0.06, respectively.....	166
Fig. A-6. Sum frequency spectra [P <sub>4 4 4 4</sub> ]Cl and P <sub>4 4 4 BuOMe</sub> ]Cl at polarization combinations <i>ssp</i> (a), <i>ppp</i> (b), <i>sps</i> (c), and <i>pss</i> (d). The offsets are 0.10, 0.15, 0.03 and 0.03, respectively .....	167
Fig. A-7. Sum frequency spectra in <i>ssp</i> of [P <sub>8 8 8 EtOMe</sub> ] Cl at three different temperatures: 0 °C, room temperature (20 °C) and 50 °C, offset by 0.05 for clarity .....	168
Fig. A-8. Sum frequency spectra of [P <sub>6 6 6 14</sub> ] [B(CN) <sub>4</sub> ]-NaCl{100} interface at <i>ssp</i> (a), <i>ppp</i> (b), <i>sps</i> (c) and <i>pss</i> (d) polarization combinations.....	169
Fig. A-9. Sum frequency spectra of [P <sub>6 6 6 14</sub> ] [B(CN) <sub>4</sub> ]-BaF <sub>2</sub> (111) interface at <i>ssp</i> (a), <i>ppp</i> (b), <i>sps</i> (c) and <i>pss</i> (d) polarization combinations .....	170
Fig. B-1. <sup>1</sup> H-NMR of [BMIM][SCN] in CD <sub>3</sub> CN.....	172
Fig. B-2. <sup>13</sup> C-NMR of [BMIM][SCN] in CD <sub>3</sub> CN.....	173
Fig. B-3. <sup>1</sup> H-NMR of [BMIM][DCA] in CDCl <sub>3</sub> .....	174
Fig. B-4. <sup>13</sup> C-NMR of [BMIM][DCA] in CDCl <sub>3</sub> .....	175
Fig. B-5. <sup>1</sup> H-NMR of [BMIM][TCM] in CD <sub>3</sub> CN .....	176
Fig. B-6. <sup>13</sup> C-NMR of [BMIM][TCM] in CD <sub>3</sub> CN .....	177
Fig. B-7. <sup>1</sup> H-NMR of [EMIM][TCB] in CD <sub>3</sub> CN.....	178
Fig. B-8. <sup>13</sup> C-NMR of [EMIM][TCB] in CD <sub>3</sub> CN.....	179
Fig. B-9. <sup>1</sup> H-NMR of [BMIM][Cl] in CDCl <sub>3</sub> , showing peaks from 1-methylimidazole starting material during insufficient drying in vacuum.....	180
Fig. B-10. IR Spectra of [BMIM][SCN], [BMIM][DCA], [BMIM][TCM] and [EMIM][TCB]	181
Fig. B-11. Raman Spectrum of [BMIM][SCN] .....	182
Fig. B-12. Raman Spectrum of [BMIM][DCA] .....	183
Fig. B-13. Raman Spectrum of [BMIM][TCM] .....	184
Fig. B-14. Raman Spectrum of [EMIM][TCB] .....	185

## LIST OF TABLES

Table 2-1. Polarization combinations in SFG and the $\chi_{xyz}^{(2)}$ elements contributing to the signal observed.....	35
Table 3-1. Measured Chloride Content of Ionic Liquids Using the Single Standard Addition Method (SSAM) After Contact With NaCl{100}.....	51
Table 4-1. Vibrational Frequencies and Peak Assignments for the Cyano Anions in IR, Raman and SFG Spectra .....	89
Table 4-2. Symmetry Approach to Anion Surface Configuration for [TCM]- and [TCB]-.....	98
Table 6-1. Observed SFG vibrational frequencies and assignments at IL–NaCl{100} and IL–BaF2(111) interfaces in the C–H stretching region at different polarization combinations..	131
Table 6-2. Observed SFG vibrational frequencies and assignments at IL–BaF2(111) interface in the C–N stretching region at various polarization combinations.....	135
Table A-1. Vibrational Assignments for Alkylammonium and Alkylpyrrolidinium ILs Used to Assign Spectra of Alkylphosphonium ILs .....	160
Table A-2. Vibrational Modes Observed for Alkyltrioctylphosphonium Chloride ILs.....	160
Table A-3. Vibrational Modes Observed for Tetraalkylphosphonium Ionic Liquids with Various Anions.....	163

## Chapter 1. Introduction

Room-temperature ionic liquids (RTILs) have drawn significant attention in the scientific community since their first discovery in 1914.<sup>1</sup> Indeed, even after all these years, these remarkable salts with melting points below 100 °C, still present a plethora of cation-anion combinations which remain to be explored, offering new and promising solutions to current scientific and technological demands. Most notable among the properties of RTILs are their conductivity, extremely low volatility, and exceptional miscibility behavior making them ideal for several applications, such as in electrochemistry,<sup>2,3</sup> catalysis,<sup>4-6</sup> and fluids engineering.<sup>7-9</sup>

Advancement in the field of ionic liquid technology requires a comprehensive understanding of their surface properties, since a wide range of chemical reactions occur mainly at interfaces. As essential media currently used in several technological applications, their accurate molecular level description at various interfaces is of utmost importance. In recent years, several techniques have been used to investigate the surface chemistry of ionic liquids; particularly, electrochemical methods, surface science techniques, and surface vibrational spectroscopy.

## 1.1. Surface Science Techniques and Vibrational Spectroscopic Studies on Ionic Liquids

Owing to the extremely low vapor pressures of RTILs,<sup>10</sup> surface science techniques have been used to characterize them as they are able to withstand demanding conditions required by such methods, namely, the ultra-high vacuum (UHV) pressures in the  $10^{-10}$  Torr range.<sup>11</sup> Because the chemical nature of the liquid surface is completely unique relative to that of the bulk, the use of surface-sensitive techniques is critical to probe such surfaces with atomic level accuracy. To name most, but not all UHV-based methods applied to RTILs would include X-ray photoelectron spectroscopy (XPS),<sup>12-16</sup> UV photoelectron spectroscopy (UPS),<sup>17,18</sup> inverse photoelectron spectroscopy (IPES),<sup>18,19</sup> metastable ion spectroscopy (MIES),<sup>17</sup> direct recoil spectroscopy (DRS),<sup>20,21</sup> near-edge absorption fine structure (NEXAFS),<sup>18</sup> and low-energy ion scattering (LEIS).<sup>12</sup> Comprehensive reviews of these UHV-based methods of surface science applied to ionic liquids have recently been reported in literature.<sup>6,11</sup> However, despite the wealth of information provided by these techniques, vibrational spectroscopy provides the most detailed model for the molecular structure and properties of ionic liquids on surfaces. More precise information at the molecular level may be derived from quantitative analysis of vibrational spectra. This, in tandem with the atomic level accuracy of surface-sensitive techniques, will serve to further the rapidly evolving field of ionic liquid surface studies.

A few notable vibrational spectroscopic techniques used to characterize ionic liquids on surfaces include, sum-frequency generation spectroscopy (SFG), infrared

reflection absorption spectroscopy (IRAS), surface-enhanced Raman scattering (SERS), and high-resolution electron energy loss spectroscopy (HREELS).

Up until the 1990's, the latter three techniques have been most useful in studies involving adsorption of molecules on metal single crystals at UHV pressures<sup>22</sup> thus, are typically not available to most neat liquid or solid-liquid interfaces. More recently, SFG has been widely used in investigating the molecular structure and orientation of several ionic liquids in various interfaces as this method is inherently surface-sensitive.<sup>23</sup> As a nonlinear, vibrational spectroscopic technique, SFG selectively detects molecules in a non-centrosymmetric environment. IRAS, on the other hand, lacks intrinsic surface sensitivity since it equally probes both the surface and bulk regions of the material. However, its high chemical resolution<sup>22</sup> allows detection of even the smallest changes in molecular structure. Moreover, it must be noted that a limitation for HREELS is the requirement for ultra-high vacuum pressures. HREELS is exclusively surface-sensitive due to the limited mean free path of electrons (few nanometers), but is limited to the UHV vacuum-liquid interface. Moreover, HREELS has the ability to collect the vibrational spectrum from 200 to 4000  $\text{cm}^{-1}$ . Although the resolution is very low,  $>50 \text{ cm}^{-1}$ , the large spectral range is useful in interpreting the ions at the surface. Other vibrational spectroscopies mentioned herein, i.e. infrared, Raman and SFG, have virtually no pressure restrictions as they are designed to work at ambient and more realistic pressure conditions with a variety of surfaces.

Vibrational spectroscopy is well suited to elucidating the details on the surface of ionic liquids. This is due to the high degree of chemical information that is provided in the vibrational spectrum. The various techniques mentioned each have advantages and

limitations but the level of information is clearly unique and highly informative. From the vibrational spectrum, information as to the identity of the molecules is available. However even more specifically, the chemical functional groups are identified as they each have unique vibrational resonances; for example, it is easy to distinguish CH<sub>2</sub>, CH<sub>3</sub>, CH, and X-CH<sub>*n*</sub> (*n*=1-3) from each other. Other functional groups are readily identified also.<sup>24</sup>

Another advantage of vibrational spectroscopy is the possibility to determine the orientation of the various functional groups at the surface. Both orientation and identity contribute to the surface properties. This is most commonly achieved using polarized infrared light at the surface. The maximum interaction (absorption) occurs when the electric vector of light is aligned to the transition dipole of the functional group. By varying the polarization of the light field and measuring the response, the orientation can be estimated. This can be performed on several vibrational modes to provide an overall structure of the ionic liquid ions at the surface.<sup>24</sup>

In some situations the vibrational peaks can be integrated and the concentration at the surface is determined. Although since the peak intensities also depend on the orientation, concentration is usually best determined by other techniques.

## 1.2. Related Literature

### 1.2.1. Air-Liquid Interfaces

There are numerous publications focused on the use of SFG spectroscopy to model the gas-liquid interface of several ionic liquids. Investigations have covered to a great extent, alkylimidazolium-based ionic liquids with various anions.<sup>25-29</sup> Other ionic liquid classes explored include ammonium<sup>30,31</sup> and pyrrolidinium-based<sup>31</sup> ILs. Recently, efforts have been extended toward investigating the surface orientation of tetraalkylphosphonium-based ionic liquids which are currently under study (See Appendix B).<sup>32</sup>

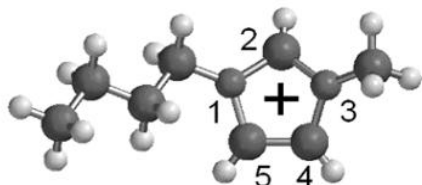


Fig. 1-1. Numbering scheme of [BMIM]<sup>+</sup>

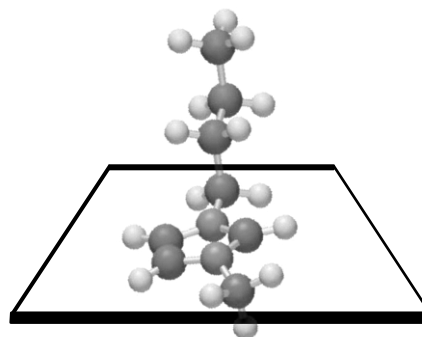


Fig. 1-2. Molecular orientation of [BMIM]<sup>+</sup> at the gas-liquid interface.

Fig. 1-1 and 1-2 depict the numbering scheme and the model for the molecular orientation of 1-butyl-3-methylimidazolium, [BMIM]<sup>+</sup>-based ionic liquids at the air-liquid interface, respectively. SFG results show that the butyl chain of the cation extends toward the gas phase with the imidazolium ring lying parallel to the surface plane. This configuration has been found to be consistent regardless of the anion<sup>27</sup> for BMIM-based

RTILs, particularly, whether the anions are composed of  $\text{Br}^-$ ,  $\text{I}^-$ ,  $\text{PF}_6^-$ ,  $\text{BF}_4^-$ ,  $(\text{CF}_3\text{SO}_2)_2\text{N}^-$  (imide),  $\text{SCN}^-$ ,  $\text{CH}_3\text{SO}_3^-$  ( $\text{MeSO}_3$ ),  $\text{CH}_3\text{SO}_4^-$  (MS), or  $(\text{CN})_2\text{N}^-$  (DCA). The SFG results reported were supported by FT-IR and polarized Raman spectroscopy with isotopic labeling. Works by Ouchi *et. al.*<sup>33</sup> have reached similar conclusions.<sup>33,34</sup>

For [BMIM][MS] and [BMIM][MeSO<sub>3</sub>], both anion and cation are found to occupy the first layer of the gas-liquid interface.<sup>26</sup> Systematic variation of the alkyl chain on both cation and anion for 1,3-dialkylimidazolium sulfates to investigate the driving force for orientation and partitioning of the ions at the air-liquid interface show findings that are consistent with the model described above.<sup>28,29</sup> Coulombic (as seen from ring orientation) and chain-chain interactions were considered in the study which suggested that both ions are found at the interface as evidenced by the presence of the methyl group vibration from the shortest chain cation and anion. The absence of ring modes from the imidazolium cation suggests that it lies parallel to the surface plane.

Using surface potential and surface tension measurements along with SFG, the results support that the relative position of the anion is at a slightly lower plane compared to the cation for [BMIM]-based ILs with anions of varying shapes and sizes. Surface potential, in addition to SFG vibrational spectra, helped determine the positions of the ions by measuring its contribution to the total potential.<sup>25</sup> Furthermore, it has been reported that at this interface, there is a decreasing trend in surface tension values as the alkyl chain on the cation is increased.<sup>29</sup>

To further illustrate the arrangement of anions at the air-liquid interface, 1-butyl-3-methylimidazolium trifluoromethanesulfonate [BMIM][OTf] has been studied using SFG.  $\text{CF}_3$  symmetric and  $\text{SO}_3$  symmetric stretching modes pertaining to the [OTf] anion

at the low-frequency region were observed implying the presence of anions at the interface. Moreover, it was found that the amplitude of the  $\text{CF}_3$  symmetric stretch peak of the [OTf] anion has an opposite sign with respect to that of the  $\text{SO}_3$  symmetric peak, indicating that [OTf] anions have polar ordering at the surface. The nonpolar  $\text{CF}_3$  group points towards the gas phase, whereas the  $\text{SO}_3$  group points toward the bulk liquid.<sup>35</sup> As for HREELS backed-up by density functional theory (DFT) calculations on 1-ethyl-3-methylimidazolium bis(trifluoromethylsulfonyl)amide, [EMIM][imide] surface – vacuum interface,<sup>36</sup> it was found that the most pronounced structures in the spectra were related to coupled antisymmetric O=S=O and  $\text{CF}_3$  stretching modes of the anion.

In SFG studies involving ammonium and pyrrolidinium-based ILs, structures were systematically varied by attaching alkyl substituents of different lengths and functional groups. Ordering of the chains at the topmost layer was found to be strongly dependent on alkyl chain length with gauche defects observed for ones with longer alkyl chains. Moreover, interfacial structure changed upon the addition of an oxygen atom in the aliphatic chain as it introduced additional interactions due to the presence of a heteroatom, i.e. hydrogen-bonding, ion-dipole and dipole-dipole. A similar structure for pyrrolidinium imides was observed in relation to imidazolium-based analogs in that the ring appears to be lying parallel to the liquid surface plane.

### **1.2.2. Solid-Liquid Interfaces**

Several publications found in the literature involving ionic liquid studies on liquid-solid surfaces include the IL/Quartz,<sup>37,38</sup> IL/ $\text{TiO}_2$ <sup>39</sup>, and IL/Pt interfaces.<sup>40-43</sup>

Data has shown that for [BMIM][BF<sub>4</sub>] and [BMIM][PF<sub>6</sub>] on the surface of an equilateral quartz prism, spectra for both ionic liquids display similar vibrations from both alkyl chain and aromatic ring. The anion size influenced the orientation of the molecule such that tilt angles from the surface normal for the aromatic ring differed for both, with [BMIM][BF<sub>4</sub>] higher than that of [BMIM][PF<sub>6</sub>]. Also, the study suggests that the anion is positioned next to the cation adsorbed to the quartz surface. The methyl group for the butyl chain lies nearly parallel to the surface for [BMIM][BF<sub>4</sub>].<sup>37</sup> Comparing these observations with similar studies done by Fitchett, Conboy<sup>44</sup>, and Rollins<sup>45</sup> on the same interface, Fitchett *et al.* postulated that as the size of the anion is increased, the orientation of the cation is tilted upward towards surface normal. Since the [PF<sub>6</sub>]<sup>-</sup> anion is 10% larger than [BF<sub>4</sub>]<sup>-</sup>, it causes the ring of the cation to tilt more toward the surface normal.<sup>37</sup> Furthermore, the authors concluded that independent of the anion composition, the imidazolium ring orients more parallel to the silica surface as the alkyl chain length decreases.<sup>45</sup>

The structure of ionic liquids on fused IR quartz modified by deuterated dodecyltricholasilane to give a hydrophobic surface has been investigated.<sup>38</sup> Using [BMIM][BF<sub>4</sub>] and [BMIM][PF<sub>6</sub>], it was found that terminal methyl group was arranged toward the alkylsilane monolayer, with the imidazolium ring lying in the plane of the interface. Orientation of the methyl group was found to be only slightly affected for both ILs since the anion was found close to the cation ring due to Coulombic interactions. Comparing results on three different interfaces, data suggests the following: 1) At the IL/quartz interface, the methyl group orient toward the surface normal as the surface becomes more hydrophobic; 2) At the gas-liquid interface, the anion does not affect the

cation orientation;<sup>27</sup> and 3) For the hydrophobic quartz interface, the orientation of the cation is influenced by the type of anion, such that the more hydrophobic anion [PF<sub>6</sub>]<sup>-</sup>, has greater attraction to the nonpolar silane monolayer, while the hydrophilic anion, [BF<sub>4</sub>]<sup>-</sup>, is more attracted to the polar C(2)-H group on the imidazolium ring. On hydrophilic surfaces, ILs form weak hydrogen bonds between the nitrogen atoms of the ring and anions adsorb to the surface causing the cation to tilt toward the surface normal.

In contrast to the mirror-like, polished quartz surface, ionic liquids on a relatively “rougher” surface of TiO<sub>2</sub> have been studied using ILs [BMIM][DCA] and [BMIM][MS] probed by SFG.<sup>39</sup> Both cation and anion were present at the interface for [BMIM][DCA] while only the cation was detected for [BMIM][MS]. The imidazolium ring lies nearly parallel to the TiO<sub>2</sub> surface as further supported by contact angle and surface charge density calculations. Specific adsorption of [DCA]<sup>-</sup> was found in contrast to a weak adsorption of [MS]<sup>-</sup> as [DCA]<sup>-</sup> tends to bind to titanium sites at the surface of TiO<sub>2</sub>. This was seen in the unusually strong SFG signal in the C-N stretching region. Moreover, strong methylene contributions were attributed to surface roughness of the TiO<sub>2</sub> as it is composed of particles of approximately 2.5 nm in diameter as opposed to a polished quartz surface.

In an effort to provide a model for ionic liquids similar to the Gouy-Chapman-Stern model, which appropriately describes the organization of solvent and ions in normal electrolytic solutions, a few studies have probed various IL/Pt electrode interfaces using SFG. To date, there is still no adequate description to explain the arrangement of the ions in pure ionic compounds such as ionic liquids adjacent to electrode surfaces. Initial studies using [BMIM][BF<sub>4</sub>] and [BMIM][PF<sub>6</sub>] ILs showed that the imidazolium

ring conformation changes from  $35^\circ$  from the surface normal at positive surface charge to  $60^\circ$  at negative surface charge. The methyl group for [BMIM][BF<sub>4</sub>] shows a more perpendicular orientation at positive potentials while for [BMIM][PF<sub>6</sub>], methyl group analysis suggests that the butyl chain is more parallel to the surface.<sup>42</sup> Moreover, the ions were found to orient at the interface depending on electrode charge with a layer structure at the electrode surface composed of a one-ion-layer of the Helmholtz-type and ruling out a multilayer structure.<sup>41</sup>

Using electrochemical impedance spectroscopy (EIS) with SFG, a description of the [BMIM][BF<sub>4</sub>]/Pt electrode interface was further investigated.<sup>43</sup> Vibrational Stark shift served as an independent measure of the thickness of the “double layer” which suggested that the ions organized in a Helmholtz-like layer in agreement with initial studies. SFG results showed that the structure at the interface was potential-dependent with anions adsorbed to the surface at positive potentials relative to the potential of zero charge (PZC). This causes the imidazolium ring to be repelled and thereby orient more along the surface normal. At negative potentials however, the cation is oriented more parallel to the surface plane with the anions repelled from the surface. A very thin “double layer” structure at the surface with ions forming a single layer (as seen from interfacial capacitance and vibrational Stark shift of CO) at the interface and screening the electrode charge was proposed. Similarly, in-situ SFG results done by Zhou, *et al.*<sup>46</sup> proved the existence of a one ion layer and a diffuse layer species. Their findings suggested that the ions on the [BMIM][OTf]/Pt interface are present as a double layer structure. It was further postulated that the adsorption/desorption hysteresis of ILs at electrode surfaces

can be changed by varying the structure of the anions and the cations, as it is most possibly an intrinsic property of the RTIL.

In contrast to the behavior observed for [BMIM][BF<sub>4</sub>] and [BMIM][PF<sub>6</sub>], potential-dependent spectra of [BMIM][DCA] at the liquid/Pt interface suggests a multilayer structure of the Helmholtz-type. Strong C–N vibrations observed for the anion suggests increased ordering as the [DCA] anion tends to align itself to the surface normal with increasing potential. Signal strength may also come from increased [DCA] concentration at the electrode surface for positive surface charge excesses. The appearance of symmetric ring vibrations from the cation at positive potentials denote that the ring is repelled from the electrode and tilting towards the surface.<sup>40</sup>

Model studies under UHV conditions aimed to better understand the interaction of IL films with oxide supports have been performed using thin films of [BMIM][imide].<sup>47</sup> With the use of IRAS in combination with DFT, thin films of the IL were grown on an atomically flat, well-ordered alumina film on NiAl(110) by evaporation. Results from the time-resolved IRAS measured during the growth and desorption of the films indicated no decomposition. Strong changes in intensity for individual anion bands were observed in the monolayer region, indicating orientation effects. The results further suggested that [imide] anions adopted a *cis* conformation in the submonolayer region, adsorbing in a slightly tilted orientation with respect to the surface and mainly interacting with the oxide support through the sulfonyl groups. The study proposed a model of the most probable orientation of the [Tf<sub>2</sub>N]<sup>−</sup> anion on Al<sub>2</sub>O<sub>3</sub>/NiAl(110) in the submonolayer region, resulting from fitting DFT calculations to IRAS measurements.

To obtain more insight into the surface chemistry of supported-IL-based catalysts, combined methods of time-resolved IRAS and XPS were used to investigate thin films of IL [BMIM][imide] deposited by physical vapor deposition (PVD) onto a model surface consists of Pd nanoparticles grown in UHV on an ordered alumina film on NiAl(110).<sup>48</sup> Results showed that the IL molecularly adsorbs onto both Pd particles and alumina at 300 K. IR spectra reveal that the anions interact with the Pd sites preferentially through the sulfonyl groups. Furthermore, upon heating to temperatures higher than 400 K, which is the desorption temperature of the IL, molecular desorption competes with decomposition. On the other hand, CO pre-adsorbed on the Pd particles is partially displaced by the IL, even at 300 K.

SERS spectra at IL/silver<sup>49,50</sup> and IL/copper<sup>51,52</sup> surfaces have been reported in literature where the first report of in situ SER was done on [BMIM][PF<sub>6</sub>] adsorbed on a silver electrode. Results showed that the cation adsorbs on the silver electrode for potentials more negative than -0.4 V vs. a Pt quasi-reference electrode (PQRE). Moreover, at potentials less negative than the PZC (ca. -1 V vs. PQRE), the cation adsorbs on the Ag surface with the imidazolium ring almost perpendicular to the surface. At negative potentials relative to the PZC however, the imidazolium ring stays almost parallel to the surface, and is reduced to a BMIM<sup>+</sup> carbene at -3.0 V.<sup>49</sup>

SERS spectra taken using Ag nanoparticles (NPs) dispersed in IL [BMIM][BF<sub>4</sub>] and from an island film spin-coated with [BMIM][BF<sub>4</sub>],<sup>50</sup> showed enhancement of the [BF<sub>4</sub>] symmetric stretching signal for Ag island films. No enhancement, however, was observed for the Ag NPs/IL interface. Results were explained on the point of view of the effect of water molecules on the structure of the IL on the different substrates used,

supporting that the presence of water in the Ag NPs/IL promoted aggregation of the Ag nanoparticles.

Electrochemical measurements in tandem with SERS on [BMIM][BF<sub>4</sub>]/copper electrode interface<sup>51</sup> reveal that the copper electrode has an electrochemical window of approximately 2.5 V in the IL and that the Cu<sub>2</sub>O film is present in the copper electrode surface prior to the SERS activation procedure. No considerable interaction of the anions and the metal surface was found, however, some cation vibrational modes show significant changes in the applied potentials as shifts in the wavenumber position and intensities. At potentials negative to the PZC, the cation interacts with the surface through a partial charge transfer culminating in the reduction of the cation at approximately -2.6 V.

A related study on the spectroelectrochemical behavior of a copper electrode in [BMIM][BF<sub>4</sub>] containing benzotriazole (BTAH) has been investigated by cyclic voltammetry and SERS.<sup>52</sup> A considerable decrease in the anodic currents in the presence of BTAH as seen in the cyclic voltammograms suggests that BTAH inhibits the oxidation of copper in the IL. The SERS results have shown that at potentials positive to the PZC for copper in the IL, a [Cu(I)BTA]<sub>n</sub> polymeric film is formed as BTAH interacts with the copper (I). The polymeric film is responsible for the corrosion inhibition process. However, at potentials negative to the PZC, BTAH is found to adsorb chemically on the copper surface. This phenomenon is determined by the observation of the  $\nu(\text{Cu-N})$  stretching mode and by the  $\delta(\text{N-H})$  bending mode.

### 1.3. Objective and Scope of the Study

#### 1.3.1. Imidazolium Ionic Liquids with Cyano-functionalized Anions

Ionic liquids with cyano-functionalized anions, despite reports of their successful preparation a few years ago<sup>53-56</sup>, have not gained much attention in the literature. As can be seen in experimental data, the properties of ionic liquids rely mainly on the structure and composition of the cation and anion pair. The tunability and versatility of their properties is a result of the ease with which the composition may be varied using a number of different combinations of the charged moieties.

Ionic liquids incorporating cyano anions are known to have low melting points, low viscosities, and high thermal stability compared to analogs lacking cyano-based anions.<sup>56-58</sup> This makes them particularly attractive for applications such as in dye-sensitized solar cells (DSCs),<sup>59-61</sup> in which the key factor for promising electrolyte systems require solvent alternatives of relatively low viscosity.

The limited use of IL-based DSCs to date, is due to the low photovoltaic performance associated with the high viscosity of ILs, which restricts mass-transfer of the photocurrent under full sunlight operation.<sup>61</sup> Indeed, ionic liquids based on dicyanamide [DCA]<sup>-</sup>, tricyanomethanide [TCM]<sup>-</sup> and tetracyanoborate [TCB]<sup>-</sup> anions, especially, have been reported to confer low viscosities, *i.e.* 17 cP (at 22 °C) for [EMIM][DCA]; 18 cP (at 22 °C) for [EMIM][TCM]; and 19 cP (at 20°C) for [EMIM][TCB].<sup>55,62</sup> These values were found to be promisingly low, compared for example, to the more popular and well-studied fluorine-containing ionic liquids such as [EMIM][Tf<sub>2</sub>N], which has a viscosity of 27 cP at 20 °C.<sup>63</sup>

Another reason why cyano-based ionic liquids have limited published data is the fact that only in recent years have they become readily available commercially. Moreover, only a few fundamental studies of their physical and chemical properties are accessible, despite several potential applications associated with their unique properties. This report serves to bridge this lack of information by providing fundamental vibrational spectroscopic data using a series of methylimidazolium-based ionic liquids with cyano-functionalized anions. Through nonlinear, surface-sensitive, optical techniques, in tandem with bulk-sensitive methods, vibrational information offered here aims to provide an accurate molecular-level description of the surface of these materials, particularly at gas-liquid and solid-liquid interfaces.

The spectroscopic data may be used later on to correlate with macroscopic physical properties of these compounds such as density, viscosity, surface tension, conductivity, vapor pressure, and many others. These properties originate from the fundamental structure and arrangement of the ions comprising them. By systematically varying the anion composition while keeping the cation constant, particular focus in answering questions regarding the effect of size, shape and anion type are addressed. Essentially, these experiments have been tailored to aid in generating a new and unified model to explain the chemistry of imidazolium ionic liquids with cyano-based anions at the gas-liquid interface and in contact with inherently-charged, solid single crystal salts.

### 1.3.2 Summary of Chapters

The theoretical background of three vibrational spectroscopies used in this study, namely, infrared, Raman, and SFG are presented in Chapter 2. An overall summary of the limitations and applicability of each technique to probe the surface is provided.

Chapter 3 presents the details of the experimental configuration, preparation and synthesis of samples, as well as data collection and analysis procedures. Spectroscopic measurement descriptions are divided so as to discuss the two interfaces: air-liquid and solid-liquid, separately.

In Chapter 4, SFG, as an inherently surface-sensitive technique, in combination with bulk-sensitive spectroscopic techniques such as FTIR and Raman, have been used to characterize the surface of cyano-containing ionic liquids, such as [BMIM][SCN], [BMIM][DCA], [BMIM][TCM], and [EMIM][TCB] at the gas-liquid interface. By structural variation of the anion while keeping the cation constant, emphasis on the molecular arrangement of the anion at the gas-liquid interface was reported; and its subsequent role in determining the surface molecular orientation of the cation. Vibrational modes seen in the C–H stretching region revealed the presence of the cation at the gas-liquid interface. The cation orientation was independent of the type of cyano-containing anion. However, a similar arrangement at the surface as reported in previous studies was found, with the imidazolium ring lying flat at the surface, and the alkyl chains pointing towards the gas phase. SFG results showed that all three anions of varying symmetry, namely, [DCA]<sup>−</sup> ( $C_{2v}$ ), [TCM]<sup>−</sup> ( $D_{3h}$ ), and [TCB]<sup>−</sup> ( $T_d$ ) in ionic liquids [BMIM]DCA, [BMIM][TCM], and [EMIM][TCB] were significantly tilted from the

surface plane, while the linear  $[\text{SCN}]^-$  in  $[\text{BMIM}][\text{SCN}]$  exhibited poor ordering, as seen in the absence of its C–N stretching mode in the SFG vibrational spectra. All work contained in this chapter has been published in *Phys. Chem. Chem. Phys.* **2012**, *14*, 5122–5131 with the following authors: Chariz Y. Peñalber, Zlata Grenoble, Gary A. Baker, and Steven Baldelli.

Chapter 5 introduces a novel experiment highlighting results of SFG studies involving the ionic liquid, 1-butyl-3-methylimidazolium dicyanamide  $[\text{BMIM}][\text{DCA}]$ , in contact with two solid single crystal salt surfaces:  $\text{BaF}_2(111)$  single crystal, and solid  $\text{NaCl}\{100\}$ . The report described the nature of an ionic liquid–(solid) salt interface using SFG, contributing a new understanding to the molecular-level interactions involved in salts, which are conceptually similar compounds (of purely ionic character) but of different physical properties (liquid vs. solid at room temperature). Results showed the presence of  $[\text{BMIM}]^+$  at the  $\text{NaCl}\{100\}$  surface, and  $[\text{DCA}]^-$  at the  $\text{BaF}_2(111)$  surface.  $[\text{BMIM}]^+$  cations adhered closely *via* Coulombic interactions to the negatively-charged  $\text{NaCl}\{100\}$  surface, while  $[\text{DCA}]^-$  anions subsequently had a strong electrostatic affinity to the positively-charged  $\text{BaF}_2(111)$  surface. Ions of the ionic liquid adsorbed to the solid salt surface to form a Helmholtz-like electric double layer. All work contained in this chapter has been published in *J. Phys. Chem. Lett.* **2012**, 844–847, with the following authors: Chariz Y. Peñalber, and Steven Baldelli.

Chapter 6 extends the novel experimental model discussed in Chapter 5, to include all four cyano-containing ionic liquids,  $[\text{BMIM}][\text{SCN}]$ ,  $[\text{BMIM}][\text{DCA}]$ ,  $[\text{BMIM}][\text{TCM}]$ , and  $[\text{EMIM}][\text{TCB}]$  studied at the surface of the two solid single crystal

salt surfaces: BaF<sub>2</sub>(111), and NaCl{100}. Spectral features in both C–H and C–N stretching regions were assigned, with a detailed discussion of the nature of surface interactions and ordering of the ionic liquid ions at the interface of the different crystals. The Helmholtz-type model, composed of a single ordered layer at the surface of the solid salt, with almost no orientational order in the second layer was found valid for ionic liquids [BMIM][SCN], [BMIM][DCA], and [BMIM][TCM]. However, for [EMIM][TCB], a strongly-bound anion layer must be present at the surface of BaF<sub>2</sub>(111), followed by an ordered layer of cations in the second layer. The experimental model obtained was correlated to existing theoretical models in the literature to explain ionic liquid charge screening effects at solid surfaces.

Chapter 7 summarizes overall findings discussed in Chapters 4–6 and provides the unified concluding remarks.

Lastly, supplementary information have been provided in Appendix B, with an account of SFG experimental results pertaining to air–liquid and solid–liquid interface studies of phosphonium–based ionic liquids presented in Appendix A.

#### 1.4. References

- (1) Welton, T. *Chem. Rev.* **1999**, *99*, 2071-2084.
- (2) Armand, M.; Endres, F.; MacFarlane, D. R.; Ohno, H.; Scrosati, B. *Nat. Mater.* **2009**, *8*, 621-629.
- (3) Su, Y.-Z.; Fu, Y.-C.; Wei, Y.-M.; Yan, J.-W.; Mao, B.-W. *ChemPhysChem* **2010**, *11*, 2764-2778.
- (4) Dyson, P. J.; Geldbach, T. J. *Electrochem. Soc. Interface* **2007**, *16*, 50-53.
- (5) Parvulescu, V. I.; Hardacre, C. *Chem. Rev.* **2007**, *107*, 2615-2665.
- (6) Steinrück, H. P.; Libuda, J.; Wasserscheid, P.; Cremer, T.; Kolbeck, C.; Laurin, M.; Maier, F.; Sobota, M.; Schulz, P. S.; Stark, M. *Adv. Mater.* **2011**, *23*, 2571-2587.
- (7) Zhao, H. *Chem. Eng. Commun.* **2006**, *193*, 1660-1677.
- (8) Mokrushin, V.; Assenbaum, D.; Paape, N.; Gerhard, D.; Mokrushina, L.; Wasserscheid, P.; Arlt, W.; Kistenmacher, H.; Neuendorf, S.; Göke, V. *Chem. Eng. Technol.* **2010**, *33*, 63-73.
- (9) Han, X.; Armstrong, D. W. *Acc. Chem. Res.* **2007**, *40*, 1079-1086.
- (10) Armstrong, J. P.; Hurst, C.; Jones, R. G.; Licence, P.; Lovelock, K. R. J.; Satterley, C. J.; Villar-Garcia, I. J. *Phys. Chem. Chem. Phys.* **2007**, *9*, 982-990.
- (11) Steinrück, H.-P. *Surf. Sci.* **2010**, *604*, 481-484.
- (12) Caporali, S.; Bardi, U.; Lavacchi, A. *J. Electron. Spectrosc. Relat. Phenom.* **2006**, *151*, 4-8.
- (13) Lockett, V.; Sedev, R.; Bassell, C.; Ralston, J. *Phys. Chem. Chem. Phys.* **2008**, *10*, 1330-1335.

- (14) Maier, F.; Cremer, T.; Kolbeck, C.; Lovelock, K. R. J.; Paape, N.; Schulz, P. S.; Wasserscheid, P.; Steinruck, H. P. *Phys. Chem. Chem. Phys.* **2010**, *12*, 1905-1915.
- (15) Smith, E. F.; Garcia, I. J. V.; Briggs, D.; Licence, P. *Chem. Commun.* **2005**, 5633-5635.
- (16) Smith, E. F.; Rutten, F. J. M.; Villar-Garcia, I. J.; Briggs, D.; Licence, P. *Langmuir* **2006**, *22*, 9386-9392.
- (17) Hofft, O.; Bahr, S.; Himmerlich, M.; Krischok, S.; Schaefer, J. A.; Kempter, V. *Langmuir* **2006**, *22*, 7120-7123.
- (18) Nishi, T.; Iwahashi, T.; Yamane, H.; Ouchi, Y.; Kanai, K.; Seki, K. *Chem. Phys. Lett.* **2008**, *455*, 213-217.
- (19) Kanai, K.; Nishi, T.; Iwahashi, T.; Ouchi, Y.; Seki, K.; Harada, Y.; Shin, S. *J. Electron Spectrosc. Relat. Phenom.* **2009**, *174*, 110-115.
- (20) Gannon, T. J.; Law, G.; Watson, P. R.; Carmichael, A. J.; Seddon, K. R. *Langmuir* **1999**, *15*, 8429-8434.
- (21) Law, G.; Watson, P. R.; Carmichael, A. J.; Seddon, K. R. *Phys. Chem. Chem. Phys.* **2001**, *3*, 2879-2885.
- (22) Hoffmann, F. M. *Surf. Sci. Rep.* **1983**, *3*, 107-107.
- (23) Wang, H.-F.; Gan, W.; Lu, R.; Rao, Y.; Wu, B.-H. *Int. Rev. Phys. Chem.* **2005**, *24*, 191-256.
- (24) Colthup, N. B.; Daly, L. H.; Wilberley, S. E. *Introduction to Infrared and Raman Spectroscopy*; Third ed.; Academic Press: San Diego, 1990.
- (25) Martinez, I. S.; Baldelli, S. *J. Phys. Chem. C* **2010**, *114*, 11564-11575.

- (26) Santos, C. S.; Rivera-Rubero, S.; Dibrov, S.; Baldelli, S. *J. Phys. Chem. C* **2007**, *111*, 7682-7691.
- (27) Rivera-Rubero, S.; Baldelli, S. *J. Phys. Chem. B* **2006**, *110*, 4756-4765.
- (28) Santos, C. S.; Baldelli, S. *J. Phys. Chem. B* **2007**, *111*, 4715-4723.
- (29) Santos, C. S.; Baldelli, S. *J. Phys. Chem. B* **2009**, *113*, 923-933.
- (30) Aliaga, C.; Baldelli, S. *J. Phys. Chem. B* **2007**, *111*, 9733-9740.
- (31) Aliaga, C.; Baker, G. A.; Baldelli, S. *J. Phys. Chem. B* **2008**, *112*, 1676-1684.
- (32) Peñalber, C.; Adamová, G.; Baldelli, S.; Seddon, K. R. *Unpublished work*.
- (33) Imori, T.; Iwahashi, T.; Ishii, H.; Seki, K.; Ouchi, Y.; Ozawa, R.; Hamaguchi, H.-o.; Kim, D. *Chem. Phys. Lett.* **2004**, *389*, 321-326.
- (34) Jeon, Y.; Sung, J.; Bu, W.; Vaknin, D.; Ouchi, Y.; Kim, D. *J. Phys. Chem. C* **2008**, *112*, 19649-19654.
- (35) Iwahashi, T.; Miyamae, T.; Kanai, K.; Seki, K.; Kim, D.; Ouchi, Y. *J. Phys. Chem. B* **2008**, *112*, 11936-11941.
- (36) Krischok, S.; Eremtchenko, M.; Himmerlich, M.; Lorenz, P.; Uhlig, J.; Neumann, A.; Ottking, R.; Beenken, W. J. D.; Hofft, O.; Bahr, S.; Kempter, V.; Schaefer, J. A. *J. Phys. Chem. B* **2007**, *111*, 4801-4806.
- (37) Romero, C.; Baldelli, S. *J. Phys. Chem. B* **2006**, *110*, 6213-6223.
- (38) Romero, C.; Moore, H. J.; Lee, T. R.; Baldelli, S. *J. Phys. Chem. C* **2007**, *111*, 240-247.
- (39) Aliaga, C.; Baldelli, S. *J. Phys. Chem. C* **2008**, *112*, 3064-3072.
- (40) Aliaga, C.; Baldelli, S. *J. Phys. Chem. B* **2006**, *110*, 18481-18491.

- (41) Baldelli, S. *J. Phys. Chem. B* **2005**, *109*, 13049-13051.
- (42) Rivera-Rubero, S.; Baldelli, S. *J. Phys. Chem. B* **2004**, *108*, 15133-15140.
- (43) Baldelli, S. *Acc. Chem. Res.* **2008**, *41*, 421-431.
- (44) Fitchett, B. D.; Conboy, J. C. *J. Phys. Chem. B* **2004**, *108*, 20255-20262.
- (45) Rollins, J. B.; Fitchett, B. D.; Conboy, J. C. *J. Phys. Chem. B* **2007**, *111*, 4990-4999.
- (46) Zhou, W.; Inoue, S.; Iwahashi, T.; Kanai, K.; Seki, K.; Miyamae, T.; Kim, D.; Katayama, Y.; Ouchi, Y. *Electrochem. Commun.* **2010**, *12*, 672-675.
- (47) Sobota, M.; Nikiforidis, I.; Hieringer, W.; Paape, N.; Happel, M.; Steinrück, H.-P.; Görling, A.; Wasserscheid, P.; Laurin, M.; Libuda, J. *Langmuir* **2010**, *26*, 7199-7207.
- (48) Sobota, M.; Schmid, M.; Happel, M.; Amende, M.; Maier, F.; Steinrück, H.-P.; Paape, N.; Wasserscheid, P.; Laurin, M.; Gottfried, J. M.; Libuda, J. *Phys. Chem. Chem. Phys.* **2010**, *12*, 10610-10621.
- (49) Santos, V. O.; Alves, M. B.; Carvalho, M. S.; Suarez, P. A. Z.; Rubim, J. *C. J. Phys. Chem. B* **2006**, *110*, 20379-20385.
- (50) Rubim, J. C.; Trindade, F. A.; Gelesky, M. A.; Aroca, R. F.; Dupont, J. J. *Phys. Chem. C* **2008**, *112*, 19670-19675.
- (51) Brandão, C. R. R.; Costa, L. A. F.; Breyer, H. S.; Rubim, J. C. *Electrochem. Commun.* **2009**, *11*, 1846-1848.
- (52) Costa, L. A. F.; Breyer, H. S.; Rubim, J. C. *Vib. Spectrosc.* **2010**, *54*, 103-106.

- (53) Brand, H.; Liebman, J. F.; Schulz, A.; Mayer, P.; Villinger, A. *Eur. J. Inorg. Chem.* **2006**, *2006*, 4294-4308.
- (54) Emel'yanenko, V. N.; Zaitsau, D. H.; Verevkin, S. P.; Heintz, A.; Voňš, K.; Schulz, A. *J. Phys. Chem. B* **2011**, *115*, 11712-11717.
- (55) Yoshida, Y.; Muroi, K.; Otsuka, A.; Saito, G.; Takahashi, M.; Yoko, T. *Inorg. Chem.* **2004**, *43*, 1458-1462.
- (56) Forsyth, S. A.; Stuart R. Batten; Qing Dai; MacFarlane, D. R. *Aust. J. Chem* **2004**, *57*, 121-124.
- (57) Wooster, T. J.; Johanson, K. M.; Fraser, K. J.; MacFarlane, D. R.; Scott, J. L. *Green Chem.* **2006**, *8*, 691-696.
- (58) MacFarlane, D. R.; Forsyth, S. A.; Golding, J.; Deacon, G. B. *Green Chem.* **2002**, *4*, 444-448.
- (59) DeSilvestro, H. *Ionic Liquids - The Panacea for Dye Solar Cells*; Dyesol Ltd., 2007.
- (60) Marszalek, M.; Fei, Z.; Zhu, D.-R.; Scopelliti, R.; Dyson, P. J.; Zakeeruddin, S. M.; Grätzel, M. *Inorg. Chem.* **2011**, *50*, 11561-11567.
- (61) Kuang, D.; Uchida, S.; Humphry-Baker, R.; Zakeeruddin, S. M.; Grätzel, M. *Angew. Chem. Int. Ed.* **2008**, *47*, 1923-1927.
- (62) Kuang, D.; Wang, P.; Ito, S.; Zakeeruddin, S. M.; Grätzel, M. *J. Am. Chem. Soc.* **2006**, *128*, 7732-7733.
- (63) Huddleston, J. G.; Visser, A. E.; Reichert, W. M.; Willauer, H. D.; Broker, G. A.; Rogers, R. D. *Green Chem.* **2001**, *3*, 156-164.

## Chapter 2. Theoretical Background

This dissertation focuses on vibrational spectroscopic techniques in the characterization of imidazolium-based ionic liquids containing cyano-functionalized anions. Particularly, sum frequency generation spectroscopy which is inherently surface sensitive, serves to determine the molecular structure of these liquids at interfaces. Surface studies are primarily important because of the fact that surfaces are ubiquitous in nature, playing an essential role in identifying potential applications of various materials for use in industry.

### 2.1. Vibrational Spectroscopy

Molecular spectroscopy studies the interaction of light with matter. This interaction between the electromagnetic radiation and the atoms or molecules corresponds to an energy matching or resonance condition described by

$$\Delta E = h\nu \quad (2-1)$$

where  $\Delta E$  pertains to the energy difference between two energy states in an atom or molecule,  $h$  is Planck's constant, and  $\nu$  is the frequency of the radiation.

One of the many techniques in molecular spectroscopy that gives fundamental information on molecular structure and allows its elucidation is vibrational spectroscopy. As a useful probe for determining the structure of small molecules and various chemical functional group frequencies, vibrational spectroscopy is indeed a useful tool in the identification and characterization of several compounds.<sup>1</sup>

Vibrational spectra are usually measured using two very different techniques, namely, infrared spectroscopy and Raman spectroscopy. In infrared spectroscopy, light of

various frequencies is passed through a sample and the transmitted light is measured over a certain frequency range. In Raman spectroscopy, transmitted light is not observed, however, the light scattered by a sample is measured. Additionally, a monochromatic light source is required for Raman spectroscopy. The discussion which follows below describes in detail, the basic theory and application of three vibrational techniques used in this study. A summary of these photon-based techniques is also provided, highlighting the merits of using them as a tool in the characterization of ionic liquids on surfaces.

### **2.1.1. Infrared Spectroscopy**

Infrared spectroscopy measures the amount of infrared light absorbed by a molecule as a function of the frequency of light. It exploits the fact that molecules have specific frequencies at which they rotate or vibrate corresponding to discrete energy levels possessed by the molecule.<sup>2</sup>

In the Born-Oppenheimer and harmonic oscillator approximations, these resonant frequencies are determined by the characteristic vibrations called normal modes. In simple molecules such as diatomic molecules, only one bond between atoms exist, which may stretch. More complex molecules have several bonds and vibrations can be coupled, leading to infrared absorptions at characteristic frequencies which may be related to chemical groups. The molecules exhibit characteristic modes of vibration with absorption frequencies, which lie in the infrared region of the spectrum. Although the IR extends from 800 nm (near IR) to 400  $\mu\text{m}$  (far IR), the fundamental region at 2.5-15  $\mu\text{m}$  (4000–650  $\text{cm}^{-1}$ ) is the area of interest generally used. The absorption bands which

appear for a given molecule in this region allow us to interpret probable functional groups and structures for the molecules from characteristic group frequencies.

The infrared spectrum of a sample is collected by passing a beam of infrared light through the sample. However, for a molecule to absorb IR radiation, it must undergo a net change in dipole moment,  $\mu$ , as described by the electric dipole transition selection rules from classical electromagnetic theory. Also, the frequency of the light must match the frequency of the molecular vibration for the molecule to absorb the IR light. This occurs by modulation of the molecular dipole moment,  $\mu$ , of the molecule, with respect to its normal coordinate,  $q$ , which occurs upon absorption. Mathematically, the intensity of individual adsorption bands can be expressed as

$$I_{IR} \propto \left( \frac{\partial \mu}{\partial q} \right)^2 \quad (2-2)$$

The intensity of absorption depends on the polarity of the bond and the concentration of the molecule or the number of bonds. The dipole moment associated with IR activity has three components in the Cartesian coordinate axes ( $\mu_x$ ,  $\mu_y$ , and  $\mu_z$ ). The vibration along the normal coordinate,  $q$ , is infrared active if any of the integral functions of the components describing the change in dipole moment with respect to the normal coordinate is nonzero, which is determined by symmetry. In other words, at least one of the components of  $\mu$  must belong the same symmetry species as  $q$ .<sup>3</sup>

### 2.1.2. Raman Spectroscopy

In contrast to infrared spectroscopy, the scattering of radiation instead of merely its absorption forms the basis for Raman spectroscopy. In such an experiment, the light is scattered from a sample after irradiation from a high intensity monochromatic source, which typically a laser. Most photons collected in the Raman measurement results from elastic scattering in which the scattered radiation is of the same frequency as the incident radiation. This is known as Rayleigh scattering.<sup>4</sup>

According to the classical electromagnetic theory, the dipole moment induced,  $\mu$ , when radiation interacts with a medium is given by

$$\vec{\mu} = \alpha \vec{E} \quad (2-3)$$

where  $E$  is the electric field, and  $\alpha$  is the polarizability, describing the macroscopic response of the material to the incoming electric field. The molecular polarizability corresponds to the ability of the electrons in a molecule to be displaced by the electromagnetic radiation. This may also written as

$$\begin{bmatrix} \mu_x \\ \mu_y \\ \mu_z \end{bmatrix} = \begin{bmatrix} \alpha_{xx} & \alpha_{xy} & \alpha_{xz} \\ \alpha_{yx} & \alpha_{yy} & \alpha_{yz} \\ \alpha_{zx} & \alpha_{zy} & \alpha_{zz} \end{bmatrix} \begin{bmatrix} E_x \\ E_y \\ E_z \end{bmatrix} \quad (2-4)$$

where the nine coefficients,  $\alpha_{ii}$ , contain Cartesian components of the polarizability tensor,  $\alpha$ . Since the tensor is symmetric, then  $\alpha_{xy} = \alpha_{yx}$ ,  $\alpha_{xz} = \alpha_{zx}$ , and  $\alpha_{yz} = \alpha_{zy}$ . Consequently, if any of the six components of the polarizability tensor changes during the vibration, the transition is Raman active. The Raman scattering is proportional to the change in polarizability tensor elements with respect to the normal coordinate,  $q$ . This may be expressed as

$$I_R \propto \left(\frac{\partial\alpha}{\partial q}\right)^2 \quad (2-5)$$

A requirement of Raman activity therefore, analogous to infrared activity, is that there must be change in molecular polarizability of the molecule. From the standpoint of molecular symmetry, a molecule is considered Raman active if any of its vibrational modes contain one of the polarizability components belonging to the same irreducible representation, as seen in the character table.<sup>3,5</sup>

The electric field produced by the polarized molecule oscillates at the same frequency as the passing electromagnetic wave, so that the molecule acts as a source to scatter radiation of that frequency in all directions. From the quantum mechanical point of view, light scattering can be regarded as transitions associated with energy levels. A molecule in the ground state absorbs an incident photon and reaches a non-stationary state ( $E_1$ ), which does not correspond to any particular quantized energy level of the atom or molecule. The molecules instantaneously return to a stationary state ( $E_0$ ) emitting a photon of the same energy that was absorbed (Rayleigh scattering). A small fraction of the scattered radiation results from inelastic scattering, where the emitted radiation is shifted to higher or lower frequencies compared to the incident radiation. The difference in frequency is equal to a natural vibration frequency of the molecule's ground electronic state and is caused by vibrational transitions that occur during the energy transfer of the scattering process. This is referred to as the Raman effect (Fig. 2-1), which is a phenomenon first observed by Sir C. V. Raman in 1928.<sup>4</sup>

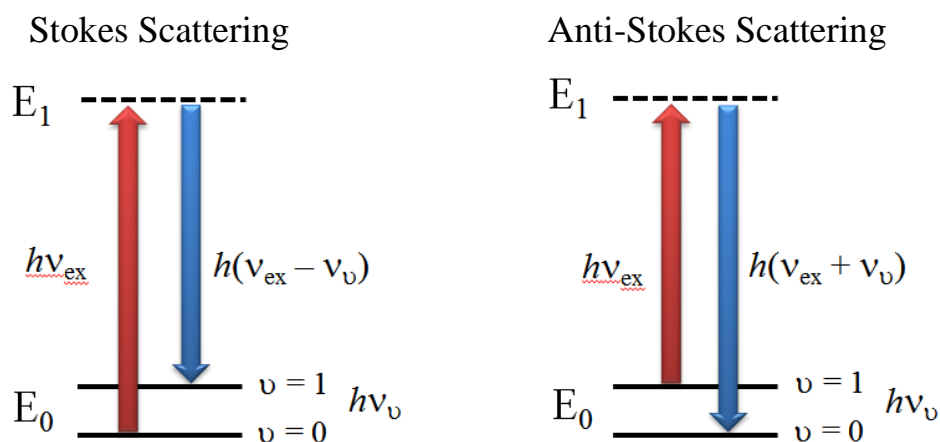


Fig. 2-1. Energy level diagrams illustrating the two types of Raman Scattering.

Usually photons of energy  $h\nu_{ex}$  (incident radiation) are absorbed by molecules in their ground vibrational state ( $\nu = 0$ ). If the molecule returns to a vibrationally excited state (not similar to the original vibrational ground state) it may emit radiation of lower frequency,  $h(\nu_{ex} - \nu_v)$  than the incident radiation and give rise to Stokes lines. Several Stokes lines are normally observed in the Raman spectrum, corresponding to different vibrations in the molecule. In another case, Raman scattering of molecules in a vibrationally excited state may also produce anti-Stokes lines with frequencies  $h(\nu_{ex} + \nu_v)$  shifted toward higher frequencies. Under normal laboratory conditions, most molecules are initially in the lowest vibrational state producing more intense Stokes lines compared to anti-Stokes, and only the former is usually considered in chemical analysis.

Raman scattering, in addition, may involve polarization of radiation which allows evaluation of the symmetry of vibration generating the scattering. This is usually expressed in terms of the polarization ratio,  $\rho$ , which is the ratio of the intensity of the

perpendicularly-polarized scattered radiation, to that of the radiation scattered parallel to the polarization of the incident light. This may be expressed as

$$\rho = \frac{I_{\perp}}{I_{\parallel}} \quad (2-6)$$

Advances in conventional Raman spectroscopy methods over the years have resulted in the introduction of techniques such as surface-enhanced Raman spectroscopy. This method takes advantage of the enhancement of the electromagnetic field of light when surfaces of metals are used to interact with the impinging radiation.

In comparison with IR spectra, the frequency shifts between the incident radiation and the Raman scattered radiation (Stokes and anti-Stokes lines) corresponds to vibrational energy levels. Hence we expect Raman spectra to yield information which may be used in connection with IR spectra for structure elucidation.

### 2.1.3. Nonlinear Optical Spectroscopy

Most optical processes, including IR and Raman spectroscopies are governed by linear optical phenomena. In such cases, a weak electric field from a light source interacts with the molecule to induce a dipole,  $\mu$ , proportional to the strength of the electric field  $E$  as given by equation 2-3. Similarly, the equation may be written as

$$\mu = \mu_0 + \alpha E \quad (2-7)$$

where  $\mu_0$  is the static dipole of the material and  $\alpha$  is the polarizability of the electrons in the molecule. For condensed phases, the bulk polarization is considered. Because static polarization is possessed by only a few materials, the induced polarization is given as

$$P = \epsilon_0 \chi^{(1)} E \quad (2-8)$$

where  $\chi^{(1)}$  is the nonlinear susceptibility, which is a macroscopic average of the polarizability, and  $\epsilon_0$  is the permittivity in vacuum.

As a result of the development of high intensity lasers, coherent light sources of sufficient intensity (reaching the order of  $\sim 2.5 \text{ kW/cm}^2$ ) were made available. This contributed to discoveries in nonlinear spectroscopy in which the interaction of high intensity electric fields induce a polarization response, which is no longer linear, but has contributions from high order terms as expressed in the equation

$$\begin{aligned} P &= P^{(1)} + P^{(2)} + P^{(3)} + \dots \\ P &= \epsilon_0 \chi^{(1)} E + \epsilon_0 \chi^{(2)} EE + \epsilon_0 \chi^{(3)} EEE \dots \end{aligned} \quad (2-9)$$

where  $\chi^{(2)}$  and  $\chi^{(3)}$  are the second and third order susceptibilities.

This dissertation particularly focuses on the second-order response to the polarization, which is a nonlinear optical effect observed when high-powered lasers are used as light sources.

When the electric field ( $E = E_1 \cos \omega t$ ) is considered, the second-order polarization takes the form,

$$\begin{aligned} P^{(2)} &= \epsilon_0 \chi^{(2)} (E_1 \cos \omega t)^2 \\ &= \frac{1}{2} \epsilon_0 \chi^{(2)} E_1^2 (1 + \cos 2\omega t) \end{aligned}$$

where  $\omega$  is the angular frequency of the light. In such a case, the dipole oscillates at twice the frequency of the incident light,  $2\omega$ , a phenomenon known as second harmonic generation, SHG. For two laser beams with different frequencies,  $\omega_1$  and  $\omega_2$ ,

$$E = E_1 \cos \omega_1 t + E_2 \cos \omega_2 t .$$

Using equation 2-9 and 2-6, and applying trigonometric identities, the resulting expression below can be obtained

$$P^{(2)} = \frac{1}{2} \epsilon_0 \chi^{(2)} E_1 E_2 [\cos(\omega_1 + \omega_2)t + \cos(\omega_1 - \omega_2)t].$$

The two incident fields result to a dipole oscillating at the sum of the two frequencies,  $\omega_1 + \omega_2$ , as well as the difference,  $\omega_1 - \omega_2$ . These optical processes are known as sum frequency generation (SFG) and the difference frequency generation (DFG).

#### **2.1.3.1. Sum Frequency Generation (SFG)**

SFG is a second-order nonlinear spectroscopic technique which is highly surface-specific because it selectively detects molecules in a non-centrosymmetric environment. This technique has a unique ability to distinguish surface molecules from that of the bulk, and is thus ideal in the study of interfaces (i.e. two-phase systems) where molecules on the surface have preferential ordering as opposed to the isotropic bulk molecules. The theory behind SFG has been well-discussed and can readily be found in several publications.<sup>6-12</sup>

SFG used in this experiment involved two pulsed laser beams namely, a 532-nm fixed visible and tunable IR ( $2000-4000 \text{ cm}^{-1}$ ), overlapped on the surface to generate a third beam, which occurs at the sum frequency of the two incident beams. The electric fields of the high-intensity input beams ( $E_{\text{IR}}$ ,  $E_{\text{vis}}$ ) induce a second-order nonlinear

polarization,  $P^{(2)}$ , on the surface. The induced polarization response, in turn, is related to the electric fields through the second order nonlinear susceptibility tensor,  $\chi^{(2)}$ . The intensity of the sum frequency beam,  $I(\omega_{SF})$ , is proportional to the square of the induced polarization  $P^{(2)}$  as described by

$$I(\omega_{SF}) \propto \left| P^{(2)} = \chi^{(2)} : E_{vis} E_{IR} \right|^2 \quad (2-13)$$

$\chi^{(2)}$  changes significantly with infrared wavenumber and has two contributions – the  $\chi_{NR}$  coming from the non-resonant background and the resonant term,  $\chi_R$ , which contains distinct vibrational modes of the molecule on the surface.

$$\chi^{(2)} = \chi_{NR}^{(2)} + \chi_R^{(2)} \quad (2-14)$$

The hyperpolarizability,  $\beta^{(2)}$ , is an average of all possible molecular orientations and contains the Raman polarizability and the IR dipole transition.  $\omega_{IR}$ ,  $\omega_q$ , and  $\Gamma_q$  represent the frequency of the IR beam, frequency of the normal mode and the damping constant of the  $q^{\text{th}}$  vibrational mode, respectively. The number of molecular modes contributing to the vibration is denoted by  $N$ . Eq 3 below shows the expression for the resonant term,  $\chi_R^{(2)}$ , such that when the infrared frequency ( $\omega_{IR}$ ) coincides with the frequency of a vibrational mode ( $\omega_q$ ) of the interfacial molecules,  $\omega_{IR} - \omega_q$  equals 0 and the magnitude of  $\chi^{(2)}$  is maximized resulting in an increase in SFG intensity.

$$\chi_R^{(2)} = \sum \left[ \frac{N \langle \beta^{(2)} \rangle}{\omega_{IR} - \omega_q + i\Gamma_q} \right] \quad (2-15)$$

Detecting the SF light as a function of IR frequency yields a vibrational spectrum of the adsorbed molecules. The magnitude of the  $\chi^{(2)}$  depends on the polar orientation of the molecule on the surface. Since SFG is a nonlinear and coherent spectroscopy, varying

the polarizations of the incident and output beams probe the various Cartesian components of the susceptibility tensor,  $\chi^{(2)}$ , from which molecular orientation with respect to the surface normal can be determined.<sup>6,13-16</sup>

Using different polarization combinations of the incoming and outgoing beams with respect to the surface normal, the molecular information at the interface can be determined by the analysis of  $\chi^{(2)}$ . The magnitude of  $\chi^{(2)}$  is sensitive to the degree of the polar orientation of the molecules. Polarization analysis of the interface allows for a determination of the molecular orientation with respect to the surface normal. Fig. 2-2 illustrates the assigned notations for plane-polarized light in *s* and *p* configurations, where *s*-polarized refers to perpendicular polarization relative to the plane of incidence (*xz* direction), and *p*-polarized is parallel to such plane.

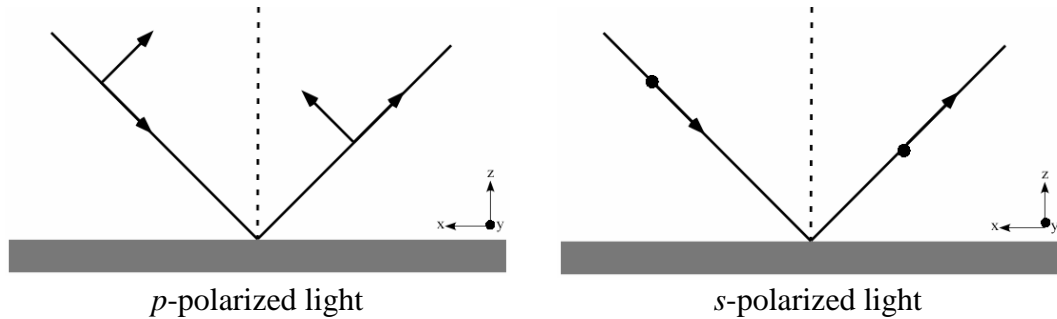


**Fig. 2-2.** Components of the incident electric fields with respect to the plane of incidence, *xz* plane.

The third rank tensor,  $\chi^{(2)}$ , is reduced by symmetry to only four non-zero components, for an isotropic surface with a  $C_\infty$  symmetry:  $\chi_{xzx}^{(2)} = \chi_{yyz}^{(2)}$ ,  $\chi_{xzx}^{(2)} = \chi_{zyy}^{(2)}$ ,  $\chi_{zxx}^{(2)} = \chi_{zyy}^{(2)}$ , and  $\chi_{zzz}^{(2)}$ . This is due to the surface being isotropic in the *x-y* plane

corresponding to a vertical mirror plane. Only four possible polarization combinations can generate sum frequency signal from these non-zero components. Table 2-1 shows the components of the susceptibility probed by the different polarization combinations. The combinations are listed in the order of sum frequency, visible, and infrared beams. The  $p$ -polarized light probes both  $x$  and  $z$  components, while the  $s$ -polarized light probes only the  $y$  component.

**Table 2-1.** Polarization combinations in SFG and the  $\chi_{XYZ}^{(2)}$  elements contributing to the signal observed

Polarization combination	Elements of $\chi_{XYZ}^{(2)}$
$ssp$	$\chi_{yyz}^{(2)}$
$ppp$	$\chi_{zzz}^{(2)}, \chi_{zxx}^{(2)}, \chi_{xzx}^{(2)}, \chi_{xxz}^{(2)}$
$sps$	$\chi_{yzy}^{(2)}$
$pss$	$\chi_{zyy}^{(2)}$

For a vibrational mode to be sum frequency active, it must be in an antisymmetric environment. The high surface sensitivity of SFG is because of the fact that the process is only allowed in non-centrosymmetric media, *via* a non-vanishing  $\chi_{XYZ}^{(2)}$  value. At interfaces, molecules are at a different environment relative to the bulk phase such that the centrosymmetric structure from the bulk is broken at the surface. This gives rise to a plane of asymmetry and therefore allows SFG to be observed.<sup>9,10,17</sup>

## 2.2. Summary

Of the three most common vibrational spectroscopies discussed, each has value depending on the precise interface or information required. The general schemes are outlined in Fig. 2-3, depicting the energy level transitions for the different vibrational spectroscopic techniques.  $E_1$  represents a stationary excited state, while  $E_2$  represents a non-stationary state. SFG involves two incident wavelengths during the excitation process while only one is involved in both IR and Raman. For comparison, only inelastic-type Raman scattering is shown in the figure.

Photon-based techniques such as Raman,<sup>1</sup> infrared,<sup>18</sup> and SFG<sup>7</sup> are beneficial as they are able to probe any interface accessible by light. This means systems such as gas-liquid, solid-liquid, and liquid-liquid are possible. Similarly, Raman and infrared absorption are not only sensitive to the molecules at the surface but also detect the bulk-phase species. When probing the interface of bulk liquids, the Raman and infrared signal originate over a distance from approximately  $10^{-7}$  to  $10^{-6}$  meters. This makes analysis or experimental design complicated if explicit surface detection is desired. IR and Raman spectroscopy typically are able to cover from  $400\text{--}4000\text{ cm}^{-1}$ , but could be limited by materials (optical window) constraints. SFG spectroscopy has the unique ability to detect molecules at the liquid surface in contact with any medium. The signal typically originates in the first nanometer at the interface where the isotropic bulk environment no longer exists. SFG is best used when the surface must be distinguished from the bulk phase and thus is ideal in the case of neat gas-liquid interface, as well as solid-liquid and liquid-liquid boundaries. The SFG spectra are usually limited to a spectral range above

1000  $\text{cm}^{-1}$  because of the IR laser source needed. This sometimes limits the species observable to the SFG.<sup>8</sup>

Overall, vibrational spectroscopy provides very useful chemical information on the surface of ionic liquids.

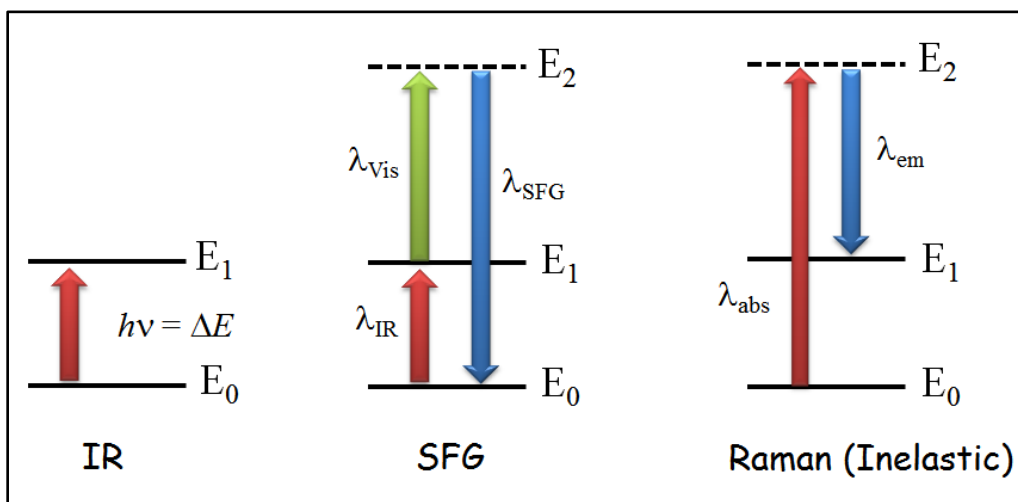


Fig. 2-3. Energy level transitions for different vibrational spectroscopic techniques: Infrared absorption (IR), SFG nonlinear spectroscopy and Raman spectroscopy (inelastic).  $E_1$  represents a stationary excited state, while  $E_2$  represents a non-stationary state. Absorption ( $\lambda_{\text{abs}}$ ) and emission ( $\lambda_{\text{em}}$ ) wavelengths for inelastic Raman scattering are shown.

### 2.3. References

- (1) Diem, M. *Introduction to Modern Vibrational Spectroscopy*; Wiley-Interscience: Michigan, 1993.
- (2) Harris, D. C.; Bertolucci, M. D. *Symmetry and Spectroscopy: An Introduction to Vibrational and Electronic Spectroscopy*; Dover Publications, Inc.: New York, 1978.
- (3) Cotton, F. A. *Chemical Applications of Group Theory*; Third ed.; John Wiley and Sons, Inc.: New York, 1990.
- (4) Long, D. A. *Raman Spectroscopy*; McGraw-Hill International Book Co.: New York, 1977.
- (5) Nakamoto, K. *Infrared and Raman Spectra of Inorganic and Coordination Compounds: Theory and applications in inorganic chemistry (Part 1)* John Wiley & Sons: New Jersey, 2009.
- (6) Wang, H.-F.; Gan, W.; Lu, R.; Rao, Y.; Wu, B.-H. *Int. Rev. Phys. Chem.* **2005**, *24*, 191-256.
- (7) Shen, Y. R. *Nature* **1989**, *337*, 519-525.
- (8) Bain, C. D. *J. Chem. Soc. Faraday Trans.* **1995**, *91*, 1281-1296.
- (9) Shen, Y. R. In *Nonlinear Spectroscopy for Molecular Structure Determination*; Field, R. W., Ed.; Blackwell, Oxford, UK: 1998, p 249-271.
- (10) Shen, Y. R. *The Journal of Physical Chemistry C* **2012**.
- (11) Shultz, M. J. *Advances in Multi-Photon Processes and Spectroscopy* **2008**, *18*, 133-199.

- (12) Morita, A.; Ishiyama, T. *Phys. Chem. Chem. Phys.* **2008**, *10*, 5801-5816.
- (13) Iimori, T.; Iwahashi, T.; Ishii, H.; Seki, K.; Ouchi, Y.; Ozawa, R.; Hamaguchi, H.-o.; Kim, D. *Chem. Phys. Lett.* **2004**, *389*, 321-326.
- (14) Ishiyama, T.; Sokolov, V. V.; Morita, A. *J. Chem. Phys.* **2011**, *134*, 024510-11.
- (15) Lu, R.; Gan, W.; Wu, B.-h.; Chen, H.; Wang, H.-f. *J. Phys. Chem. B* **2004**, *108*, 7297-7306.
- (16) Wu, H.; Zhang, W.-K.; Gan, W.; Cui, Z.-F.; Wang, H.-F. *J. Chem. Phys.* **2006**, *125*, 133203-12.
- (17) Lambert, A. G.; Davies, P. B.; Neivandt, D. J. *Appl. Spectrosc. Rev.* **2005**, *40*, 103 - 145.
- (18) Greenler, R. G. *J. Chem. Phys.* **1966**, *44*, 310-315.

## Chapter 3. Experimental Treatment

### 3.1. Ionic Liquid Samples

[BMIM][SCN]<sup>1,2</sup> and [BMIM][DCA]<sup>3-5</sup> were synthesized and purified in the lab using combined procedures provided in the literature. Samples were characterized by <sup>1</sup>HNMR, <sup>13</sup>CNMR, FTIR, and Raman Spectroscopy (see appendix A).

#### 3.1.1. [BMIM][SCN]

The compound was synthesized by mixing 1-methylimidazole (50 mL/0.63 mol, Sigma-Aldrich ≥99%) with 1-chlorobutane (72 mL/0.69 mol, Sigma-Aldrich 99%) utilizing a 1:1.1 molar ratio. The resulting mixture was refluxed under nitrogen gas at a temperature of ~65 °C for 72 h as shown in Fig. 3-1. The product, 1-butyl-3-methylimidazolium chloride ([BMIM][Cl]) (Fig. 3-2), was then washed three times with 50 mL portions of ethyl acetate and dried under vacuum. The anion was further exchanged by reacting [BMIM][Cl] (41 mL/0.27 mol) with 2 equivalents of KSCN (52 g/0.54 mol, Sigma-Aldrich ≥99%) in 200 mL acetone, and stirred for 48 hours at room temperature. The resulting suspension was filtered repeatedly and dried under vacuum using a rotary evaporator, to remove the volatile solvent. Additionally, filtration of the product through Celite® (Filter agent, Celite® 521, Aldrich) ensured the removal of solid NaCl, followed by aqueous extraction in dichloromethane. Washing was done to remove the residual chloride, which was monitored qualitatively, until no chloride was detected through the AgNO<sub>3</sub> test. Using the chloride ion-selective electrode, chloride concentration in the washings was monitored until readings resembled that of clean

Millipore water (~250 mV) after which, two more aqueous washings were performed. A more detailed description of quantitative analysis of chloride in the samples is presented in Section 3.2.2.1. Further purification was done by overnight stirring of the ionic liquid in methanol with activated charcoal, followed by filtration using a glass frit and drying under vacuum using a rotary evaporator, followed by drying in a glass vacuum line up to a pressure of  $\sim 5 \times 10^{-5}$  Torr in a glass vacuum line (Section 3.2.1, Fig. 3-4). A slightly yellow-colored product was obtained in the final step, as opposed to a red-colored ionic liquid reported in the literature procedure.<sup>1</sup> The overall scheme for the synthesis is illustrated in Fig. 3-3, route B for anion exchange.

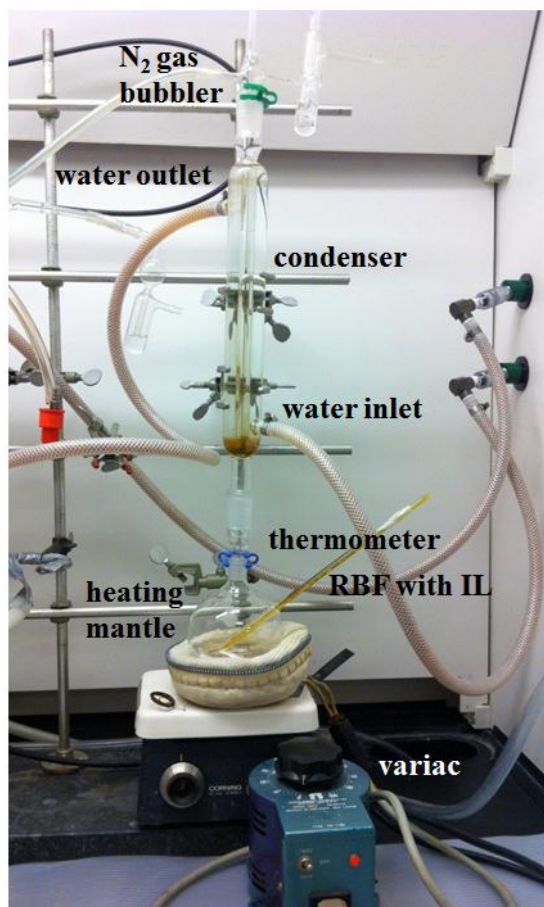


Fig. 3-1. Reflux setup for the synthesis of [BMIM][Cl].



Fig. 3-2. Appearance of [BMIM][Cl] after reflux reaction.

### 3.1.2. [BMIM][DCA]

A similar procedure as in the synthesis of [BMIM][SCN] was followed except that  $\text{NaN}(\text{CN})_2$  (29.4 g/0.33 mol, Sigma-Aldrich 96 %) instead of KSCN, was used to react with [BMIM][Cl] (50 mL/0.3 mol) for the anion exchange.<sup>5</sup> The purification step was repeated as often as necessary, until a clear colorless to a very slightly yellow-colored product was obtained. The overall scheme for the synthesis is illustrated in Fig. 3-3, route A for anion exchange.

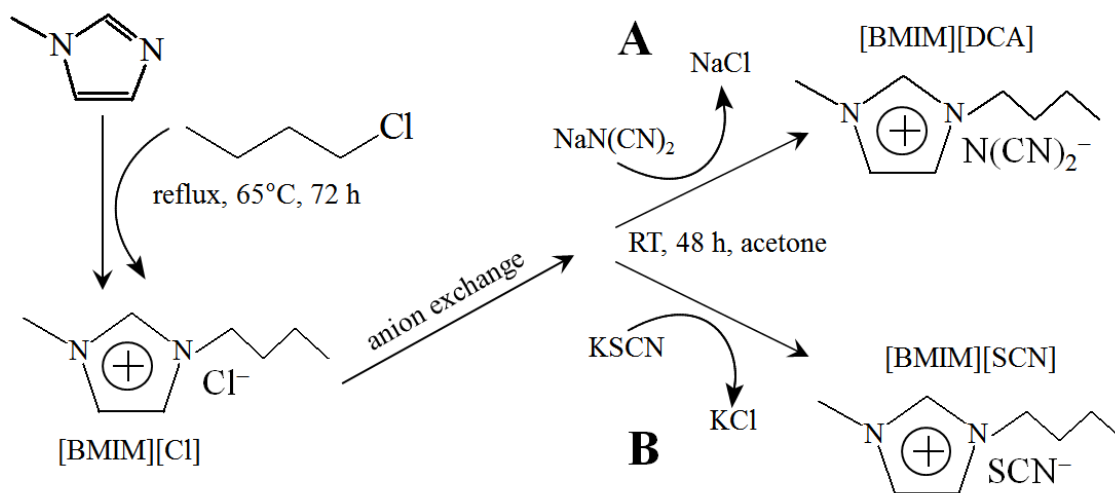


Fig. 3-3. Synthesis routes for the preparation of [BMIM][DCA] (A) and [BMIM][SCN] (B) ionic liquids.

### 3.1.3. [BMIM][TCM] and [EMIM][TCB]

[BMIM][TCM] was synthesized and characterized by Dr. Gary A. Baker at Oak Ridge National Laboratory. [EMIM][TCB] was provided by Merck™ courtesy of Dr. Florian Maier of the Universität Erlangen-Nürnberg.

## 3.2. Purification and Preparation Prior To Measurements

### 3.2.1. Drying under High Vacuum

To perform surface-sensitive spectroscopic measurements on ionic liquids, it is important for samples to be dried under high vacuum pressures, because surface measurements, unlike bulk-phase measurements, are ultimately sensitive to the smallest amount of impurity. Aside from residual chloride from the synthesis, the primary impurity known to significantly affect the SFG measurements is water. Therefore, considering in addition, the hygroscopic nature of ionic liquids prepared in this study, samples were maintained at critical purity level for surface measurements by drying in a home-built glass vacuum line until a sample base pressure of  $\sim 5 \times 10^{-5}$  Torr was reached.

The vacuum line used to dry ionic liquid samples was custom-built using Pyrex® glass. Fig. 3-4 shows a picture of the assembly, with the specific parts labeled. The line was equipped with an ionization gauge for measuring pressure, a turbo molecular pump backed by a mechanical pump, and liquid nitrogen traps.

In the absence of a sample, the base pressure of the line in full operation was  $\sim 2 \times 10^{-6}$  Torr, as recorded by the ionization gauge. The design utilized high vacuum valves and O-ring joint fittings which allowed samples to be attached directly to the line. Heating tapes, which were temperature-controlled by a variac, were wrapped externally around the glass line and used to heat the line up to  $\sim 60-80$  °C for overnight cleaning prior to drying samples.

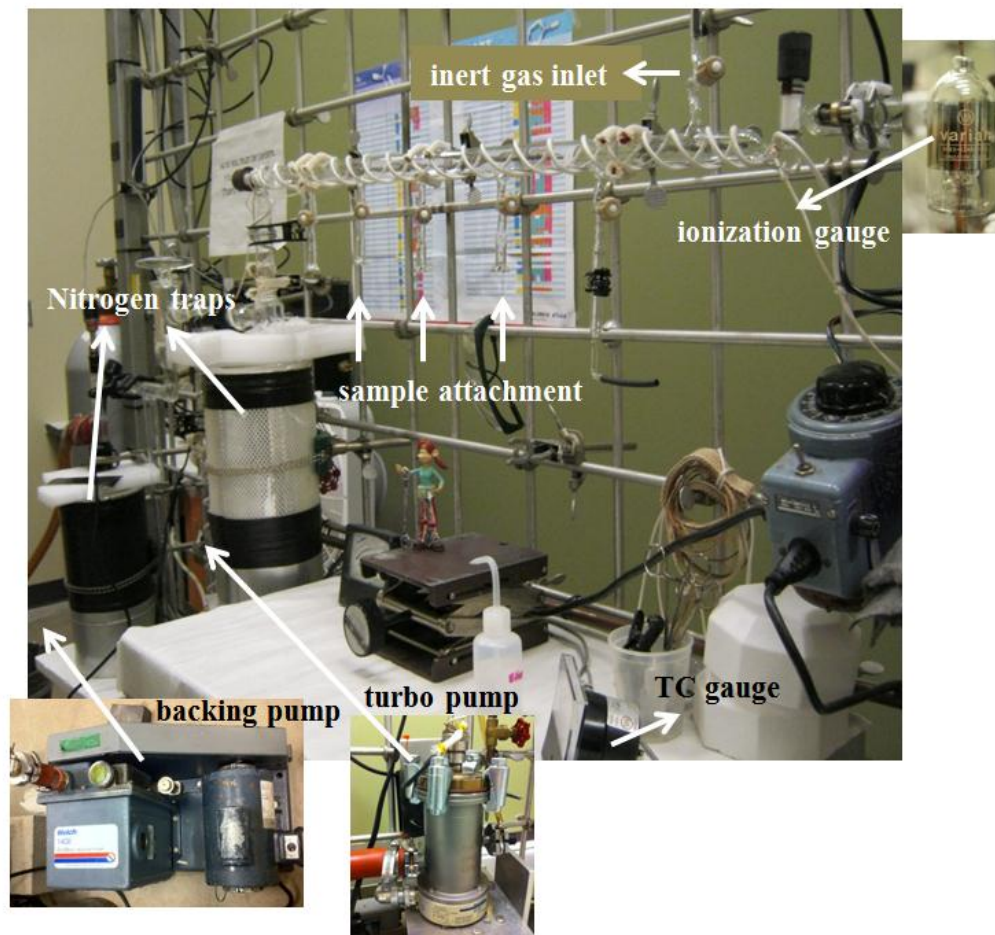


Fig. 3-4. Custom-built glass vacuum line with base pressure  $\sim 2 \times 10^{-6}$  Torr.

Overnight cleaning of the line by heating was performed especially when drying of one ionic liquid sample was followed by another sample of a different anion or cation. This served to minimize introduction of impurities between different types of samples. Additionally, the assembly was equipped with a purging system for introducing an inert gas to allow back-filling of the line. Back-filling techniques are especially useful for measurements done at the air-liquid interface, as well as in cleaning of optical windows of SFG vacuum cells. The latter procedure was performed when viscous liquid samples (especially ionic liquids) unevenly wet the surface of optical windows during the drying process. This step is critical because if optical windows of vacuum cells are not cleaned properly, the SFG signal intensity noticeably decreases.

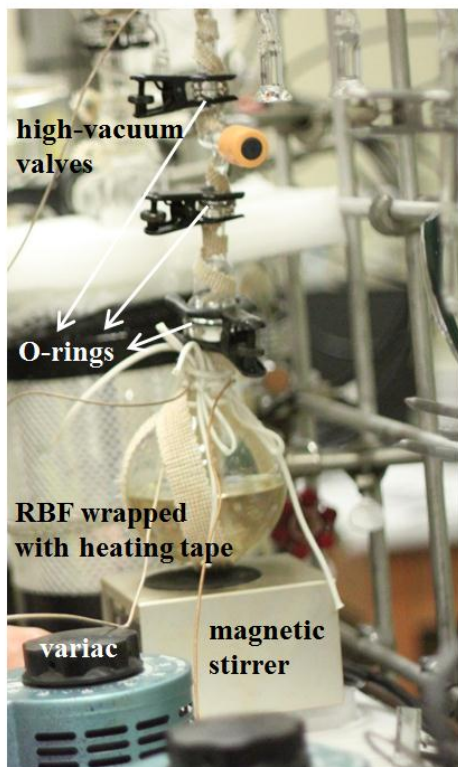


Fig. 3-5. Heated drying of [BMIM][Cl] on vacuum line prior to further characterization.

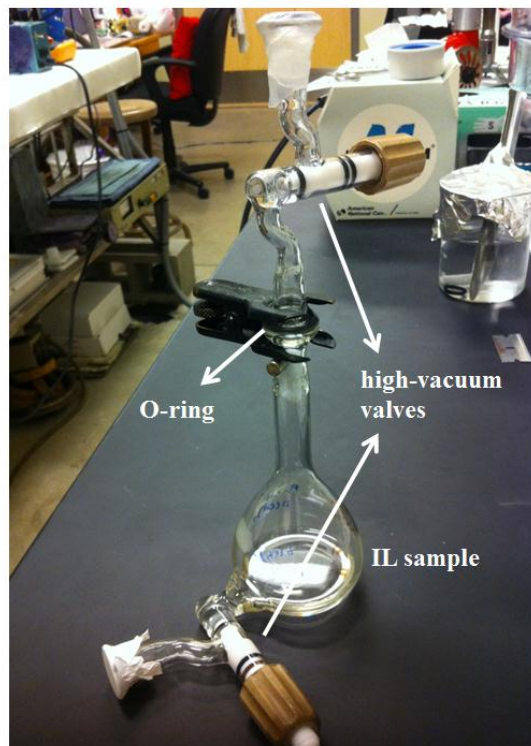


Fig. 3-6. Vacuum cell used for drying ionic liquids up to  $\sim 10^{-5}$  Torr.

Because [BMIM][Cl] serves as a precursor in the preparation of cyano-containing ionic liquid samples, it was important to affirm its purity prior to anion exchange reactions. Following its synthesis and purification using activated charcoal, the [BMIM][Cl] product was further purified by drying under high vacuum with continuous stirring and heating below  $\sim 60^{\circ}\text{C}$ .

Figs. 3-5 and 3-6 show the setup for heated drying in the vacuum line, depicting the use of variac-controlled heating tapes externally wrapped around a round-bottom flask, extending towards the vacuum line. Heating was done to keep the sample in the liquid state, at the same time, to ensure the removal of the starting material, 1-methylimidazole. The chemical shifts in the  $^1\text{H}$ NMR for H-(C4)-(C5)-H appears distinctly in 1-methylimidazole, which is easily distinguishable from those of the [BMIM][Cl] (see Fig B-9, Appendix B), and therefore serves as a good test for product purity prior to further metathesis reactions. Moreover, the cyano-containing ionic liquids, [BMIM][SCN] and [BMIM][DCA] resulting from anion exchange of [BMIM][Cl] with corresponding potassium and sodium salts of the anions, tend to colorize upon prolonged heating due to thermal degradation<sup>6</sup> such that samples were dried (without heating) in the glass line using the vacuum cell shown in Fig. 3-6, which effectively holds pressures in the  $\sim 10^{-5}$  Torr range.

### 3.2.2. Purity Analysis

#### 3.2.2.1 Chloride Analysis

Previous studies have found that all ionic liquids made by metathesis from the corresponding sodium salt have high chloride contents due to unreacted starting material, as the metathesis does not proceed to completion.<sup>7</sup> A high level of residual chloride consequently affects the properties of ionic liquids by increasing viscosity while decreasing density. Additionally, <sup>1</sup>HNMR spectra of chloride-contaminated samples have revealed effects on the chemical shifts of imidazolium ring protons,<sup>7,8</sup> attributed to an increase in cohesive forces through hydrogen bonding with chloride ions. On the other hand, evidence from previous studies have shown that a reduction in hydrogen bonding capability leads to an increase in viscosity for imidazolium-based ionic liquids.<sup>9</sup>

The amount of chloride for samples included in this study was analyzed using a chloride ion-selective electrode (ISE) from Weiss Research. The electrode is known to be sensitive in the concentration range of 1.8 to 35,500 ppm with a reproducibility of  $\pm 2\%$ . The ISE was used in the purification step, during aqueous extraction of the ionic liquid in dichloromethane, to monitor chloride content in the water washings. Actual chloride content in the ionic liquid was not determined immediately after the synthesis; rather, the readings in the aqueous washings were used to establish the point at which chloride concentration was found to be below the detection limit of the ISE. This limit is equivalent to the voltage reading of the ISE for Millipore water ( $\sim 250$  mV). Measurement was done by immersing the ISE in the aqueous washings and comparing the readings with Millipore water. Throughout the purification step, the electrode was rinsed

thoroughly and blot-dried to avoid cross-contamination. The protocol for the washing procedure described above for the removal of chloride has been established previously.<sup>10,11</sup> For ionic liquid samples treated in the same manner, and in which actual chloride concentrations were detected, reported chloride contents were found to be <100 ppm.<sup>12</sup>

In this study, all samples were dried in the glass vacuum line following purification steps which ensured that the ionic liquids were free of any organic impurity which may impart color (*i.e.* treatment with activated charcoal in methanol). Actual chloride content in the samples was determined using the ISE after SFG measurements in both air-liquid and solid-liquid interfaces had been performed. Measurements were done on 1.0 mL aliquot samples of the ionic liquid diluted to 100 mL. 2.0 mL of 5 M NaNO<sub>3</sub> was added to adjust the ionic strength of the sample solution according to ISE manufacturer's specifications.<sup>13</sup> Readings were taken and allowed to stabilize over a time period of 1–2 minutes. A representative calibration curve using [BMIM][Cl] as a standard for the external calibration method (ECM) in the analysis of chloride is depicted in Fig. 3-7. For [EMIM][TCB], the standard [EMIM][Cl] instead of [BMIM][Cl] was used for calibration. Using identical concentration ranges for [BMIM][Cl], response curves for calibration using [EMIM][Cl] were found to be similar, as depicted in Fig. 3-8. From calculations using the calibration curves, actual chloride concentrations,  $x$ , were found to be  $50 > x < 100$  ppm for all samples.

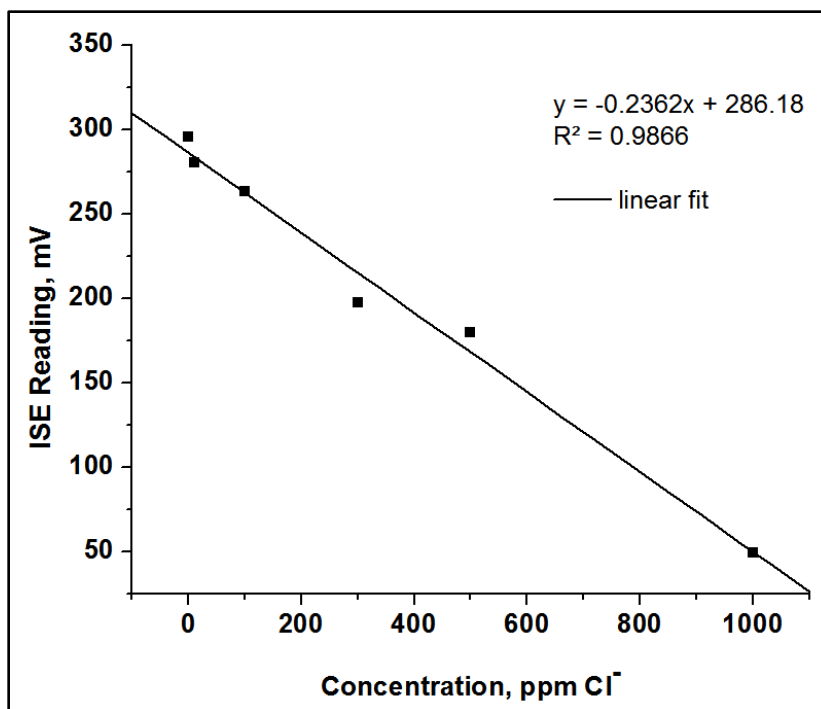


Fig. 3-7. Calibration curve using [BMIM][Cl].

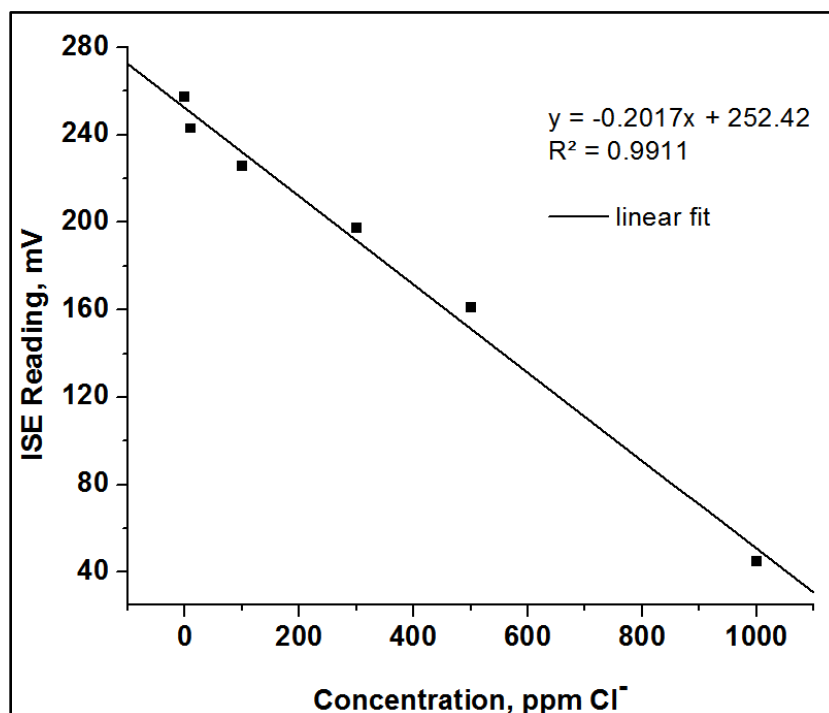


Fig. 3-8. Calibration curve using [EMIM][Cl].

The single standard addition method (SSAM), in addition to the external calibration method, was employed in the analysis of chloride to determine its level after ionic liquids have been in contact with the NaCl{100} window. Standard addition methods are particularly useful in the analysis of complex samples in which the matrix effects (sample environment in the absence of the analyte) may be likely and/or substantial.<sup>14</sup> A standard addition method can take several forms. Owing to its simplicity, the most common method, known as “spiking” was employed in this study. Specifically, an important advantage of using this technique as opposed to using the external calibration method is that interference effects of the different anions with the electrode are minimized as they are accounted for in the measurement of total response of the spiked samples.

In the analysis, a sample aliquot size of 0.5 mL was used for each ionic liquid sample, which was added with a known amount of internal standard. [BMIM][Cl] was used as an internal standard in the chloride analysis for [BMIM][SCN], [BMIM][DCA] and [BMIM][TCM]. For [EMIM][TCB], [EMIM][Cl] was added instead of [BMIM][Cl]. All samples were diluted to a final total volume of 100 mL. The readings using “spiked samples” were compared to those of the pure samples (using equal sample aliquot sizes of 0.5 mL), from which the concentration of the pure samples were calculated. Equation 3-1 shown below, served as a working equation for the calculation of chloride contents in the original sample.

$$\frac{Rspl}{Cspl} = \frac{Rspl + std}{Cspl + std} \quad (\text{Eq. 3-1})$$

where  $Rspl$  = response of the sample

$Cspl$  = concentration of the sample

$Rspl + std$  = response of the sample with added standard

$Cspl + std$  = concentration of the sample with added standard

Results of the chloride analysis using the standard addition method are tabulated in Table 3-1. Accuracy of the measurements were within  $\pm 100$  ppm out of two measurements. The levels show chloride contents much higher than the initial readings of  $< 100$  ppm especially for [EMIM][TCB], as this particular ionic liquid noticeably dissolved the surface of NaCl{100} window. It should be noted that the NaCl{100} windows were not reusable after one experiment has been performed with the ionic liquid, as once the liquid was in contact with the solid salt, the surface became visibly rough. This was observed after the ionic liquid was washed off the crystal surface with methanol solvent, indicating that the physical interaction between the solid-liquid system altered its original surface properties.

Table 3-1. Measured Chloride Content of Ionic Liquids Using the Single Standard Addition Method (SSAM) After Contact With NaCl{100} Window

Ionic Liquid	[Cl] in ppm	Equivalent [Cl] in mol/L
[BMIM][SCN]	~800	0.022
[BMIM][DCA]	~700	0.020
[BMIM][TCM]	~700	0.020
[EMIM][TCB]	~1200	0.034

To compare the results between the two methods in the chloride determinations, ECM and SSAM, ECM results for [BMIM][SCN] was found at ~500 ppm; [BMIM][DCA] at ~400 ppm; [BMIM][TCM] at ~300 ppm; and [EMIM][TCB] at ~800 ppm. The difference between the measurements using the two methods is significant, especially for [EMIM][TCB] where SSAM results were found greatest (at ~400 ppm higher than in ECM) possibly due to the dissolution of the crystal in the ionic liquid. However, it is difficult to infer from the different values obtained which one estimates the true concentration, as both techniques are suitable for the analysis. It is noteworthy to mention though that while ECM does not take into account matrix effects, SSAM does, which may result to different values obtained in the sample.<sup>14</sup> It is a recommendation of this thesis that further careful measurements be done to determine the difference between the two analytical techniques used. Unfortunately, because of the small amount of sample available for the analysis, especially for [BMIM][TCM] and [EMIM][TCB], the accuracy of the two techniques in determining levels of chloride was not established firmly in this study. Further information to provide confirmation of results on the efficiency, effectiveness and accuracy of the analytical techniques must be performed in the future.

#### **3.2.2.2. Water Content**

All ionic liquid samples were dried in a glass vacuum line down to a pressure of  $\leq 5 \times 10^{-5}$  Torr. Values for specific water vapor pressure can be determined using the Henry's law constant established by Brennecke, *et al.*<sup>15,16</sup> At a base pressure of  $2 \times 10^{-5}$ , the mole fraction of water was calculated to be at  $1.5 \times 10^{-7}$ .<sup>10</sup>

### 3.3. SFG Spectroscopic Measurements

Details of the SFG spectrometer setup have been described in previous papers.<sup>17-19</sup> Briefly, a picosecond pulsed Nd:YAG laser with a fundamental 1064-nm output was used to pump an optical parametric generator/amplifier (OPG/OPA, LaserVision) system to generate a fixed visible (532-nm) and frequency tunable IR ( $2000\text{-}4000\text{ cm}^{-1}$ ) beam. The fixed visible and IR beams follow a co-propagating geometry and are overlapped at the sample surface at an angle of  $50^\circ$  and  $60^\circ$  from the surface normal, respectively. The SFG signal is collected via a gated integrator and computer-controlled using LabVIEW software. Detailed descriptions and illustrations of the setup are discussed below.

#### 3.3.1. Nd:YAG Laser



Fig. 3-9. Nd:YAG laser system

The laser system used in the experiments is an EKSPLA PL2251A, Nd:YAG with a fundamental 1064-nm beam, approximately  $\sim 8\text{ mm}$  in diameter. The instrument generates pulses of  $\sim 20\text{ ps}$  with a repetition rate of  $20\text{ Hz}$ . Maximum output energy of the fundamental beam is at  $\sim 50\text{ mJ}$  with  $<1.5\%$  stability. The heart of the system is a diode

pumped passively mode-locked master oscillator employing Nd:YVO<sub>4</sub> laser material. Mode-locking is achieved by means of a saturable absorber. Fig. 3-9 shows a picture of the laser cavity. The laser system roughly consists of three parts: the master oscillator, the regenerative amplifier, and power amplifier. Further details on its specifications are available in the literature.<sup>20</sup>

### 3.3.2. Optical Parametric Generation/Amplification System

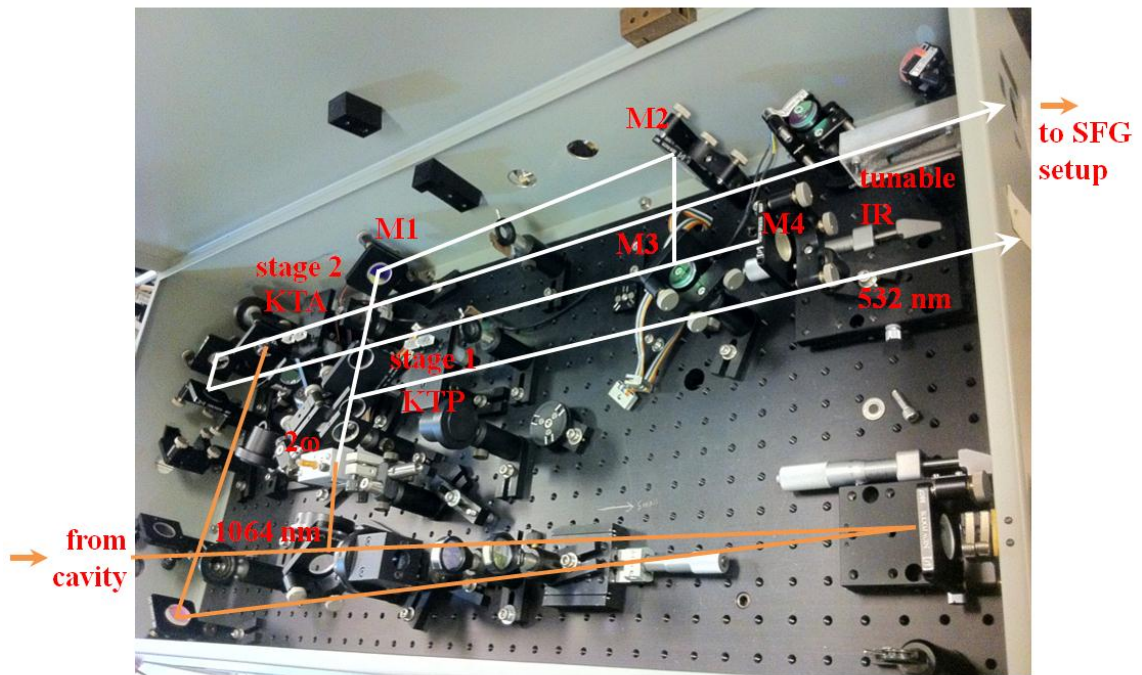


Fig. 3-10. Top view of LaserVision OPG/OPA system with beam configuration.

The LaserVision system uses a combination optical parametric generation (OPG) and optical parametric amplification (OPA) to convert the fundamental 1064-nm beam into a fixed visible and tunable mid-infrared radiation using nonlinear crystals, KTP (KTiOPO<sub>4</sub>) and KTA (KTiAsO<sub>4</sub>). The OPG/OPA system is shown in Fig. 3-10, tracing

the beam path of the fundamental output from the Nd:YAG through the various components of the system.

A high intensity source, Nd:YAG laser was used to pump the parametric system, with the horizontally-polarized 1064-nm beam sent into the OPG/OPA and separated into two beams by a beam splitter. The first beam was frequency doubled using a KTP crystal to produce a fixed 532-nm beam while the other was sent through a delay line. A half-wave plate before the KTA crystal controlled the conversion efficiency and intensity of the 532-nm beam. The 532-nm beam was further separated by a second beam splitter following the frequency-doubling crystal: One beam was directed towards the SFG spectroscopy setup and used as the fixed visible source; while the other was directed towards the KTP crystals for stage 1 conversion. In stage 1, as the beam reached the nonlinear KTP crystal from left to right in the figure, optical parametric generation was achieved. Two resulting beams of different frequencies were generated in this process, known as the *idler* (longer wavelength, lower energy) and *signal* (shorter wavelength, higher energy) beams, respectively. Three mirrors (M1, M2, and M3) in stage 1 reflect only the 532-nm beam allowing the *idler* and *signal* to pass through M3, and reflect back into the KTP crystals through M4. As the 532-nm beam recombined with the *idler* (generated during the first pass), optical parametric amplification process was generated on the second pass of both *idler* and *signal*. Because M4 is mounted on a translational stage, fine adjustments on the temporal overlap of the beams can be made.

The residual 532-nm was then removed following the first stage. The *idler* wave (tunable at 710–880 nm) separated from the *signal* wave by a polarizer, was then

recombined with the 1064-nm fundamental beam and sent through the KTA crystals in stage 2 for a difference frequency mixing process. Parametric generation yielded a signal beam from 1.35–5.0  $\mu\text{m}$ . The crystals of equal length, both mounted on a motor and used in both parametric stages were angle-tuned using LaserVision software to control their rotation, achieve phase matching and compensate for beam displacement. By rotating the crystals in the plane parallel to the optical table, in which its optical axis lie, the refractive index of light polarized in similar direction was changed, resulting in the generation of tunable mid-infrared light from 2000–4000  $\text{cm}^{-1}$ .<sup>21</sup>

Following the OPG/OPA system, the 532-nm and tunable IR beam are sent to the SFG sample stage through the use of mirrors, lenses and various optical components. Fig. 3-11 shows the dimensions and beam path from the OPG/OPA system towards the sample stage.

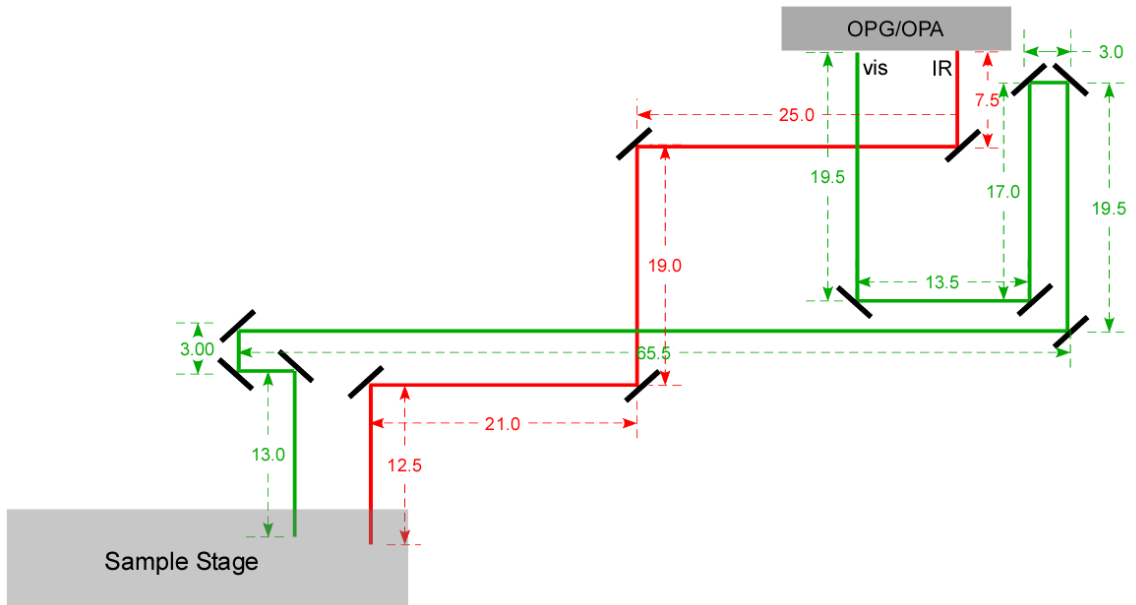


Fig. 3-11. Beam path and setup dimensions (in inches) from OPG/OPA system to sample stage.

### 3.3.3. SFG Optical Setup

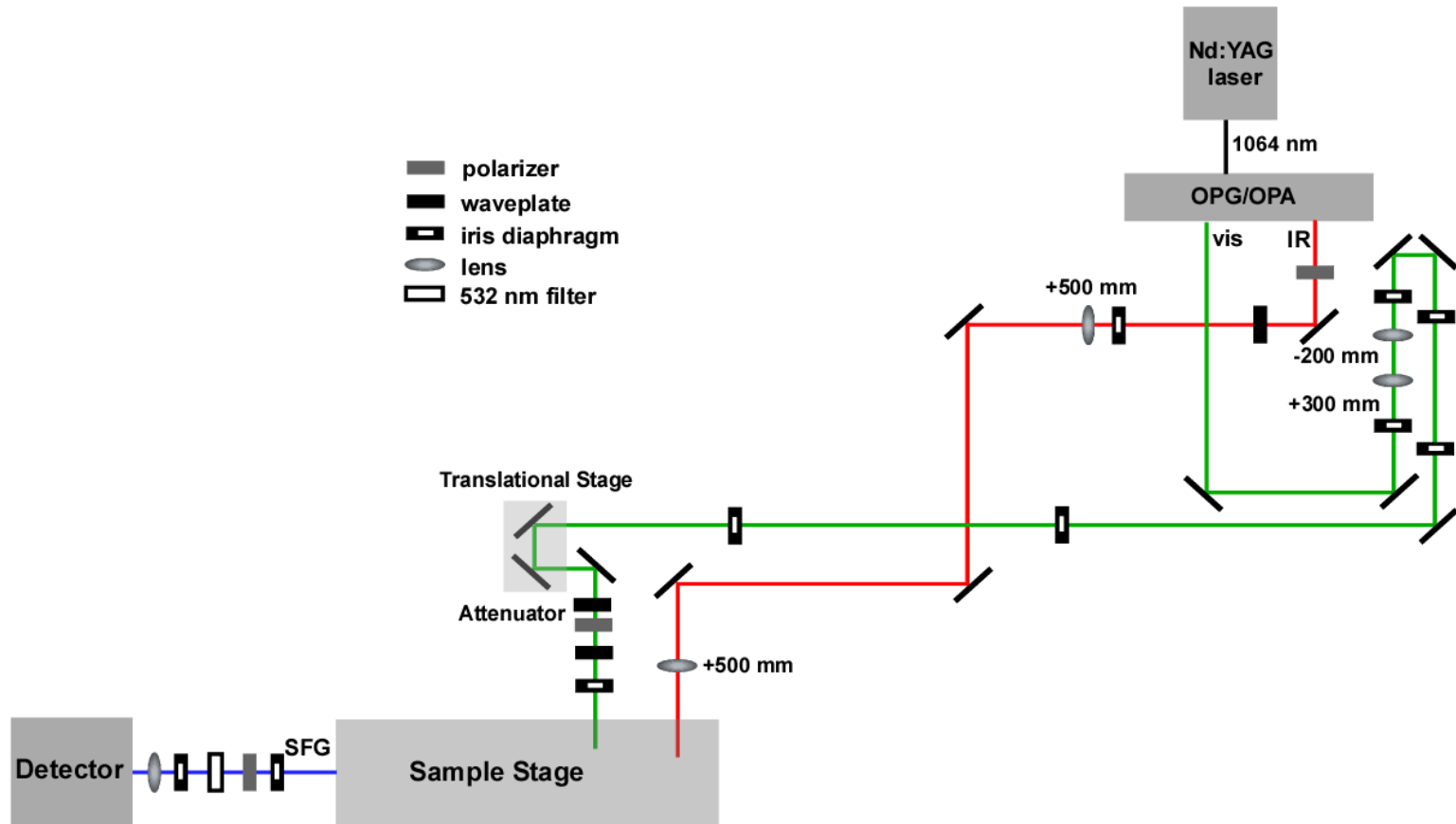


Fig. 3-12. Overall scheme of SFG optical setup

A schematic diagram of the overall SFG optical setup including all optical components is shown in Fig. 3-12. A He-Ne laser is used to overlap with the infrared beam for alignment. Both the tunable IR and 532-nm beams come out vertically polarized from the OPG/OPA. To change the polarization of the beam relative to the plane of incidence (which is the plane of the optical table) the IR beam first passes through a tunable zero-order retardation plate. Using gold and silver mirrors, the IR beam is then directed towards the sample stage. Two CaF<sub>2</sub> (+500 mm) lenses placed along the beam path were used to focus the beam and compensate for energy loss resulting from the long path traversed by the beam.

Coming from the OPG/OPA system, the tunable IR is delayed by about ~6 ns. In order to achieve spatial and temporal overlap between the tunable IR and 532-nm beam, the 532-nm beam was allowed to traverse a longer path than the IR beam. In addition, a translational stage to allow adjustment of the timing of the 532-nm beam to match that of the IR was incorporated in the setup. Prior to the translational stage, two lenses (-200 mm and +300 mm) were placed along the beam path, which served as a telescope to control the size of the visible beam. A half-wave plate and Glan-laser polarizer combination, which follows the translational stage, served as an attenuator used to control the intensity of the visible beam. After the attenuator, another waveplate was placed to control the beam polarization prior to the sample stage.

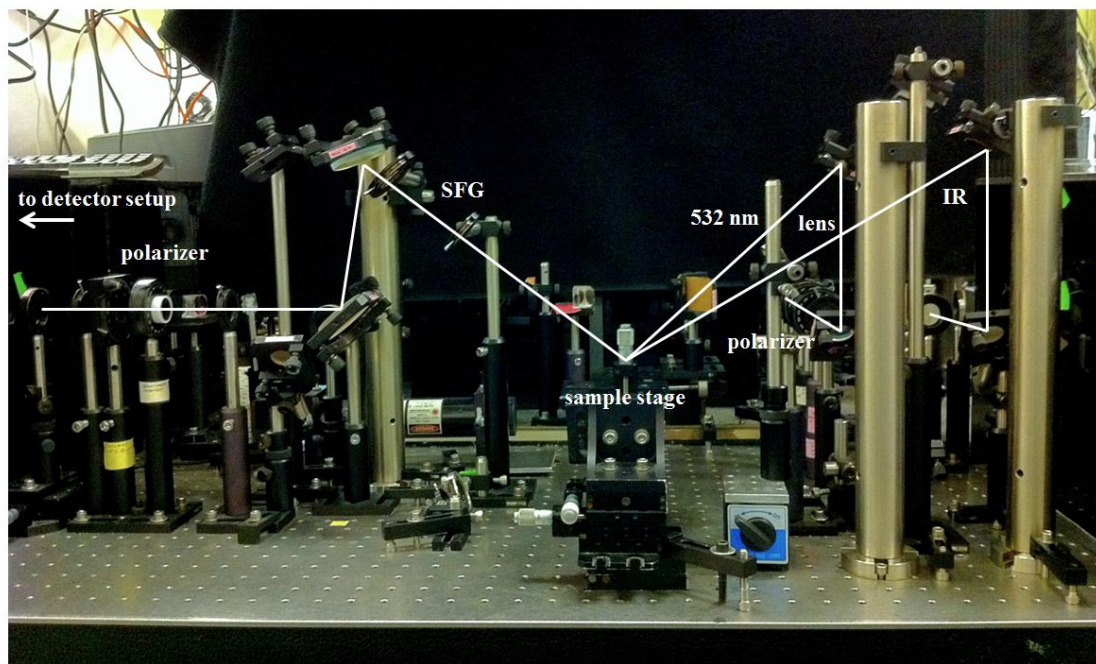


Fig. 3-13. SFG sample stage and beam configuration.

At the sample stage, illustrated in Fig. 3-13, the tunable IR and 532-nm beams were set at incident angles of  $60^\circ$  and  $50^\circ$  with respect to the surface normal, respectively. Both beams were polarized prior to hitting the sample using a Glan-laser polarizer. A  $\text{BaF}_2$  (+200mm) lens focused the IR beam toward the sample surface, to improve its energy. A He-Ne laser, used to trace the beam path of the IR as well iris diaphragms were used to align the beams. The spatial and temporal overlap of the tunable IR and 532-nm beams at the surface of the sample generated the sum frequency signal.

### 3.3.4. Signal Detection System

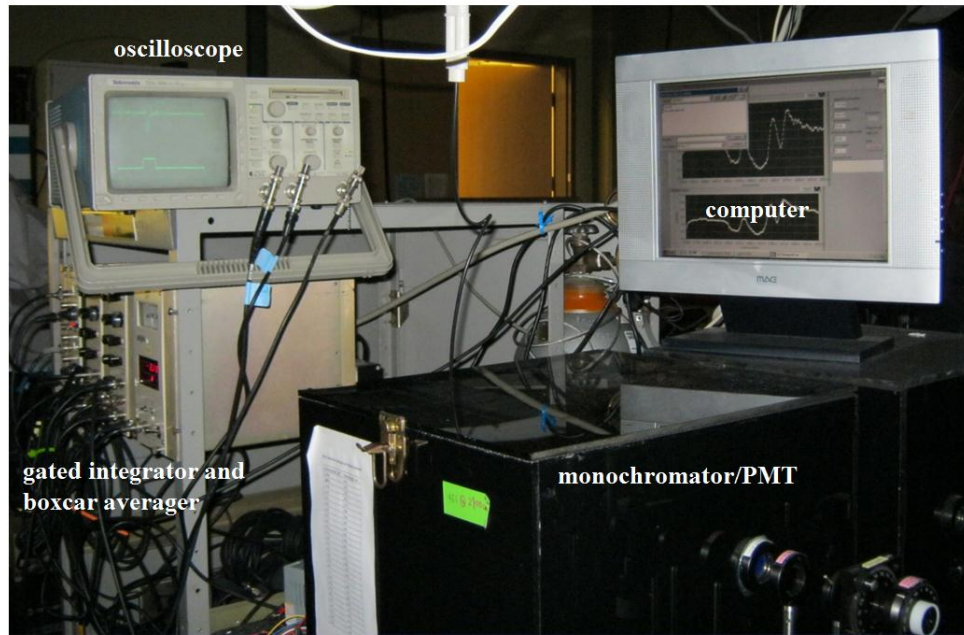


Fig. 3-14. SFG detection system

The sum frequency signal traced by a He-Ne laser was reflected off the surface of the sample and passed through a Glan-laser polarizer for polarization control prior to reaching the detection system. The signal was then focused towards a 515-nm short pass optical filter, which was used to remove residual 532-nm signal prior to reaching the monochromator. The filtered SFG signal was then collected by a photomultiplier tube (PMT, Hamamatsu R3788). This served to amplify the signal prior to sending a voltage response to a gated integrator and boxcar averager (Stanford Research Systems, SR250). The boxcar was triggered externally from the Nd:YAG laser creating a 25-ns width gate. Signal falling within this gate (which was synchronized with the laser pulses) was integrated, minimizing noise generated by stray room light. A computer interface

(Stanford Research Systems, SR245) averaged and integrated the boxcar output. The electronic signal was further controlled *via* a LabView program (National Instruments), which collected the data from the detection system, as the infrared frequency was scanned at a rate of  $1\text{ cm}^{-1}$  per second. All data were plotted at an average of 20 shots per point. The setup for the detection system is shown in Fig. 3-14, showing the oscilloscope, used in visualizing the signal output, the gated integrator and boxcar averager, a computer, and the monochromator/PMT assembly.

### 3.3.5. Calibration and Standards

Wavenumber calibration for tunable IR was done using a polystyrene film (0.038 mm thick) standard. The film was mounted along the IR beam path and spectra were recorded in transmission configuration in the C–H stretching region ( $2750\text{--}3150\text{ cm}^{-1}$ ) using gold as a substrate. The experimental peak assignments were compared to theoretical assignments. A reasonable peak shift difference of  $\pm 2$  wavenumbers was considered acceptable. However, in cases where the shift was significant, re-calibration of motor positions using the software was performed until the wavenumbers matched theoretical assignments. A typical spectrum of the polystyrene standard with labeled peaks is shown in Fig. 3-15.

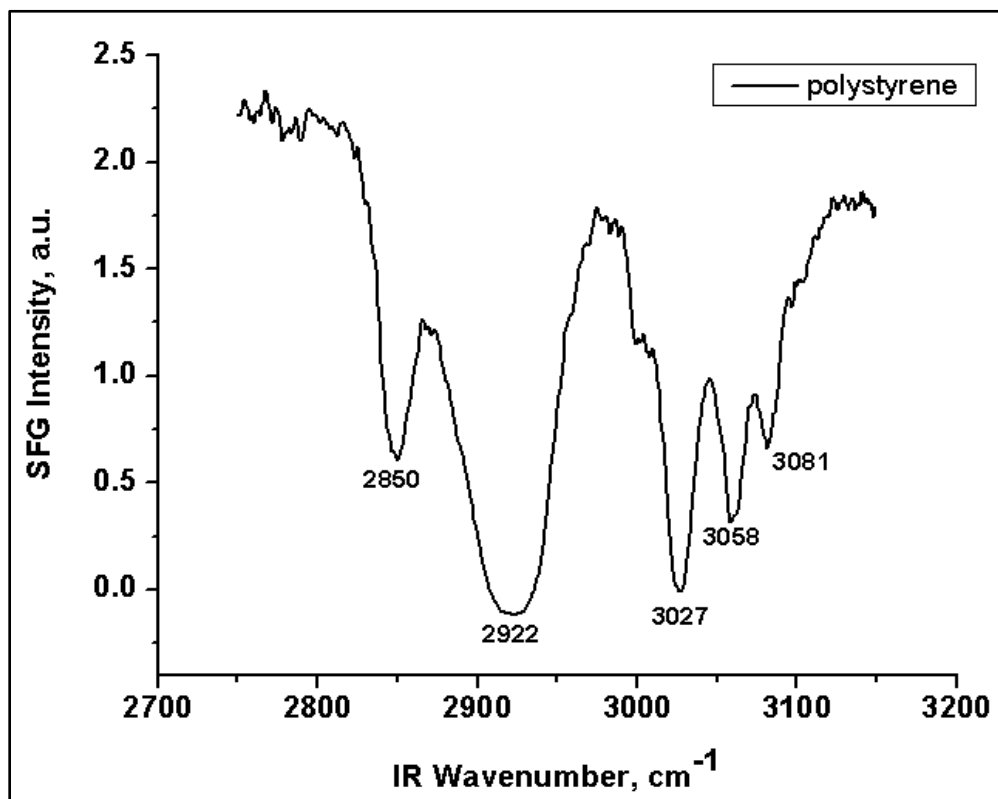


Fig. 3-15. SFG spectrum of 0.038 mm polystyrene standard.

Another standard reference included spectra from a clean gold substrate taken prior to sample measurements, used to correct the energy of the IR beam. Figs. 3-16 and 3-17 show the SFG spectra of gold taken in *ppp* polarization in the C–H and C–N stretching regions, respectively.

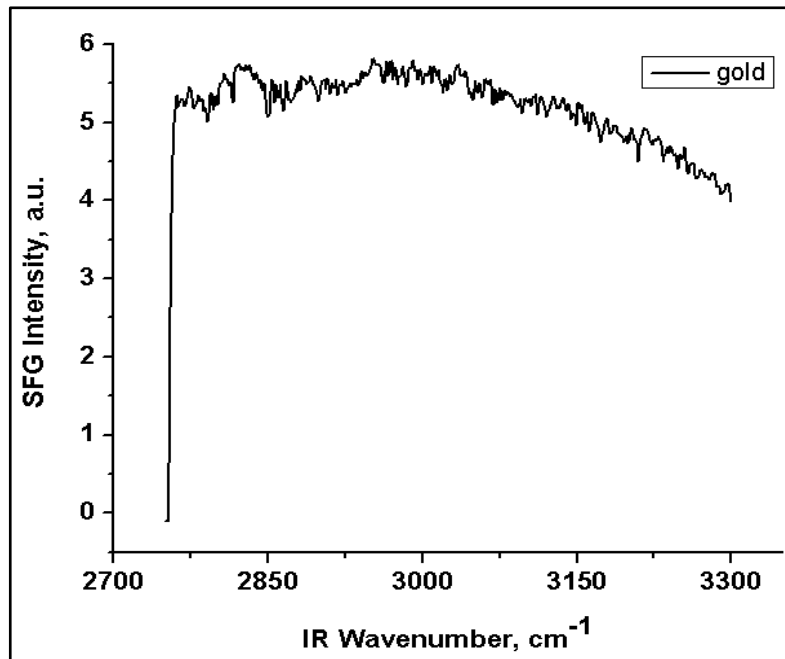


Fig. 3-16. SFG spectrum of gold at the C-H region.

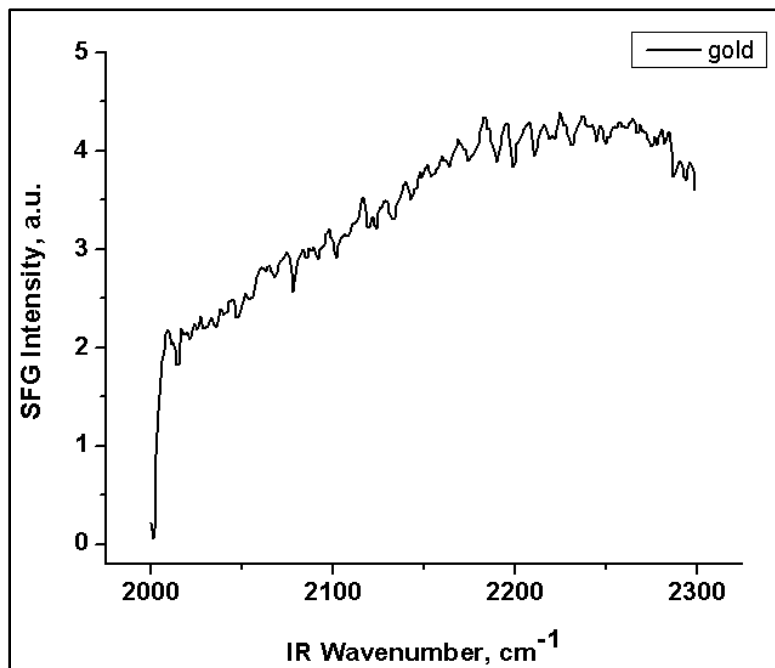


Fig. 3-17. SFG spectrum of gold at the C-N region.

To compare intensities of spectra obtained on different days, a standard solution of hexadecanol in water was used as a reference. Spectra for hexadecanol in *ssp* and *psp* polarizations were measured prior to the ionic liquid sample. Spectra in the off-polarization namely, *psp*, was taken in order to calibrate the IR waveplate. The signal using this combination must be null, otherwise, any resonance would indicate that the IR beam was leaking through the waveplate. The spectra obtained were used to normalize all ionic liquid spectra in the C–H stretching region, through the intensity of the CH<sub>3</sub> symmetric stretch peak at  $\sim 2879\text{ cm}^{-1}$ . A typical spectrum of the hexadecanol standard is seen in Fig. 3-17, showing the methyl symmetric stretch observed with relatively high intensity.

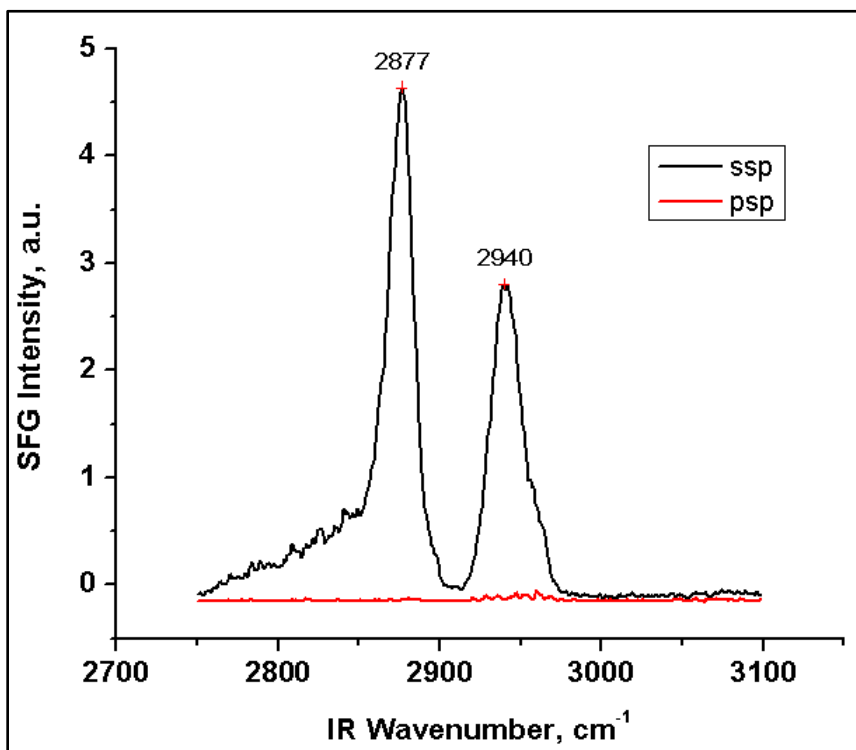


Fig. 3-18. SFG spectrum of standard hexadecanol solution (aqueous) in *ssp* and *psp* polarizations.

### 3.4. SFG at the Air Liquid–Interface

#### 3.4.1. SFG Cell

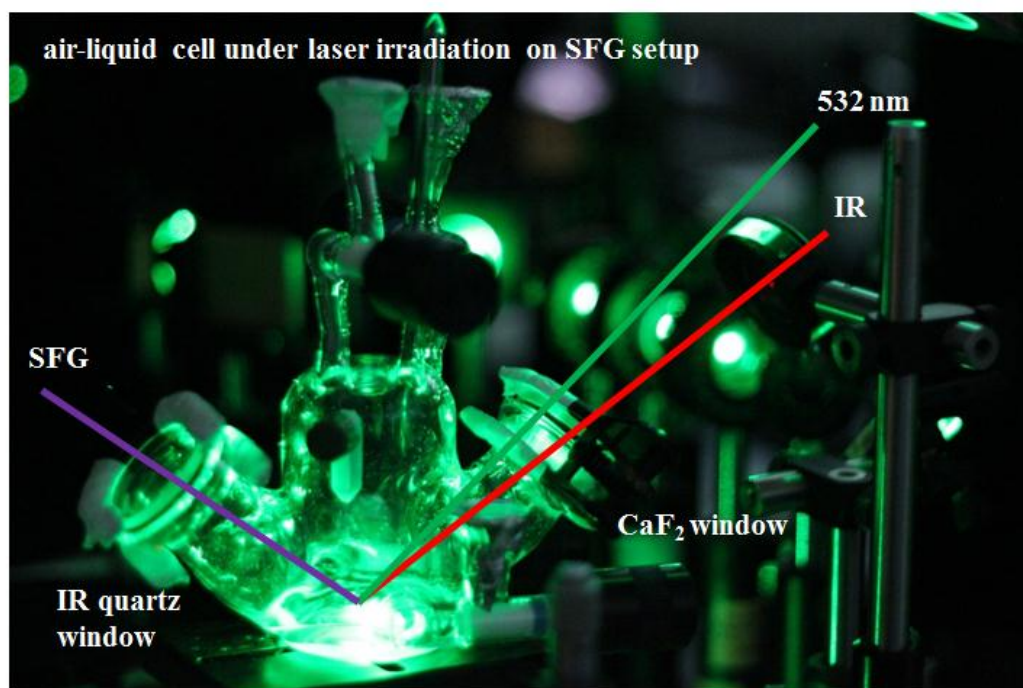
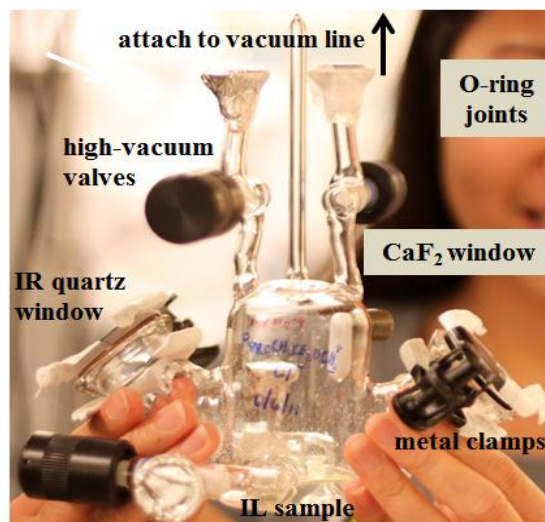


Fig. 3-19. Vacuum cell for SFG measurements at the air-liquid interface .

All ionic liquid samples were contained in a custom-designed SFG cell<sup>3</sup> made of Pyrex® glass, equipped with high-vacuum valves and O-ring fittings. To ensure non-reactivity of samples with materials used for vacuum sealing, Kalrez® O-rings were utilized as well as Teflon® stopcocks. The SFG cell utilized CaF<sub>2</sub> and IR quartz windows for incident and output beams, respectively. Samples were introduced by filtration into the SFG vessel and dried in a glass vacuum line (Fig. 3-4). Ionic liquids were dried until a desired pressure of  $\leq 5 \times 10^{-5}$  Torr was reached, and occasionally heated (up to ~60 °C) with a heat gun to hasten the drying process. Fig. 3-20 shows the SFG cell with filtration setup attached to the glass line during vacuum drying. The samples are known to be thermally stable at the heating temperature used. Once the desired pressure was reached, the samples while attached to the vacuum line, were back-filled with ultra-high purity nitrogen gas to a slight overpressure prior to SFG measurements.



Fig. 3-20. SFG cell for air-liquid measurements with filtration setup attached to vacuum line for drying.

### 3.4.2. Data Collection and Analysis

Data were collected at an average of 5 scans per polarization combination at a scan rate of  $1 \text{ cm}^{-1}/\text{s}$  using 20 laser shots per point. Absorption by the bulk liquid and the changing efficiency of the OPG/OPA system, however, cause fluctuations in the IR beam. To correct for such deviations, SFG signal from a clean gold substrate was taken before any sample measurement and used to divide each spectrum. Tunable IR wavenumber calibration was also performed using polystyrene. Four different polarization combinations were taken for ionic liquid samples, namely, *ssp* (*s*-polarized SFG beam, *s*-polarized visible beam, and *p*-polarized IR beam), *ppp*, *sps*, and *pss*. Furthermore, SFG intensity for individual spectrum was normalized against the intensity of the  $\text{CH}_3$  symmetric stretch peak in *ssp* of a standard solution of hexadecanol in water. Finally, using equation 3 as a fitting function, spectra were fitted via Origin 7.0 Professional nonlinear curve fitting.

### 3.5. SFG at the Solid Salt–Liquid Interface

#### 3.5.1. IL–BaF<sub>2</sub>(111) Interface

The experimental design to allow SFG spectroscopic measurements involving dielectric single crystal salt surfaces in contact with ionic liquids was introduced in this study. The solid–liquid SFG cell, made of Pyrex® glass can hold a total liquid volume of ~7.2 mL. It made use of an earlier design first introduced in a previous publication.<sup>22</sup>

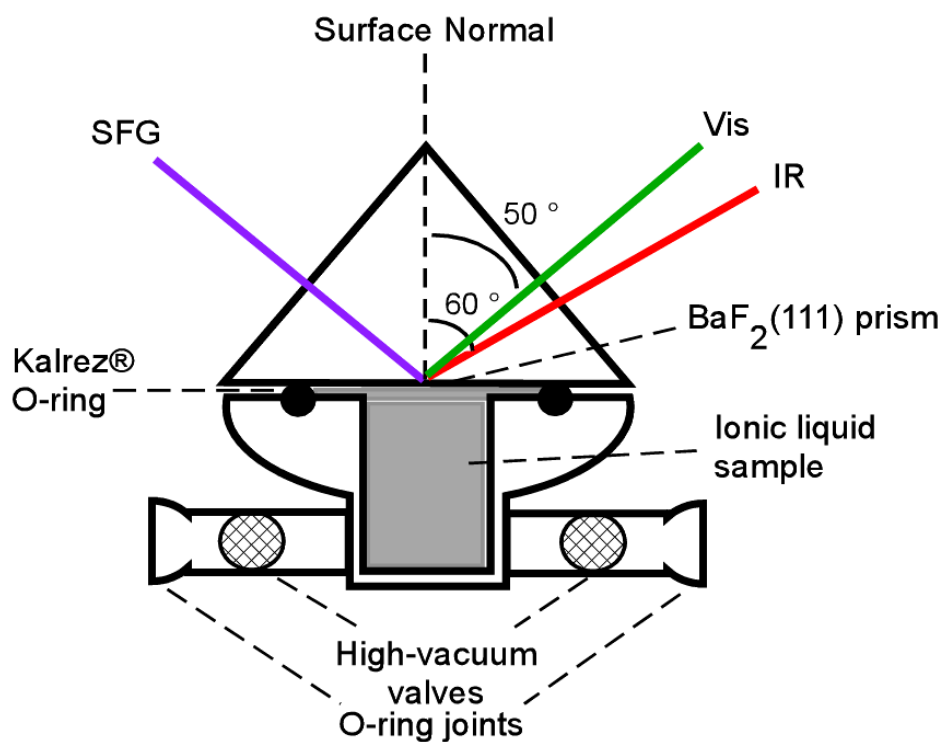
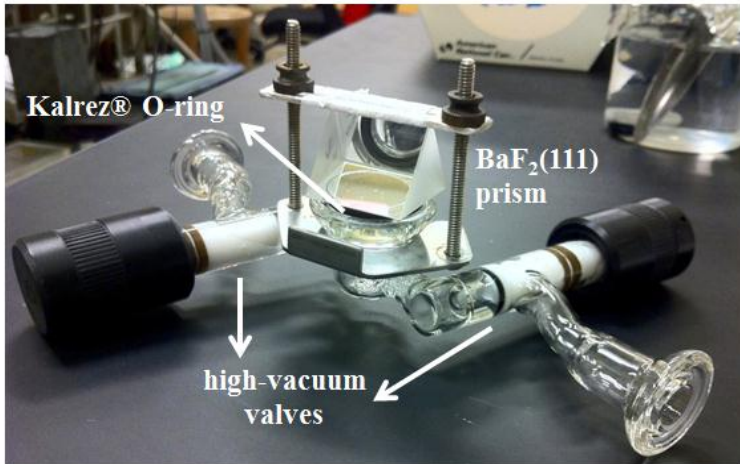


Fig. 3-21. Schematic illustration of solid-liquid SFG cell configuration for SFG measurements at the IL-BaF<sub>2</sub>(111) interface.

The setup used for experiments done on  $\text{BaF}_2(111)$ -ionic liquid interface is shown in Figs. 3-21 and 3-22, containing the  $\text{BaF}_2(111)$  prism (all edges 25.4 mm, United Crystals). The (111) surface of the prism was directly in contact with the ionic liquid sample, while all other prism surfaces where the incoming and outgoing beams hit were not oriented. Metal clamps were used to hold the salt prism in place and Kalrez® O-rings were utilized for all surfaces in which the ionic liquid samples came into direct contact.

### **3.5.2. IL- $\text{NaCl}\{100\}$ Interface**

For studies done at the  $\text{NaCl}\{100\}$ -ionic liquid interface, a similar design was used except that a flat  $\text{NaCl}\{100\}$  optical window (25 mm x 4 mm, Koch Crystal Finishing, Inc.) instead of a prism was used. The salt window was attached to the top and sealed to the glass cell with Kalrez® O-rings using metal clamps before pumping down to high-vacuum pressure. Fig. 3-23 shows a picture of the setup.

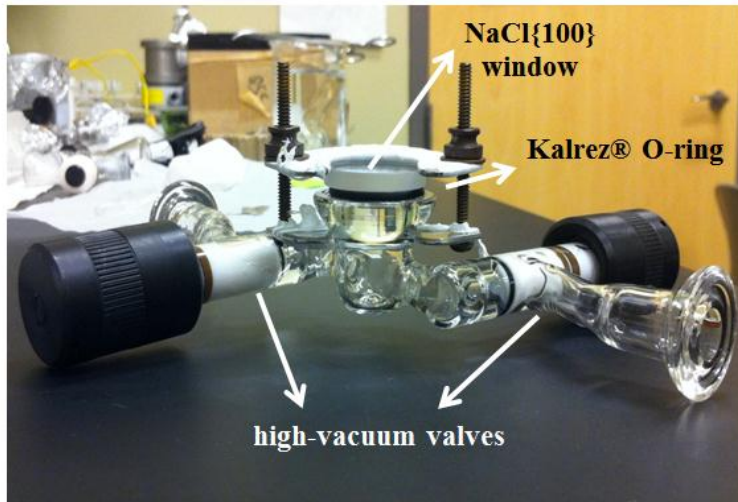


**Side view**

**Top view**



Fig. 3-22. Experimental setup for IL-BaF<sub>2</sub>(111) interface studies.



**Side view**

**Top view**

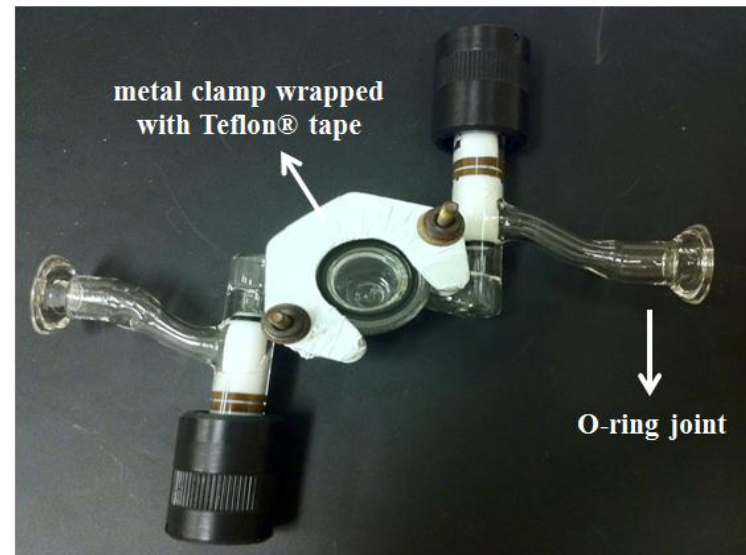


Fig. 3-23. Experimental setup for IL-NaCl{100} interface studies.

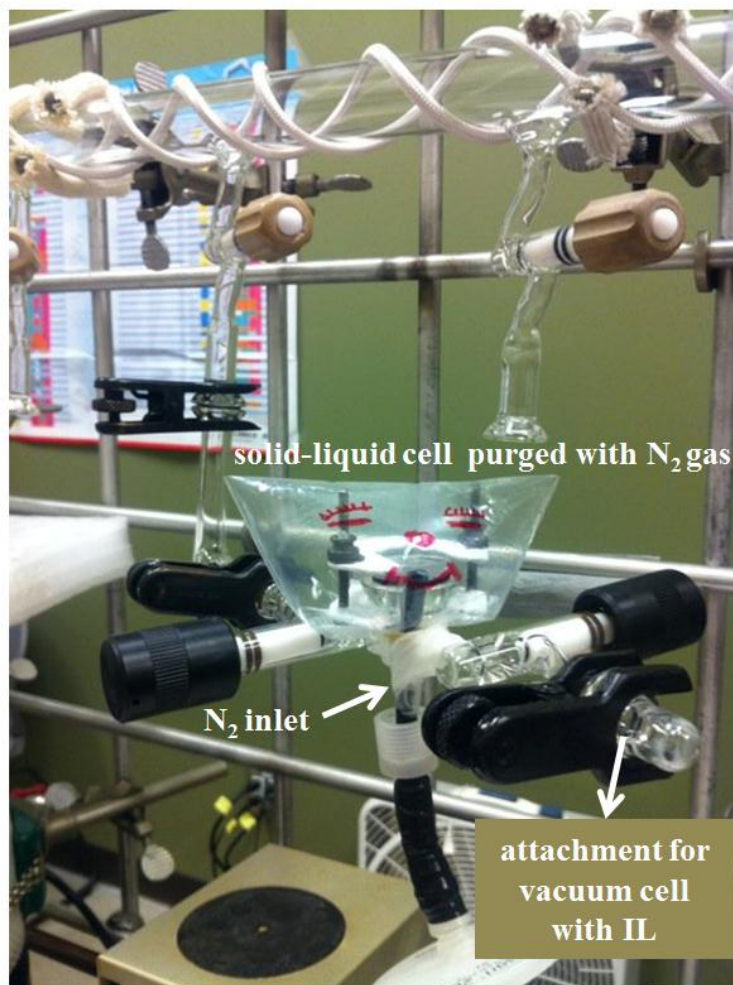


Fig. 3-24. Experimental setup for vacuum drying of empty NaCl{100}-liquid interface cell prior to introducing IL sample.

Because the salt window was sensitive to moisture, it was kept in an enclosed environment at all times prior to and during the measurements. Throughout the vacuum drying process of the solid-liquid assembly, the salt window was wrapped with a Ziploc® plastic bag sealed with rubber bands and parafilm, and purged slowly with nitrogen gas. Fig. 3-24 shows a picture of the experimental setup for drying of the cell in the vacuum line up to  $\sim 5 \times 10^{-5}$  Torr prior to introducing the ionic liquid sample.

### 3.5.3. Purge Box Design and Setup

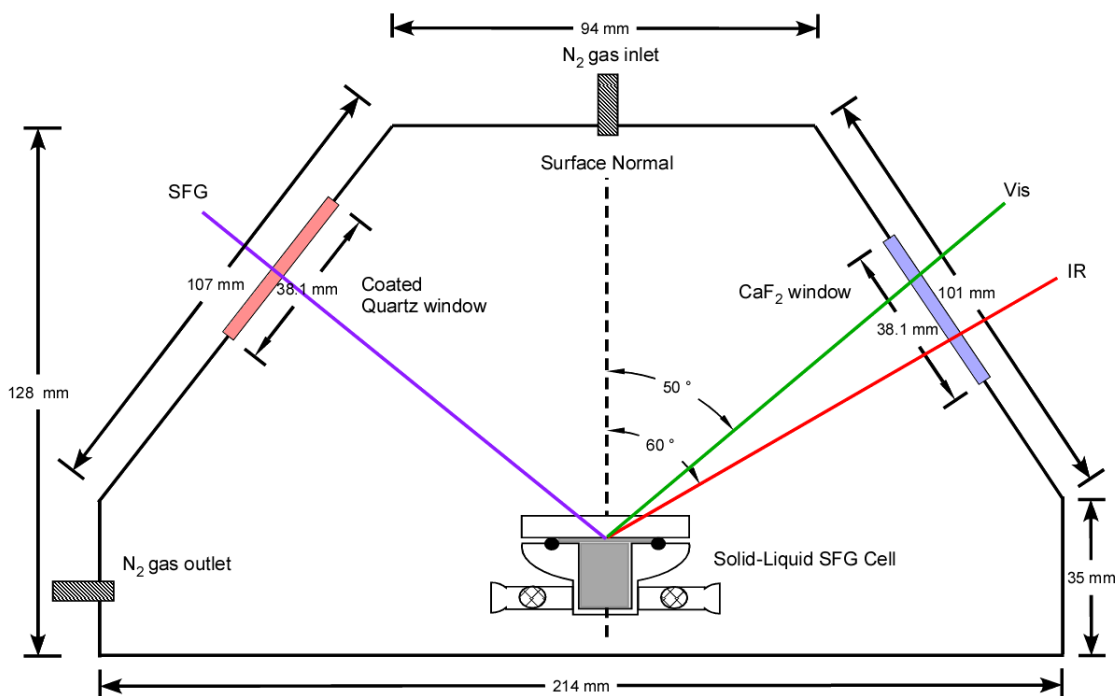


Fig. 3-25. Schematic illustration and dimensions of novel purge box design for SFG spectroscopic measurements at the IL-NaCl{100} interface.

Owing to the salt window's sensitivity to moisture, a purge box enclosure was necessary for experiments at the NaCl{100}-ionic liquid interface, allowing measurements under controlled conditions, *i.e.* under nitrogen gas atmosphere. Fig. 3-25 shows a schematic illustration and dimensions of the home-built purge box setup containing the solid-liquid sample cell with a flat NaCl{100} window.

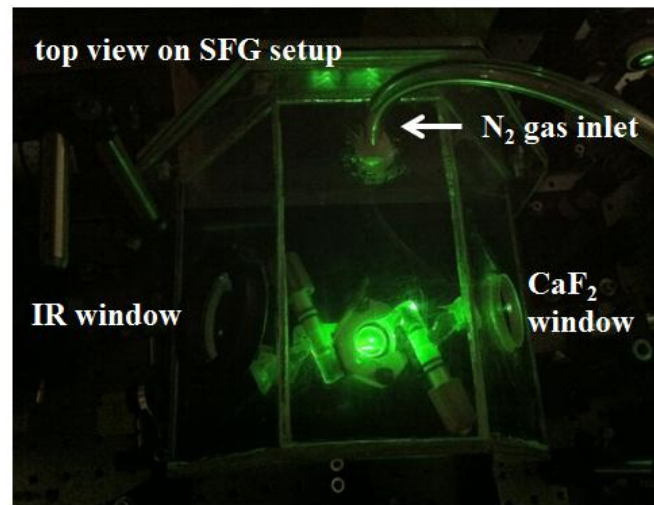
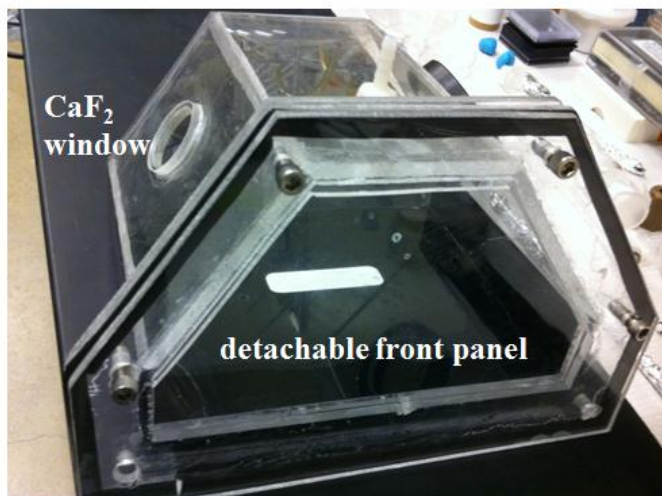
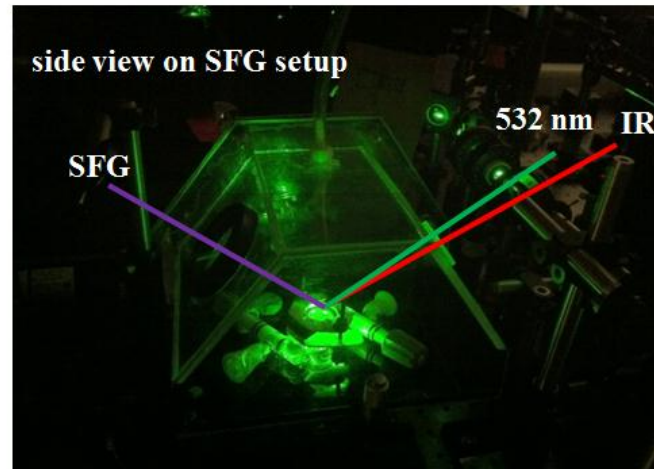
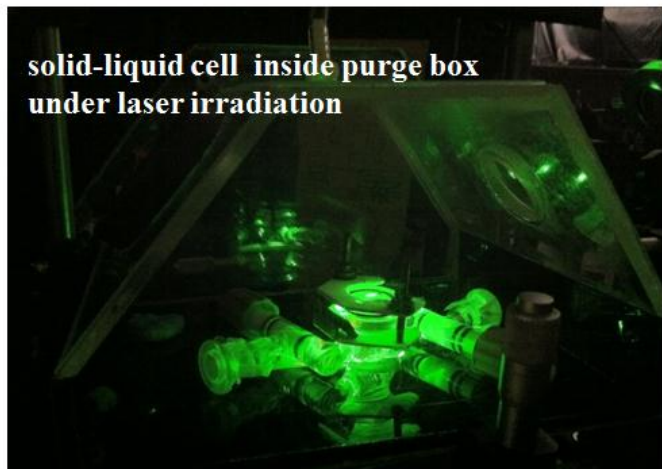


Fig. 3-26. Configuration of purge box assembly on SFG setup during real-time data acquisition.

The purge box design was custom-built to be mounted on the SFG spectrometer setup, made of Plexiglass®, equipped with a CaF<sub>2</sub> window for incoming IR beam, a coated quartz window for outgoing SFG beam, and an inlet and outlet for continuous inert gas purging. The front panel was detachable as shown in Fig. 3-26, where the solid-liquid assembly was introduced.

All ionic liquid samples were dried separately in a vessel attached to a glass vacuum line equipped with a mechanical pump, a turbo molecular pump and liquid nitrogen traps, until a desired pressure of  $\leq 5 \times 10^{-5}$  Torr was reached. Air-less transfer of the sample, from the drying vessel to a previously dried and cleaned solid-liquid SFG cell, kept under the same high-vacuum pressure as the liquid sample, was made possible by the use of home-built sample containers equipped with O-ring fittings and high-vacuum valves. Once the desired pressure was reached, the ionic liquid sample in the volumetric flask (see Fig.3-6), while attached to the vacuum line was back-filled with ultra-high purity nitrogen gas to a slight overpressure. The flask containing the ionic liquid purged with nitrogen gas was then detached from the vacuum line and connected to the solid-liquid SFG cell which was also attached to the line (see Fig. 3-24). The latter was then evacuated, and the liquid sample from the volumetric flask was transferred airlessly to the solid-liquid cell by opening the high vacuum valves to direct the flow of the liquid.

The sample was then mounted on the laser spectroscopy setup for SFG measurements. The solid-liquid SFG cell assembly with the NaCl {100} flat window was contained in a home-built purge box enclosure, and flushed continuously with

nitrogen gas during the SFG measurements to prevent salt window contact with moisture in the atmosphere. The latter treatment was not necessary, however, for measurements involving the BaF<sub>2</sub>(111) prism as it was not sensitive to moisture. For such experiments, the entire solid-liquid assembly was mounted directly on the optical setup.

#### **3.5.4. Data Collection and Analysis**

A scan rate of 1 cm<sup>-1</sup>/s, using 20 laser shots per point was used in the data collection, at an average of at least 5 scans. In cases where signal was low, *i.e.* for samples with inherent color or measurements taken in the C–N region, a maximum of 10 scans to increase signal to noise ratio was performed. Wavenumber calibration for tunable IR was done using a polystyrene standard. Spectra from a clean gold substrate taken prior to sample measurements, and spectra from a standard solution of hexadecanol in water in *ssp*, were used to normalize sample spectra in the C–H stretching region, through the intensity of the CH<sub>3</sub> symmetric stretch peak at ~2879 cm<sup>-1</sup>. Spectra in all four polarization combinations namely, *ssp*, *ppp*, *sps*, and *pss* for ionic liquid samples were measured. Finally, Origin 7.0 professional nonlinear curve fitting software was used in processing final SFG spectra using equation (3) as a fitting function.

#### **3.6. Infrared Spectroscopy**

Infrared spectra were recorded at room temperature using a Thermo Nicolet Avatar 360 FTIR Spectrometer in the 400-4000 cm<sup>-1</sup> range. A drop of dry ionic liquid was pressed between CaF<sub>2</sub> windows and taken for measurement.

### 3.7. Raman Spectroscopy

Measurements for all four ionic liquids were taken with a polarized incident beam of approximately 120-mW power at the sample point. The in-house built Raman instrument has capabilities for both Raman spectral analysis in conventional mode, and in total internal reflection (TIR) Raman mode. It is equipped with a 488-nm wavelength laser line (Innova 318 Series by Coherent), a back illuminated charge-coupled device (DU-BR by Andor Technology), a spectrograph with 100- $\mu\text{m}$  slit width and 85-mm focusing optics (Kaiser Optical, 1.8 fi), and a high-frequency transmission grating with approximately 2600 grooves/mm and reciprocal resolution of 2.2  $\text{cm}^{-1}/\text{pixel}$  (Kaiser Optical Instruments).

The spectra for [EMIM][TCB] and [BMIM][SCN] were acquired (with samples contained in NMR tubes) in conventional Raman mode with a horizontally-polarized excitation beam, and 5 sec acquisition time. [BMIM][DCA] was analyzed as a neat liquid placed in the sampling cell that is usually used for TIR-Raman with an acquisition time of 0.1 msec. [BMIM][TCM], however, was analyzed by drop-casting a thin film on the flat surface of a silica hemisphere and taking the spectrum in TIR-Raman mode with *p*-polarized incident light, at acquisition time of 0.1 msec. The different acquisition modes were chosen for optimizing spectral quality, and minimizing the fluorescent background over the range 1200-3500  $\text{cm}^{-1}$ .

### 3.8. References

- (1) Kamal, A.; Chouhan, G. *Tetrahedron Lett.* **2005**, *46*, 1489-1491.
- (2) Rivera-Rubero, S.; Baldelli, S. *J. Phys. Chem. B* **2006**, *110*, 4756-4765.
- (3) Aliaga, C.; Baldelli, S. *J. Phys. Chem. B* **2007**, *111*, 9733-9740.
- (4) Kaerkkainen, J.; Asikkala, J.; Laitinen, R. S.; Lajunen, M. K. Z. *Naturforsch. B. Chem. Sci.* **2004**, *59*, 763-770.
- (5) Liu, Q.; Janssen, M. H. A.; van Rantwijk, F.; Sheldon, R. A. *Green Chem.* **2005**, *7*, 39-42.
- (6) Wooster, T. J.; Johanson, K. M.; Fraser, K. J.; MacFarlane, D. R.; Scott, J. L. *Green Chem.* **2006**, *8*, 691-696.
- (7) Seddon, K. R.; Stark, A.; Torres, M.-J. *Pure Appl. Chem.* **2000**, *72*, 2275-2287.
- (8) Avent, A. G.; Chaloner, P. A.; Day, M. P.; Seddon, K. R.; Welton, T. J. *Chem. Soc., Dalton Trans.* **1994**, 3405-3413.
- (9) Hunt, P. A. *J. Phys. Chem. B* **2007**, *111*, 4844-4853.
- (10) Rivera, S. Ph.D. Thesis, University of Houston, 2006.
- (11) Santos, C. S. Ph.D. Thesis, University of Houston, 2008.
- (12) Rivera-Rubero, S.; Baldelli, S. *J. Phys. Chem. B* **2006**, *110*, 15499-15505.
- (13) "Glass-body, Double-Junction Combination Chloride Ion-Selective Electrode Instruction Manual"; Manufacturer's Manual, Weiss Research, 2010.
- (14) Skoog, D. A.; Holler, J. F.; Nieman, T. A. *Principles of Instrumental Analysis*; 5th ed.; Harcourt Brace and Company: Philadelphia, 1998.

- (15) Anthony, J. L.; Maginn, E. J.; Brennecke, J. F. *J. Phys. Chem. B* **2002**, *106*, 7315-7320.
- (16) Anthony, J. L.; Maginn, E. J.; Brennecke, J. F. *J. Phys. Chem. B* **2001**, *105*, 10942-10949.
- (17) Baldelli, S. *Acc. Chem. Res.* **2008**, *41*, 421-431.
- (18) Baldelli, S. *J. Phys. Chem. B* **2003**, *107*, 6148-6152.
- (19) Santos, C. S.; Baldelli, S. *J. Phys. Chem. B* **2009**, *113*, 923-933.
- (20) "*PL2251 Series Laser: Technical Description and User Manual*"; EKSPLA: Lithuania, 2010.
- (21) "*Operation and Maintenance Manual for Custom for KTP/KTA/AgGaSe2 OPG/OPA System*"; LaserVision, 2001.
- (22) Aliaga, C.; Baldelli, S. *J. Phys. Chem. C* **2008**, *112*, 3064-3072.

## Chapter 4. Surface Characterization of Imidazolium-based Ionic Liquids with Cyano-functionalized Anions at the Gas-Liquid Interface Using Sum Frequency Generation Spectroscopy\*

### 4.1. Introduction

Since their first discovery in 1914<sup>1</sup> until today, room-temperature ionic liquids (RTILs) continue to provide the scientific community a plethora of research opportunities to explore their unique and interesting properties. With their extremely low volatility, distinct conductivity properties, and exceptional miscibility behavior, ionic liquids have indeed found an indispensable role in a wide range of applications.<sup>2-8</sup>

Advancement in the field of ionic liquid technology requires a comprehensive understanding of their surface properties, because a wide range of chemical reactions occur mainly at interfaces. As essential media currently used in electrochemical applications<sup>2</sup> and gas-separation technology,<sup>8,9</sup> their accurate molecular level description at the gas-liquid interface is of utmost importance.

Surface science techniques<sup>5,10</sup> have been widely used to characterize RTILs, owing to their unique ability to withstand demanding conditions required by such methods. However, despite the atomic level accuracy and the wealth of information provided by these techniques, vibrational spectroscopy gives the most detailed model for molecular structure, due to the high degree of chemical information provided in the vibrational spectrum. Not only can information as to the identity of the molecule be found in the spectra, but even more specifically, chemical functional groups are identified

---

\* Reproduced with permission from *Phys. Chem. Chem. Phys.* **2012**, *14*, 5122–5131.

due to their unique vibrational resonances.<sup>11</sup> Vibrational spectroscopy is able to distinguish one functional group from another, making it a clearly unique and highly informative technique, well-suited to elucidating the details of molecular structure of ionic liquid surfaces.

There are numerous publications focused on the use of SFG spectroscopy to model the gas-liquid interface of several ionic liquids.<sup>12-18</sup> These studies have covered to a great extent, alkyimidazolium-based ionic liquids with various anions. To date, however, most of these studies have concentrated on determining the surface molecular orientation of the cation moiety. Therefore, in this study, emphasis on the molecular arrangement of the anion and its subsequent role (if any) in determining the surface molecular orientation of the cation is presented. Probing vibrational resonances in both C–H and C–N regions of the spectrum, and structural variation of the anion while keeping the cation constant, provides the avenue for this unique investigation.

The cation and anion structures of ionic liquids involved in this work are illustrated in Fig. 4-1, showing the numbering scheme of the alkydimethylimidazolium [RMIM]<sup>+</sup> cation, with various anions containing cyano groups, such as thiocyanate [SCN]<sup>-</sup>, dicyanamide [DCA]<sup>-</sup>, tricyanomethanide [TCM]<sup>-</sup> and tetracyanoborate [TCB]<sup>-</sup>. Specifically, ionic liquids studied here include 1-butyl-3-methylimidazolium thiocyanate [BMIM][SCN], 1-butyl-3-methylimidazolium dicyanamide [BMIM][DCA], 1-butyl-3-methylimidazolium tricyanomethanide [BMIM][TCM] and 1-ethyl-3-methylimidazolium tetracyanoborate [EMIM][TCB]. Anions such as [DCA]<sup>-</sup> and [TCM]<sup>-</sup> in ionic liquids confer low viscosity.<sup>19-21</sup> Tricyanomethanide-based ionic liquids have low melting points,

are thermally stable and have electrical conductivities similar to dicyanamide ionic liquids.<sup>22,23</sup> However, surface tension measurements of tricyanomethanide- and dicyanamide-containing ionic liquids have shown anomalously high values for their large molar volume, with surface tension data comparable to those of salts with metal tetrachloride cations.<sup>24</sup> As cyano-functionalized ionic liquids, to date, have not gained particular attention in the literature, this study which includes an anion progression from a linear  $\text{SCN}^-$ , to a tetrahedral  $[\text{B}(\text{CN})_4]^-$ , provides information on the effect of varying the anion structure on the surface molecular arrangement, crucial to the understanding of the surface chemistry of these ionic liquids at the gas-liquid interface.

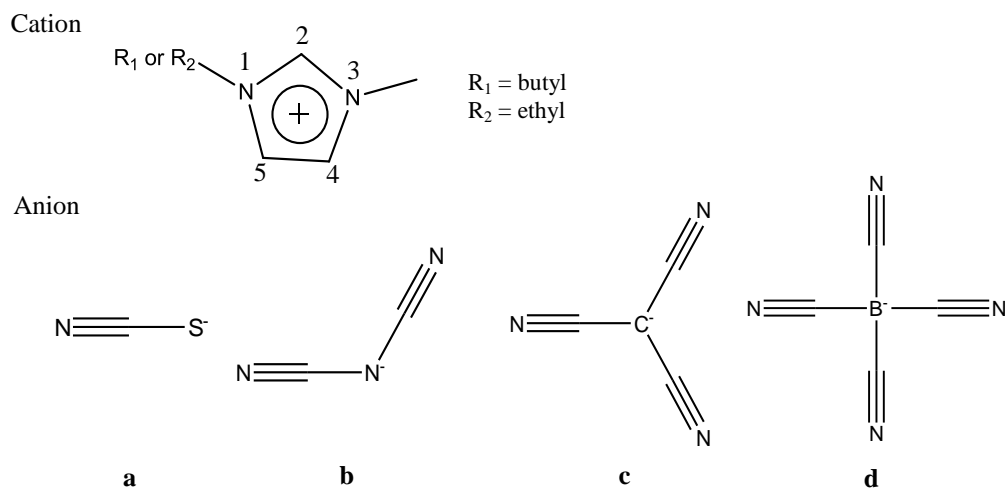


**Fig 4-1.** Imidazolium cation structure with numbering scheme, and structures of various anions involved in this work: a) thiocyanate  $[\text{SCN}]^-$ , b) dicyanamide  $[\text{DCA}]^-$ , c) tricyanomethanide  $[\text{TCM}]^-$ , and d) tetracyanoborate  $[\text{TCB}]^-$ .

## 4.2. Experimental Method

**4.2.1. Samples.** [BMIM][SCN]<sup>14,25</sup> and [BMIM][DCA]<sup>17,26</sup> were synthesized and purified in our lab using combined procedures provided in the literature described in Section 3.1. Samples were characterized by <sup>1</sup>HNMR, <sup>13</sup>CNMR, FTIR, and Raman Spectroscopy. [BMIM][TCM] was synthesized and characterized by Dr. Gary A. Baker (The University of Missouri-Columbia), while [EMIM][TCB] was provided courtesy of Dr. Florian Maier (Universität Erlangen-Nürnberg).

The purification and preparation of samples prior to measurements, which included drying in high vacuum atmospheres up to  $\sim 5 \times 10^{-5}$  Torr in a custom-built glass vacuum line, have been described in Section 3.2. The section further discussed purity analysis of samples through water-content and chloride level determinations.

**4.2.2. Data Collection and Analysis.** Section 3.3 gives a detailed discussion of the SFG spectrometer setup. A picosecond pulsed Nd:YAG laser with a fundamental 1064-nm output was used to pump an optical parametric generator/amplifier (OPG/OPA, LaserVision) system to generate a fixed visible (532-nm) and frequency tunable IR (2000-4000  $\text{cm}^{-1}$ ) beam. The fixed visible and IR beams followed a co-propagating geometry and were overlapped at the liquid surface at an angle of 50° and 60° from the surface normal, respectively.

All spectra were calibrated using polystyrene, gold, and hexadecanol standards described in Section 3.3.5. SFG data collection procedures are outlined in Section 3.4.2, while Sections 3.6 and 3.7 provides the protocol for infrared and Raman spectroscopic measurements, respectively. For SFG, four different polarization combinations were

taken for all ionic liquid samples, namely, *ssp*, *ppp*, *sps*, and *pss*. Data was collected at an average of 5 scans per polarization combination at a scan rate of  $1 \text{ cm}^{-1}/\text{s}$  using 20 laser shots per point. Using equation 2-15 as a fitting function, spectra were fitted *via* Origin 7.0 Professional nonlinear curve fitting.

### 4.3. Results and Discussion

**4.3.1. Peak Assignments.** Emphasis on the features and assignments of the anion spectra are presented here. Similar results for the [BMIM]<sup>+</sup> and [EMIM]<sup>+</sup> cation spectra were found in this study and have been thoroughly discussed in previous publications.<sup>14-17</sup> It is important to note that spectral acquisition for [BMIM][TCM] using Raman and SFG have been difficult, due to the color of the sample (see Fig. B-13, Appendix B). For this reason, Raman spectra for [BMIM][TCM] have been corrected, particularly by background baseline subtraction.

**4.3.2. Infrared Spectra.** FTIR spectra of all ionic liquids studied are shown in Fig. 4-2 for the lower spectral region (1900-2300 cm<sup>-1</sup>) near the C–N stretching mode, and the higher spectral region (2700-3300 cm<sup>-1</sup>) near the C–H stretching mode, on independent and arbitrary intensity scales. Vibrational resonances for the [BMIM]<sup>+</sup> cation display five or six overlapped peaks as observed in previous studies of [BMIM][Br] and [BMIM][PF<sub>6</sub>].<sup>14</sup> In contrast however, weaker vibrations around ~2940-2990 cm<sup>-1</sup> were observed for the [EMIM]<sup>+</sup>, as expected.<sup>27,28</sup>

In the C–N spectral region (1900-2300 cm<sup>-1</sup>), a single peak was observed for all ionic liquids, except for [BMIM][DCA], which showed three peaks. The peak of highest intensity in the spectra of [BMIM][DCA], found at ~2131 cm<sup>-1</sup> corresponds to the antisymmetric C–N stretch, while the peak at ~2192 is assigned to the symmetric C–N stretch. However, the peak at ~2229 cm<sup>-1</sup> can be assigned to a combination band of the symmetric and antisymmetric C–N stretching modes.<sup>29</sup>

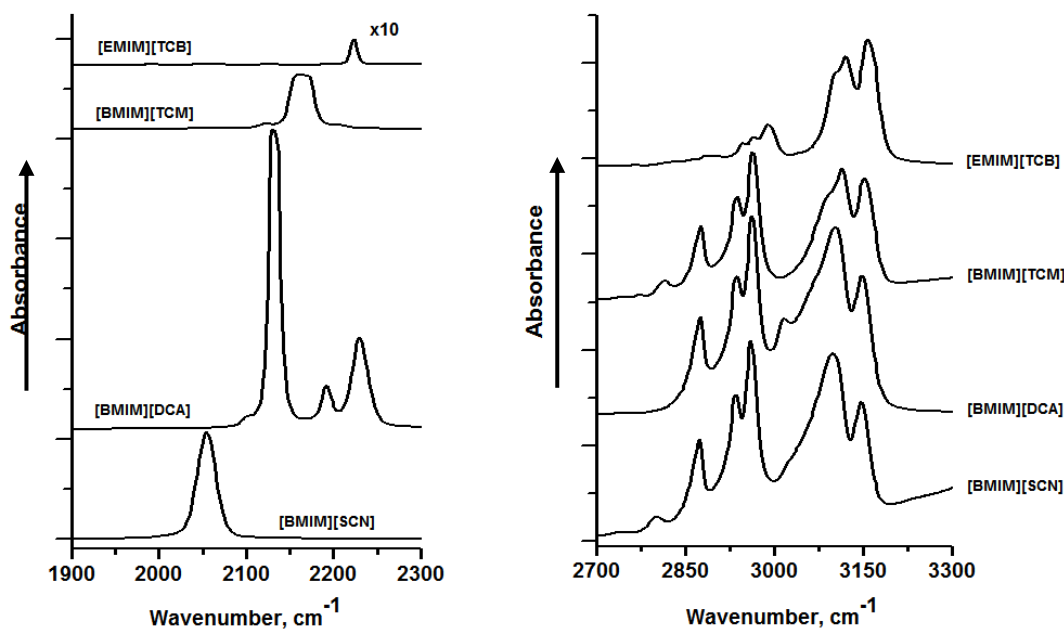


**Fig 4-2.** FTIR spectra of ionic liquids plotted near the C–N stretching region (1900-2300  $\text{cm}^{-1}$ ) and near the C–H stretching region (2700-3300  $\text{cm}^{-1}$ ), offset for clarity.

For [BMIM][SCN], a single peak at  $\sim 2054 \text{ cm}^{-1}$  was found, corresponding to the anion C–N stretching mode,  $\nu$ , while [BMIM][TCM] showed a peak at  $\sim 2161 \text{ cm}^{-1}$  assigned to  $\nu_{\text{degen}}$ . [EMIM][TCB] showed a peak at  $\sim 2223 \text{ cm}^{-1}$  assigned to  $\nu_{\text{degen}}$ , which is of weakest intensity compared to all other ionic liquids studied, shown in Fig. 4-2 and amplified (x10) for clarity.

**4.3.3. Raman Spectra.** Raman spectra of all four ionic liquids are shown in Fig. 4-3, in both C–H and C–N stretching regions, on separate and arbitrary intensity scales.

The cation shows strong Raman signals in the C–H stretching region wherein all three compounds that contain [BMIM]<sup>+</sup> cations exhibit a similar pattern, with methyl antisymmetric vibrational modes dominating the spectrum. The C–H stretching region of

the [EMIM]<sup>+</sup> cation shows weaker signals from the CH<sub>2</sub> symmetric vibrations. This is due to the [EMIM]<sup>+</sup> cation having only one methylene group present in the ethyl ligand vs. three methylene groups in the butyl chain of the [BMIM]<sup>+</sup> cation. In addition, a strong signal contribution from the methyl group exists, with higher Raman cross section. Due to their most pronounced vibrational modes in the C–H stretching region, spectral features of the ionic liquid [BMIM][DCA] are discussed in detail below.

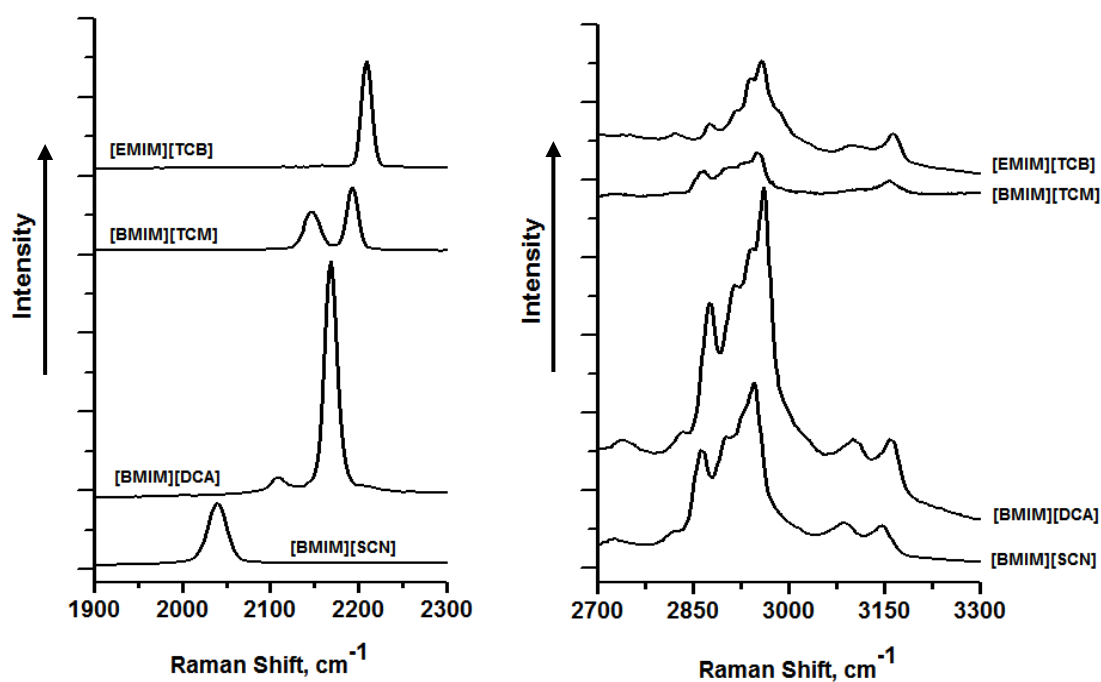


**Fig 4-3.** Raman spectra of ionic liquids plotted near the C–N stretching region (1900-2300 cm<sup>-1</sup>) and near the C–H stretching region (2700-3300 cm<sup>-1</sup>), offset for clarity.

The two small peaks found at ~2739 and ~2834 cm<sup>-1</sup> have been assigned to overtones of the fundamental C–H deformation modes.<sup>14,30</sup> Four strong C–H vibrational modes are found in the frequency region between ~2850 and ~3100 cm<sup>-1</sup> that are characteristic of CH<sub>2</sub> and CH<sub>3</sub> symmetric and antisymmetric stretching modes, and their

Fermi resonance. The peak at  $\sim 2873\text{ cm}^{-1}$  is assigned to the  $\text{CH}_3$  symmetric stretch. The region between  $\sim 2900$  and  $\sim 2960\text{ cm}^{-1}$  shows three discernible peaks that have been assigned to the  $\text{CH}_2$  antisymmetric vibrations at  $\sim 2913\text{ cm}^{-1}$ , the  $\text{CH}_3$  Fermi resonance at  $2941\text{ cm}^{-1}$ , and the  $\text{CH}_3$  antisymmetric modes at  $\sim 2960\text{ cm}^{-1}$ . The H–C(4)–C(5)–H ring modes are clearly shown with their antisymmetric mode at  $\sim 3103\text{ cm}^{-1}$  followed by the symmetric mode at  $\sim 3163\text{ cm}^{-1}$ . The vibrational modes that are characteristic of the N– $\text{CH}_3$  stretching vibrations and typically observed in  $[\text{BMIM}]^+$  at around  $\sim 3000\text{ cm}^{-1}$  could not be identified.<sup>15</sup>

Strong Raman signals from the symmetric vibrational modes of the cyano functional group in all four samples were observed. The Raman scattering signal at  $\sim 2209\text{ cm}^{-1}$  for the tetracyanoborate anion shows at higher frequency, relative to the symmetric vibrational modes of the other anions, namely, the symmetric vibration at  $\sim 2193\text{ cm}^{-1}$  for tricyanomethanide, followed by  $\sim 2192\text{ cm}^{-1}$  for dicyanamide, and  $\sim 2041\text{ cm}^{-1}$  for thiocyanate. The red shift of the latter symmetric modes is consistent with the increasing atomic mass of the respective central atom.

The antisymmetric modes are present as weak signals in the Raman spectra of both tetracyanoborate and dicyanamide anion. One unusual exception is the strong signal seen at  $\sim 2148\text{ cm}^{-1}$  in the  $[\text{TCM}]^-$  spectrum that appears to be a degenerate vibrational mode characteristic for molecules that belong to the  $D_{3h}$  symmetry group. However, this assignment is not firm for the  $[\text{TCM}]^-$  anion. Literature studies<sup>31,32</sup> that discuss anions with the same symmetry, i.e., the nitrate functional group, do not confirm any strong contributions from its antisymmetric mode.

Literature studies specifically related to the tricyanomethanide anion confirm the presence of two Raman peaks but are inconclusive about their exact vibrational mode assignments and peak intensities.<sup>33</sup> In previous Raman studies of tetracyanoborate salts,<sup>34</sup> only one stretching mode has been observed in the Raman spectra near the C–N stretching region since the  $a_1$  and  $t_2$  modes are degenerate. Table 4-1 shows a summary of the vibrational frequencies and peak assignments for the cyano anions in the IR and Raman spectra, as well as SFG discussed below.

**Table 4-1.** Vibrational Frequencies and Peak Assignments for the Cyano Anions in IR, Raman and SFG Spectra.

Anion type	IR (cm <sup>-1</sup> )	Raman (cm <sup>-1</sup> )	SFG, <i>ssp</i> (cm <sup>-1</sup> )	SFG, <i>ppp</i> (cm <sup>-1</sup> )
[SCN] <sup>-</sup>	2054 v (s)	2041 v (s)	N.A.	N.A.
[DCA] <sup>-</sup>	2131 v <sub>as</sub> (s) 2192 v <sub>s</sub> (w) 2229 v <sub>comb</sub> (m)	2133 v <sub>as</sub> (w) 2192 v <sub>s</sub> (s)	2125 v <sub>as</sub> 2185 v <sub>s</sub> 2218 v <sub>comb</sub>	2132 v <sub>as</sub> 2180 v <sub>s</sub> 2237 v <sub>comb</sub>
[TCM] <sup>-</sup>	2161 v <sub>degen</sub> (s)	2148 v <sub>degen</sub> (s) 2193 v <sub>s</sub> (s)	2160	N.A.
[TCB] <sup>-</sup>	2223 v <sub>degen</sub> (w)	2158 v <sub>degen</sub> (w) 2209 v <sub>s</sub> (s)	2221	N.A.

(s) strong, (m) medium, w (weak) in relative signal intensity

**4.3.4. SFG Spectra.** Sum frequency spectra of all ionic liquids at the different polarization combinations are presented in Fig. 4-4a and Fig. 4-4b. Solid lines indicate a fit to the data in square dots, using equation 3 as a fitting function. Solid lines for data in open circles serve as a guide to the spectra in which curve fitting was not performed, due to the low signal to noise ratio or lack of signal in the actual spectra. Standard deviations between scans are indicated as error bars. All four polarization combinations for the C–H

stretching region are shown for each ionic liquid type from top to bottom (A–D). Plots are drawn for each ionic liquid type in a way that best displays the spectral features, i.e. similar intensity scales are shown for the *ssp* and *ppp* for each ionic liquid, and another independent scale for *sps* and *pss*.

Spectral profile for [BMIM][SCN] and [BMIM][DCA] appear similar to previous results as reported in earlier publications for the [BMIM]<sup>+</sup> cation.<sup>12,14,17</sup> Two strong peaks in the *ssp* spectra that have been assigned to the symmetric methyl stretch split by a Fermi resonance peak (at ~2879 cm<sup>-1</sup> and ~2943 cm<sup>-1</sup>) dominate the C–H stretching region. Likewise, the spectra for [EMIM][TCB] is comparable to that of [EMIM][PF<sub>6</sub>] for the [EMIM]<sup>+</sup> cation.<sup>15,16</sup> All symmetric modes for the [EMIM]<sup>+</sup> cation (N–CH<sub>2</sub> at ~2925 cm<sup>-1</sup>, C–CH<sub>3</sub> at ~2951 cm<sup>-1</sup>, N–CH<sub>3</sub> at ~2971 cm<sup>-1</sup> and H–C(4)–C(5)–H at ~3190 cm<sup>-1</sup>) were observed including the Fermi resonance peak splitting for the C–CH<sub>3</sub> symmetric<sup>16</sup> at ~2886 cm<sup>-1</sup>. A lack of signal in the *ppp* and *sps* spectra is generally due to a large orientational distribution of the methyl groups.<sup>35</sup> We note here that [BMIM][TCM] has fluorescent background (see Fig. B-13, Appendix B) due to the color of the sample, which affected the measurements. However, all the data shows that the cation, independent of the anion type, appears to have a similar orientation as previously reported in previous studies, in which the imidazolium ring lies flat with its C<sub>2</sub> axis parallel to the surface plane, the alkyl chain projecting towards the gas phase, and methyl group average tilt angle close to ~50° from the surface normal.<sup>14-17</sup>

Fig. 4-5 shows the SFG spectra of all four ionic liquids in *ssp* polarization combination, except for [BMIM][DCA], which gives discernible peaks in both *ssp* and

*ppp* polarizations. All anions except for  $[\text{SCN}]^-$  (in Fig. 4-5,A) show signal in the C–N stretching region. (Black solid lines in the figure serve as a guide to the spectra since curve fitting was not performed.)

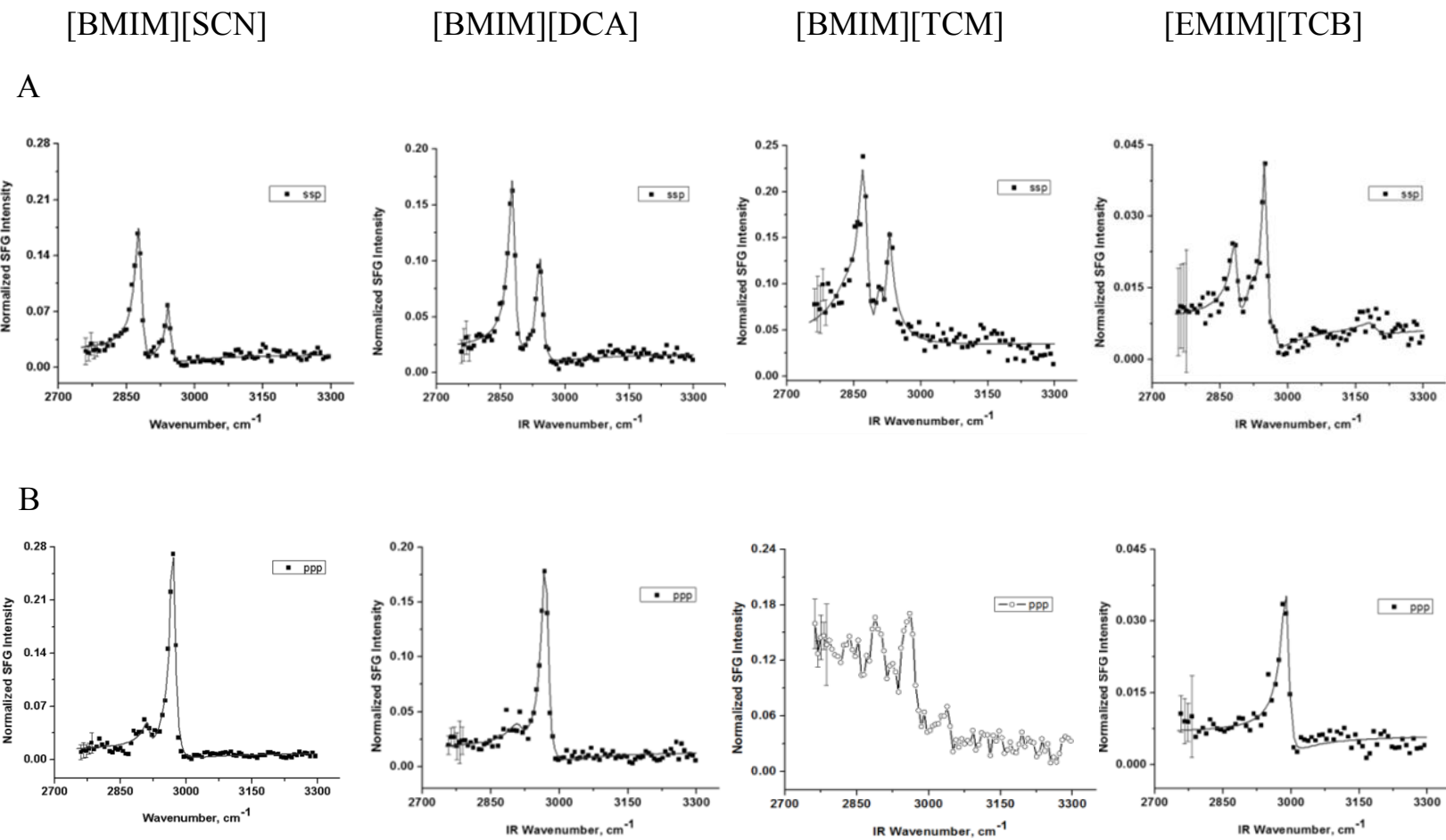


**Fig 4-4a.** Sum frequency spectra of ionic liquids in the C–H stretching region at polarization combinations *ssp* (A) and *ppp* (B).

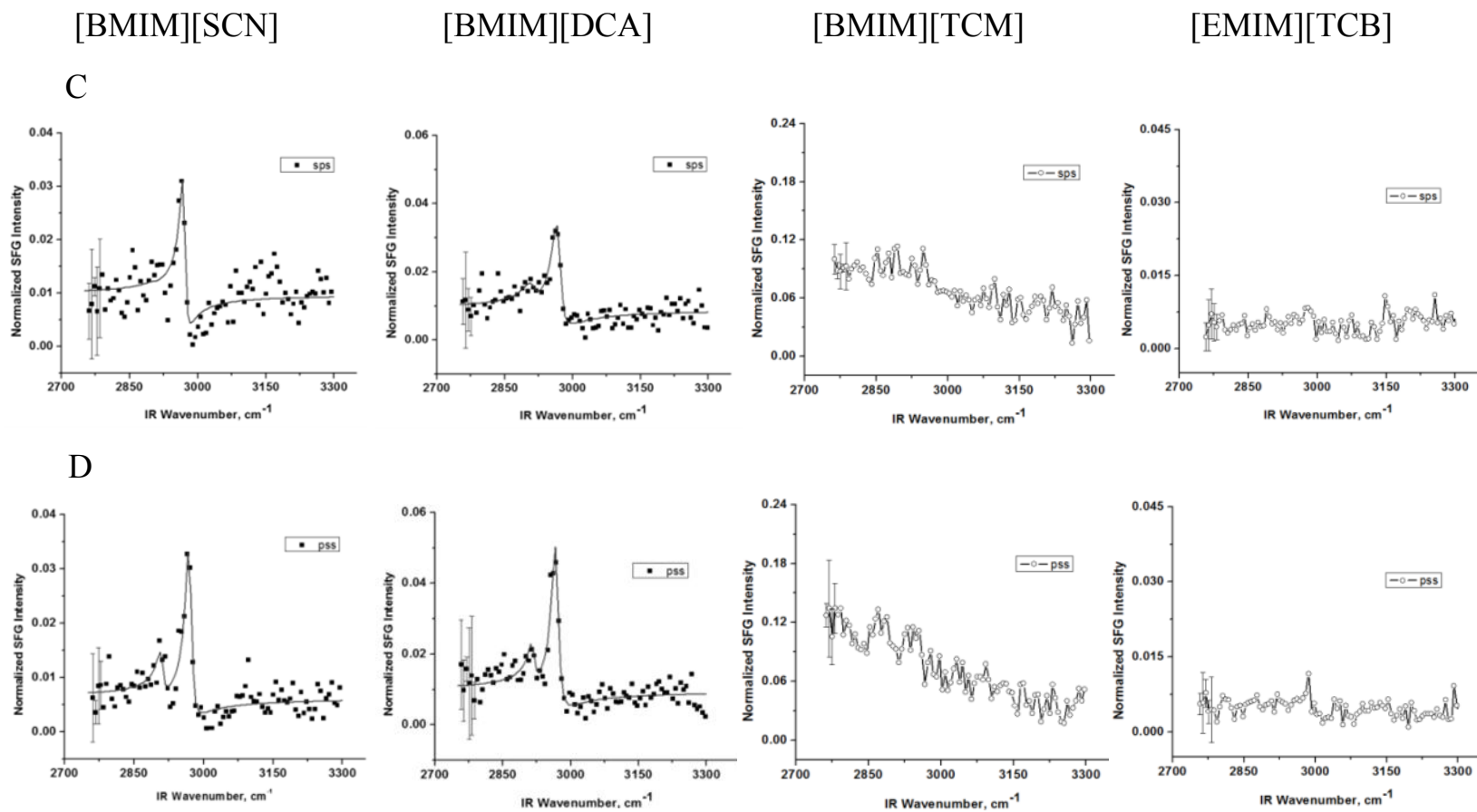
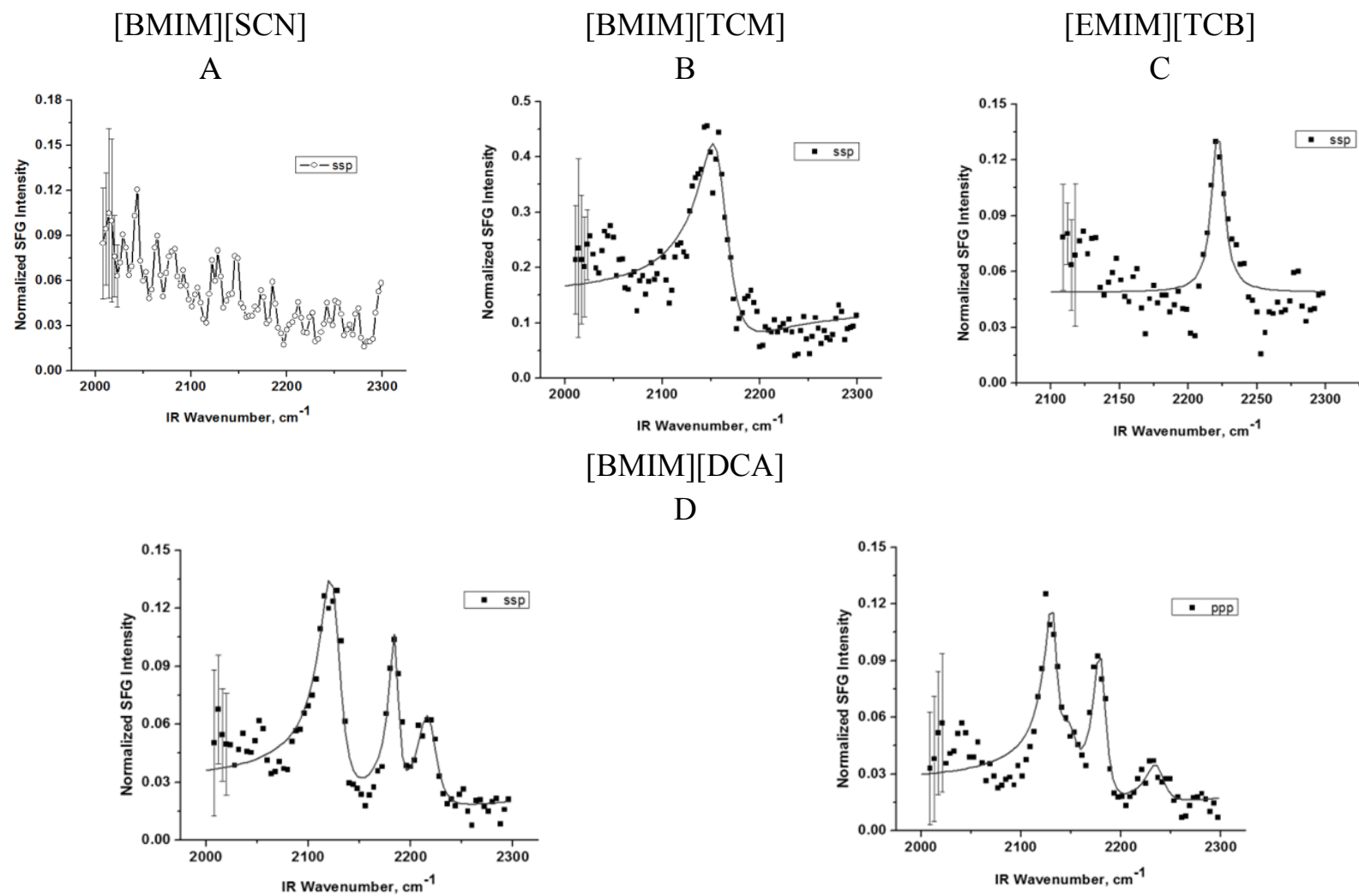


Fig 4-4b. Sum frequency spectra of ionic liquids in the C–H stretching region at polarization combinations *sps* (C) and *pss* (D).



**Fig 4-5.** Sum frequency spectra of ionic liquids in the C–N stretching region at *ssp* polarization combination for [BMIM][SCN] (A), [BMIM][TCM] (B), [EMIM][TCB] (C) and both *ssp* and *ppp* combinations for [BMIM][DCA] (D).

Earlier assignments as to the spectra of [BMIM][DCA] (Fig. 4-5,D) have been confirmed, where three peaks show in the *ssp* combination, corresponding to modes for the antisymmetric C–N stretch at  $\sim 2125\text{ cm}^{-1}$ , the symmetric C–N stretch at  $\sim 2185\text{ cm}^{-1}$  and the combination band of the symmetric and antisymmetric C–N at  $\sim 2218\text{ cm}^{-1}$  (Table 1). Furthermore, an additional peak appears in the *ppp* spectra at  $\sim 2150\text{ cm}^{-1}$ , which is assigned to vibrations from isonitrile moieties as previously discussed in earlier studies.<sup>17</sup> Other peaks seen in the *ppp* spectra which are of relatively good intensity, occur at  $\sim 2132$ ,  $\sim 2180$  and  $\sim 2237\text{ cm}^{-1}$  corresponding to the antisymmetric C–N stretch, symmetric C–N stretch, and the combination band of the antisymmetric and symmetric C–N stretch, respectively.

Both [EMIM][TCB] (Fig. 4-5,C) and [BMIM][TCM] (Fig. 4-5,B) show a single peak at  $\sim 2221\text{ cm}^{-1}$  and  $\sim 2160\text{ cm}^{-1}$  respectively. The peak at  $\sim 2221\text{ cm}^{-1}$  for [EMIM][TCB] appears strongly in the Raman spectra (at  $\sim 2209\text{ cm}^{-1}$ ) but very weakly in the IR spectra (at  $\sim 2223\text{ cm}^{-1}$ ). In previous studies of [EMIM][TCB], the peak found at  $\sim 2222\text{ cm}^{-1}$  has been assigned to the C–N stretching band, which is well-documented for the [TCB]<sup>−</sup> anion in combination with monovalent cations. Moreover, it was found that a large distortion of the anion structure in the ionic liquid seemed improbable, due to weak interactions between the cation and the anion, as seen from the limited direct overlap of the cation and anion bands in existing spectroscopic data.<sup>36</sup> However, it was assumed that the anion was probably not of pure  $T_d$  symmetry. The fact that both [TCM]<sup>−</sup> and [TCB]<sup>−</sup> give signal in the spectra means that the symmetry at the surface must be broken, in such a way that the anions adopted a preferred orientation along the surface normal.

Previous studies<sup>32,37,38</sup> on related structures such as nitrate and benzene, possessing  $D_{3h}$  and  $D_{6h}$  symmetry, respectively, have revealed their presence at the air-liquid interface in the SFG spectra. For a molecule to give SFG signal, it must be in a non-centrosymmetric environment. As a result of this, vibrational modes must be both Raman and IR active. For both  $[\text{TCM}]^-$  and  $[\text{TCB}]^-$  in the bulk phase, this is not the case. As the data shows (Fig. 4-2 and 4-3, Table 1), the symmetric modes that are strong in the Raman spectra are weak in the IR spectra, while those with high intensity in the infrared are weak in the Raman data, showing near exclusion.<sup>39</sup> Thus, the surface is able to lower the symmetry of the anions such that their signals appear in the SFG spectra, suggesting a preferred molecular orientation.

A more specific orientation for  $[\text{TCM}]^-$  and  $[\text{TCB}]^-$  is estimated by the symmetry and observed SFG spectra. In reference to the  $[\text{DCA}]^-$  anion which has a  $C_{2v}$  point group symmetry, detailed orientation analysis calculations from previous studies<sup>17</sup> (Fig. 4-6) have revealed that the  $C_2$  axis of symmetry for the said anion has a tilt ranging from  $46^\circ$  to  $90^\circ$  for tilt angles corresponding to the twist interval of  $0^\circ$  to  $30^\circ$ .

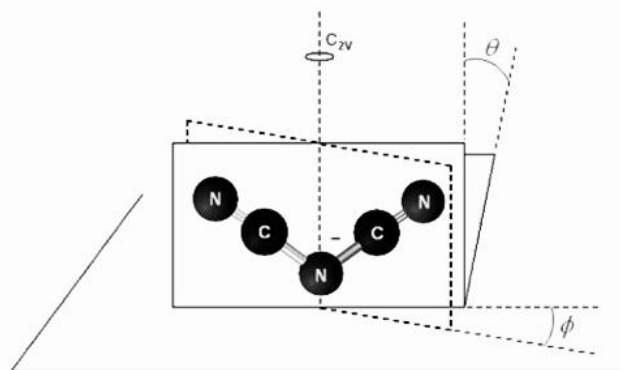


**Fig 4-6.**  $[\text{DCA}]^-$  anion showing  $C_2$  axis of symmetry.<sup>17</sup>

If the anions [TCM]<sup>-</sup> and [TCB]<sup>-</sup> have a lower symmetry (i.e. are not of pure  $D_{3h}$  and  $T_d$  symmetry, respectively) in the ionic liquid, corresponding to the fact that their signals appear in the SFG spectra, the established orientation analysis results of the [DCA]<sup>-</sup> anion can be used to infer their molecular arrangement at the surface. In this regard, we consider the [DCA]<sup>-</sup> anion as a sub-unit of [TCM]<sup>-</sup> and [TCB]<sup>-</sup>. For example, since the antisymmetric stretching mode from [TCM]<sup>-</sup> is not observed, the orientation of the anion must be different from that of [DCA]<sup>-</sup>; wherein the  $C_3$  symmetry axis of [TCM]<sup>-</sup> should be parallel to the surface plane, with one cyano group in [TCM]<sup>-</sup> pointing up out of the surface, while the two remaining cyano groups are directed down towards the bulk. In the case where two cyano domains point upwards, a spectrum with both symmetric and antisymmetric modes should be observed similar to the case of the [DCA]<sup>-</sup> anion. The same concept is inferred for [TCB]<sup>-</sup>, in which one cyano group is pointing up towards the gas phase, while the other three are directed down towards the bulk liquid phase. These conclusions are further supported using a symmetry perspective and correlation tables for the  $T_d$  and  $D_{3h}$  point groups, to lower symmetries of  $C_{2v}$  or  $C_{\infty v}$ .<sup>11,40</sup> Table 2 summarizes the arguments for anion surface configuration through a symmetry approach. In general, since only one mode is observed for both [TCM]<sup>-</sup> and [TCB]<sup>-</sup>, results suggest that only one of the  $-C\equiv N$  groups is projecting out of the interface giving a  $C_{\infty v}$ -like mode.

**Table 4-2.** Symmetry Approach to Anion Surface Configuration for [TCM]<sup>-</sup> and [TCB]<sup>-</sup>.

Anion	Anion point group symmetry	Lower symmetry adapted (surface effect)	Representation		Vibrations Expected	Expt'l Observation	Surface Configuration
			Anion point group symmetry	Lower symmetry adapted			
[TCM] <sup>-</sup>	$D_{3h}$	$C_{2v}$	$e'$	$a_1 + b_2$	symmetric & antisymmetric	2160 $\nu_{\text{sym}}$	$C_{\infty v}$
[TCB] <sup>-</sup>	$T_d$	$C_{2v}$	$e$	$a_1 + a_2$	symmetric	2221 $\nu_{\text{sym}}$	$C_{2v}$ or $C_{\infty v}$

The effect of the surface to a lower symmetry group causes the degenerate modes to change representation. For the [TCM]<sup>-</sup> anion,  $e'$  in  $D_{3h}$  symmetry, transforms to  $a_1$  and  $b_2$  in  $C_{2v}$  symmetry. Thus, the [TCM]<sup>-</sup> should have both a symmetric and antisymmetric mode at the surface. Since only one is observed, it is possible that the  $a_1$  vibration is for  $C_{\infty v}$ , i.e. only one  $-C\equiv N$  is projecting out into the gas phase. This argument is limited by the strength of the  $b_2$  mode, which is not known independently.

For [TCB]<sup>-</sup> anion however, the representation  $e$  in  $T_d$  symmetry transforms only into symmetric  $a_1 + a_2$  modes in the  $C_{2v}$  point group. Because antisymmetric modes are absent in the spectra of [TCB]<sup>-</sup>, by symmetry, it is difficult to distinguish between the  $C_{2v}$  and  $C_{\infty v}$  conformations in [TCB]<sup>-</sup>. Furthermore, considering a possible  $C_{3v}$  configuration at the interface for [TCB]<sup>-</sup> is unlikely, because  $e$  modes in  $T_d$  merely transform into  $e$  modes in  $C_{3v}$  as well.

Only [BMIM][SCN] displayed no discernible peaks in SFG in the C–N stretching region as opposed to a single peak observed in both IR (at  $\sim 2054 \text{ cm}^{-1}$ ) and Raman ( $\sim 2041 \text{ cm}^{-1}$ ), among all ionic liquids studied. This result, although surprising, could give an insight on the possible surface molecular arrangement of the linear [SCN]<sup>-</sup> anion at

the gas-liquid interface. Recent results on SFG studies of [BMIM][SCN] in contact with a solid single crystal BaF<sub>2</sub> (111) surface (see Chapter 6)<sup>41</sup> show a strong peak at ~2050 cm<sup>-1</sup> such that the absence of a signal from measurements at the gas-liquid interface must be a consequence of the anion configuration at the surface. The absence of the signal may have occurred due to two possible reasons: either the anion is not present at the surface, or it is not well-oriented at the interface. Poor orientation of the anion may arise due to the delocalization of the charge in the linear molecule ( $\text{S}^-\text{C}\equiv\text{N} \leftrightarrow \text{S}=\text{C}=\text{N}^-$ ), that may cancel out polar ordering at the surface.

#### 4.4. Conclusion

Combined vibrational techniques such as FTIR, Raman, and SFG spectroscopies have been used for surface characterization of cyano-containing ionic liquids [BMIM][SCN], [BMIM][DCA], [BMIM][TCM], and [EMIM][TCB] at the gas-liquid interface. Observation of vibrational modes in the C–N stretching region indicated the presence of the anions at the gas-liquid interface for all ionic liquids studied, except for [SCN]<sup>−</sup> in [BMIM][SCN], in which no modes at the C–N stretching region were observed. [TCM]<sup>−</sup> was found to be well-oriented with a C<sub>3</sub> axis parallel to the surface, while [TCB]<sup>−</sup> displayed a weaker signal compared to [DCA]<sup>−</sup> and [TCM]<sup>−</sup> and was found to be less ordered than both anions previously mentioned.

In addition, vibrational modes seen in the C–H stretching region, revealed the presence of the cation at the gas-liquid interface, with an orientation that is independent of the type of cyano-containing anion, and a similar arrangement at the surface as reported in previous studies revealing the imidazolium ring lying flat at the surface, and the alkyl chains pointing towards the gas phase. Although detailed calculation and analysis of the specific orientation of the anions relative to the surface normal is not available here, this study concludes that anions of varying symmetry such as [DCA]<sup>−</sup> (C<sub>2v</sub>), [TCM]<sup>−</sup> (D<sub>3h</sub>) and [TCB]<sup>−</sup> (T<sub>d</sub>) in ionic liquids [BMIM]DCA, [BMIM][TCM], and [EMIM][TCB] are significantly tilted from the surface plane at the gas-liquid interface.

#### 4.5. References

- (1) Welton, T. *Chem. Rev.* **1999**, *99*, 2071-2084.
- (2) Armand, M.; Endres, F.; MacFarlane, D. R.; Ohno, H.; Scrosati, B. *Nat. Mater.* **2009**, *8*, 621-629.
- (3) Dyson, P. J.; Geldbach, T. J. *Electrochem. Soc. Interface* **2007**, *16*, 50-53.
- (4) Parvulescu, V. I.; Hardacre, C. *Chem. Rev.* **2007**, *107*, 2615-2665.
- (5) Steinrück, H. P.; Libuda, J.; Wasserscheid, P.; Cremer, T.; Kolbeck, C.; Laurin, M.; Maier, F.; Sobota, M.; Schulz, P. S.; Stark, M. *Adv. Mater.* **2011**, *23*, 2571-2587.
- (6) Zhao, H. *Chem. Eng. Commun.* **2006**, *193*, 1660-1677.
- (7) Mokrushin, V.; Assenbaum, D.; Paape, N.; Gerhard, D.; Mokrushina, L.; Wasserscheid, P.; Arlt, W.; Kistenmacher, H.; Neuendorf, S.; Göke, V. *Chem. Eng. Technol.* **2010**, *33*, 63-73.
- (8) Han, X.; Armstrong, D. W. *Acc. Chem. Res.* **2007**, *40*, 1079-1086.
- (9) Bara, J. E.; Lessmann, S.; Gabriel, C. J.; Hatakeyama, E. S.; Noble, R. D.; Gin, D. L. *Ind. Eng. Chem. Res.* **2007**, *46*, 5397-5404.
- (10) Steinrück, H.-P. *Surf. Sci.* **2010**, *604*, 481-484.
- (11) Colthup, N. B.; Daly, L. H.; Wilberley, S. E. *Introduction to Infrared and Raman Spectroscopy*; Third ed.; Academic Press: San Diego, 1990.
- (12) Martinez, I. S.; Baldelli, S. *J. Phys. Chem. C* **2010**, *114*, 11564-11575.
- (13) Santos, C. S.; Rivera-Rubero, S.; Dibrov, S.; Baldelli, S. *J. Phys. Chem. C* **2007**, *111*, 7682-7691.

- (14) Rivera-Rubero, S.; Baldelli, S. *J. Phys. Chem. B* **2006**, *110*, 4756-4765.
- (15) Santos, C. S.; Baldelli, S. *J. Phys. Chem. B* **2007**, *111*, 4715-4723.
- (16) Santos, C. S.; Baldelli, S. *J. Phys. Chem. B* **2009**, *113*, 923-933.
- (17) Aliaga, C.; Baldelli, S. *J. Phys. Chem. B* **2007**, *111*, 9733-9740.
- (18) Aliaga, C.; Baker, G. A.; Baldelli, S. *J. Phys. Chem. B* **2008**, *112*, 1676-1684.
- (19) Wooster, T. J.; Johanson, K. M.; Fraser, K. J.; MacFarlane, D. R.; Scott, J. L. *Green Chem.* **2006**, *8*, 691-696.
- (20) Forsyth, S. A.; Stuart R. Batten; Qing Dai; MacFarlane, D. R. *Aust. J. Chem* **2004**, *57*, 121-124.
- (21) Yoshida, Y.; Muroi, K.; Otsuka, A.; Saito, G.; Takahashi, M.; Yoko, T. *Inorg. Chem.* **2004**, *43*, 1458-1462.
- (22) Brand, H.; Liebman, J. F.; Schulz, A.; Mayer, P.; Villinger, A. *Eur. J. Inorg. Chem.* **2006**, *2006*, 4294-4308.
- (23) Emel'yanenko, V. N.; Zaitsau, D. H.; Verevkin, S. P.; Heintz, A.; VoÅŸ, K.; Schulz, A. *J. Phys. Chem. B* **2011**, *115*, 11712-11717.
- (24) Martino, W.; Fernandez de la Mora, J.; Yoshida, Y.; Saito, G.; Wilkes, J. *Green Chem.* **2006**, *8*, 390-397.
- (25) Kamal, A.; Chouhan, G. *Tetrahedron Lett.* **2005**, *46*, 1489-1491.
- (26) Kaerkkainen, J.; Asikkala, J.; Laitinen, R. S.; Lajunen, M. K. Z. *Naturforsch. B. Chem. Sci.* **2004**, *59*, 763-770.

- (27) Talaty, E. R.; Raja, S.; Storhaug, V. J.; Dolle, A.; Carper, W. R. *J. Phys. Chem. B* **2004**, *108*, 13177-13184.
- (28) Berg, R. W. *Monatshefte für Chemie / Chemical Monthly* **2007**, *138*, 1045-1075.
- (29) Davies, M.; Jones, W. J. *J. Trans. Faraday Soc.* **1958**, *54*, 1454-1463.
- (30) Tyrode, E.; Rutland, M. W.; Bain, C. D. *J. Am. Chem. Soc.* **2008**, *51*, 17434-17445.
- (31) McLaughlin, R. P.; Bird, B.; Reid, P. J. *Spectrochim. Acta, Part A* **2002**, *58*, 2571-2580.
- (32) Xu, M.; Tang, C. Y.; Jubb, A. M.; Chen, X.; Allen, H. C. *J. Phys. Chem. C* **2009**, *113*, 2082-2087.
- (33) Dixon, D. A.; Calabrese, J. C.; Miller, J. S. *J. Am. Chem. Soc.* **1986**, *108*, 2582-2588.
- (34) Kupperts, T.; Bernhardt, E.; Willner, H.; Rohm, H. W.; Kockerling, M. *Inorg. Chem.* **2005**, *44*, 1015-1022.
- (35) Wang, H.-F.; Gan, W.; Lu, R.; Rao, Y.; Wu, B.-H. *Int. Rev. Phys. Chem.* **2005**, *24*, 191-256.
- (36) Scheers, J.; Johansson, P.; Jacobsson, P. *J. Electrochem. Soc.* **2008**, *155*, A628-A634.
- (37) Jubb, A. M.; Hua, W.; Allen, H. C. *Acc. Chem. Res.* **2012**, *45*, 110-119.
- (38) Santos, C. S.; Baldelli, S. *J. Phys. Chem. C* **2008**, *112*, 11459-11467.

(39) Diem, M. *Introduction to Modern Vibrational Spectroscopy*; Wiley-Interscience: Michigan, 1993.

(40) Nakamoto, K. *Infrared and Raman Spectra of Inorganic and Coordination Compounds: Theory and applications in inorganic chemistry (Part 1)* John Wiley & Sons: New Jersey, 2009.

(41) Peñalber, C.; Baldelli, S. *Unpublished work*.

## Chapter 5. Observation of Charge Inversion of an Ionic Liquid at the Solid Salt-Liquid Interface by Sum Frequency Generation Spectroscopy\*

### 5.1. Introduction

Ionic liquids (ILs) have found a unique and important role in several industrial applications due to their remarkable properties. Although they are generally considered solvents, their structural versatility allows specific properties to be tuned, such that they offer far greater technological potential, as new applications emerge from the growing number of scientific research in the field.<sup>1</sup> Current ionic liquid studies are directed towards characterizing their behavior at vacuum-liquid interfaces using various surface science techniques.<sup>2,3</sup> Understanding the chemical nature of surfaces is indispensable because most essential chemical applications occur mainly at the boundary between two phases. Ionic liquid interactions at solid surfaces may play a role at important processes including direct exfoliation of natural graphite flakes into a dispersion of graphene in ionic liquid media.<sup>4</sup> Due to their potential for use in electrochemical sensing applications, earlier studies<sup>5,6</sup> have focused on the ionic liquid–solid interface, in an attempt to understand their reaction mechanisms relative to conventional solvents. Moreover, previous propositions have been made to present a view of the electric double-layer structure at the ionic liquid–metal electrode interface using electrochemical techniques and vibrational spectroscopy.<sup>7-11</sup> These studies have attempted to describe the organization of ions in purely ionic materials at the surface of an electrified metal, as

---

\* Reproduced with permission from *J. Phys. Chem. Lett.* **2012**, 844–847.

there are so far, only a limited number of appropriate models applicable to this interface.<sup>12-14</sup> The Gouy–Chapman–Stern model strictly explains ionic behavior in normal electrolytic solutions, in which ions are solvated and non-interacting. Because ionic liquids are unique systems composed of purely charged species of various chemical functionality in the absence of a molecular solvent, the model fails to explain their ionic behavior at solid surfaces. New models that account for strong, short-range Coulomb correlations in these materials at liquid–solid interfaces are therefore indispensable.<sup>12,13,15-18</sup> Moreover, because these models, although appropriate for the interface are to a great extent, currently based on theoretical simulations, there is a pressing need for the development of experimental models in order to validate them.

That ionic liquids remain liquid at room temperature, is in fact one of their most intriguing properties. This has triggered much interest to examine their chemistry. This report contributes to understanding the molecular-level interactions involved in salts, which are conceptually similar compounds (of purely ionic character) but of different physical properties (liquid *vs.* solid at room temperature), placed in contact with each other. SFG spectroscopy of the ionic liquid, 1-butyl-3-methylimidazolium dicyanamide [BMIM][DCA], in contact with two different solid salt surfaces, BaF<sub>2</sub>(111) single crystal and solid NaCl{100}, are included in this report. The choice of the two solid salt surfaces is motivated by a distinction in the inherent nature of the solid surface charge, in which BaF<sub>2</sub>(111) surface is considered to be positively-charged (barium-enriched)<sup>19-21</sup>, while NaCl{100} is negatively-charged (chloride-enriched).<sup>22</sup> Two central ideas form the basis of these results: 1) Ionic liquid counter-ions adsorb to the surface of the solid depending

on its inherent surface charge; and 2) Ions in the liquid remain oriented within the first layer adjacent to the surface but not beyond. Moreover, another important assumption considered here is that Coulombic forces (aside from dipole, hydrogen-bonding and dispersive forces) play the most significant role in the interactions between the purely ionic salt surfaces of the liquid and solid. The distinction between the positively-charged  $\text{BaF}_2(111)$  and the negatively-charged  $\text{NaCl}\{100\}$  presumably dictates the corresponding interfacial molecular arrangement of the ionic liquid cation and anion constituents into a Helmholtz-like layer.

As an inherently surface-sensitive technique, SFG selectively detects molecules in a non-centrosymmetric environment, distinguishing surface molecules having a preferential ordering at the interface as opposed to the isotropic bulk-phase molecules. As a vibrational spectroscopic technique, the high degree of chemical information seen in the SFG spectra, gives a detailed model for molecular structure and arrangement of the cation and anion at the boundary between the pure ionic liquid and solid salt surfaces, thereby providing insight into the specific interfacial chemistry involved.

## 5.2 Experimental Method

The synthesis of [BMIM][DCA] ionic liquid has been discussed in Section 3.1.2. The sample was purified and dried in a glass vacuum line up to a pressure of  $\sim 5 \times 10^{-5}$  Torr prior to measurements, as described in Section 3.2.

The SFG spectrometer setup discussed in Section 3.3, involved a picosecond pulsed Nd:YAG laser with a fundamental 1064-nm output was used to pump an optical parametric generator/amplifier (OPG/OPA, LaserVision) system to generate a fixed visible (532-nm) and frequency tunable IR (2000-4000  $\text{cm}^{-1}$ ) beam. The fixed visible and IR beams followed a co-propagating geometry and were overlapped at the liquid surface at an angle of  $50^\circ$  and  $60^\circ$  from the surface normal, respectively.

The experimental setup for measurements at the IL-BaF<sub>2</sub>(111) interface has been described and illustrated in Section 3.5.1 (Fig. 3-21 and Fig. 3-22). Air-less transfer of the dried ionic liquid sample are found in Section 3.5.3.

All spectra were calibrated using polystyrene, gold, and hexadecanol standards described in Section 3.3.5. Finally, data collection procedures for the solid-liquid interface are found in Section 3.5.4.

### 5.3. Results and Discussion

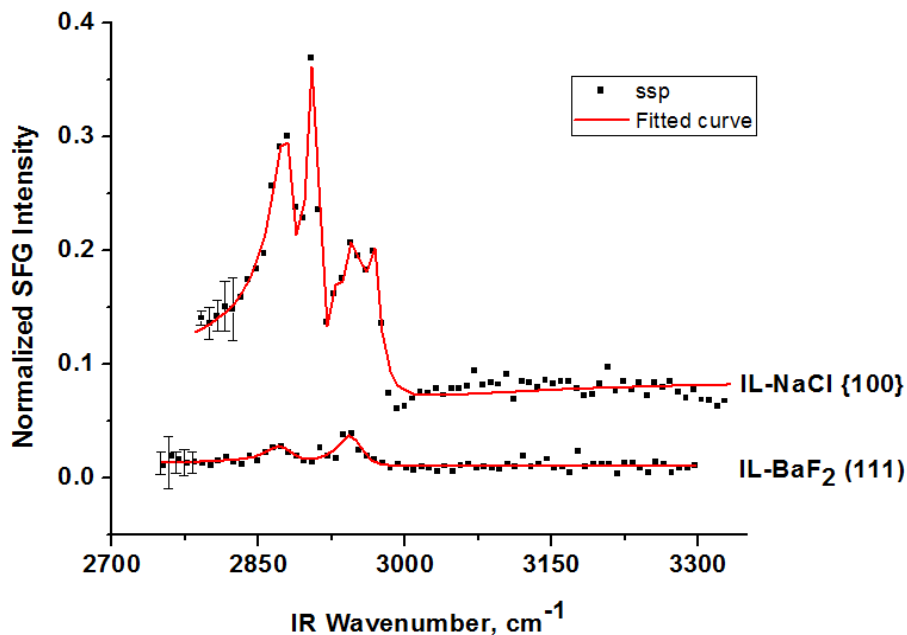


**Fig. 5-1.** Sum frequency spectra (*ssp*) in the C–H stretching region of [BMIM][DCA] in contact with solid surfaces, NaCl{100} and BaF<sub>2</sub>(111). Spectra are offset by 0.05.

Fig. 5-1 shows the SFG spectra of [BMIM][DCA] in contact with NaCl{100} and BaF<sub>2</sub>(111) surfaces in the C–H stretching region using *ssp* polarization combination. Characteristic peaks pertaining to vibrational modes of the [BMIM]<sup>+</sup> cation<sup>23,24</sup> are directly observed in the spectra, which appear significantly enhanced at the IL–NaCl{100} interface as opposed to a fairly low-intensity cation signal at the IL–BaF<sub>2</sub>(111) interface. However, spectra taken in the C–N stretching region (shown in Figure 2) reveal the reverse situation in which an inversion of signal intensity is observed, in that vibrational bands assigned to the [DCA]<sup>–</sup> anion are significantly enhanced at the IL–BaF<sub>2</sub>(111) interface, while absent at the IL–NaCl{100} interface. Consequently, these results follow well the pre-supposition that the [BMIM]<sup>+</sup> cations adhere closely *via*

Coulombic interactions to the negatively-charged NaCl{100} surface. In the same manner, the [DCA]<sup>-</sup> anions subsequently have a strong electrostatic affinity to the positively-charged BaF<sub>2</sub>(111) surface, as seen in the strong signal intensity assigned to C–N vibrational modes of the anion in the spectra.<sup>10,25</sup>

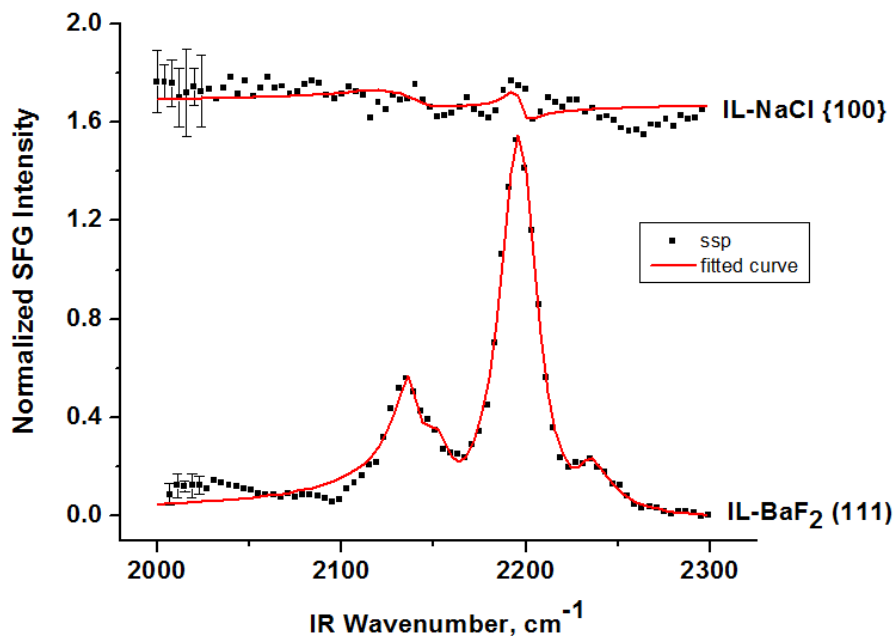


**Fig. 5-2.** Sum frequency spectra (*ssp*) in the C–N stretching region of [BMIM][DCA] in contact with solid surfaces, NaCl{100} and BaF<sub>2</sub>(111). Spectra are offset by 1.65.

Therefore, the present observations support that the solid salt surface has a single layer of strongly ordered ions, with a second layer composed of the counter-charge which lacks orientational order. The evidence lies in the absence of vibrational modes from both the cation and anion at the interface, which otherwise would have been observed in the spectra if an ordered second layer existed. Screening of the surface charge of the solid salt by the first layer explains these findings, such that a Helmholtz-type model composed

of a single ordered layer at the surface of the solid salt with almost no orientational order in the second layer is proposed for the IL–(solid) salt interface.

In contrast to our findings, recent high-energy x-ray reflectivity studies<sup>26</sup> have reported the existence of pronounced molecular layering in ILs at a charged sapphire(001) surface suggesting a layer model with anions and cations clearly separated into distinct layers. Moreover, atomic force microscopy (AFM) measurements have reported earlier the presence of electrostatically-bound layers of 1-ethyl-3-methylimidazolium  $[\text{C}_2\text{mim}]^+$  cation on the surface of various solid substrates, particularly on high surface charge mica surfaces, where cations were found to be strongly bound.<sup>27,28</sup> Furthermore, molecular dynamics simulations<sup>29</sup> done to investigate the interaction of the ionic liquid 1-butyl-3-methylimidazolium bis(trifluoromethylsulfonyl)imide,  $[\text{BMIM}][\text{Tf}_2\text{N}]$ , with  $\text{NaCl}(100)$  crystal have revealed that despite the ionic nature of  $\text{NaCl}$ , the surface was in fact covered by the most hydrophobic components ( $-\text{CF}_3$  and butyl groups) of the ionic liquid rather than the polar ones. To quote Sieffert and Wipff<sup>29</sup> directly on their conclusions regarding the ionic  $\text{NaCl}/[\text{BMIM}][\text{Tf}_2\text{N}]$  interface system: “Near the interface, the orientation of the IL ions is not isotropic, and the ions display some ordering, without forming regular layers, however.”

Although this report does not include a detailed calculation of the orientation of the ions at the solid salt surfaces, our results show that the  $[\text{BMIM}]^+$  cation must be oriented with the imidazolium ring parallel to the  $\text{NaCl}\{100\}$  surface plane due to the absence of imidazolium ring modes in the spectra. Moreover, the alkyl chains are likely

oriented toward the solid surface. These findings are consistent with earlier molecular dynamics simulations on the same interface done by Sieffert and Wipff,<sup>29</sup> which reported that the crystal surface of NaCl(100) was solvated by less polar IL constituents (i.e. butyl group) rather than the polar ones (i.e. imidazolium ring). This SFG investigation shows that the alkyl chains do not form a dense, highly ordered chain packing as observed by the presence of CH<sub>2</sub> peaks in the SFG spectrum at 2849 cm<sup>-1</sup> and 2912 cm<sup>-1</sup>. Furthermore, the planar structure of the charged imidazolium ring (with estimated surface area occupied = 22.25 Å<sup>2</sup>)<sup>30</sup> limits alkyl group coverage on the surface. Based on the vibrational modes seen in the C–H stretching region of the spectra, this study shows that the neutral alkyl chains are likely pointing towards the solid salt surface, rather than the bulk ionic liquid phase. It must be stressed here, however, that the dominant interaction influencing the chemistry between the solid salt surface and the ionic liquid is governed primarily, by electrostatic attraction (with imidazolium ring being the charged moiety) and secondarily, by the neutral alkyl chains. Sieffert and Wipff,<sup>29</sup> further proposed a specific ordering within the first layer denoting ions ordered parallel to the surface which agrees with our findings on the imidazolium ring configuration. However, it must be noted that the MD simulations performed on the 100 face of NaCl with [BMIM][Tf<sub>2</sub>N], do not take into account a key aspect such as the crystal surface relaxation<sup>22</sup> for solid surfaces, which plays an important role in influencing the ordering of IL constituents in our actual spectroscopic experiment.

The [DCA]<sup>-</sup> orientation at BaF<sub>2</sub>(111) surface is likely arranged with the imide nitrogen toward the salt surface. These results show that by electrostatic interaction, IL

cations adhere to the negatively-charged NaCl{100} surface, while IL anions adhere to the positively-charged BaF<sub>2</sub>(111) surface. Because our spectroscopic technique is inherently surface-sensitive, the fact that we do not see vibrational modes coming from both cation and anion on either of the solid salt surfaces under study suggests that IL ordering at these solid surfaces is present up to a single layer only. The low surface charge from the dielectric salt is essentially screened within the first layer, followed by the bulk liquid. Recent calculations<sup>30</sup> have revealed a measured average surface potential of [BMIM][DCA] equal to  $0.37 \pm 0.02$  V at the gas-liquid interface, which varies as a function of anion-cation configuration. For the solid-liquid interface described in this study, the solid salt surface charge density can be estimated to be  $\sim 3 \text{ e nm}^{-2}$ , using the lattice parameter of NaCl{100}. To calculate the value of the effective charge on the salt surface that needs to be compensated by the ionic liquid, surface relaxation effects for the topmost layer exposed<sup>22</sup> must be taken into account. Therefore, the surface charge density must be  $\ll 3 \text{ e nm}^{-2}$ . The charge-screening effect is supported by previous atomistic molecular simulations<sup>18</sup> which suggested that ionic liquids provide excellent electrostatic screening at a distance of 1–2 nm, for electrode surfaces with ‘intermediate’ and ‘high’ charge densities between  $\pm 0.5 \text{ e nm}^{-2}$  and  $\pm 1 \text{ e nm}^{-2}$ . After 2–3 nm from the charged wall, the Poisson potential was found to reach the bulk value. Moreover, a voltage drop of about 0.7 V has been observed going from an uncharged wall towards the bulk.<sup>31</sup> Current results are further in agreement with the atomistic simulations, which state that at low charge densities the cations in the first layer near a negative wall are preferentially aligned flat against the wall.<sup>18</sup>

To compare current SFG spectroscopic results reported here to x-ray reflectivity measurements<sup>26</sup>, the following statements are noted: For the solid salt-ionic liquid interface, if extensive layering (i.e. cations and anions clearly separated into distinct layers) is present, the interfacial surface region is non-centrosymmetric, such that SFG response is visible. However, if the layering occurs as a bilayer-type structure (similar to those of lipids), the surface region is centrosymmetric, such that SFG response is invisible.<sup>32</sup> Unlike SFG, x-ray reflectivity measurements are sensitive to ordering of the bilayer-type. Because the present experimental observations reveal no dense packing of alkyl chains at the interface, bilayer-type structures are unlikely. Furthermore, because vibrational modes coming from both the cation and anion are absent at a single solid salt surface (BaF<sub>2</sub>(111) or NaCl{100}), the liquid is essentially isotropic after the first layer.

Furthermore, to make a direct comparison between our current results with models proposed by Federov, Kornyshev and co-workers<sup>12,13,17</sup> on effects such as overscreening and crowding for finite-sized ions is not straight-forward. The models explain high-charge density surfaces while this investigation involves nonpolar crystal salt surfaces of low charge density. Unlike the capacitance and theoretical calculations, the crystal surfaces probed here are of very low potential compared to the simulations, such that the above-mentioned effects are not observed. The amount of cations adsorbed to the surface approximately balances the charge on the surface, such that overscreening and crowding effects even within the first layer, for the system does not exist. The first layer simply neutralizes the charge on the surface of the ionic salt, without an excess of ions from the ionic liquid to counter the surface charge. In addition, the current findings

included in this report, are consistent with previous experimental results<sup>7,9</sup> for the behavior of ionic liquids at solid-liquid interfaces at electrode potentials near the PZC (potential of zero charge), and at electrically neutral dielectric surfaces.<sup>33-36</sup>

#### 5.4. Conclusion

Overall, the current results are consistent with IL interaction pre-suppositions, centered on the inherent surface charge of the solids, as basis for the interaction of ionic liquid ion constituents. A Helmholtz-type model composed of a single ordered layer at the surface of the solid salt, with almost no orientational order in the second layer is found at the IL–(solid) salt interface. An overall picture of the molecular structure at the solid-liquid interface following this model is illustrated in Fig. 5-3.

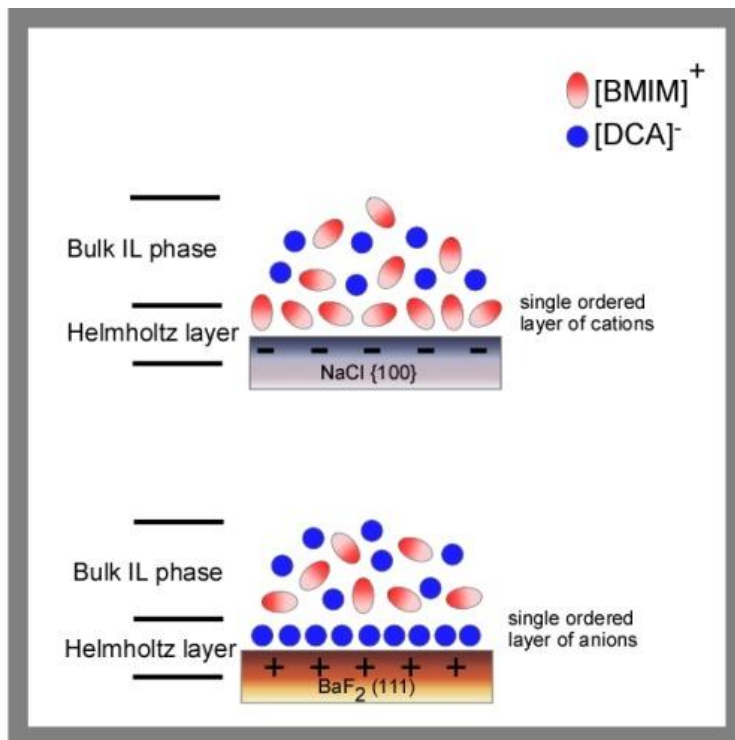


**Fig. 5-3.** Helmholtz model for the molecular structure of [BMIM][DCA] in contact with solid single crystal salt surfaces, NaCl{100} and BaF<sub>2</sub>(111).

## 5.5. References

- (1) Rogers, R. D. *Nature* **2007**, *447*, 917-918.
- (2) Steinrück, H.-P. *Surf. Sci.* **2010**, *604*, 481-484.
- (3) Steinrück, H. P.; Libuda, J.; Wasserscheid, P.; Cremer, T.; Kolbeck, C.; Laurin, M.; Maier, F.; Sobota, M.; Schulz, P. S.; Stark, M. *Adv. Mater.* **2011**, *23*, 2571-2587.
- (4) Wang, X.; Fulvio, P. F.; Baker, G. A.; Veith, G. M.; Unocic, R. R.; Mahurin, S. M.; Chi, M.; Dai, S. *Chem. Commun.* **2010**, *46*, 4487-4489.
- (5) Silvester, D. S. *Analyst* **2011**, *136*, 4871-4882.
- (6) Barrosse-Antle, L. E.; Bond, A. M.; Compton, R. G.; O'Mahony, A. M.; Rogers, E. I.; Silvester, D. S. *Chem. – Asian J.* **2010**, *5*, 202-230.
- (7) Baldelli, S. *J. Phys. Chem. B* **2005**, *109*, 13049-13051.
- (8) Rivera-Rubero, S.; Baldelli, S. *J. Phys. Chem. B* **2004**, *108*, 15133-15140.
- (9) Baldelli, S. *Acc. Chem. Res.* **2008**, *41*, 421-431.
- (10) Aliaga, C.; Baldelli, S. *J. Phys. Chem. B* **2006**, *110*, 18481-18491.
- (11) Zhou, W.; Inoue, S.; Iwahashi, T.; Kanai, K.; Seki, K.; Miyamae, T.; Kim, D.; Katayama, Y.; Ouchi, Y. *Electrochem. Commun.* **2010**, *12*, 672-675.
- (12) Bazant, M. Z.; Storey, B. D.; Kornyshev, A. A. *Phys. Rev. Lett.* **2011**, *106*, 046102.
- (13) Fedorov, M. V.; Kornyshev, A. A. *J. Phys. Chem. B* **2008**, *112*, 11868-11872.

- (14) Georgi, N.; Kornyshev, A. A.; Fedorov, M. V. *J. Electroanal. Chem.* **2010**, *649*, 261-267.
- (15) Lynden-Bell, R. M.; Del Pópolo, M. G.; Youngs, T. G. A.; Kohanoff, J.; Hanke, C. G.; Harper, J. B.; Pinilla, C. C. *Acc. Chem. Res.* **2007**, *40*, 1138-1145.
- (16) Kornyshev, A. A. *J. Phys. Chem. B* **2007**, *111*, 5545-5557.
- (17) Fedorov, M. V.; Georgi, N.; Kornyshev, A. A. *Electrochem. Commun.* **2010**, *12*, 296-299.
- (18) Lynden-Bell, R. M.; Frolov, A. I.; Fedorov, M. V. *Phys. Chem. Chem. Phys.* **2012**, *14*, 2693-2701.
- (19) Kelly, R. *Surf. Sci.* **1979**, *90*, 280-318.
- (20) Matthias, E.; Nielsen, H. B.; Reif, J.; Rosén, A.; Westin, E. *J. Vac. Sci. Technol. B* **1987**, *5*, 1415-1422.
- (21) Vogt, J.; Henning, J.; Weiss, H. *Surf. Sci.* **2005**, *578*, 57-70.
- (22) Vogt, J. *Phys. Rev. B: Condens. Matter* **2007**, *75*, 125423.
- (23) Rivera-Rubero, S.; Baldelli, S. *J. Phys. Chem. B* **2006**, *110*, 4756-4765.
- (24) Santos, C. S.; Baldelli, S. *J. Phys. Chem. B* **2009**, *113*, 923-933.
- (25) Aliaga, C.; Baldelli, S. *J. Phys. Chem. B* **2007**, *111*, 9733-9740.
- (26) Mezger, M.; Schroder, H.; Reichert, H.; Schramm, S.; Okasinski, J. S.; Schoder, S.; Honkimaki, V.; Deutsch, M.; Ocko, B. M.; Ralston, J.; Rohwerder, M.; Stratmann, M.; Dosch, H. *Science* **2008**, *322*, 424-428.
- (27) Atkin, R.; Warr, G. G. *J. Phys. Chem. C* **2007**, *111*, 5162-5168.

- (28) Hayes, R.; El Abedin, S. Z.; Atkin, R. *J. Phys. Chem. B* **2009**, *113*, 7049-7052.
- (29) Sieffert, N.; Wipff, G. *J. Phys. Chem. B* **2007**, *111*, 7253-7266.
- (30) Martinez, I. S.; Baldelli, S. *J. Phys. Chem. C* **2010**, *114*, 11564-11575.
- (31) Fedorov, M. V.; Lynden-Bell, R. M. *Phys. Chem. Chem. Phys.* **2012**, *14*, 2552-2556.
- (32) Nishida, T.; Johnson, C. M.; Holman, J.; Osawa, M.; Davies, P. B.; Ye, S. *Phys. Rev. Lett.* **2006**, *96*, 077402.
- (33) Aliaga, C.; Baldelli, S. *J. Phys. Chem. C* **2008**, *112*, 3064-3072.
- (34) Romero, C.; Baldelli, S. *J. Phys. Chem. B* **2006**, *110*, 6213-6223.
- (35) Romero, C.; Moore, H. J.; Lee, T. R.; Baldelli, S. *J. Phys. Chem. C* **2007**, *111*, 240-247.
- (36) Baldelli, S.; Bao, J.; Wu, W.; Pei, S.-s. *Chem. Phys. Lett.* **2011**, *516*, 171-173.

## Chapter 6. Sum Frequency Generation Spectroscopy of Imidazolium-based Ionic Liquids with Cyano-functionalized Anions at the Solid Salt-Liquid Interface

### 6.1. Introduction

Ionic liquids containing cyano-based anions have limited published data despite their successful preparation a few years ago.<sup>1-4</sup> A survey of the literature reveals that only in recent years have they become readily available commercially. For these reasons, only a few fundamental studies of their physical and chemical properties are accessible.<sup>5</sup>

Incorporating cyano anions in ionic liquids result to unique qualities which find several potential applications in current electrochemical challenges.<sup>6</sup> Probing the ionic liquid–solid interface is particularly interesting for electrochemical sensing technology, and the need to understand their reaction mechanism relative to conventional solvents is indispensable.<sup>7,8</sup> For ionic liquids with cyano anions, recent experimental data confirm desirable properties such as low melting points, low viscosities, and high thermal stability compared to those with non-cyano-based anion analogs.<sup>9-11</sup> This makes them particularly attractive for applications such as in dye-sensitized solar cells (DSCs),<sup>12-14</sup> in which the key factor for promising electrolyte systems require solvent alternatives of relatively low viscosity.

The limited use of IL-based DSCs to date, is due to the low photovoltaic performance associated with the high viscosity of ILs, which restricts mass-transfer of the photocurrent under full sunlight operation.<sup>14</sup> Indeed, ionic liquids based on dicyanamide [DCA]<sup>-</sup>, tricyanomethanide [TCM]<sup>-</sup> and tetracyanoborate [TCB]<sup>-</sup> anions, especially,

have been reported to confer low viscosities, *i.e.* 17 cP (at 22 °C) for [EMIM][DCA]; 18 cP (at 22 °C) for [EMIM][TCM]; and 19 cP (at 20°C) for [EMIM][TCB].<sup>3,15</sup> These values were found to be promisingly low, compared for example, to the more popular and well-studied fluorine-containing ionic liquids such as [EMIM][Tf<sub>2</sub>N], which has a viscosity of 27 cP at 20 °C.<sup>2</sup>

This report serves to bridge the lack of information on basic physical and chemical properties of imidazolium-based ionic liquids with cyano-functionalized anions by providing fundamental vibrational spectroscopic data using a systematic series incorporating a linear to tetrahedral cyano-based anion moiety. Because of their potential as non-volatile electrolytes in electrochemical sensors, and in the context of voltammetric sensing at solid–liquid interfaces, their behavior in contact with single crystal salts containing an inherent surface charge is characterized. The central idea behind the choice of solid surfaces for study has been described in an earlier publication, with an account of related investigations pertaining to the ionic liquid–metal electrode interface using electrochemical techniques and vibrational spectroscopy.<sup>16</sup> These previous efforts have motivated, to a great extent, this attempt to confirm and provide an accurate model related to current propositions on the electric double layer structure of ionic liquids on solid surfaces. Through a nonlinear, surface-sensitive, optical technique, SFG, vibrational information offered here aims to provide an accurate molecular-level description of the surface of these materials, particularly at the solid-liquid interface.

## 6.2. Experimental Method

### 6.2.1. Samples

Synthetic preparation of [BMIM][SCN] and [BMIM][DCA] have been described in detail in Section 3.1. Both ionic liquids were prepared in our lab while [BMIM][TCM] was synthesized and characterized by Dr. Gary A. Baker (The University of Missouri-Columbia). [EMIM][TCB] was obtained from Merck, courtesy of Dr. Florian Maier (Universität Erlangen-Nürnberg).<sup>17</sup> In addition to <sup>1</sup>H-NMR, <sup>13</sup>C-NMR, FTIR, and Raman spectra of the samples<sup>17</sup>, purity has been determined through analysis of chloride content found below the calibrated detection limit of a chloride ion-selective electrode (Weiss Research) and estimation of water content at a base sample pressure of  $\sim 2 \times 10^{-5}$  Torr, in which the samples were dried, prior to spectroscopic measurements (Section 3.2).<sup>16,17</sup>

### 6.2.2. Experimental Setup and Sample Preparation Prior to SFG Measurements

Sections 3.5.2 and 3.5.3 describes the experimental design to allow SFG spectroscopic measurements involving dielectric single crystal salt surfaces in contact with ionic liquids introduced in this study. Fig. 3-23 provides a picture of the IL–NaCl{100} cell assembly while Fig. 3-24 shows the setup during the vacuum drying procedure. The purge box design used to contain the solid-liquid cell has been illustrated in Fig. 3-25 and Fig. 3-26. The protocol for air-less transfer of the ionic liquid from the drying vessel to the solid-liquid cell has been described in Section 3.5.3.

### 6.2.3. SFG Spectroscopy System and Data Collection

Details on data collection (Section 3.5.4) and instrumental configuration have been discussed in Section 3.3.<sup>17</sup> A fixed visible (532 nm) and a tunable IR beam (2000–4000  $\text{cm}^{-1}$ ) generated from an OPG/OPA system, were overlapped at the sample surface in a co-propagating geometry, at an angle of 50° and 60° from the surface normal, respectively. Signal was detected *via* a monochromator/PMT setup and data acquired using a gated integrator and boxcar averager.

A scan rate of 1  $\text{cm}^{-1}/\text{s}$ , using 20 laser shots per point was used in the data collection, at an average of at least 5 scans. To increase signal to noise ratio, a maximum of 10 scans was used in cases where signal was low, *i.e.* for samples with inherent color or measurements taken in the C–N region. Calibration prior to measurement of samples using polystyrene, gold, and hexadecanol standards described in Section 3.3.5. Spectra in all four polarization combinations namely, *ssp*, *ppp*, *sps*, and *pss* for ionic liquid samples were measured. Using equation 2-15 as a fitting function, spectra were fitted *via* Origin 7.0 Professional nonlinear curve fitting.

## 6.3. Results and Discussion

### 6.3.1. SFG Spectra

Vibrational modes observed in two different regions of the spectrum of the two crystal salt surfaces are presented here. The higher frequency region ( $2750\text{--}3300\text{ cm}^{-1}$ ) at the C–H stretching mode, probes vibrational frequencies assigned to the cation, while the lower frequency region ( $2000\text{--}2300\text{ cm}^{-1}$ ) at the C–N stretching mode, probes vibrational frequencies of the anion.

Figs. 6-1, 6-2a, and 6-2b show sum frequency spectra of ionic liquids in the C–H and C–N stretching regions observed at NaCl{100} and BaF<sub>2</sub>(111) surfaces, respectively, while Fig. 6-3 shows [EMIM][TCB] at the BaF<sub>2</sub>(111) surface only. It was not possible to obtain spectra at the [EMIM][TCB]–NaCl{100} interface because [EMIM][TCB] dissolved the surface of NaCl{100} crystal, causing too much scattering of the laser beams, which made signal acquisition difficult. Solid lines in the figures indicate a fit to the data in square dots, using equation 2-15 as a fitting function. However, for surfaces in which ionic liquid samples gave no apparent signal (Fig. 6-1,A and Fig. 6-2b,C–D), spectra did not require fitting and were plotted in open circles with solid lines. The solid lines in these plots serve as a guide to demonstrate the lack of features in the spectra. Because spectra have been normalized against standard references, such as gold and hexadecanol solution, intensities can be compared, such that spectra are plotted on similar intensity scales by ionic liquid type, in *ssp*, *ppp*, and *sps* polarizations. Resonances observed in *pss* polarization overlaps with *sps*, such that spectra are provided in the

supporting information (Figs. 6-1S, 6-2S and 6-3S). It is important to note that for methyl and methylene groups of the cation, all the symmetric modes and their Fermi resonances have their strongest features in the *ssp* spectra. However, no resonances were observed near the C–N stretching region at the IL–NaCl{100} interface for all ionic liquid samples (Fig. 6-1S, supporting information). Moreover, except for [EMIM][TCB] shown in Fig. 6-3, no resonances (very weak for [BMIM][SCN] and [BMIM][DCA] in *ssp* spectra, Fig. 6-2S in supporting information) have been found near the C–H stretching region for BaF<sub>2</sub>(111) surface.

### 6.3.2. Peak Assignments

All assignments of vibrational modes observed in the SFG spectra in both C–H and C–N stretching regions are summarized in Tables 6-1 and 6-2. As evidenced by the features observed in the spectra, data generally supports that the ionic liquid cation predominates the surface of NaCl{100}, while the anion predominates the surface of BaF<sub>2</sub>(111). Strong resonances were observed at the C–H stretching region for the IL–NaCl{100} interface, and at the C–N stretching region for the IL– BaF<sub>2</sub>(111) interface. Therefore, emphasis in the discussion is centered in these specific interfaces and corresponding spectral regions as they mark the most significant findings, and serve to characterize the chemistry involved. For these reasons, all other results have been presented in the supporting information. Moreover, this section provides a detailed explanation of these observations highlighting the presence, as well as the lack of features in the spectra. More importantly, it must be noted, that the inherent nature of the solid

crystal salt surface plays a key role in influencing the extent of interaction with the ionic liquid. Further details of specific features in the spectra are discussed in the following.

### 6.3.3. NaCl{100} Surface

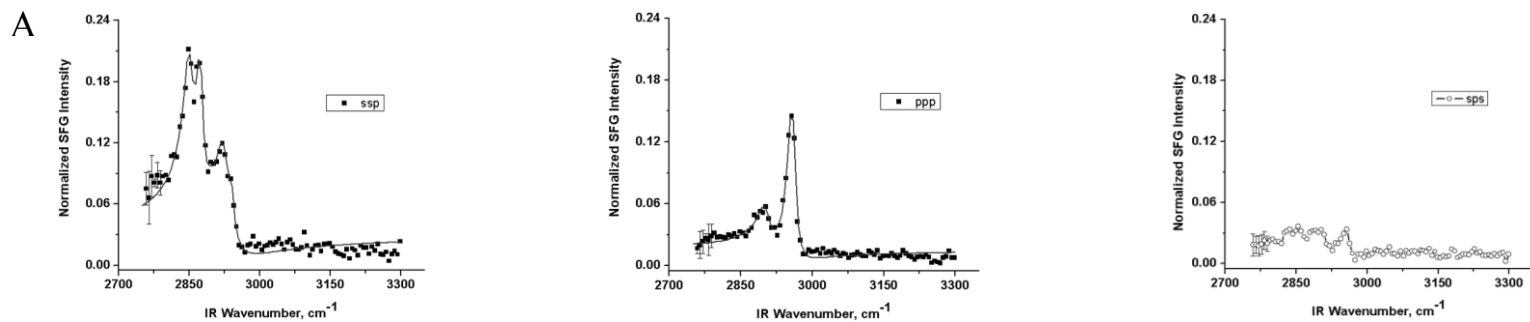
SFG spectra in *ssp*, *ppp*, and *sps* polarizations at the C–H stretching region for IL–NaCl{100} interface are shown in Fig. 6-1. All three ionic liquids namely, [BMIM][SCN], [BMIM][DCA] and [BMIM][TCM] show strong resonances in the *ssp* spectra, which are assigned to methyl and methylene groups of the butyl chain of the [BMIM]<sup>+</sup> cation. Signal profiles for all three ionic liquids looked very similar. Specifically, a characteristic peak was observed at  $\sim 2850\text{ cm}^{-1}$ , which is assigned to the symmetric methylene stretching vibration ( $d^+$ ), at  $\sim 2875\text{ cm}^{-1}$  due to the symmetric methyl stretching vibration ( $r^+$ ), and at  $\sim 2930\text{ cm}^{-1}$  assigned to the Fermi resonance mode of the symmetric methyl stretching vibration ( $r^+_{FR}$ ). The  $r^+_{FR}$  mode for [BMIM][SCN] was notably shifted to lower frequency compared to both [BMIM][DCA] and [BMIM][TCM]. However, the Fermi resonance mode assigned to the symmetric methylene stretching vibration ( $d^+_{FR}$ ) at  $\sim 2910\text{ cm}^{-1}$ , clearly appeared for both [BMIM][DCA] and [BMIM][TCM] but was indistinguishable for [BMIM][SCN].

In *ppp* polarization, the broad peak at  $\sim 2880\text{ cm}^{-1}$ , which has been previously assigned to the antisymmetric methylene stretching mode ( $d^-$ ) in normal chain alcohols<sup>18</sup> was within the noise level, and is therefore not assigned. However, a peak at  $\sim 2960\text{ cm}^{-1}$  dominated the *ppp* spectra, and is assigned to the antisymmetric methyl stretching mode

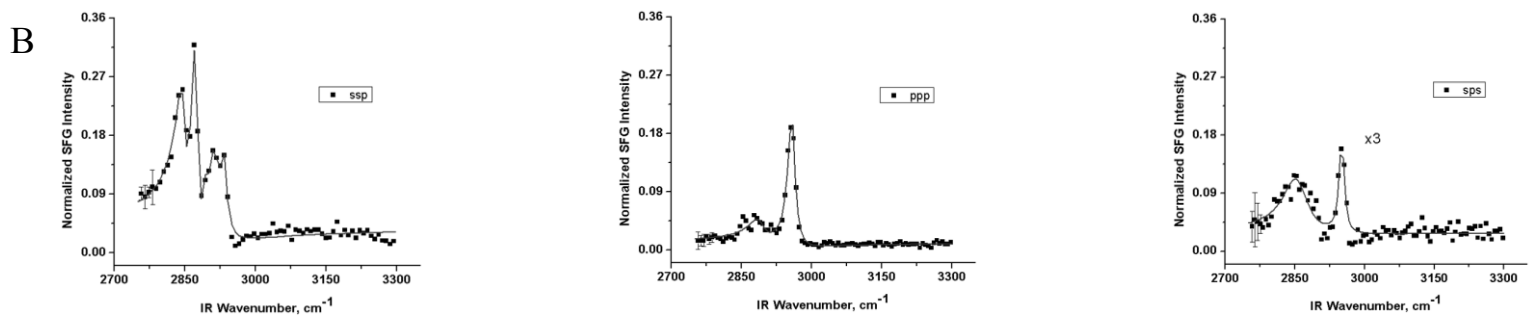
( $r^-$ ). This same peak appears very weakly in both *sps* and *pss* spectra for all ionic liquids except for [BMIM][SCN], wherein no resonances in the latter two polarizations were observed.

In the C–N stretching region (Fig. 6-1S, supporting information), no discernible peaks were observed for all ionic liquid samples. All peak assignments discussed here are summarized in Table 6-1.

[BMIM][SCN]-NaCl{100}



[BMIM][DCA]-NaCl{100}



[BMIM][TCM]-NaCl{100}

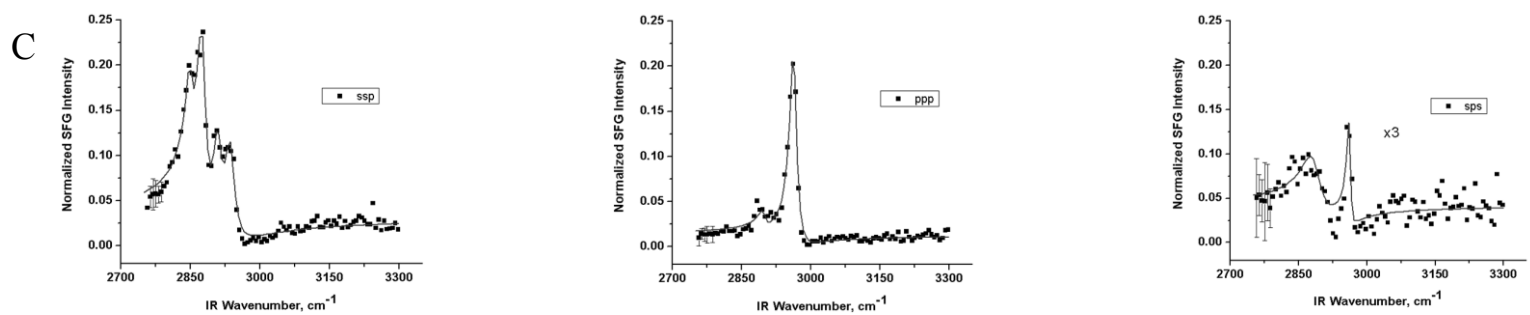
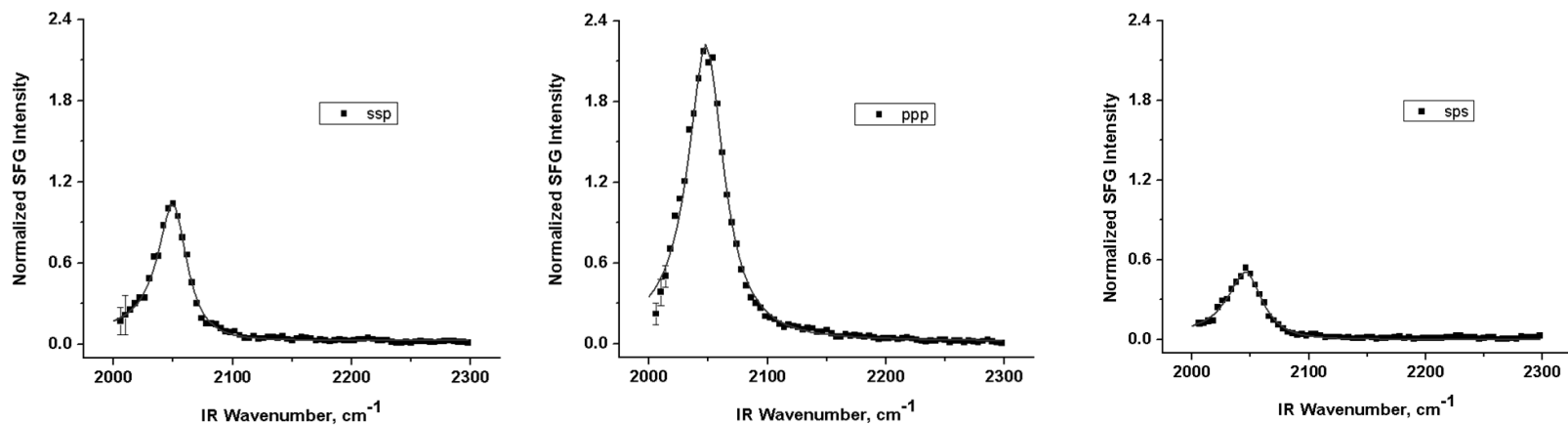


**Fig. 6-1.** Sum frequency spectra at the IL–NaCl{100} interface near the C–H stretching region at different polarization combinations.

A. [BMIM][SCN]-BaF<sub>2</sub>(111)



B. [BMIM][DCA]-BaF<sub>2</sub>(111)

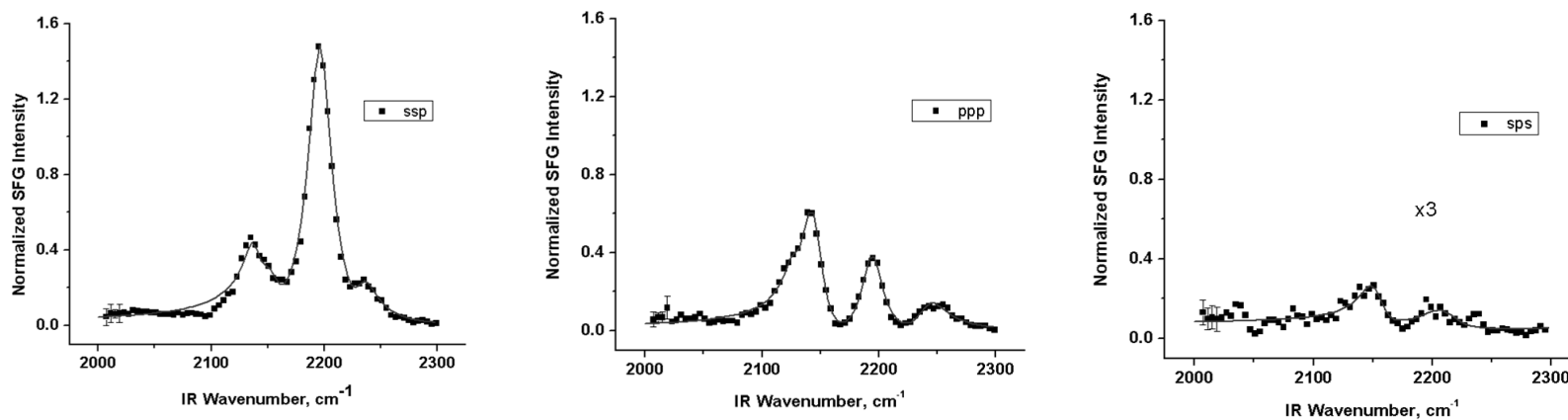
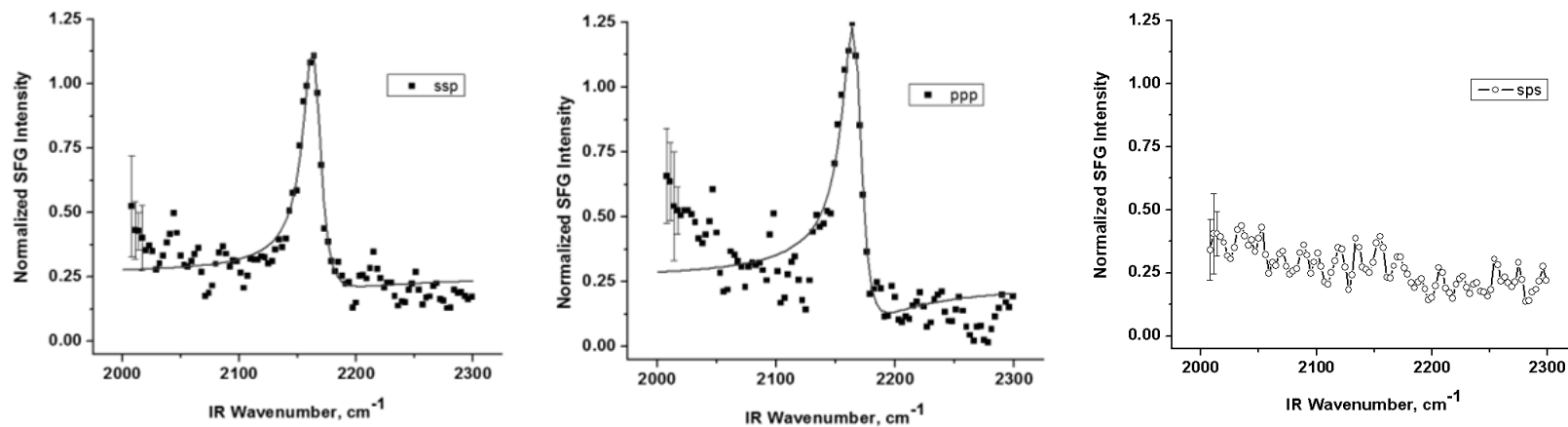


**Fig. 6-2a.** Sum frequency spectra at [BMIM][SCN]-BaF<sub>2</sub>(111) and [BMIM][DCA]-BaF<sub>2</sub>(111) interfaces near the C-N stretching region at different polarization combinations.

C. [BMIM][TCM]-BaF<sub>2</sub>(111)



129

D. [EMIM][TCB]-BaF<sub>2</sub>(111)

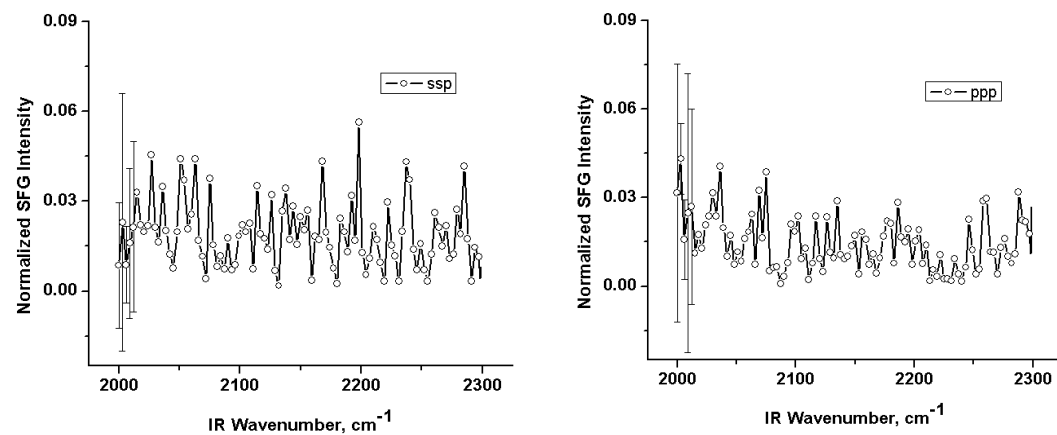


**Fig. 6-2b.** Sum frequency spectra at [BMIM][TCM]-BaF<sub>2</sub>(111) and [EMIM][TCB]-BaF<sub>2</sub>(111) interfaces near the C-N stretching region at different polarization combinations.

[EMIM][TCB]-BaF<sub>2</sub>(111)

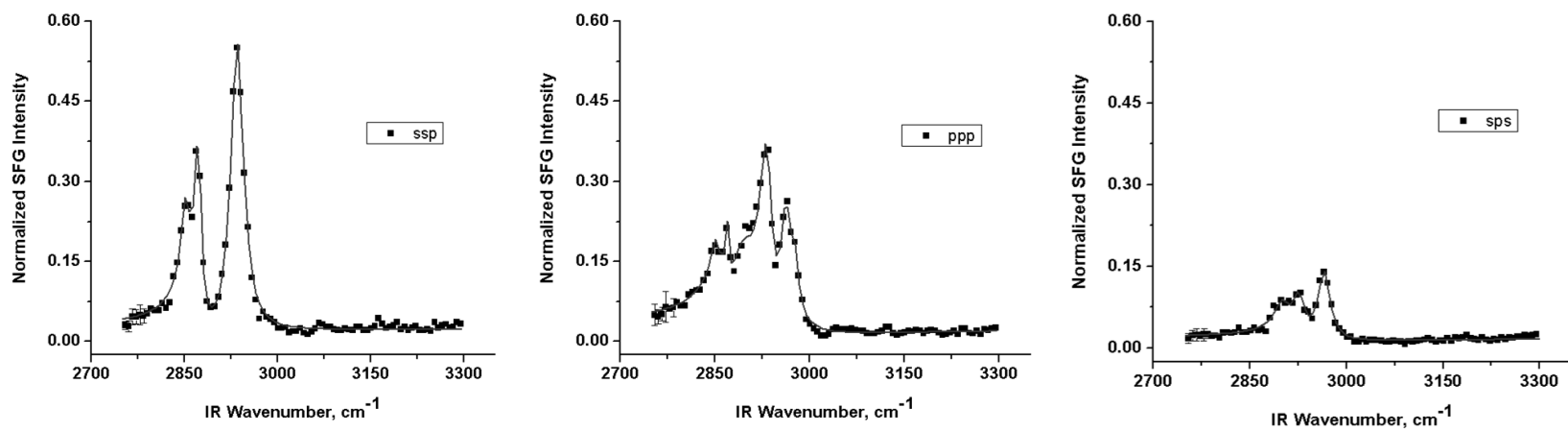


**Fig. 6-3.** Sum frequency spectra of [EMIM][TCB]-BaF<sub>2</sub>(111) interface in the C-H stretching region at different polarization combinations.

**Table 6-1.** Observed SFG vibrational frequencies and assignments at IL–NaCl{100} and IL–BaF<sub>2</sub>(111) interfaces in the C–H stretching region at different polarization combinations.

IL	IL–NaCl{100} Frequency in cm <sup>-1</sup> , assignment (intensity)	IL–BaF <sub>2</sub> (111) Frequency in cm <sup>-1</sup> , assignment (intensity)
[BMIM][SCN]	<i>ssp</i> 2853 <i>d</i> <sup>+</sup> (s), 2875 <i>r</i> <sup>+</sup> (s), 2924 <i>r</i> <sup>+</sup> <sub>FR</sub> (m) <i>ppp</i> 2959 <i>r</i> <sup>-</sup> (m)	<i>ssp</i> 2945 <i>r</i> <sup>+</sup> (m), 3116 H-C4-C5 <i>H</i> <sub>asym</sub> (vw), 3159 H-C4-C5- <i>H</i> <sub>sym</sub> (vw)
[BMIM][DCA]	<i>ssp</i> 2849 <i>d</i> <sup>+</sup> (s), 2874 <i>r</i> <sup>+</sup> (s), 2912 <i>d</i> <sup>+</sup> <sub>FR</sub> (m) 2932 <i>r</i> <sup>+</sup> <sub>FR</sub> (m) <i>ppp</i> 2959 <i>r</i> <sup>-</sup> (m) <i>sps</i> 2951 <i>r</i> <sup>-</sup> (vw) <i>pss</i> 2954 <i>r</i> <sup>-</sup> (vw)	<i>ssp</i> 2946 <i>r</i> <sup>+</sup> (vw)
[BMIM][TCM]	<i>ssp</i> 2852 <i>d</i> <sup>+</sup> (s), 2877 <i>r</i> <sup>+</sup> (s) 2910 <i>d</i> <sup>+</sup> <sub>FR</sub> (m), 2936 <i>r</i> <sup>+</sup> <sub>FR</sub> (m) <i>ppp</i> 2964 <i>r</i> <sup>-</sup> (s) <i>sps</i> 2961 <i>r</i> <sup>-</sup> (vw) <i>pss</i> 2965 <i>r</i> <sup>-</sup> (vw)	***
[EMIM][TCB]	---	<i>ssp</i> 2855 <i>d</i> <sup>+</sup> (s), 2873 <i>r</i> <sup>+</sup> <sub>FR</sub> (s), 2935 <i>r</i> <sup>+</sup> (s) <i>ppp</i> 2855 <i>d</i> <sup>+</sup> (m), 2872 <i>r</i> <sup>+</sup> (m), 2900 <i>d</i> <sup>-</sup> (m), 2932 <i>r</i> <sup>+</sup> <sub>FR</sub> (s), 2963 <i>r</i> <sup>-</sup> (m) <i>sps</i> 2903 <i>d</i> <sup>-</sup> (w), 2927 <i>d</i> <sup>-</sup> (w), 2966 <i>r</i> <sup>-</sup> (w) <i>pss</i> 2904 <i>d</i> <sup>-</sup> (w), 2929 <i>d</i> <sup>-</sup> (w), 2966 <i>r</i> <sup>-</sup> (w)

(s) strong, (m) medium, w (weak), vw (very weak); \*\*\* No SFG signal observed --- Crystal salt surface dissolved by IL  
(*r*<sup>+</sup>) methyl symmetric stretch, (*r*<sup>+</sup><sub>FR</sub>) Fermi Resonance of methyl symmetric, (*r*<sup>-</sup>) methyl antisymmetric stretch,  
(*d*<sup>+</sup>) methylene symmetric stretch, (*d*<sup>+</sup><sub>FR</sub>) Fermi Resonance of methylene symmetric, (*d*<sup>-</sup>) methylene antisymmetric stretch

#### 6.3.4. BaF<sub>2</sub>(111) Surface

Figs. 6-2a and 6-2b show SFG spectra at the C–N stretching region in *ssp*, *ppp*, and *sps* polarizations for IL–BaF<sub>2</sub>(111) interface. All *pss* spectra corresponded with the *sps* spectra as expected, and are provided in the supporting information (Fig. 6-2S). Strong resonances were observed in *ssp* and *ppp* spectra for [BMIM][SCN], [BMIM][DCA], and [BMIM][TCM]; however, no peaks were observed for [EMIM][TCB].

In *ssp* polarization, the characteristic peak at  $\sim 2051\text{ cm}^{-1}$  for [BMIM][SCN] is due to the anion C $\equiv$ N stretching mode ( $\nu$ ). The same mode appeared in all other polarization combinations, which is consistent with C $_{\infty v}$  symmetry, but the peak was slightly shifted to lower frequency. In *ppp* combination, this peak occurred at highest intensity, which was  $\sim$ double as that in *ssp*. In order to verify that the consistently strong signal comes from the monolayer, off-polarizations were measured, shown in Fig.4S in the supporting information. From the spectra obtained, no peaks were visible in off-polarizations *pps*, *psp*, *spp*, and *sss*, as expected. Thus, it was confirmed that the signal indeed came from the monolayer of ionic liquid, which was strongly-bound and well-ordered at the surface of the solid salt.

For [BMIM][DCA], the most intense peak in *ssp* occurred at  $\sim 2197\text{ cm}^{-1}$ , which is due to the symmetric C $\equiv$ N stretching mode ( $\nu_s$ ) of the anion. This was followed by much weaker peaks at  $\sim 2139\text{ cm}^{-1}$  due to the antisymmetric C $\equiv$ N stretch ( $\nu_{as}$ ), and at  $\sim 2234\text{ cm}^{-1}$  assigned to the combination band of the symmetric and antisymmetric C $\equiv$ N

stretching modes ( $\nu_s + \nu_{as}$ ). In *ppp* however, the strongest peak at  $\sim 2145 \text{ cm}^{-1}$  is assigned to the antisymmetric ( $\nu_{as}$ ) mode of the anion, while the symmetric ( $\nu_s$ ) and combination ( $\nu_s + \nu_{as}$ ) modes occurred at  $\sim 2194 \text{ cm}^{-1}$  and  $\sim 2242 \text{ cm}^{-1}$ , respectively. The antisymmetric mode ( $\nu_{as}$ ) at  $\sim 2152 \text{ cm}^{-1}$  appeared very weakly in the *sps* spectra, and was slightly shifted to a lower frequency at  $\sim 2148 \text{ cm}^{-1}$  in the *pss* spectra (Fig. 2S–B in supporting information).

For [BMIM][TCM], the peak at  $\sim 2165 \text{ cm}^{-1}$  with relatively strong intensity in both *ssp* and *ppp* spectra is assigned to the symmetric ( $\nu_s$ ) C $\equiv$ N stretching mode of the anion. No peaks were visible in the *sps* and *pss* combinations. Because the signal was completely absent for [EMIM][TCB], spectra were measured in *ssp* and *ppp* polarizations only. Table 6-2 summarizes all observed frequencies and assignments of peaks at the IL–BaF<sub>2</sub>(111) interface at the C $\equiv$ N stretching region discussed in this section.

In the C–H stretching region, none of the ionic liquids showed strong resonances. Very weak peaks, which were shifted at higher frequencies compared to those observed on the NaCl{100} surface appeared in the *ssp* spectra of [BMIM][SCN] and [BMIM][DCA] (Fig. 2S–A in supporting information). However, in both cases, the signal level was barely discernible and completely absent in all other polarization combinations. For [BMIM][SCN] specifically, the presence of imidazolium ring modes at  $\sim 3116 \text{ cm}^{-1}$  and  $3159 \text{ cm}^{-1}$  were observed very weakly, while the  $r^+$  mode at  $\sim 2945 \text{ cm}^{-1}$  appeared to be relatively more intense at this particular interface. Peaks in *ssp* for [BMIM][DCA] at the BaF<sub>2</sub>(111) surface were significantly weaker by a factor of  $\sim 10$ , compared to those at the NaCl{100} surface and were within the noise level, such that to

account for their presence was not justifiable. In *ppp* polarization, vibrational modes were completely absent in the C–H stretching region.

The [EMIM][TCB]–BaF<sub>2</sub>(111) interface as shown in Fig. 6-3, presents a unique case wherein no resonances at the C–N stretching region were found. However, strong and distinct features appeared in the spectra at the C–H stretching region. These features can be attributed to the [EMIM]<sup>+</sup> cation. As expected, spectra appeared to be different compared to those observed for [BMIM]<sup>+</sup>, wherein the most intense band found in *ssp* polarization was centered at ~2935 cm<sup>-1</sup>, assigned to the methyl symmetric stretching (*r*<sup>+</sup>) mode. This was followed by comparatively less intense peaks at ~2873 cm<sup>-1</sup> and ~2855 cm<sup>-1</sup>, which contain contributions from the symmetric methyl Fermi resonance (*r*<sup>+</sup><sub>FR</sub>) and methylene stretching modes (*d*<sup>+</sup>). In *ppp* polarization, all peaks were relatively weaker than in *ssp*, however, additional peaks were observed in the spectra namely, at ~2900 cm<sup>-1</sup> due to the antisymmetric methylene stretch (*d*<sup>-</sup>), and at ~2963 cm<sup>-1</sup> due to the antisymmetric methyl stretch (*r*<sup>-</sup>). In both *sps* and *pss* (Fig. 6-3S, supporting information) polarizations, the antisymmetric modes (*d*<sup>-</sup> and *r*<sup>-</sup>) were observed very weakly in the spectra. The peak for the antisymmetric methylene stretch appeared more of a doublet rather than the usually broad peak centered at ~2880 cm<sup>-1</sup>. However, these peaks which appeared in both *sps* and *pss*, correspondingly overlap with the more intense resonances observed in the *ppp* spectra.

**Table 6-2.** Observed SFG vibrational frequencies and assignments at IL–BaF<sub>2</sub>(111) interface in the C–N stretching region at various polarization combinations.

IL		IL–BaF <sub>2</sub> (111) Frequency in cm <sup>-1</sup> , assignment (intensity)
[BMIM][SCN]	<i>ssp</i>	2051 v (vs)
	<i>ppp</i>	2048 v (vs)*
	<i>sps</i>	2047 v (vs)
	<i>pss</i>	2047 v (vs)
[BMIM][DCA]	<i>ssp</i>	2139 v <sub>as</sub> (w), 2197 v <sub>s</sub> (vs) 2234 v <sub>s</sub> + v <sub>as</sub> (vw)
	<i>ppp</i>	2145 v <sub>as</sub> (m), 2194 v <sub>s</sub> (w), 2242 v <sub>s</sub> + v <sub>as</sub> (vw)
	<i>sps</i>	2152 v <sub>as</sub> (vw)
	<i>pss</i>	2148 v <sub>as</sub> (vw)
[BMIM][TCM]	<i>ssp</i>	2164 v <sub>s</sub> (s)
	<i>ppp</i>	2167 v <sub>s</sub> (s)
[EMIM][TCB]		***

(vs) very strong (s) strong, (m) medium, w (weak), vw (very weak); \*\*\* No SFG signal observed;  
\*intensity ~twice as strong as *ssp*; C–N stretching signal absent at IL–NaCl{100} interface

### 6.3.5 Discussion

The presence of strong resonances in the C–H stretching region indicates that the cation dominates the surface of NaCl{100}. This behavior was consistent for [BMIM][SCN], [BMIM][DCA] and [BMIM][TCM] ionic liquids. The vibrational modes observed were specifically associated with characteristic frequencies of the butyl chain attached to the imidazolium ring. The presence of methylene stretching vibrations in the *sps* spectra of all three ionic liquids suggested that the alkyl chains did not form a dense packing. However, the absence of imidazolium ring modes showed a configuration similar to that observed at the gas–liquid interface, wherein the ring was oriented almost parallel to the plane of the surface.

Correspondingly, the absence of vibrational modes in the C–N stretching region of the IL–NaCl{100} (Fig. 6-1S, B, supporting information) interface confirmed that the anion was not ordered at the surface of the salt. This supports the initial presupposition that the inherently negative surface charge density of NaCl{100} (estimated from the lattice parameter of the crystal to be  $\lll 3 \text{ e/nm}^2$ )<sup>16</sup> attracts positively charged moieties. Layering effects therefore were not observed at the said interface beyond the first layer; in which case, vibrational modes from the cation and the anion would have been detected in the spectra. Because vibrational modes of the anion were absent in the spectra, this study shows that the inherent charge from the surface of the solid crystal is effectively screened within the first layer, consistent with a Helmholtz-type model of the electric double layer at the interface.

This leads us to examine the IL–BaF<sub>2</sub>(111) interface where the reverse situation was observed. For [BMIM][SCN], [BMIM][DCA], and [BMIM][TCM] ionic liquids, relatively strong resonances assigned to the anion were seen in the spectra at the BaF<sub>2</sub>(111) surface. Consequently, resonances for the cation in the C–H stretching region were very weak compared to those observed at the NaCl{100} surface, and were completely absent for [BMIM][TCM] (See Fig. 6-2S, supporting information).

Specifically for [BMIM][SCN], resonances observed in the C–N stretching region were strongest compared to all other ionic liquids, and relatively unusual in the intensity scale typically observed in the lower frequency region (see Fig. 6-2, A). This data was complemented by the C–H stretching region spectra, in which the  $\nu^+$  mode at  $\sim 2945\text{ cm}^{-1}$  was of medium intensity relative to those observed at the NaCl{100} surface. Considering these results at both C–H and C–N stretching regions, it is therefore inferred that the linear [SCN]<sup>−</sup> anion must be strongly bound to the BaF<sub>2</sub>(111) surface by electrostatic interaction. The strong affinity of the [SCN]<sup>−</sup> anion in the first layer evidenced by unusually strong resonances in the spectra, promotes ordering of the cations to counter the charge in the second layer. Therefore, the cation resonances of [BMIM][SCN] were visible in the C–H stretching region on the surface of BaF<sub>2</sub>(111), albeit weak in intensity. Furthermore, only in this specific system were the imidazolium ring modes detected in the spectra, showing a unique interaction – and as a result, arrangement – at this interface. These observations support layering effects in which the anion is strongly bound to the solid surface in the first layer with an effective negative surface excess charge. This is followed by a cation layer in the second layer which

counters the charge excess. Moreover, because the resonances observed in the second layer were very weak, we conclude that only partial ordering within this layer is present. Additionally, the imidazolium ring configuration must be tilted away from the surface plane, as evidenced by the presence of weak ring modes at  $\sim 3116\text{ cm}^{-1}$  and  $3159\text{ cm}^{-1}$  in the spectra.

However, unlike the case of [BMIM][SCN], layering effects present up the second layer for [BMIM][DCA] on the surface of  $\text{BaF}_2(111)$  were not observed. At this interface, the layering dropped quite abruptly after the first layer. This was seen in the presence of strong resonances of the anion in the C–N stretching region, with barely discernible signal observed in the C–H stretching region. Indeed, it is difficult to take into account the very weak signal in the C–H stretching region as it is barely above the noise level. Moreover, for [BMIM][TCM], resonances in the C–H stretching region were completely absent. Therefore, for [BMIM][DCA] and [BMIM][TCM] ionic liquids, the Helmholtz model for the electric double layer at the IL– $\text{BaF}_2(111)$  interface applies.

We then use the initial argument observed for [BMIM][SCN], in order to explain the unusual behavior of [EMIM][TCB] ionic liquid on the surface of  $\text{BaF}_2(111)$  surface. In such a case, the anion in the first layer was very strongly bound to the inherently positive surface of the salt. This resulted to a partial negative excess charge within the first layer of anions, which gave rise to partial layering effects in the second layer.  $[\text{BMIM}]^+$  cations found in the second layer presumably countered the negative surface excess charge in the first layer. Applying this analogy, we believe that at the  $\text{BaF}_2(111)$ –[EMIM][TCB] interface, the strong resonances from the cation observed stem

from the interaction between the [EMIM]<sup>+</sup> cation with [TCB]<sup>-</sup> anions strongly bound to the solid surface. This conclusion presupposes that the [TCB]<sup>-</sup> anion therefore must be present in the first layer to initially screen the charge from the BaF<sub>2</sub>(111) surface.

Surprisingly however, our data clearly shows the absence of any vibrational resonance assignable to the [TCB]<sup>-</sup> anion. The reason for this is that the IR active mode of the anion is ~4 orders of magnitude weaker (see Fig. 4-2) compared to that of the [SCN]<sup>-</sup> anion. At the gas-liquid interface for example, the vibrational mode from the [TCB]<sup>-</sup> anion at ~2221 cm<sup>-1</sup> was obtained only by averaging a minimum of 10 scans, which still resulted to a relatively low signal to noise ratio (see Fig. 4-5, C). For these reasons, we have considered the invisibility of the signal from the [TCB]<sup>-</sup> anion a consequence of the limitation of our technique in detecting weak SFG-active modes, which originate primarily from the exclusive strengths of both IR- and Raman-active modes characteristic of the molecule involved.

This presumption is supported by the fact that the resonance modes from the [EMIM]<sup>+</sup> cation are unusually strong at the BaF<sub>2</sub>(111) surface, suggesting an ordered system. This result seems counter-intuitive knowing the fact that the BaF<sub>2</sub>(111) surface is inherently positive. Considering the results obtained at the BaF<sub>2</sub>(111)-[BMIM][SCN], the evidence shows that surface negative excess from [TCB]<sup>-</sup> anions strongly bound within the first layer dictate the strong ordering of the [EMIM]<sup>+</sup> cation on the second layer. Additionally, the [EMIM]<sup>+</sup> cation being less bulky orient within the second layer relatively well compared to the [BMIM]<sup>+</sup> cation (in [BMIM][SCN]) which exhibits only

partial ordering. This conclusion is further reinforced by the fact that none of the ring modes were present in the former.

To compare the present results with previous related studies, atomic force microscopy (AFM) measurements have revealed the presence of electrostatically-bound layers of [EMIM]<sup>+</sup> cations on the surface of various solid substrates, particularly on high surface charge mica.<sup>19,20</sup> Likewise, high-energy X-ray reflectivity studies reported the existence of pronounced molecular layering in ionic liquids at a charged sapphire(001) surface proposing a model composed of anions and cations separated into distinct layers.<sup>21</sup>

The current results presented in this report do not suggest pronounced layering at the surface of the two dielectric single crystal salts. However, theoretical models proposed by Federov, Kornyshev and co-workers<sup>22-24</sup> explaining the overscreening effects predicted at electrode surfaces with infinitesimally small charges support current experimental observations particularly at the BaF<sub>2</sub>(111)–[EMIM][TCB] interface, and partly at the BaF<sub>2</sub>(111)–[BMIM][SCN] interface. As can be seen in these particular systems, the double layer structure at the surface of the salt appears to be more complicated than the simple one-layer thick structure such that further details are relevant. In accordance to the theoretical treatments previously proposed, the strongly-bound layer of anions populating the first layer results to a much larger counter-ion charge delivered near the crystal salt surface than required to effectively neutralize the initial surface charge from the crystal. The second layer then compensates it by the charge of the opposite sign (cations) until the excess charge delivered is screened.

Therefore the extent of the layering is dictated primarily by the magnitude of the excess charge. The overscreening effect has been known to manifest itself in several phenomena involving dense ionic and dipolar systems. For the particular interface systems discussed here, the overscreening effect extends only until the second layer.

Moreover, molecular dynamics (MD) simulations previously reported for [BMIM][Tf<sub>2</sub>N] ionic liquid in contact with the 100 face of the NaCl<sup>25</sup> agree with our current observations. The reports suggested a surface covered by the most hydrophobic components, with a specific ordering within the first layer denoting ions ordered parallel to the surface. Furthermore, the short-range screening effect observed here are supported by other recent simulations<sup>26</sup> proposing excellent electrostatic screening by ionic liquids at charged walls covering a distance of 1–2 nm.

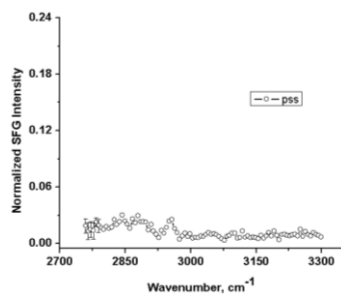
## 6.4. Conclusion

Imidazolium-based ionic liquids with cyano-functionalized anions at the surface of two different single crystal salts such as NaCl{100} and BaF<sub>2</sub>(111) has been characterized using SFG. Results showed that for [BMIM][SCN], [BMIM][DCA] and [BMIM][TCM] ionic liquids, the [BMIM]<sup>+</sup> cation strongly adhered to the surface of NaCl{100} as evidenced by strong resonances in the C–H stretching region. Consequently, the BaF<sub>2</sub>(111) surface was populated by the cyano-based anions as observed in the strong vibrational modes in the C–N stretching region. A Helmholtz-type model for a single ordered layer at the surface of the crystal salt was found for such systems.

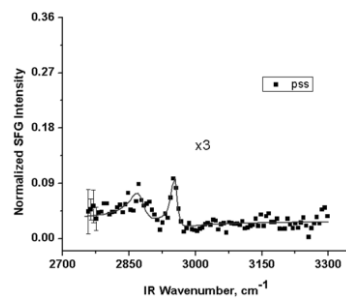
On the other hand, a specific interaction for [EMIM][TCB] has been observed, wherein the strongly-bound layer of anions populating the first layer resulted to a much larger counter-ion charge delivered near the crystal salt surface than required to effectively neutralize the initial surface charge from the crystal. As a result, strong resonances from the cation were observed at the BaF<sub>2</sub>(111) surface suggesting a more complicated structure of the double layer at the interface, than a simple Helmholtz-type model. Overscreening and layering effects up to the second layer were therefore valid in this particular system.

## 6.5 Supporting Information

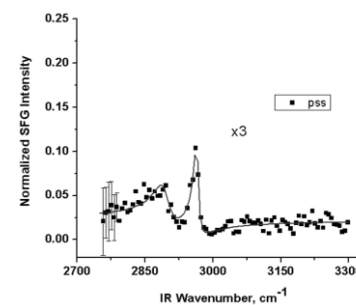
[BMIM][SCN]-NaCl{100}  
A) C-H Region



[BMIM][DCA]-NaCl{100}



[BMIM][TCM]-NaCl{100}



B) C-N Region

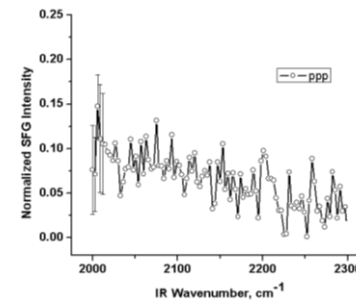
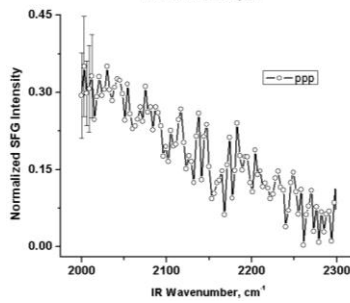
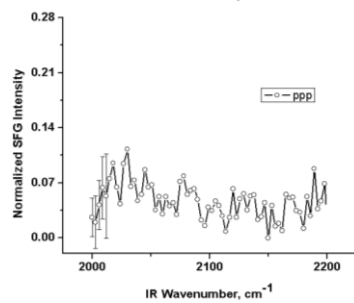
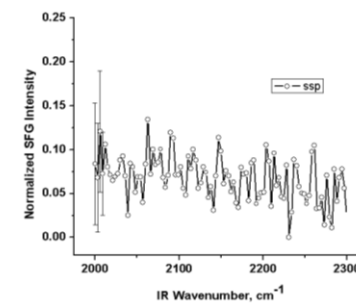
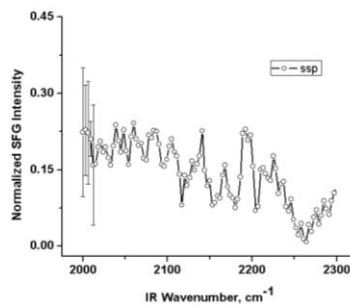
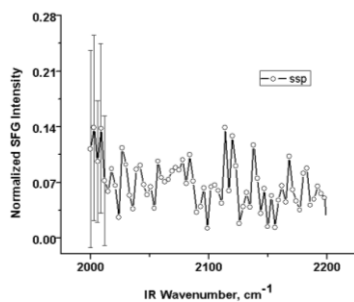
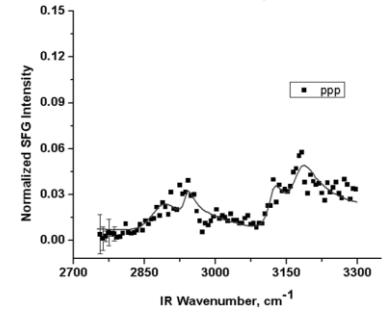
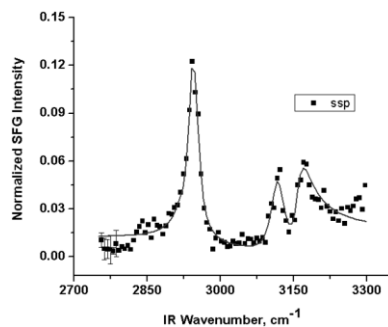
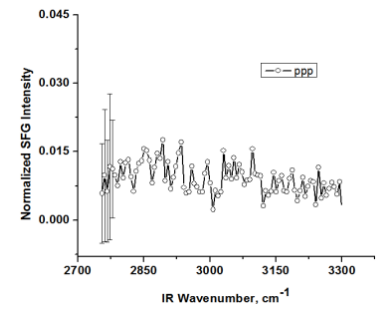
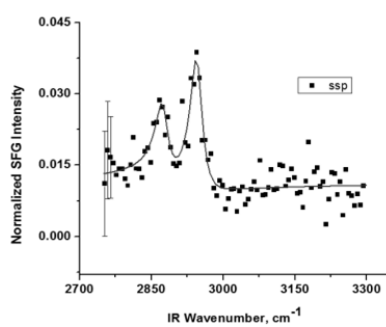


**Fig. 6-1S.** SFG spectra of IL-NaCl(100) interface: A) near the C-H stretching region in *pss*; and B) near the C-N stretching region in *ssp* and *ppp* polarizations.

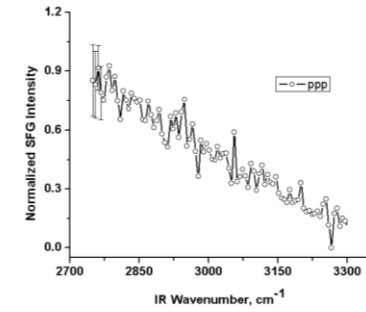
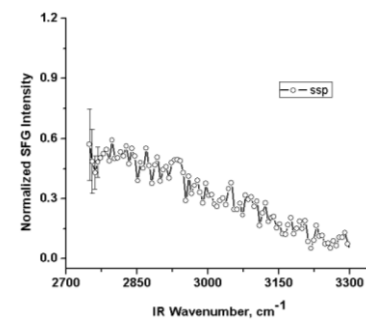
[BMIM][SCN]-BaF<sub>2</sub>(111)  
A) C-H Region



[BMIM][DCA]-BaF<sub>2</sub>(111)



[BMIM][TCM]-BaF<sub>2</sub>(111)



B) C-N Region

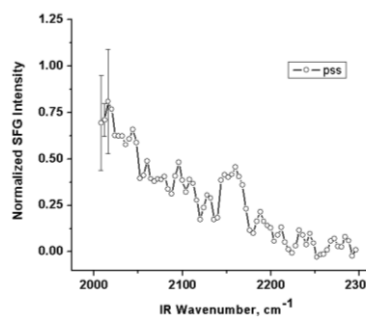
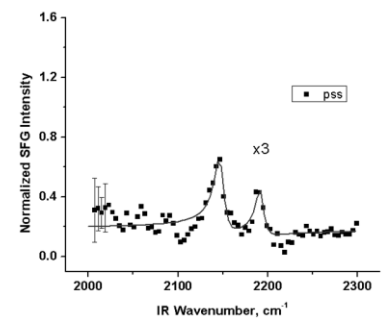
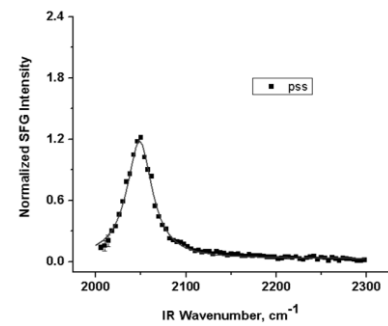


Fig. 6-2S. SFG spectra of IL-BaF<sub>2</sub>(111) interface: A) near the C-H stretching region in *ssp* and *ppp*; and B) near the C-N stretching region in *pss* polarization.

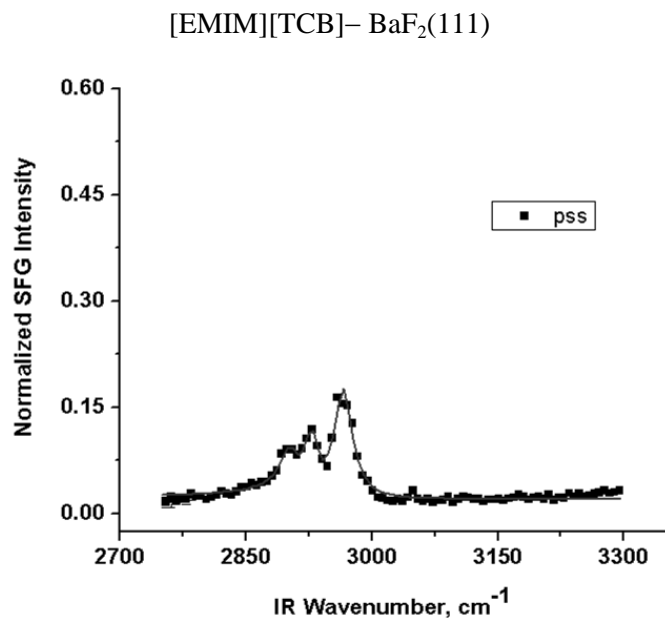


Fig. 6-3S. SFG spectra of [EMIM][TCB]-BaF<sub>2</sub>(111) interface near the C-H stretching region in *pss*.

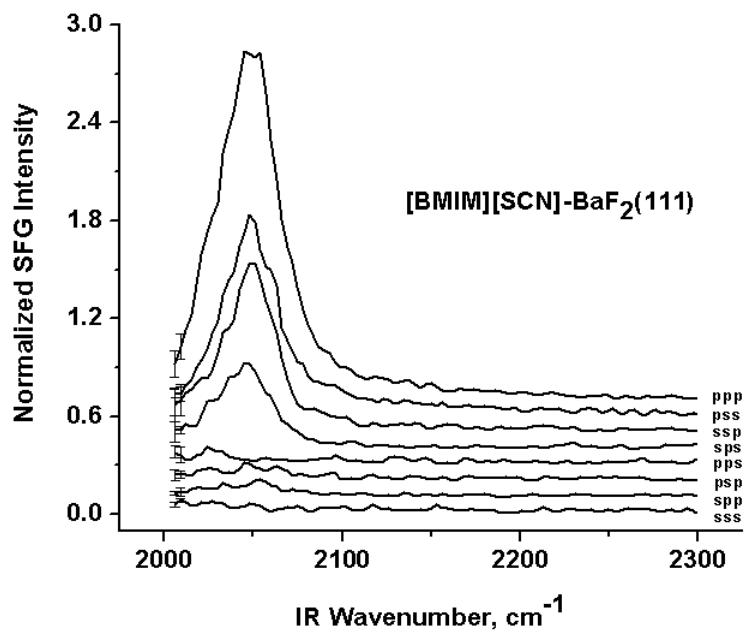


Fig. 6-4S. SFG spectra of [BMIM][SCN]-BaF<sub>2</sub>(111) interface near the C-N stretching region at all polarization combinations.

## 6.6. References

- (1) Yoshida, Y.; Baba, O.; Saito, G. *J. Phys. Chem. B* **2007**, *111*, 4742-4749.
- (2) Huddleston, J. G.; Visser, A. E.; Reichert, W. M.; Willauer, H. D.; Broker, G. A.; Rogers, R. D. *Green Chem.* **2001**, *3*, 156-164.
- (3) Yoshida, Y.; Muroi, K.; Otsuka, A.; Saito, G.; Takahashi, M.; Yoko, T. *Inorg. Chem.* **2004**, *43*, 1458-1462.
- (4) Brand, H.; Liebman, J. F.; Schulz, A.; Mayer, P.; Villinger, A. *Eur. J. Inorg. Chem.* **2006**, *2006*, 4294-4308.
- (5) Emel'yanenko, V. N.; Zaitsau, D. H.; Verevkin, S. P.; Heintz, A.; VoÅÿ, K.; Schulz, A. *J. Phys. Chem. B* **2011**, *115*, 11712-11717.
- (6) Armand, M.; Endres, F.; MacFarlane, D. R.; Ohno, H.; Scrosati, B. *Nat. Mater.* **2009**, *8*, 621-629.
- (7) Silvester, D. S. *Analyst* **2011**, *136*, 4871-4882.
- (8) Barrosse-Antle, L. E.; Bond, A. M.; Compton, R. G.; O'Mahony, A. M.; Rogers, E. I.; Silvester, D. S. *Chem. – Asian J.* **2010**, *5*, 202-230.
- (9) Forsyth, S. A.; Stuart R. Batten; Qing Dai; MacFarlane, D. R. *Aust. J. Chem* **2004**, *57*, 121-124.
- (10) Wooster, T. J.; Johanson, K. M.; Fraser, K. J.; MacFarlane, D. R.; Scott, J. L. *Green Chem.* **2006**, *8*, 691-696.
- (11) MacFarlane, D. R.; Forsyth, S. A.; Golding, J.; Deacon, G. B. *Green Chem.* **2002**, *4*, 444-448.

- (12) DeSilvestro, H. *Ionic Liquids - The Panacea for Dye Solar Cells*; Dyesol Ltd., 2007.
- (13) Marszalek, M.; Fei, Z.; Zhu, D.-R.; Scopelliti, R.; Dyson, P. J.; Zakeeruddin, S. M.; Grätzel, M. *Inorg. Chem.* **2011**, *50*, 11561-11567.
- (14) Kuang, D.; Uchida, S.; Humphry-Baker, R.; Zakeeruddin, S. M.; Grätzel, M. *Angew. Chem. Int. Ed.* **2008**, *47*, 1923-1927.
- (15) Kuang, D.; Wang, P.; Ito, S.; Zakeeruddin, S. M.; Grätzel, M. *J. Am. Chem. Soc.* **2006**, *128*, 7732-7733.
- (16) Peñalber, C. Y.; Baldelli, S. *J. Phys. Chem. Lett.* **2012**, 844-847.
- (17) Peñalber, C. Y.; Grenoble, Z.; Baker, G. A.; Baldelli, S. *Phys. Chem. Chem. Phys.* **2012**, *14*, 5122-5131.
- (18) Wang, H.-F.; Gan, W.; Lu, R.; Rao, Y.; Wu, B.-H. *Int. Rev. Phys. Chem.* **2005**, *24*, 191-256.
- (19) Atkin, R.; Warr, G. G. *J. Phys. Chem. C* **2007**, *111*, 5162-5168.
- (20) Hayes, R.; El Abedin, S. Z.; Atkin, R. *J. Phys. Chem. B* **2009**, *113*, 7049-7052.
- (21) Mezger, M.; Schroder, H.; Reichert, H.; Schramm, S.; Okasinski, J. S.; Schoder, S.; Honkimaki, V.; Deutsch, M.; Ocko, B. M.; Ralston, J.; Rohwerder, M.; Stratmann, M.; Dosch, H. *Science* **2008**, *322*, 424-428.
- (22) Bazant, M. Z.; Storey, B. D.; Kornyshev, A. A. *Phys. Rev. Lett.* **2011**, *106*, 046102.

- (23) Fedorov, M. V.; Kornyshev, A. A. *J. Phys. Chem. B* **2008**, *112*, 11868-11872.
- (24) Fedorov, M. V.; Kornyshev, A. A. *Electrochim. Acta* **2008**, *53*, 6835-6840.
- (25) Sieffert, N.; Wipff, G. *J. Phys. Chem. B* **2007**, *111*, 7253-7266.
- (26) Lynden-Bell, R. M.; Frolov, A. I.; Fedorov, M. V. *Phys. Chem. Chem. Phys.* **2012**, *14*, 2693-2701.

## Chapter 7. Concluding Remarks

Ionic liquids containing cyano-functionalized anions of varying symmetry from linear to tetrahedral, such as thiocyanate  $[\text{SCN}]^-$ , dicyanamide  $[\text{DCA}]^-$ , tricyanomethanide  $[\text{TCM}]^-$ , and tetracyanoborate  $[\text{TCB}]^-$  have been characterized at the gas-liquid and solid-liquid interface.

Using a nonlinear, surface-sensitive vibrational technique, SFG, in combination with bulk-sensitive techniques such as FTIR and Raman spectroscopy, anions from ionic liquids  $[\text{BMIM}][\text{DCA}]$ ,  $[\text{BMIM}][\text{TCM}]$ , and  $[\text{EMIM}][\text{TCB}]$  have been found to be significantly tilted from the surface plane at the gas-liquid interface. However, the linear  $[\text{SCN}]^-$  in  $[\text{BMIM}][\text{SCN}]$  exhibited poor ordering, as seen in the absence of its C–N stretching mode in the SFG vibrational spectra. The cation orientation was independent of the type of cyano-containing anion. Moreover, a similar arrangement at the surface as reported in previous studies was found, with the imidazolium ring lying flat at the surface, and the alkyl chains pointing towards the gas phase.

Based on the behavior observed at two solid salt surfaces with a different inherent surface charge, namely,  $\text{BaF}_2(111)$  single crystal and solid  $\text{NaCl}\{100\}$ , molecular-level interactions involved in salts of different physical properties (liquid vs. solid at room temperature) have been presented. SFG data proved that ionic liquid counter-ions adsorb to the surface of the solid depending on its inherent surface charge:  $[\text{BMIM}]^+$  cations adhered closely *via* Coulombic interactions to the negatively-charged  $\text{NaCl}\{100\}$  surface, while  $[\text{SCN}]^-$ ,  $[\text{TCM}]^-$ , and  $[\text{DCA}]^-$  anions revealed a strong electrostatic affinity to the positively-charged  $\text{BaF}_2(111)$  surface. Moreover, studies showed that ions in the liquid

remain oriented within the first layer adjacent to the surface but not beyond. These findings were consistent with a Helmholtz-like electric double layer at the interface of the salts.

On the other hand, a specific interaction has been observed at the  $\text{BaF}_2(111)$ –[EMIM][TCB] interface, in which a strongly-bound layer of anions populating the first layer resulted to a much larger counter-ion charge delivered near the crystal salt surface than required to effectively neutralize the initial surface charge from the crystal. As a result, strong resonances from the cation were observed at the  $\text{BaF}_2(111)$  surface, suggesting a more complicated structure of the double layer at the interface, than a simple Helmholtz-type model. Overscreening and layering effects up to the second layer observed at this interface were supported by the evidence seen for the  $\text{BaF}_2(111)$ –[BMIM][SCN] system. In the latter case,  $[\text{BMIM}]^+$  cation (in [BMIM][SCN]) exhibited unusually strong resonances in the C–N stretching region, which were complemented by relatively medium intensity resonances in the C–H stretching region, suggesting a strongly-bound anion in the first layer, with partial ordering of cations in the second layer.

## APPENDIX A

### PHOSPHONIUM IONIC LIQUIDS

#### I. SFG of Tetraalkylphosphonium-based Ionic Liquids at the Air-Liquid Interface

##### Introduction

One important advantage of phosphonium ionic liquids is the fact that they are readily prepared at low cost.<sup>1</sup> As opposed to imidazolium-based ionic liquids, tetraalkylphosphonium salts do not have acidic protons or aromatic rings such that the potential for interaction with various solutes is little.<sup>2</sup> Consequently, better lubrication and anti-wear ability is observed upon substitution of the imidazolium ring with a phosphonium cation as alkylimidazoliums cause corrosion of substrates when used as lubricants.<sup>3</sup> Compared to quaternary nitrogen-based cations, phosphonium cations tend to exhibit higher thermal stability<sup>4</sup> and decompose completely to volatile products in a single step leaving no significant residues.<sup>5</sup>

The structures of ionic liquids studied in this work are illustrated in Fig. A-1. Samples include a series of six alkyltrioctylphosphonium chlorides, in which the fourth alkyl chain is systematically varied from  $n = 4, 5, 8, 10, 12,$  and  $14$ . Tetraoctylphosphonium chloride,  $[P_{8888}]Cl$ , represents the symmetrical cation in the sequence. Moreover, methyl(diethyl)butylphosphonium bis{(trifluoromethyl)sulfonyl}-amide, which has a relatively low symmetry compared to all the other cations is also included in this work, as well as cyano-functionalized ionic liquids namely, trioctyl(5-cyanopentyl)phosphonium bromide, trihexyl(3-cyanopropyl)phosphonium bromide, and

tetradecyl(tri-*n*-hexyl)phosphonium tetracyanoborate. The progression and variation in the sequence of all ionic liquids involved in this work, clearly provides a crucial understanding of the surface chemistry of phosphonium-based ionic liquids.

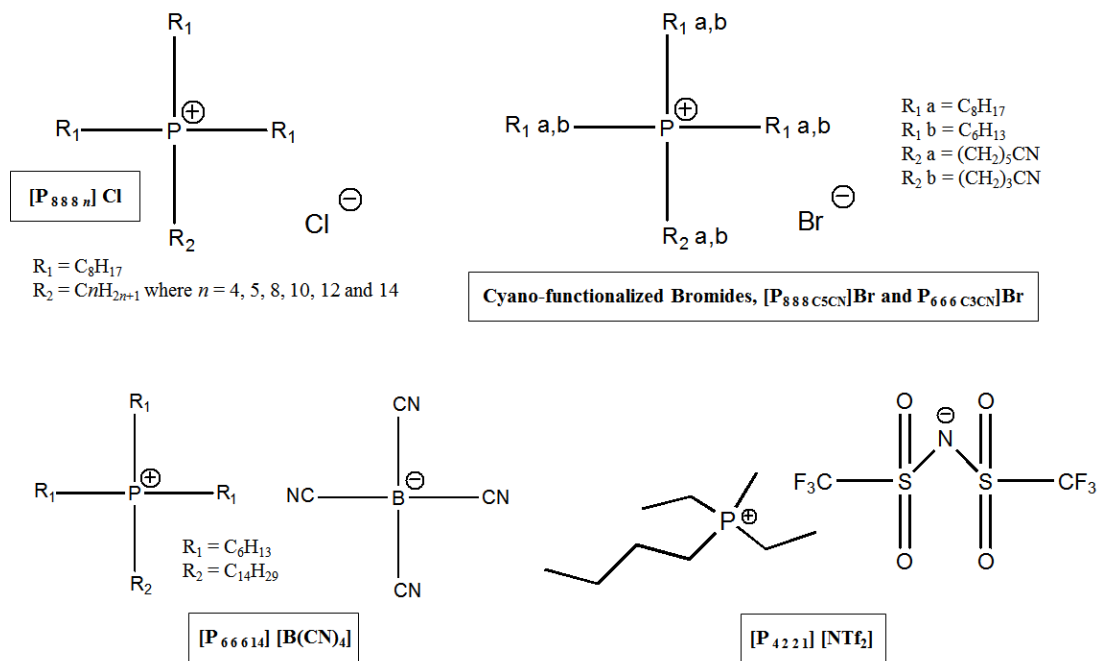


**Fig. A-1.** Structures of the ionic liquids investigated, which includes a series of six different alkyltrioctylphosphonium chlorides, trioctyl(5-cyanopentyl)phosphonium bromide, trihexyl(3-cyanopropyl)phosphonium bromide, tetradecyl(tri-*n*-hexyl)-phosphonium tetracyanoborate and methyl(diethyl)butylphosphonium bis{(trifluoromethyl)sulfonyl} amide.

In order to assign the vibrational resonances observed in tetraoctylphosphonium chloride, [P<sub>8888</sub>]Cl series, three ionic liquids were further studied, namely, tetrabutylphosphonium chloride [P<sub>4444</sub>]Cl, tributyl(4-methoxybutyl)phosphonium chloride [P<sub>444-BuOMe</sub>]Cl, and trioctyl(2-methoxyethyl)phosphonium chloride [P<sub>888-EtOMe</sub>]Cl. The structures are shown in Fig. A-2.

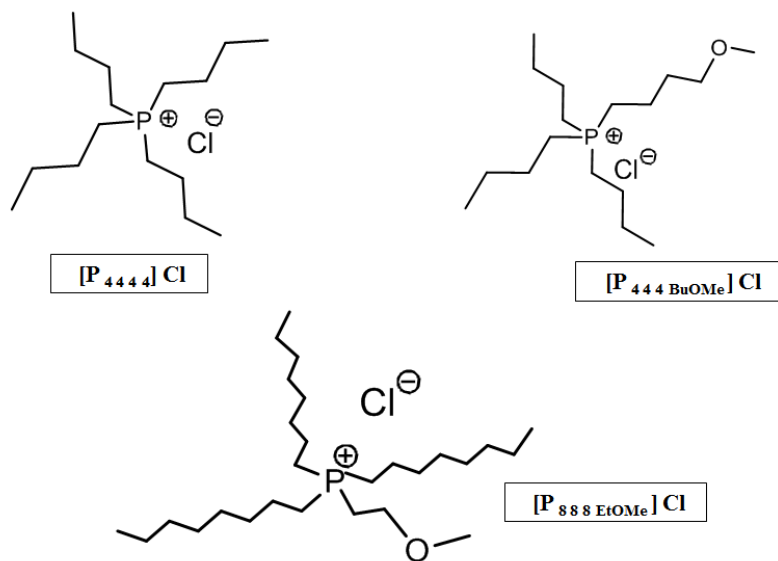


**Fig. A-2.** Structures of the ionic liquids tetrabutylphosphonium chloride  $[P_{4444}]Cl$ , tributyl(4-methoxybutyl)phosphonium chloride  $[P_{444-BuOMe}]Cl$  and trioctyl(2-methoxyethyl)phosphonium chloride  $[P_{888-EtOMe}]Cl$ .

## Experimental Method

**Samples.** All phosphonium-based ionic liquids were synthesized and fully characterized by Adamova, *et al.*<sup>6</sup> except for  $P_{4,2,2,1}[NTf_2]$  and  $P_{6,6,6,14}[B(CN)_4]$ , which were R&D samples provided by Cytec Industries (Canada) and Merck.  $[P_{4444}]Cl$ ,<sup>7</sup>  $[P_{444-BuOMe}]Cl$  and  $[P_{888-EtOMe}]$  were synthesized by Dr. Natalia Plechkova of Queen's University Ionic Liquid Laboratories (QUILL). Extensive characterization included NMR spectroscopy ( $^1H$ ,  $^{13}C$  and  $^{31}P$  NMR), mass spectrometry, elemental carbon and hydrogen, halide and water contents, differential scanning calorimetry (DSC), thermogravimetric analysis (TGA), density and viscosity measurements. Moreover, molar volumes as a function of temperature were estimated via a group contribution method as well as thermal expansion coefficients calculated from density data. A brief description of synthetic details is provided below. The synthesis of  $[P_{8,8,8,4}]Cl$  involved the use of chloroalkanes of mid-range volatility requiring the use of a microwave reactor while thermal reflux was employed for all remaining alkyltrioctylphosphonium chloride samples.

**Synthesis of  $[P_{8,8,8,4}]Cl$ .** Trioctylphosphine (1 mol eq.) was mixed with chloroalkane (1.1 mol eq.) in a glass microwave vial containing a stirring bar, and kept under nitrogen atmosphere. Transfer of the mixture to the shield vessel utilized rubber septa (Suba-Seal<sup>®</sup>) providing air and moisture-tight seal, and a glove bag (Atmosbag<sup>®</sup>) to prevent atmospheric exposure. The mixture was then placed inside the microwave cavity under the following reaction conditions: Ramp (5 min) to 180 °C; hold at 180 °C (30 min), medium stirring, 500 W (50% max) power; pressure reached 3 bars; average sample volume, 16 cm<sup>3</sup>. Completed reaction was then cooled down, after which the product was

transferred to a round-bottomed flask and dried *in vacuo* for 48 hours at 65 °C. The final product obtained at 97% yield was a colourless liquid with water content reported to be at 425 ppm.

**Synthesis of [P<sub>8 8 8 n</sub>]Cl, n = 5, 8, 10, 12 and 14.** Trioctylphosphine (1 mol eq.) and chloroalkane (1.1 mol eq.) were placed in a round-bottomed flask. The mixture was stirred and heated in a silicone oil bath up to 145 °C under a reflux condenser connected to a Schlenk line continually flushed with nitrogen. The reaction took 12 to 16 hours depending on the alkyl chain length of the chloroalkane used. To remove excess 1-chloroalkane, (C<sub>n</sub>H<sub>2n+1</sub>Cl), where n ≥ 5, the product was dissolved in hexane and extracted with water. Finally, the product was dried *in vacuo* for 48 hours prior to analysis. All ionic liquids were synthesized at 89-96 % yield. All samples were obtained as colourless liquids except for [P<sub>8 8 8 14</sub>]Cl which appeared to be pale yellow. Water content values ranged from 411 ppm ([P<sub>8 8 8 5</sub>]Cl) to 218 ppm ([P<sub>8 8 8 14</sub>]Cl), with values decreasing as the length of the fourth alkyl chain was increased.

**Synthesis of [P<sub>8 8 8 C5CN</sub>]Br and [P<sub>6 6 6 C3CN</sub>]Br.** A similar procedure for the synthesis of [P<sub>8 8 8 n</sub>]Cl was followed using 1 mol eq. of trialkylphosphine and 1.1 mol eq. of bromoalkanenitrile. However, the reaction mixture was heated up to 110 °C instead of 145 °C and maintained for 12 hours. The excess bromoalkanenitrile starting material, was separated from the product by dissolving the mixture in hexane, followed by extraction with water. Finally, both products were dried *in vacuo* for 48 hours prior to analysis.

**Sample Preparation Prior to SFG Measurements.** Fully characterized samples were sent directly from QUILL Research Centre in Belfast and were used as received. All ionic liquid samples were contained in a custom-designed SFG cell<sup>8</sup> made of Pyrex® glass and equipped with high-vacuum valves and O-ring fittings. Drying in high vacuum atmospheres in a custom-built glass vacuum line, have been described in Section 3.2. Samples were pumped until a desired pressure of  $\leq 5 \times 10^{-5}$  Torr was reached, and occasionally heated (up to less than 60 °C) with a heat gun to hasten the drying process. The samples are known to be thermally stable at the heating temperature used.

Specifically for [P<sub>4 2 2 1</sub>][NTf<sub>2</sub>] sample, a more constant heating up to less than 60 °C using an insulated heating tape was necessary as the sample tended to solidify at room temperature when atmospheric moisture was directly in contact with it. When sufficiently dry however, [P<sub>4 2 2 1</sub>][NTf<sub>2</sub>] remained liquid at room temperature. Moreover, [P<sub>4 4 4 4</sub>][Cl] has a melting point of 62-66 °C, such that drying in the vacuum line was done with heating above the melting temperature and all SFG measurements were done at ~70 °C. Once the desired pressure was reached, the samples while attached to the vacuum line were back-filled with ultra-high purity nitrogen gas to a slight overpressure prior to SFG measurements.

**SFG Spectroscopy System.** The SFG spectrometer setup has been described in section 3.3. A picosecond pulsed Nd:YAG laser with a fundamental 1064-nm output is used to pump an optical parametric generator/amplifier (OPG/OPA, LaserVision) system to generate a fixed visible (532-nm) and frequency tunable IR (2000-4000 cm<sup>-1</sup>) beam. The fixed visible and IR beams follow a co-propagating geometry and are overlapped at the

liquid surface at an angle of 50° and 60° from the surface normal, respectively. The SFG signal is collected via a gated integrator and computer-controlled using LabVIEW software.

**Data Collection and Analysis.** All spectra were calibrated using polystyrene, gold and hexadecanol standards described in Section 3.3.5. SFG data collection procedures have been outlined in Section 3.4.2. Data were collected at an average of 5 scans per polarization combination at a scan rate of 1 cm<sup>-1</sup>/s using 20 laser shots per point. Using equation 2-15 as a fitting function, spectra were fitted via Origin 7.0 Professional nonlinear curve fitting. Four different polarization combinations were taken for all ionic liquid samples, namely, *ssp*, *ppp*, *sps*, and *pss*.

## Results and Discussion

**Alkyltrioctylphosphonium Chloride Series.** The sum frequency spectra in the C–H stretching region of 2750-3100  $\text{cm}^{-1}$  taken at four different polarization combinations for all alkyltrioctylphosphonium chlorides,  $[\text{P}_{888n}]\text{Cl}$ , where  $n = 4, 5, 8, 10, 12$  and  $14$  are displayed in Fig. A-3, offset in the same plot.

It is important to note in the spectra as presented, that the variation in this series of samples allows for determining characteristic changes in the vibrational bands as the number of carbons in the fourth alkyl substituent is increased or decreased from the perspective of the fully symmetrical cation analog,  $[\text{P}_{8888}]\text{Cl}$ . Vibrational mode assignments for a series of alkylammonium and alkylpyrrolidinium-based ionic liquids have been discussed previously<sup>14</sup> and are presented in Table A-1. The peaks for all vibrational modes observed in this study are summarized in Table A-2.

In *ssp* polarization, the spectra show vibrations corresponding to  $d^+$ ,  $r^+$ ,  $d^+_{FR}$  and  $r^+_{FR}$  modes. An additional mode observed in the spectra, which is assigned to the  $r^-$  mode, while absent for the series with  $n = 4, 5, 8,$  and  $10$ , is visible for the last two alkyltrioctylphosphonium chlorides with  $n = 12$  and  $14$ . Moreover, for  $n = 4, 5, 8,$  and  $10$ , the  $r^+$  mode is the most intense band while for  $n = 12$  and  $14$ , there is a sharp switch in the intensity of the bands such that the  $d^+$  mode surpasses the intensity of the  $r^+$  mode. Along with this switch is the appearance of the  $r^-$  mode and noticeable signal enhancement of the  $d^+_{FR}$  mode, whose peak occurred as a mere shoulder initially for members in the series with alkyl chains up to  $n = 10$ .

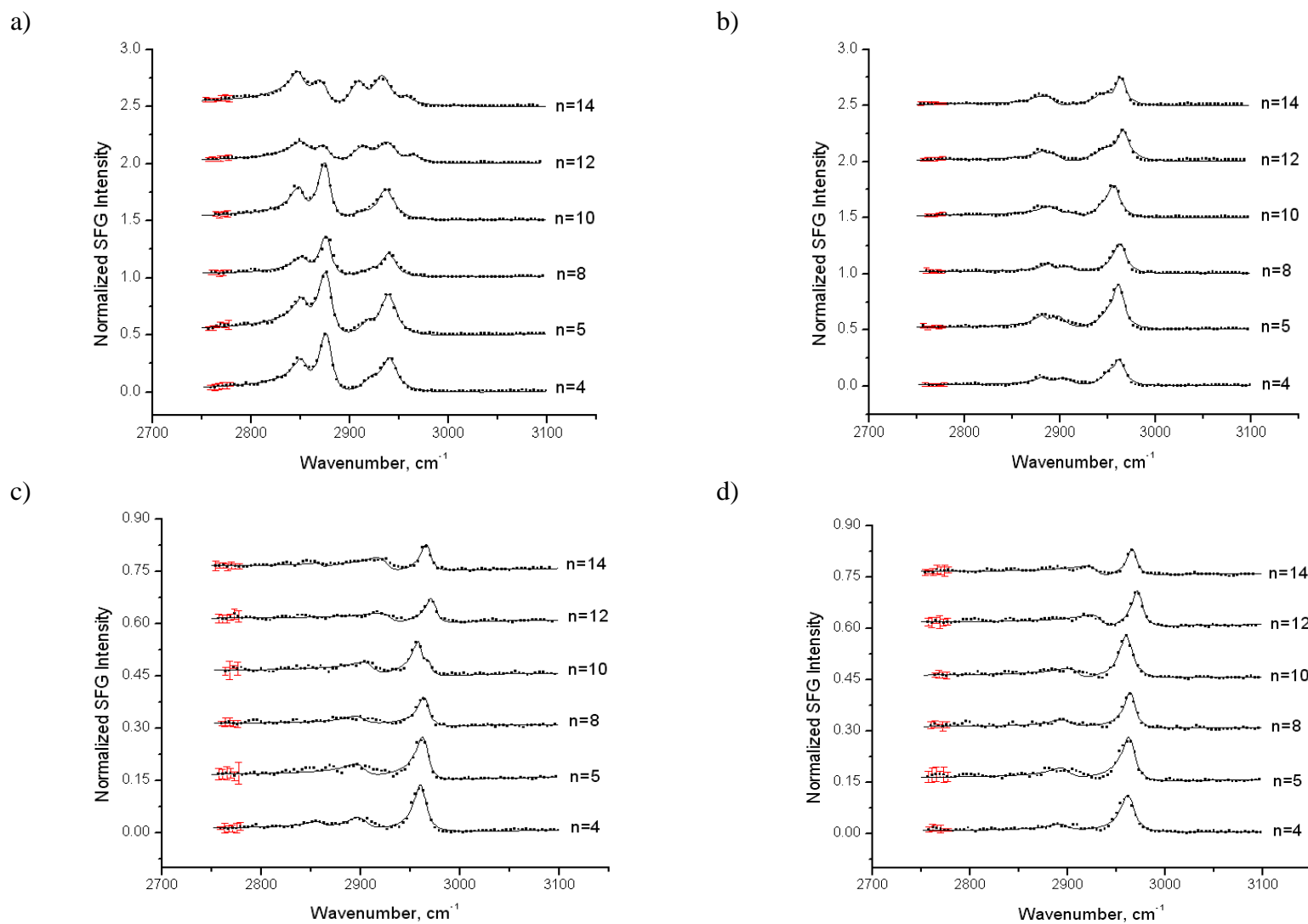


**Fig. A-3.** Sum frequency spectra of alkyltriethylphosphonium chlorides,  $[\text{P}_{88n}]\text{Cl}$  where  $n = 4, 5, 8, 10, 12$  and  $14$  at polarization combinations ssp (a), ppp (b), sps (c), and pss (d). The offsets are 0.50, 0.50, 0.15 and 0.15, respectively.

**Table A-1.** Vibrational Assignments for Alkylammonium and Alkylpyrrolidinium ILs Used to Assign Spectra of Alkylphosphonium ILs <sup>14</sup>

Vibrational Mode	Wavenumber (cm <sup>-1</sup> )
symmetric methyl stretch, $r^+$	2870–2880
antisymmetric methyl stretch, $r^-$	2960–2970
methyl Fermi resonance, $r^+_{FR}$	2931–2942
symmetric methylene stretch, $d^+$	2845–2858
antisymmetric methylene stretch, $d^-$	~2910
methylene Fermi resonance, $d^+_{FR}$	~2920

**Table A-2.** Vibrational Modes Observed for Alkyltrioctylphosphonium Chloride Ionic Liquids

$[P_{888}n]Cl$	Peak Assignment (frequency, cm <sup>-1</sup> )													
	$d^+$		$r^+$			$d^-$		$d^+_{FR}$		$r^+_{FR}$		$r^-$		
	<i>ssp</i>		<i>ssp</i>	<i>ppp</i>	<i>ppp</i>	<i>sps</i>	<i>ssp</i>	<i>ppp</i>	<i>ssp</i>	<i>ppp</i>	<i>ssp</i>	<i>ppp</i>	<i>sps</i>	
$n = 4$	2853		2877	2884	2906	2901	2924	–	2940	2952	–	2962	2961	
5	2854		2877	2882	2900	2901	2920	–	2939	2950	–	2962	2964	
8	2855		2879	2890	2909	2899	2923	–	2942	–	–	2963	2965	
10	2851		2876	2898	–	2911	2913	2917	2937	–	–	2959	2959	
12	2854		2875	2883	–	2930	2915	2897	2938	2950	2963	2965	2972	
14	2851		2872	2879	–	2925	2910	2890	2932	2948	2955	2963	2967	

( $r^+$ ) methyl symmetric stretch, ( $r^+_{FR}$ ) Fermi Resonance of methyl symmetric, ( $r^-$ ) methyl antisymmetric stretch,  
( $d^+$ ) methylene symmetric stretch, ( $d^+_{FR}$ ) Fermi Resonance of methylene symmetric, ( $d^-$ ) methylene antisymmetric stretch

In *ppp* polarization, the spectra are dominated by the  $r^-$  mode, being the most intense band. The  $r_{FR}^+$  mode, while barely visible for  $n = 4, 5, 8,$  and  $10$  occurs as a noticeable shoulder for  $n = 12$  and  $14$ . As for bands of weak intensity present in the *ppp* spectra,  $d_{FR}^+$  modes for  $n = 10, 12,$  and  $14$  can be seen. However, for  $n = 4, 5,$  and  $8,$   $d_{FR}^+$  modes are absent and only the  $d^-$  mode can be observed. In particular, the symmetrical  $[P_{8\ 8\ 8}]Cl$  has bands assigned to the  $r^+$  and  $d^-$  occurring as a well-defined split as opposed to a broad band.

The *pss* and *sps* spectra likewise show the  $r^-$  mode as the most intense peak as well as a weak contribution from the  $d^-$  peak. For  $[P_{8\ 8\ 8\ 10}]Cl$  in the *sps*, a residual peak at  $2968\text{ cm}^{-1}$  is additionally observed.

**Tetraalkylphosphoniums with other anions.** Fig. A-4 displays the sum frequency spectra of  $[P_{8\ 8\ 8}C_5CN]Br,$   $[P_{6\ 6\ 6}C_3CN]Br,$   $[P_{4\ 2\ 2\ 1}][NTf_2]$  and  $[P_{6\ 6\ 6\ 14}][B(CN)_4]$  at four different polarization combinations and offset in the same plot. From this set of spectra, we expect changes in the spectral profile as a cyano-group is added to the cation moiety as well as changes coming from the substitution of the chloride or bromide anions with more bulky constituents such as bis{(trifluoromethyl)sulfonyl}amide,  $[NTf_2]^-$  and tetracyanoborate  $[B(CN)_4]^-$ . Also, particularly interesting in this section is the addition of the highly unsymmetrical  $[P_{4\ 2\ 2\ 1}][NTf_2]$  to the series. Table A-3 summarizes the peak assignments for this particular set.

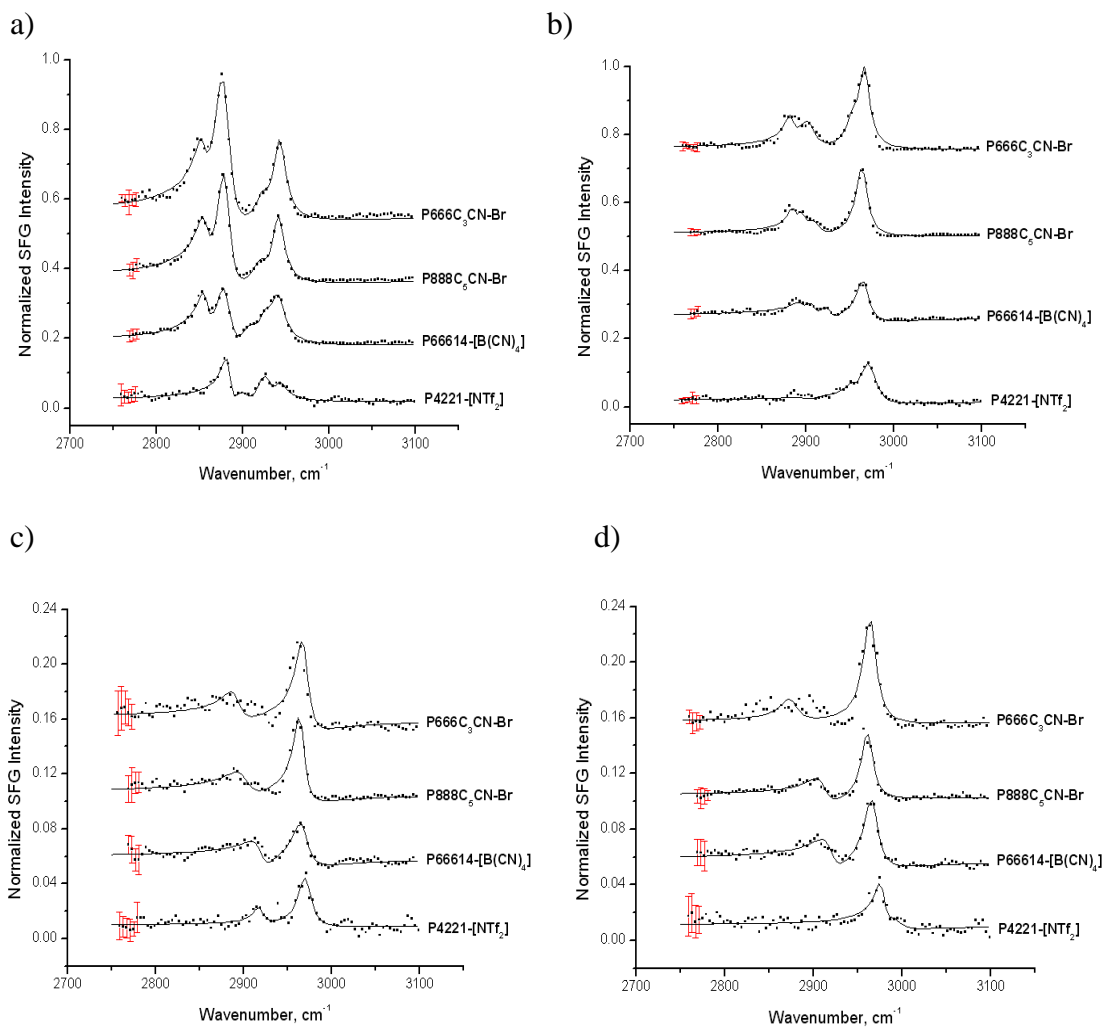


**Fig. A-4.** Sum frequency spectra of tetraalkylphosphonium ionic liquids with various anions at polarization combinations ssp (a), ppp (b), sps (c), and pss (d). The offsets are 0.18, 0.25, 0.05, and 0.05, respectively.

**Table A-3.** Vibrational Modes Observed for Tetraalkylphosphonium Ionic Liquids with Various Anions

Ionic Liquid	Peak Assignment (frequency, $\text{cm}^{-1}$ )											
	$d^+$		$r^+$		$d^-$		$d^+_{FR}$		$r^+_{FR}$		$r^-$	
	<i>ssp</i>	<i>ssp</i>	<i>ppp</i>	<i>ppp</i>	<i>sps</i>	<i>ssp</i>	<i>ppp</i>	<i>ssp</i>	<i>ppp</i>	<i>ssp</i>	<i>ppp</i>	<i>sps</i>
$[\text{P}_{666}\text{C}_3\text{CN}]\text{Br}$	2855	2879	2883	2903	2892	2925	–	2942	2954	–	2966	2969
$[\text{P}_{888}\text{C}_5\text{CN}]\text{Br}$	2857	2880	2886	2896	2901	2922	2910	2940	–	–	2964	2965
$\text{P}_{66614}[\text{B}(\text{CN})_4]$	2858	2880	–	–	2920	{2909}	{2909}	2939	2945	–	2966	2968
$\text{P}_{4221}[\text{NTf}_2]$	–	2884 <sup>a</sup> 2901 <sup>b</sup>	–	2900	2901	–	–	2925 <sup>c</sup> 2940 <sup>d</sup>	2954	–	2973	2965

<sup>a</sup>Butyl and ethyl<sup>c</sup>Ethyl<sup>b</sup>Terminal methyl attached to P<sup>d</sup>Butyl $(r^+)$  methyl symmetric stretch,  $(r^+_{FR})$  Fermi Resonance of methyl symmetric,  $(r^-)$  methyl antisymmetric stretch, $(d^+)$  methylene symmetric stretch,  $(d^+_{FR})$  Fermi Resonance of methylene symmetric,  $(d^-)$  methylene antisymmetric stretch

**[P<sub>8 8 8</sub> C<sub>5</sub>CN]Br and [P<sub>6 6 6</sub> C<sub>3</sub>CN]Br.** The *ssp* spectra for both compounds appear very similar to that of the [P<sub>8 8 8 n</sub>]Cl series where  $n = 4, 5, 8,$  and  $10$  such that  $d^+, r^+, d^+_{FR},$  and  $r^+_{FR}$  modes dominate the spectra. Similarly, the  $r^+$  mode is found to be the most intense just as it was seen in alkyltrioctylphosphonium chlorides for up to  $n = 10$ . This shows that variation of the fourth alkyl chain by the addition of a cyano functional group has little or no effect on the average orientation of the cation chain contributing to the observed vibrational frequency, noting the similar ionic radii of the anions, Br and Cl. For the *ppp* combination, the vibrational modes appear similar as well when compared to the alkyltrioctylphosphonium chlorides except for the appearance of two different vibrational modes. All three modes namely, the  $r^+, d^-,$  and  $r^-$  modes are present in both ionic liquids, however the  $r^+_{FR}$  mode at  $2954\text{ cm}^{-1}$  is only observed for [P<sub>6 6 6</sub> C<sub>3</sub>CN]Br. On the other hand, the  $d^+_{FR}$  mode at  $2910\text{ cm}^{-1}$  which is absent in [P<sub>6 6 6</sub> C<sub>3</sub>CN]Br can be observed in [P<sub>8 8 8</sub> C<sub>5</sub>CN]Br. Lastly, the *sps* and *pss* spectra for both ionic liquids appear similarly dominated by  $d^-$  and  $r^-$  modes with the latter being much more intense.

**[P<sub>4 2 2 1</sub>][NTf<sub>2</sub>].** Four distinct peaks are visible in the *ssp* spectra for this highly unsymmetrical analog. The peak at  $2884\text{ cm}^{-1}$  assigned to the  $r^+$  mode contain contributions coming from both butyl and ethyl groups attached to the cation. The peak at  $2901\text{ cm}^{-1}$  which is also an  $r^+$  mode, is characteristic for the vibration of the terminal methyl attached to phosphorus as in trimethylphosphine.<sup>15</sup> The peak at  $2925\text{ cm}^{-1}$  is assigned to the  $r^+_{FR}$  mode from the ethyl chains while the peak at  $2945\text{ cm}^{-1}$  comes from the  $r^+_{FR}$  of the butyl chain.<sup>7,13,16</sup> For the *ppp* spectra, the  $r^+_{FR}$  and  $r^-$  modes are visible as

well as the  $d^-$  mode, although appearing within the noise level. For both *sps* and *pss* spectra, the  $r^-$  mode is the most intense, however, the  $d^-$  mode at  $2918\text{ cm}^{-1}$  is only observed in the *sps* combination. Consequently, an additional shoulder at  $2990\text{ cm}^{-1}$  absent in the *sps* spectra is observed in the *pss* combination.

**[P<sub>66614</sub>][B(CN)<sub>4</sub>]**. The *ssp* spectra show five peaks corresponding to four distinct modes. The peak at  $2858\text{ cm}^{-1}$  corresponds to the  $d^+$  mode while the peak at  $2880\text{ cm}^{-1}$  corresponds to the  $r^+$  mode. Two peaks occurring at  $2909$  and  $2927\text{ cm}^{-1}$  are both assigned to one vibrational mode,<sup>17</sup>  $d^+_{FR}$ . The peak at  $2939\text{ cm}^{-1}$  in the *ssp* pertains to the  $r^+_{FR}$  mode. Both peaks at  $2909$  and  $2927\text{ cm}^{-1}$  are also found visible in the *ppp* spectra. In addition, the  $r^+_{FR}$  mode at  $2945\text{ cm}^{-1}$  and the  $r^-$  at  $2966\text{ cm}^{-1}$  are observed. Like all other alkylphosphonium chlorides, the *sps* and *pss* spectra of this compound are dominated by a weak  $d^-$  mode and a much more intense  $r^-$  mode.

**[P<sub>888EtOMe</sub>]Cl and [P<sub>8884</sub>]Cl.**

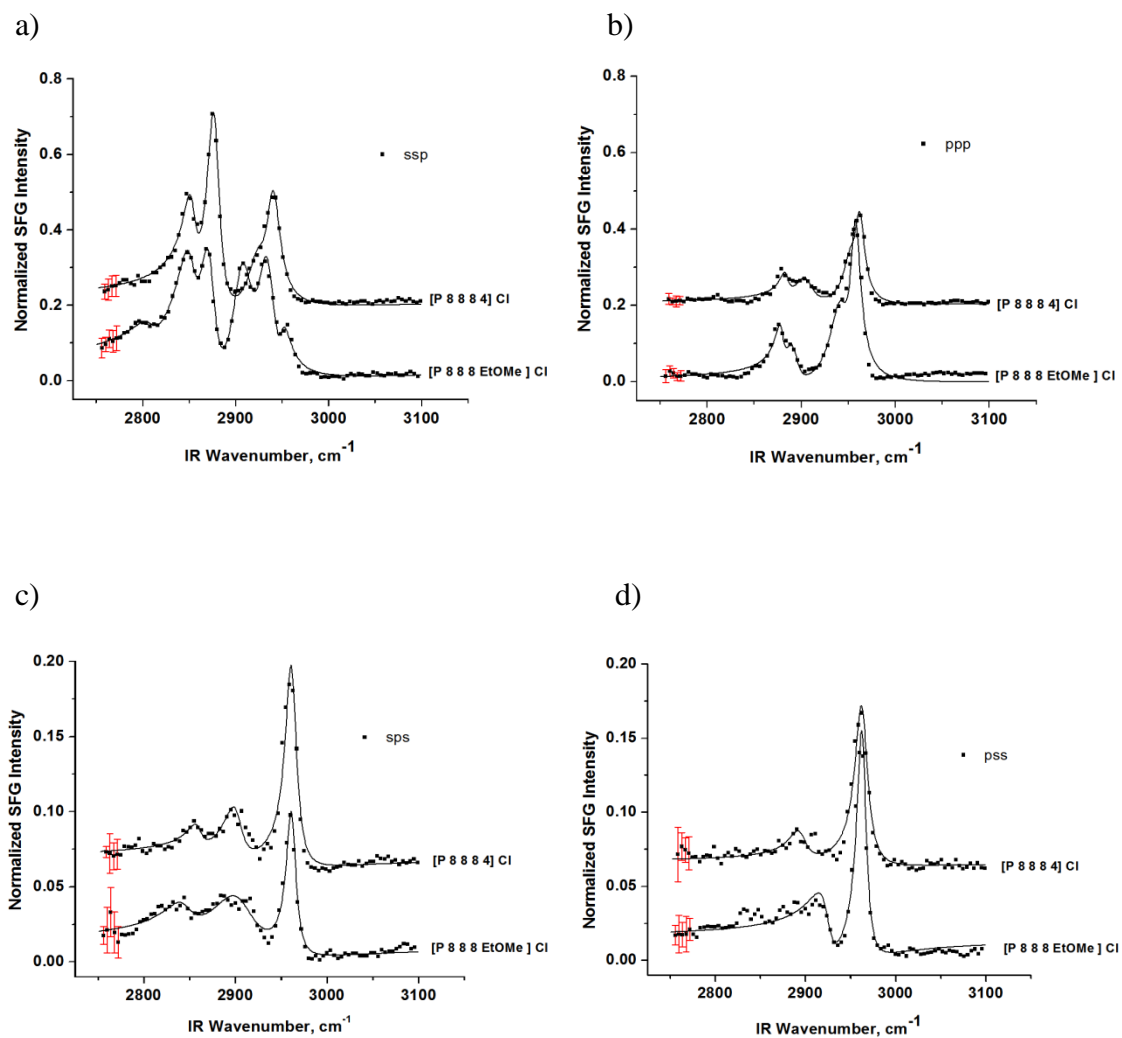


**Fig. A-5.** Sum frequency spectra of [P<sub>888EtOMe</sub>]Cl and [P<sub>8884</sub>]Cl at polarization combinations ssp (a), ppp (b), sps (c), and pss (d). The offsets are 0.20, 0.20, 0.06, and 0.06, respectively.

**[P<sub>4444</sub>]Cl and P<sub>444</sub>BuOMe]Cl.**

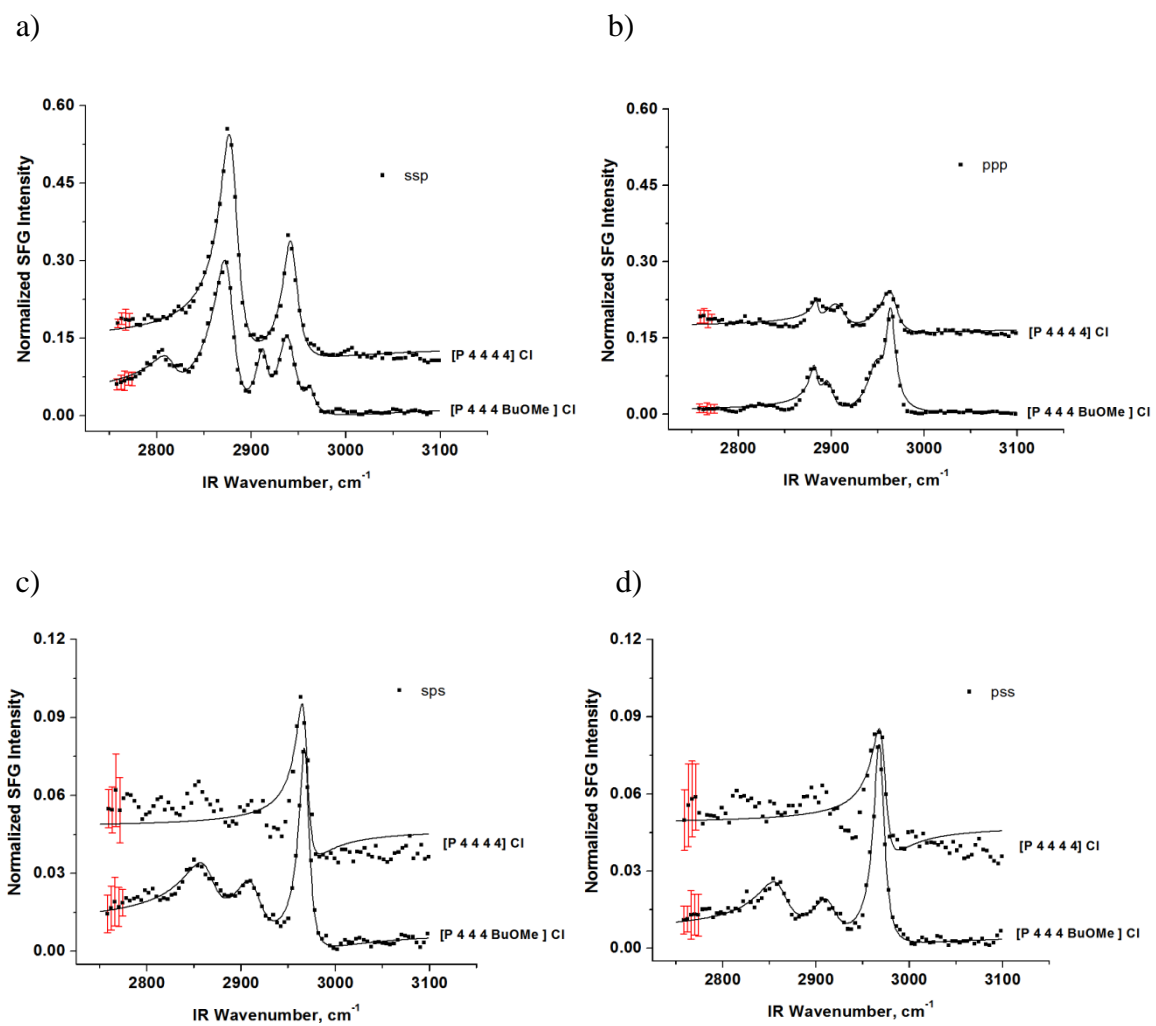


**Fig. A-6.** Sum frequency spectra [P<sub>4444</sub>]Cl and P<sub>444</sub>BuOMe]Cl at polarization combinations ssp (a), ppp (b), sps (c), and pss (d). The offsets are 0.10, 0.15, 0.03, and 0.03, respectively.

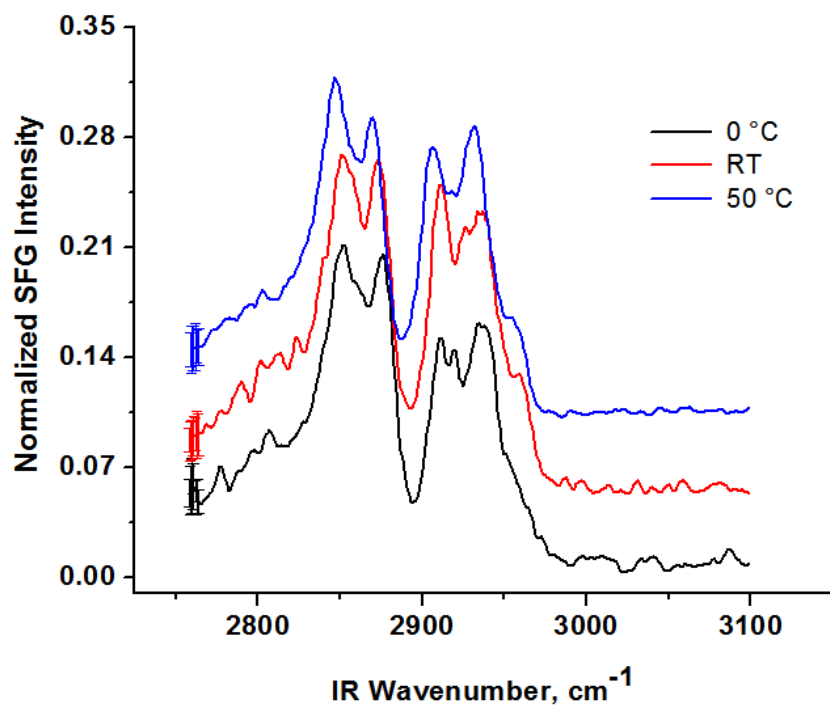


**Fig. A-7.** Sum frequency spectra in *ssp* of [P<sub>8.8</sub>EtOMe]Cl at three different temperatures: 0 °C, room temperature (20 °C), and 50 °C, offset by 0.05 for clarity.

## II. SFG of Tetraalkylphosphonium-based Ionic Liquids at Solid-Liquid Interfaces

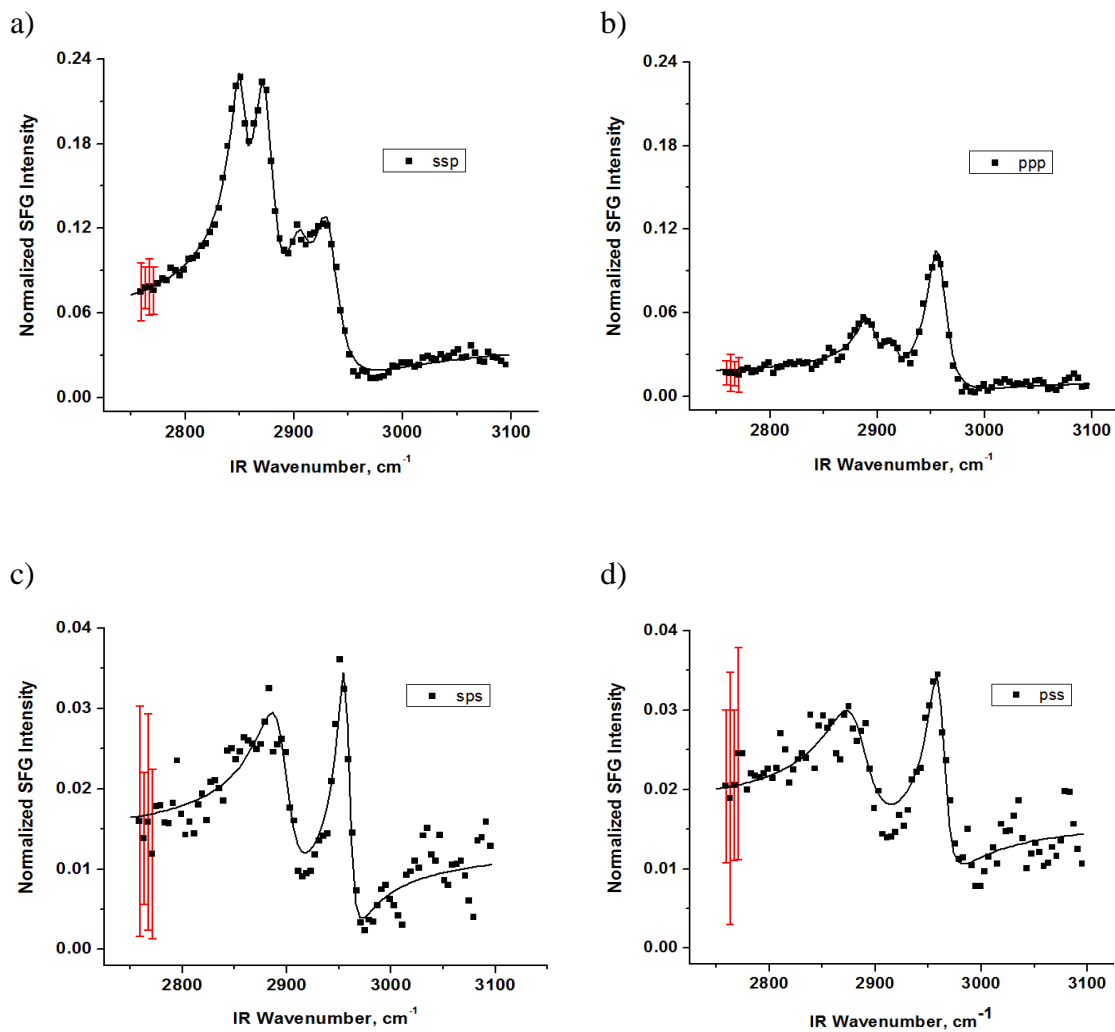


**Fig. A-8.** Sum frequency spectra of  $[P_{66614}][B(CN)_4] - NaCl\{100\}$  interface at *ssp* (a), *ppp* (b), *sps* (c), and *pss* (d) polarization combinations.

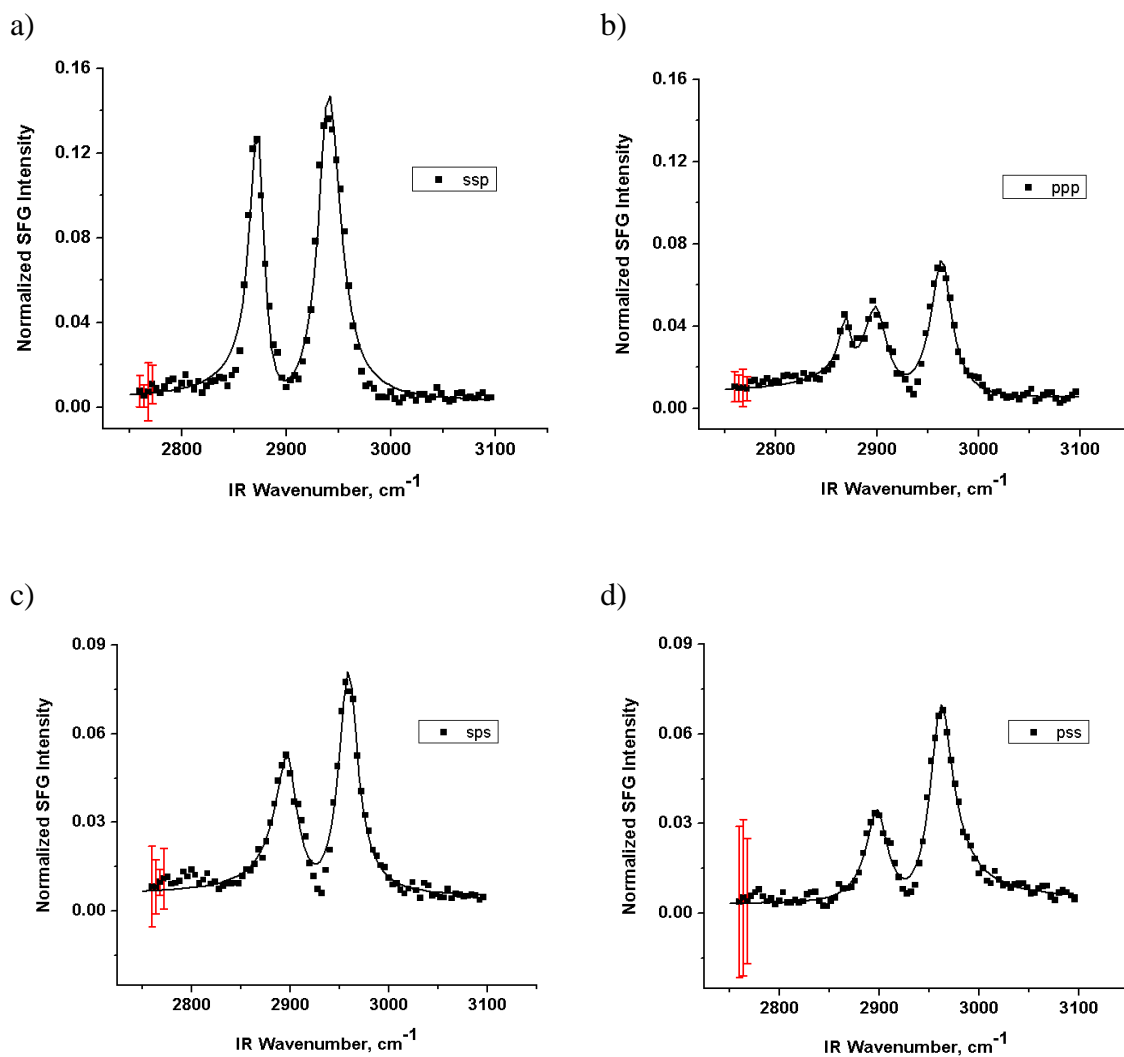


**Fig. A-9.** Sum frequency spectra of [P<sub>6,6,14</sub>] [B(CN)<sub>4</sub>] – BaF<sub>2</sub>(111) interface at *ssp* (a), *ppp* (b), *sps* (c), and *pss* (d) polarization combinations.

## References

- (1) Bradaric, C. J.; Downard, A.; Kennedy, C.; Robertson, A. J.; Zhou, Y. *Green Chem.* **2003**, *5*, 143-152.
- (2) Avent, A. G.; Chaloner, P. A.; Day, M. P.; Seddon, K. R.; Welton, T. J. *Chem. Soc., Dalton Trans.* **1994**, 3405-3413.
- (3) Liu, X.; Zhou, F.; Liang, Y.; Liu, W. *Wear* **2006**, *261*, 1174-1179.
- (4) Xie, W.; Xie, R.; Pan, W.-P.; Hunter, D.; Koene, B.; Tan, L.-S.; Vaia, R. *Chem. Mater.* **2002**, *14*, 4837-4845.
- (5) Wooster, T. J.; Johanson, K. M.; Fraser, K. J.; MacFarlane, D. R.; Scott, J. L. *Green Chem.* **2006**, *8*, 691-696.
- (6) Adamova, G.; Gardas, R. L.; Rebelo, L. P. N.; Robertson, A. J.; Seddon, K. R. *Dalton Trans.* **2011**, *40*, 12750-12764.
- (7) Adamova, G.; Gardas, R. L.; Nieuwenhuyzen, M.; Puga, A. V.; Rebelo, L. P. N.; Robertson, A. J.; Seddon, K. R. *Dalton Trans.* **2011**, *41*, 8316-8332.
- (8) Aliaga, C.; Baldelli, S. *J. Phys. Chem. B* **2007**, *111*, 9733-9740.
- (9) Baldelli, S. *Acc. Chem. Res.* **2008**, *41*, 421-431.
- (10) Baldelli, S. *J. Phys. Chem. B* **2003**, *107*, 6148-6152.
- (11) Santos, C. S.; Baldelli, S. *J. Phys. Chem. B* **2009**, *113*, 923-933.

APPENDIX B  
SUPPLEMENTARY INFORMATION

I. NMR Spectra

Fig. B-1.  $^1\text{H}$ -NMR of [BMIM][SCN] in  $\text{CD}_3\text{CN}$

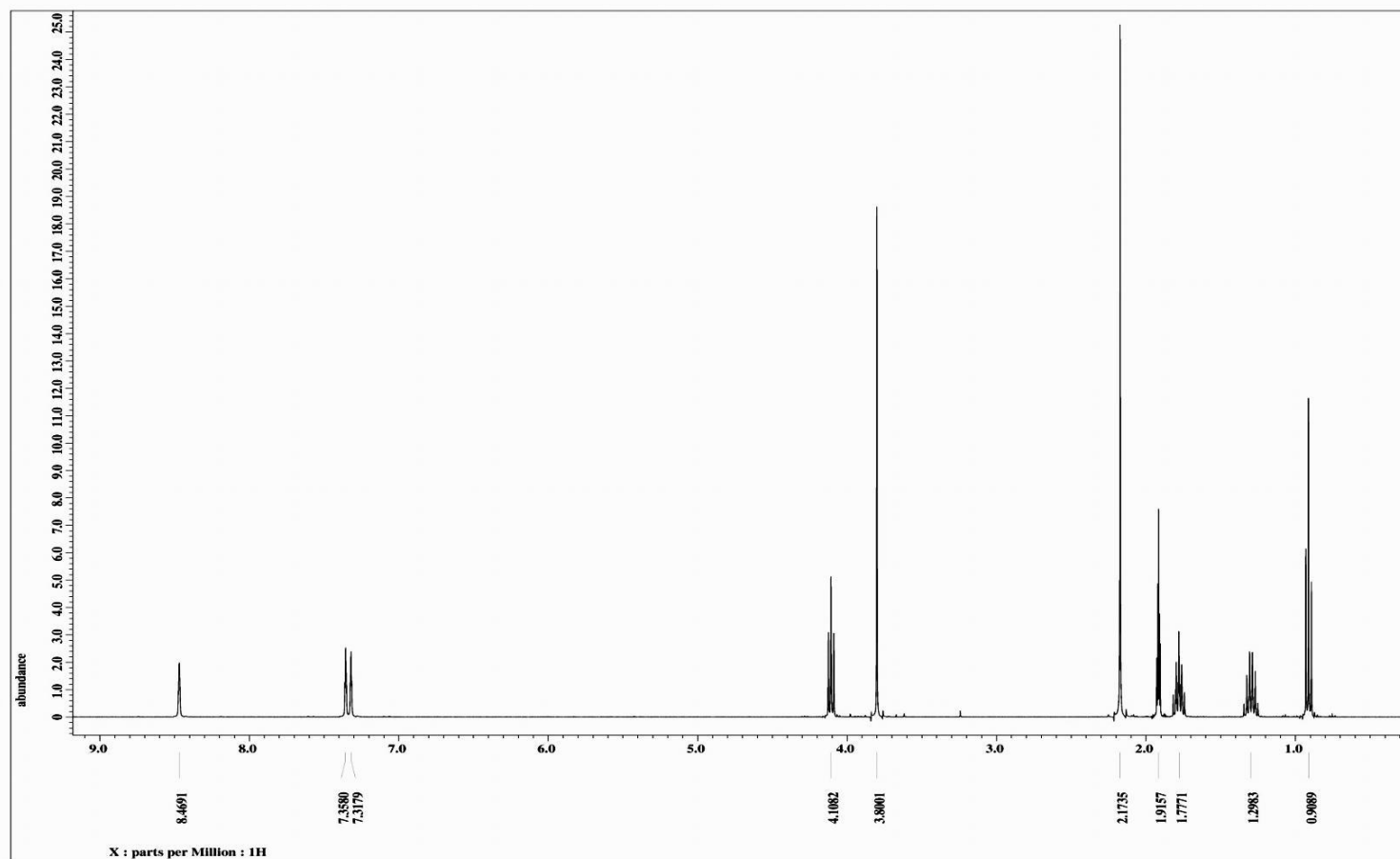


Fig. B-2.  $^{13}\text{C}$ -NMR of [BMIM][SCN] in  $\text{CD}_3\text{CN}$

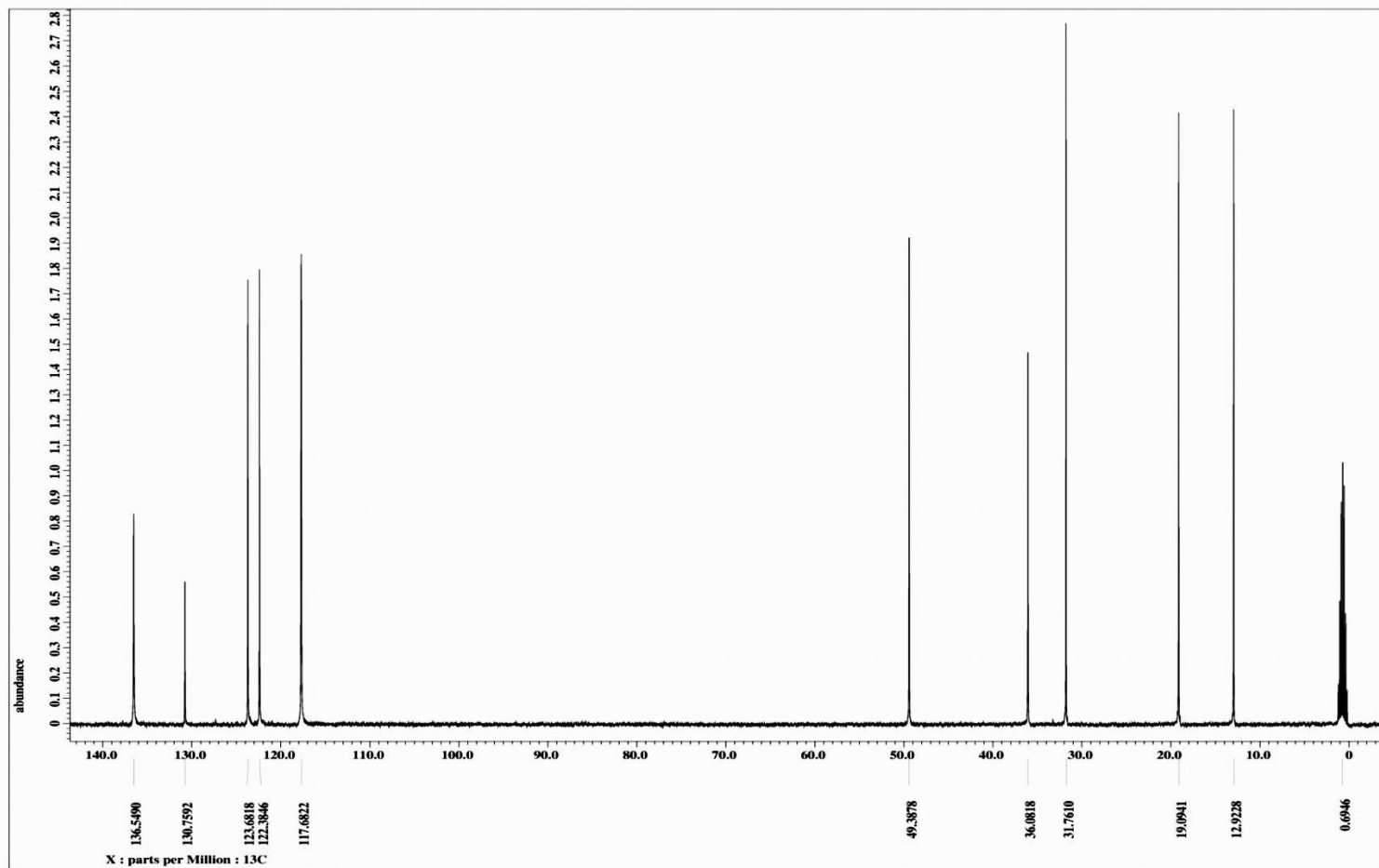


Fig. B-3.  $^1\text{H-NMR}$  of [BMIM][DCA] in  $\text{CDCl}_3$

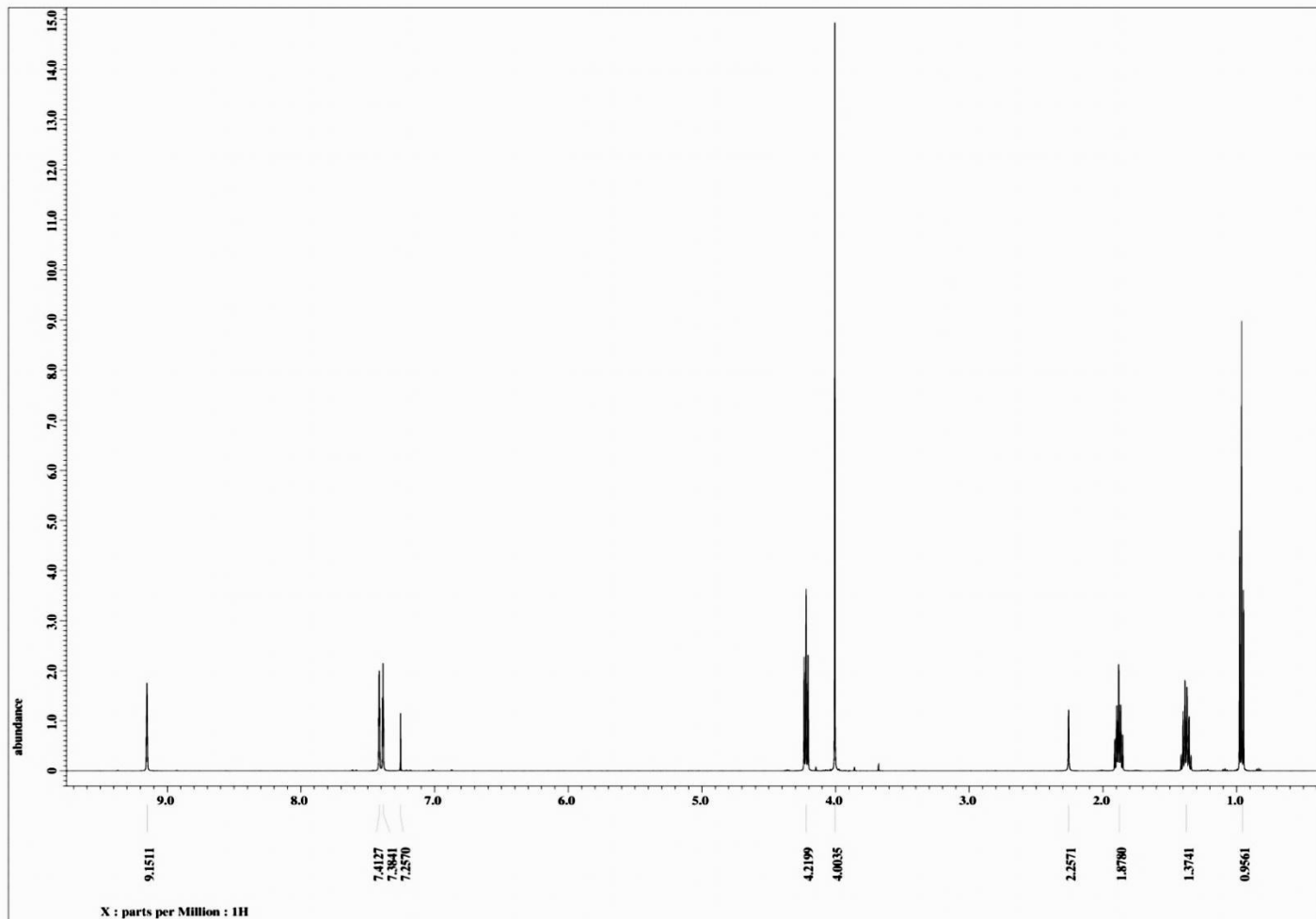


Fig. B-4.  $^{13}\text{C}$ -NMR of [BMIM][DCA] in  $\text{CDCl}_3$

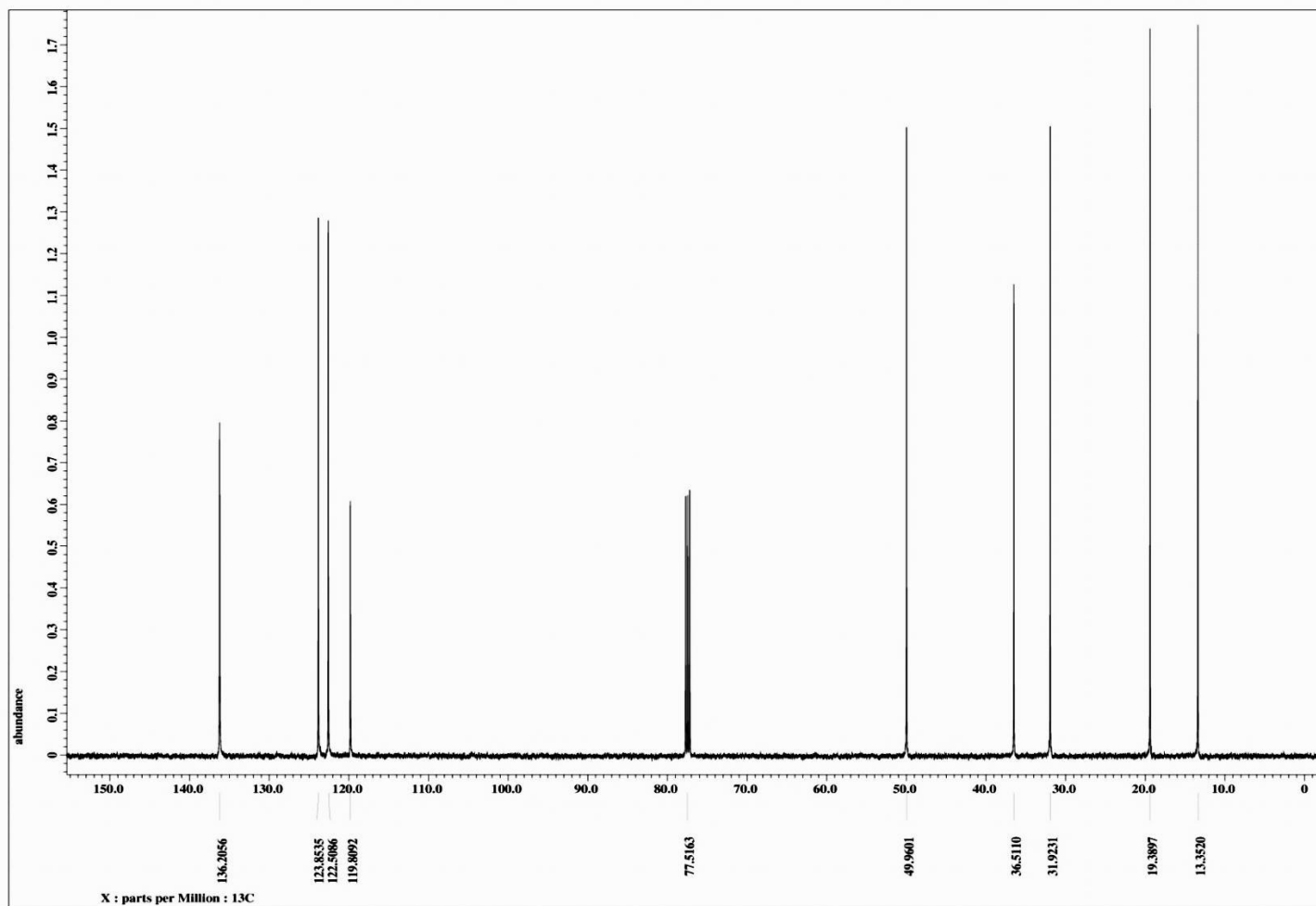


Fig. B-5.  $^1\text{H-NMR}$  of [BMIM][TCM] in  $\text{CD}_3\text{CN}$

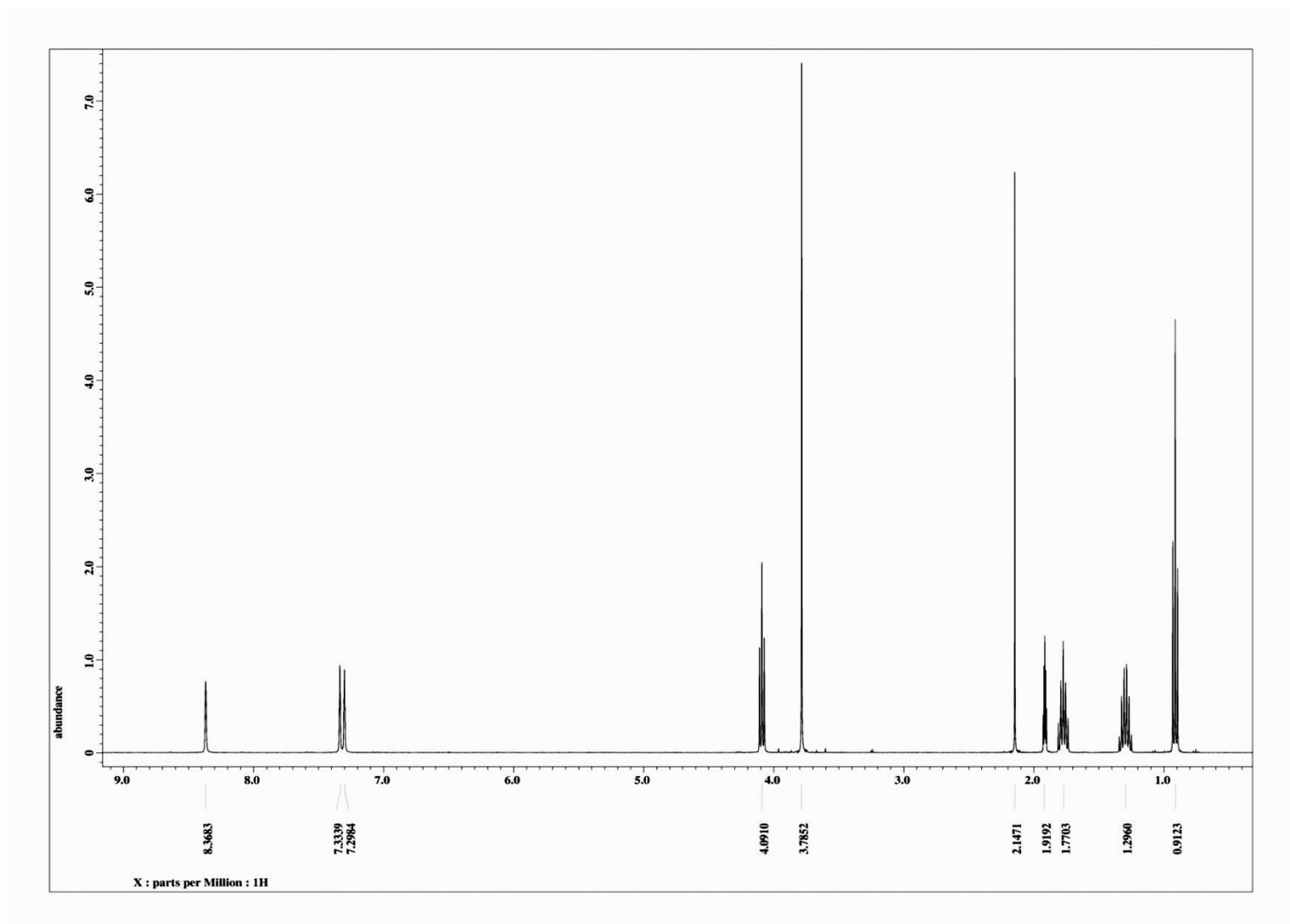


Fig. B-6.  $^{13}\text{C}$ -NMR of [BMIM][TCM] in  $\text{CD}_3\text{CN}$

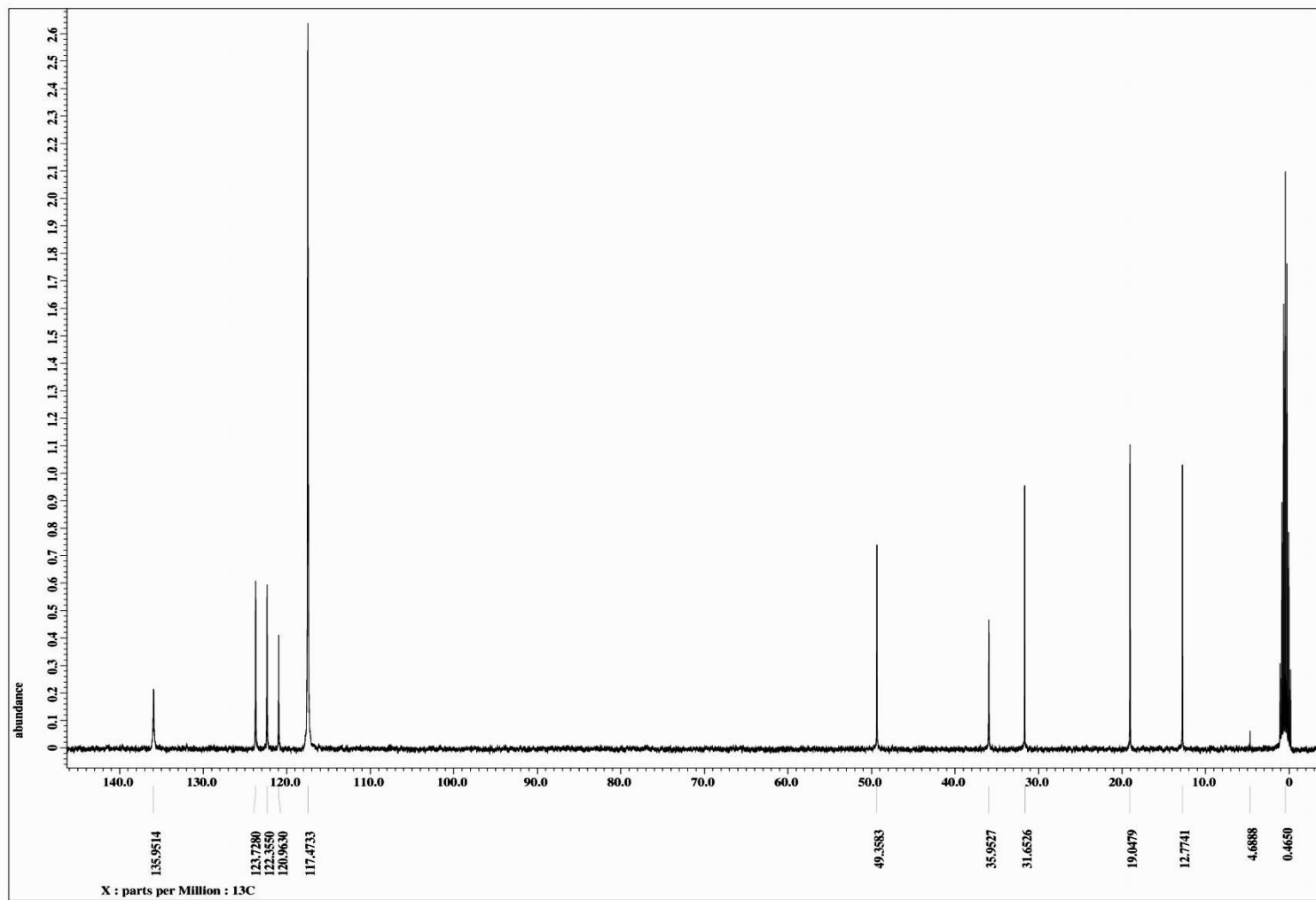


Fig. B-7.  $^1\text{H-NMR}$  of  $[\text{EMIM}][\text{TCB}]$  in  $\text{CD}_3\text{CN}$

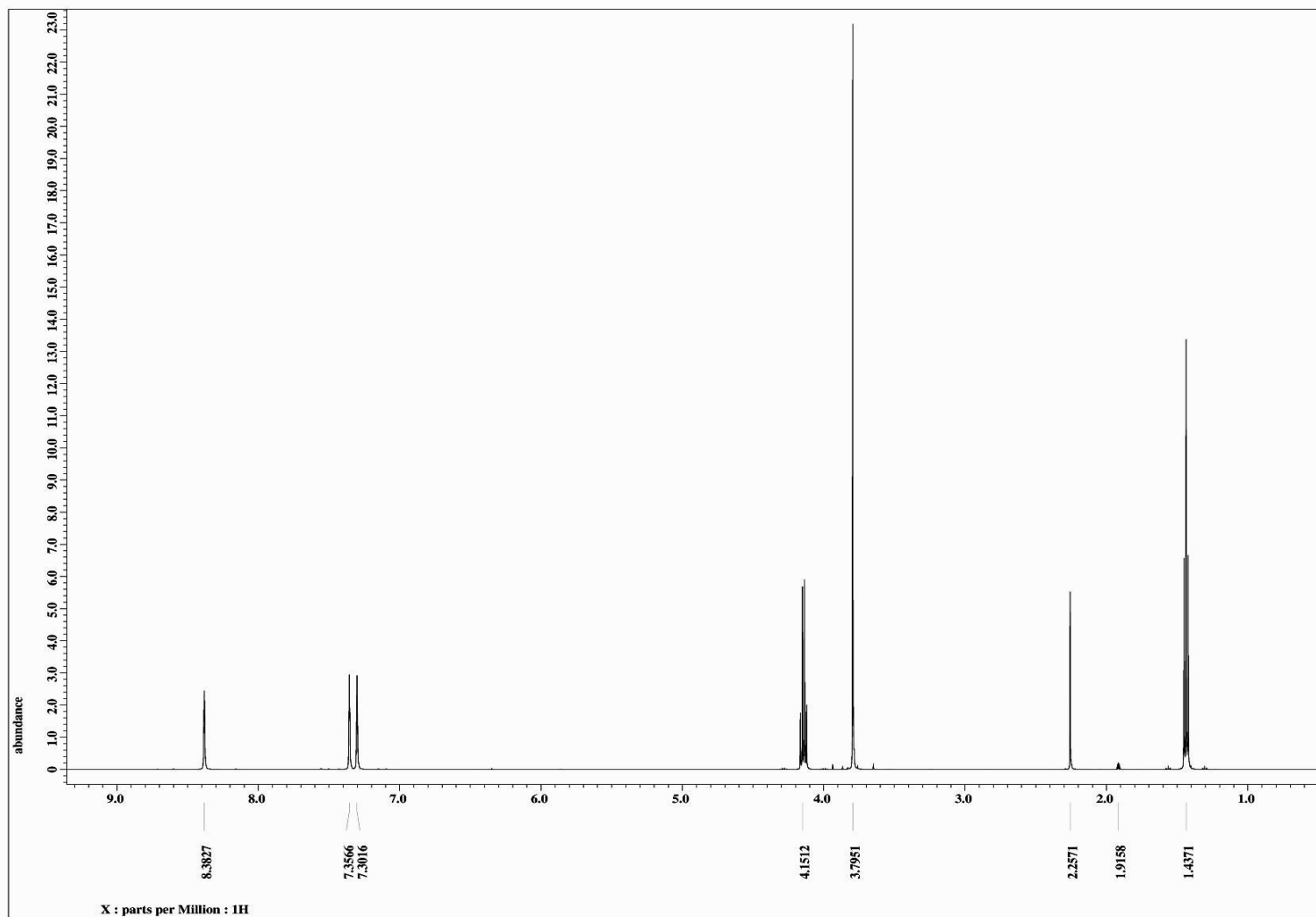


Fig. B-8.  $^{13}\text{C}$ -NMR of [EMIM][TCB] in  $\text{CD}_3\text{CN}$

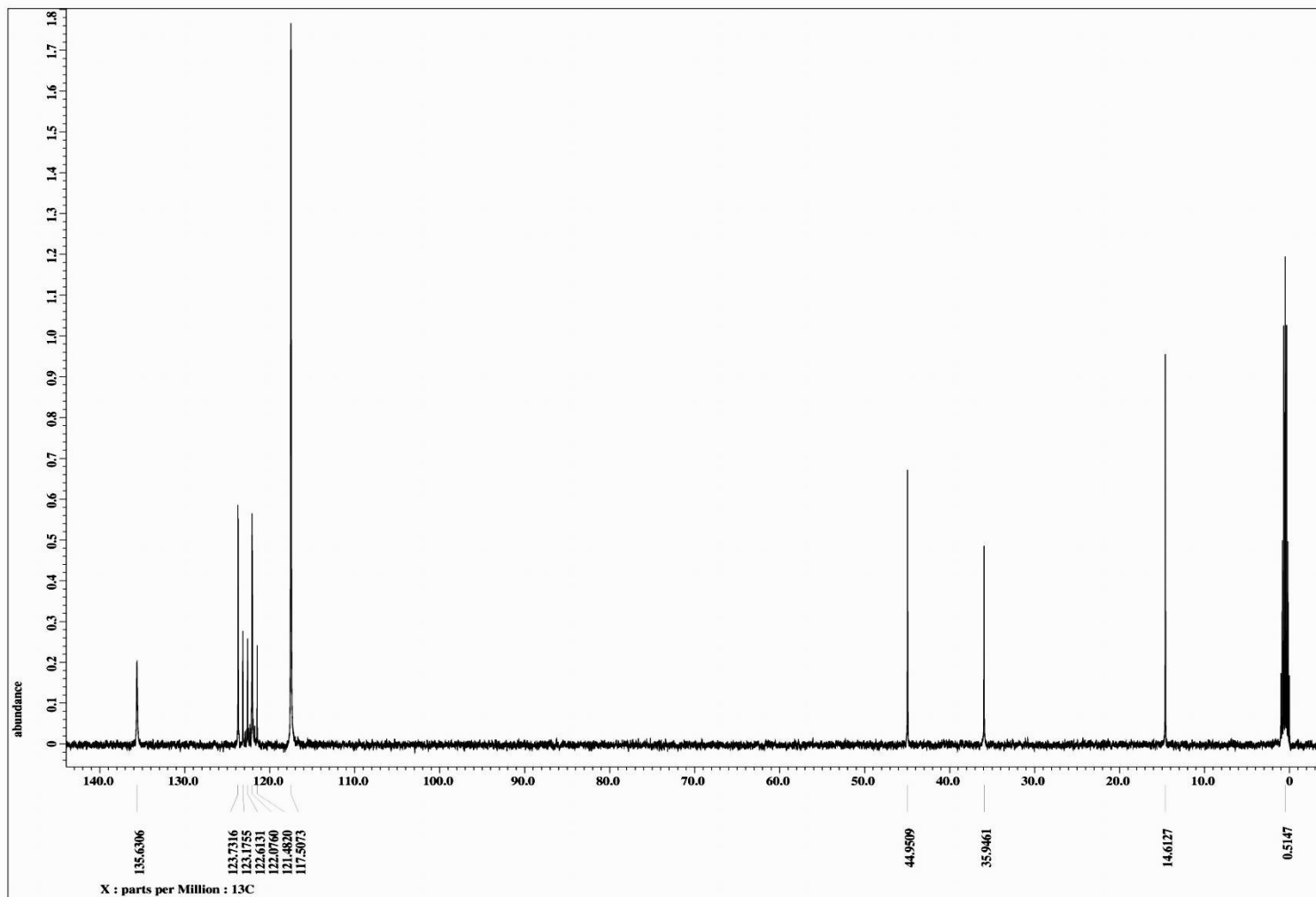
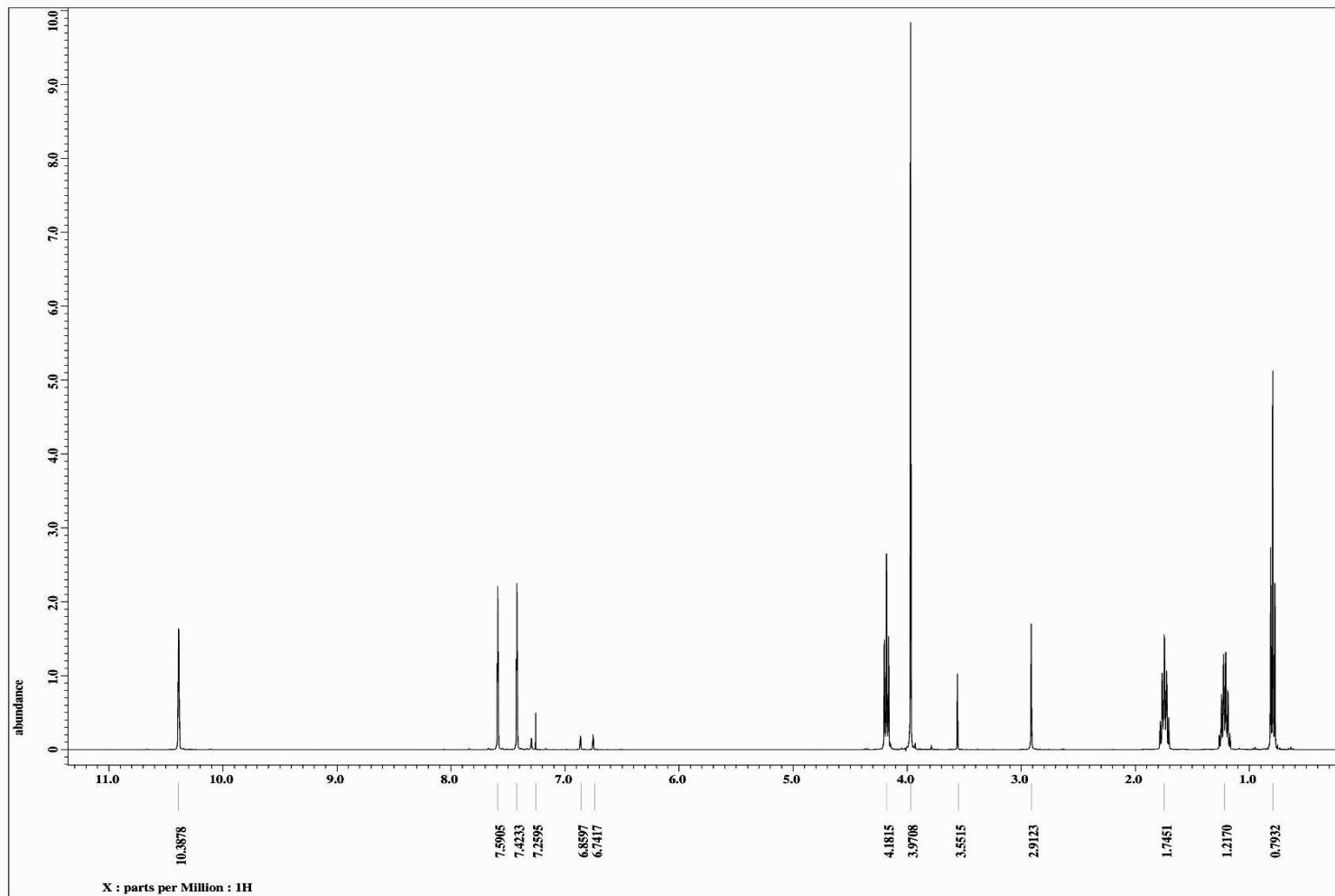
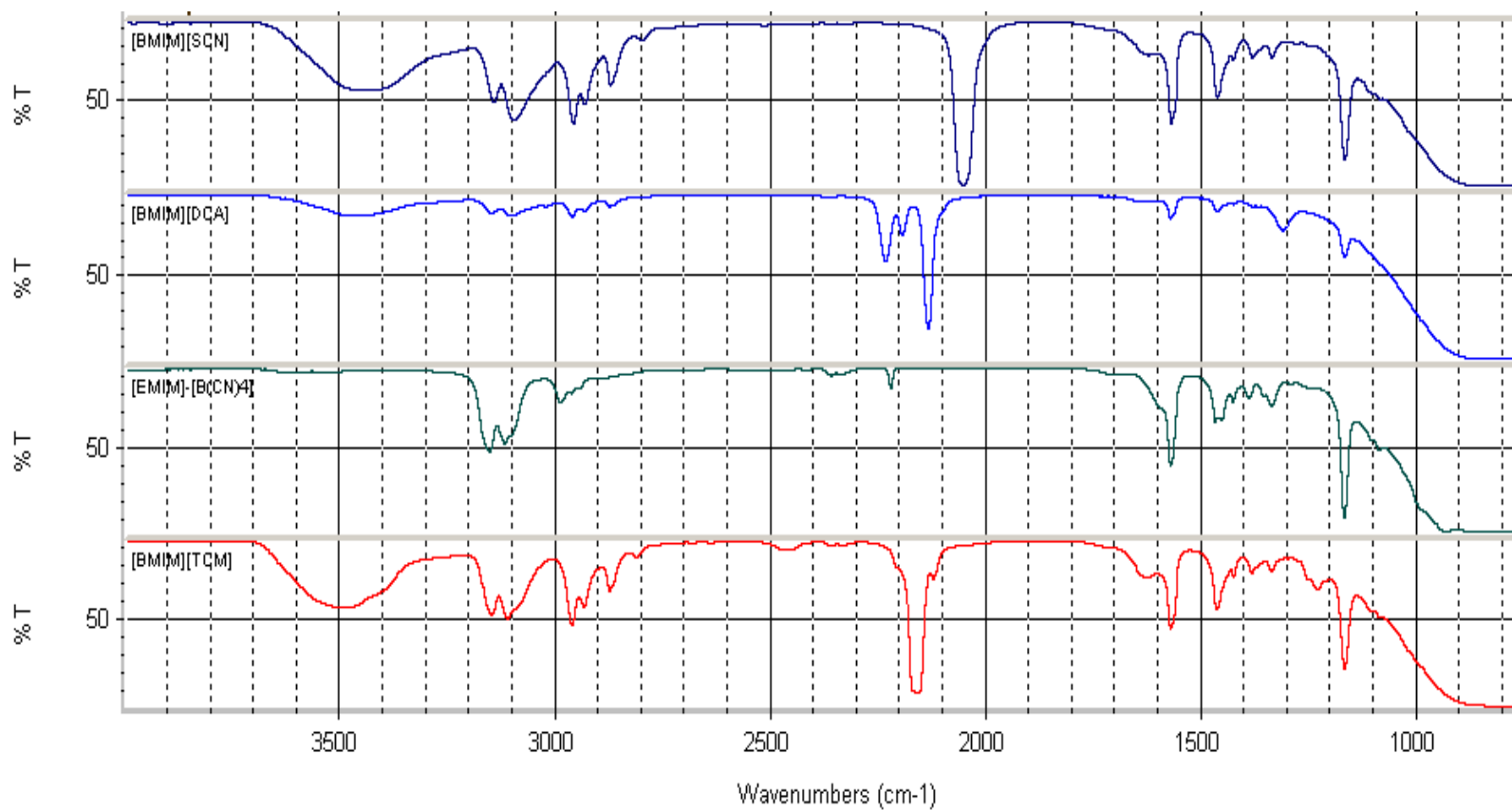


Fig. B-9.  $^1\text{H-NMR}$  of  $[\text{BMIM}][\text{Cl}]$  in  $\text{CDCl}_3$ , showing peaks from 1-methylimidazole starting material during insufficient drying in vacuum.



## II. Infrared Spectra

Fig. B-10. IR Spectra of [BMIM][SCN], [BMIM][DCA], [BMIM][TCM] and [EMIM][TCB]



### III. Raman Spectra

Fig. B-11. Raman Spectrum of [BMIM][SCN]

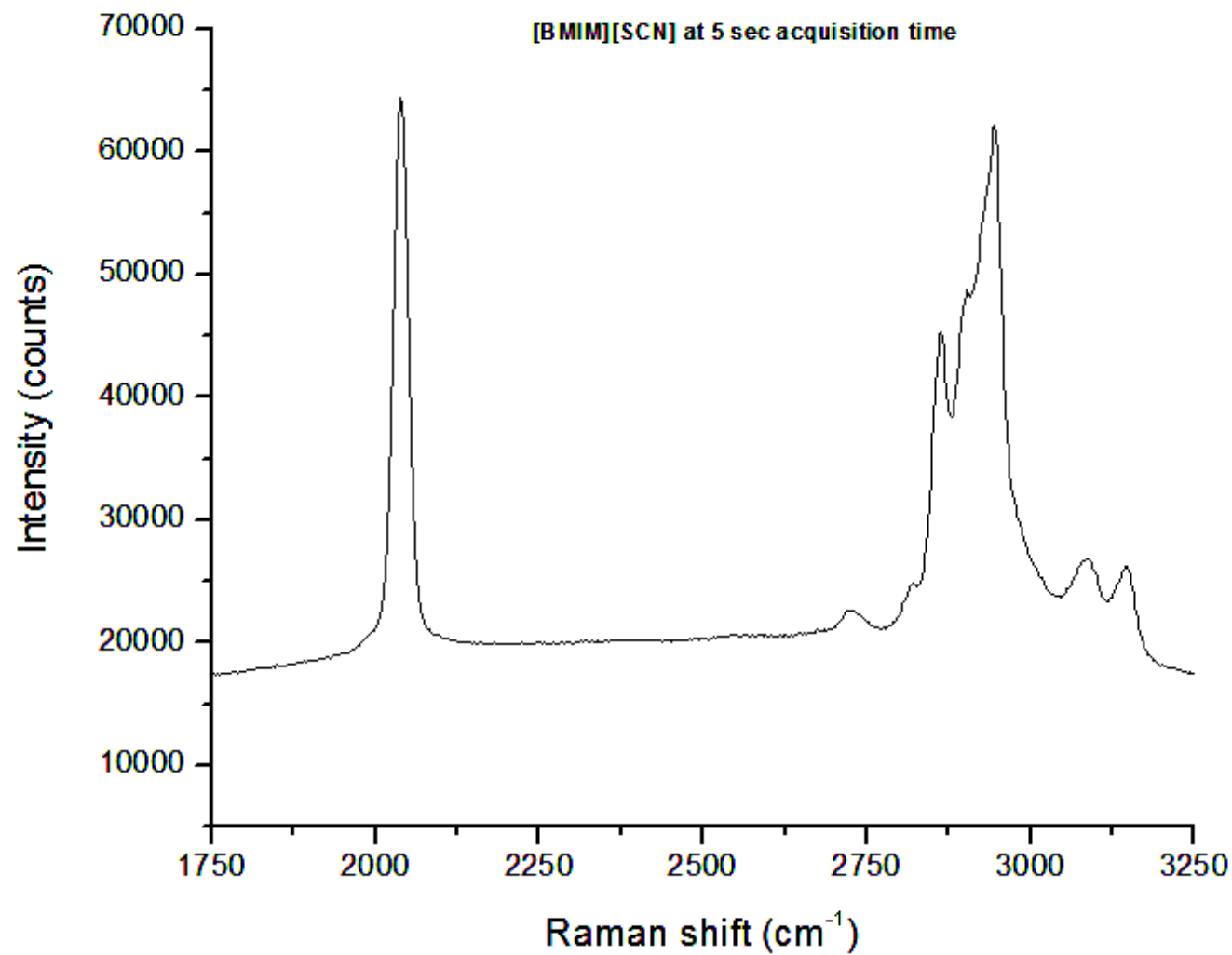


Fig. B-12. Raman Spectrum of [BMIM][DCA]

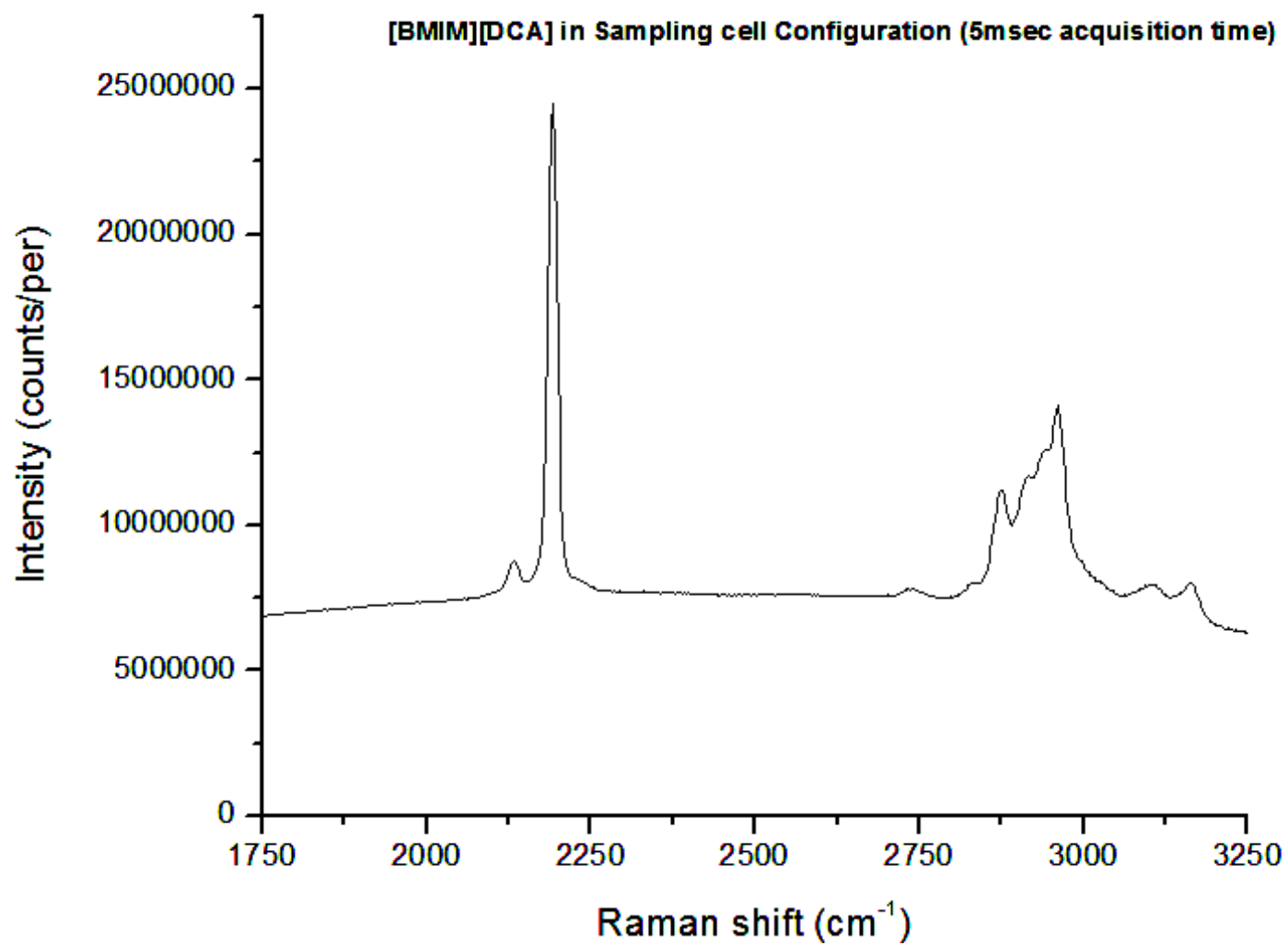


Fig. B-13. Raman Spectrum of [BMIM][TCM]

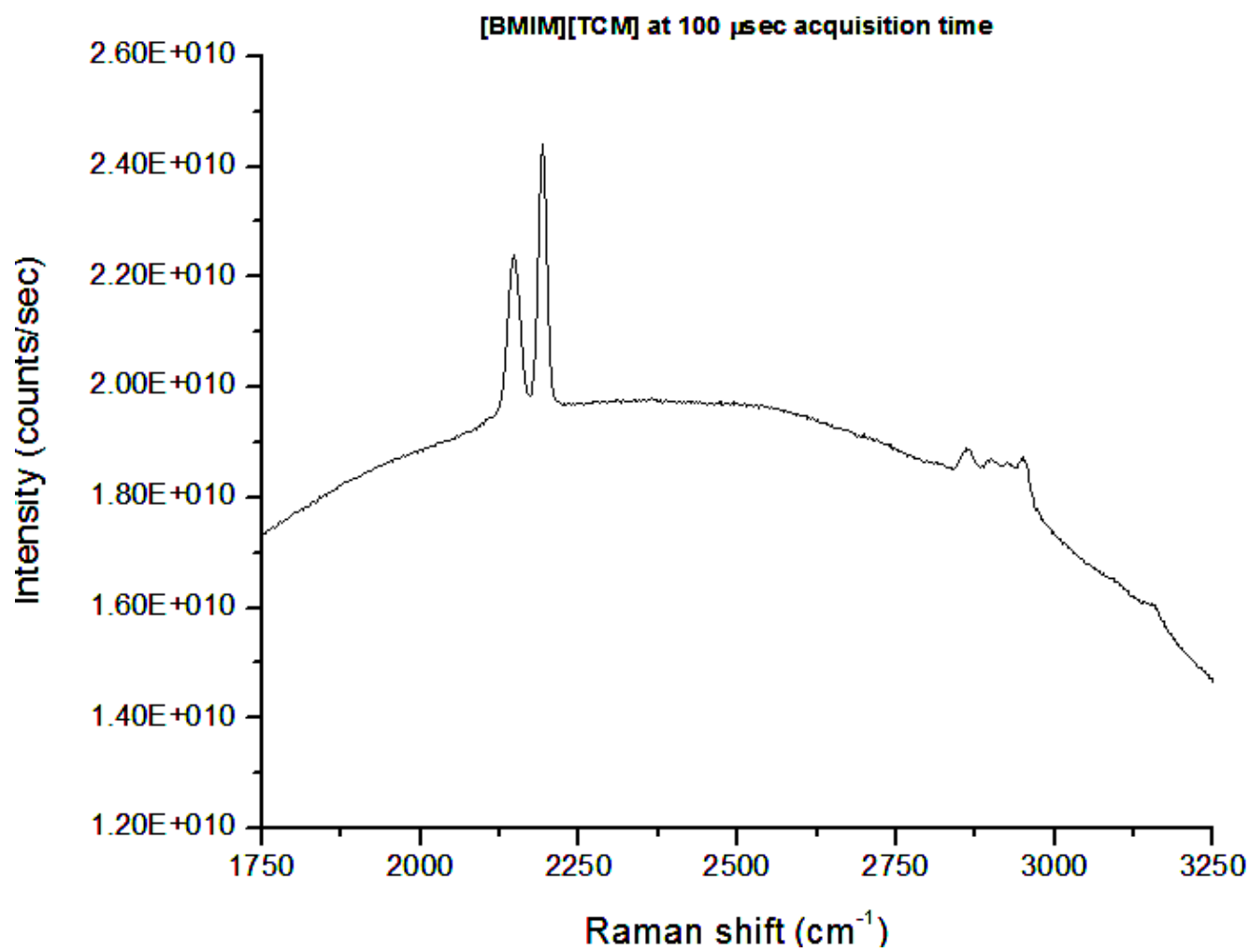


Fig. B-14. Raman Spectrum of [EMIM][TCB]

